Contents

Streszczenie pracy

Badania korelacji barion-barion w relatywistycznych zderzeniach jądrowych rejestrowanych w eksperymencie STAR

Projekt jest elementem badań prowadzonych w ramach eksperymentu STAR (Solenoidal Tracker At RHIC) w Laboratorium BNL (Brookhaven National Laboratory) z wykorzystaniem zderzacza ciężkich jonów RHIC (Relativistic Heavy Ion Collider)- (opis kompleksu eksperymentalnego znajduje się w Rozdziale 5). Celem eksperymentu STAR jest, ogólnie mówiąc, badanie własności materii jądrowej w ekstremalnych stanach gęstości i temperatur. Oczekuje się, że w warunkach uzyskanych wskutek zderzeń ciężkich jonów (np. jąder złota) przy energii w środku masy rzędu 200 GeV/nukleon wytworzony zostanie stan materii jądrowej zwany plazmą kwarkowo-gluonową (QGP). Wytworzenie QGP nie tylko stwarza możliwości badania własności i oddziaływań najdrobniejszych składników struktury materii, ale także stanowi odtworzenie jej stanu w pierwszych mikrosekundach istnienia Wszechświata, zgodnie z hipotezą Wielkiego Wybuchu.

Rozdział 1 zawiera wprowadzenie do fizyki zderzeń ciężkich jonów; pokrótce opisano podstawy chromodynamiki kwantowej (ang. 'Quantum Chromodynamics'- QCD) oraz przedstawiono strukturę diagramu fazowego.

Wyniki pierwszych lat pomiarów prowadzonych z pomocą czterech eksperymentów w BNL rzeczywiście pokazały symptomy wytworzenia stanu materii w którym uwolnione zostały kwarkowe stopnie swobody. Efekty "gaszenia dżetów"(ang. 'jet quenching') - obserwowane w azymutalnych rozkładach cząstek, anomalnych stosunków krotności - wyrażane za pomocą tzw. czynnika modyfikacji jądrowej (ang. 'nuclear modification factor'), efekty ruchów kolektywnych - demonstrowane poprzez wartości współczynnika opisującego tzw. przepływy eliptyczne (ang. 'elliptic flow') i wiele innych, odpowiadają przejściu ze stanu materii hadronowej do stanu materii kwarkowej. Wytworzony stan różni się jednak od oczekiwanego stanu nieodziałujących

kwarków; zbliżony jest raczej swymi własnościami do idealnej cieczy.
Rozdział 2 opisuje aktualny status wyników eksperymentalnych i poszukiwań stanu plazmy. Wyraźnie rozróżniono sektor procesów miękkich (w zakresie niskich pędów: $p < 2$ GeV/c) oraz twardych (dla $p > 2$ GeV/c).
Jednym z efektów, który nadal nie znajduje zadawalającego objaśnienia, jest rozwój w czasie i przestrzeni procesu emisji cząstek z gorącego i ekspandującego układu powstałego w wyniku kolizji ciężkich jonów. Efekt ten, znany pod kyptonimem 'RHIC HBT puzzle', jest faktycznie zbiorem kilku prawidłowości obserwowanych w wynikach pomiarów korelacyjnych, a nie dających się ułożyć w spójny obraz z innymi charakterystykami emitowanych cząstek, obserwowanymi równocześnie. (HBT oznacza tu efekt korelacyjny obserwowany dla par cząstek identycznych). Zagadka wyników pomiarów korelacyjnych widoczna jest głównie w korelacjach naładowanych pionów. Korelacje tych cząstek emitowanych z największymi krotnościami, są bowiem najlepiej zbadane. W tym kontekście szczególnego znaczenia nabierają rezultaty pomiaru korelacji w układach barionowych.
Rozdział 4 przedstawia metodologię badania korelacji dwucząstkowych oraz przegląd najważniejszych wyników eksperymentalnych. Został przedstawiony opis korelacji dla par cząstek identycznych (z wyraźnym podziałem na pary fermionowe i bozonowe) oraz nieidentycznych.
Celem przedstawionej pracy jest analiza dwucząstkowych korelacji pędowych w obszarze małych prędkości względnych dla układów dwubarionowych np. proton-proton, antyproton-antyproton, proton-antyproton oraz w układach dwucząstkowych z udziałem hiperonów. W wyniku tych badań powstał spójny opis oddziaływań w stanie końcowym (ang. 'Final State Interaction'- FSI) dla układów złożonych z różnych kombinacji barionów i antybarionów. Wyznaczone zostały również średnie rozmiary obszarów emisji źródeł emitujących bariony dla dwóch energii zderzenia (62 oraz 200 GeV liczonych na nukleon w środku masy układu zderzajacych się jąder) i trzech centralności zderzenia (zderzenia centralne, średniocentralne oraz peryferyjne liczone w zależności od procentowego udziału przekroju czynnego na badaną reakcję).
Wyniki tej analizy zostały dokładnie omówione w Rozdziale 6 (poświęconym eksperymentalnym szczegółom analizy par dwubarionowych) oraz w Rozdziale 7. Porównanie z otrzymanymi już rezultatami badania korelacji w układach mezon-mezon oraz z przewidywaniami dwóch modeli teoretycznych: UrQMD (Ultra-relativistic Quantum Molecular Model) i EPOS (gdzie nazwa modelu jest skrótem od: Energy-conserving quantum mechanical multiple-scattering approach, Partons, Off-shell remnants, Splitting of parton ladders)- zostało umieszczone w Rozdziale 8.

Wnioski z pracy zostały przedstawione w Rozdziale 9 i dotyczą następujących aspektów:

- W odróżnieniu od korelacji identycznych mezonów, a w szczególności pionów, gdzie efekty korelacyjne są głównie rezultatem statystyki kwantowej (ang. 'Quantum Statistics'- QS) - korelacje w układach dwubarionowych są przede wszystkim następstwem oddziaływań w stanie końcowym (ang. 'Final State Interactions'- FSI), kulombowskich i silnych. Po drugie, bariony są cząstkami o zasadniczo większych masach niż piony czy kaony, a emitowane protony są w dużej części, przy energiach akceleratora RHIC, składnikami zderzających się pocisków nawet w obszarze małych pospieszności. Dlatego bardzo ważne jest poznanie czasowo-przestrzennej ewolucji procesu ich emisji oraz roli jaką odgrywają w relacjach pomiędzy ruchami termicznymi i kolektywnymi gorącej i ekspandującej materii utworzonej w wyniku zderzenia. Porównanie wyników uzyskanych dla par protonów z analogicznymi wynikami dla par antyprotonów oraz korelacjami w układzie proton-antyproton, a także z udziałem hiperonów i zestawienie uzyskanych rezultatów z istniejącymi już wynikami dla par mezon-mezon, mają zasadnicze znaczenie dla uzyskania kompletnego obrazu końcowego etapu procesu zderzenia relatywistycznych jonów. Właśnie niespójność równoczesnego opisu przez modele hydrodynamiczne jednocząstkowych rozkładów pędowych oraz korelacji dwucząstkowych, stanowi główny element 'RHIC HBT puzzle'.

- Po raz pierwszy udało się uzyskać spójny obraz korelacji barionowych. Po raz pierwszy także możliwe stało się badanie korelacji dla układów złożonych z cząstek charakteryzujących się niską krotnością produkcji. Przeprowadzone do tej chwili badania w ramach przedstawianej tu pracy pokazały nie mierzone nigdy wcześniej korelacje dla par antyproton-antyproton. Jako jeden z elementów realizacji tego projektu przeprowadzona została także analiza wpływu tzw. korelacji szczątkowych (ang. 'residual correlations') na funkcje korelacyjne badanych układów dwunukleonowych. Uwzględnienie korelacji szczątkowych jest szczególnie istotne w przypadku barionów, ponieważ znaczna część tych, które są rejestrowane, pochodzi z rozpadów wskutek oddziaływań słabych i reprezentuje korelacje dla innego układu, w dodatku zdeformowane kinematyką rozpadu. Dotychczas nie było potrzeby szczegółowej analizy tego typu efektów. Niewielkie krotności barionów produkowanych w zderzeniach przy niższych energiach, w szczególności krotności hiperonów, praktycznie uniemożliwiały wykonanie szczegółowej analizy dla układów innych niż dwuprotonowe. Fakt ten sprawiał również, że rola korelacji szczątkowych nie była zbyt duża. Przy energiach akceleratora RHIC i dużej akceptancji

detektora STAR rola tego typu efektów nie może być pominięta w analizie. Opracowana w ramach tego projektu technika uwzględnienia korelacji szczątkowych może zostać zastosowana również i do innych par cząstek, gdzie wpływ korelacji szczątkowych na mierzone korelacje jest istotny.

- Jeszcze jeden rodzaj analizy danych jest szczególnie istotny dla niniejszego projektu. Chodzi o korelacje cząstek nieidentycznych umożliwiające wyznaczenie czasowo-przestrzennych asymetrii w emisji dwóch typów cząstek np. protonow i antyprotonow lub protonów i hiperonów. Analiza taka, niemożliwa dla układów cząstek identycznych, polega mówiąc najprościej, na wydzieleniu przypadków, w których cząstka określonego typu, np. antyproton, emitowana jest z większą prędkością niż druga cząstka analizowanej pary. Wydzielenie takiego przypadku oraz komplementarnej sytuacji przeciwnej i zastosowanie dedykowanej temu procedury analizy danych umożliwia uzyskanie informacji, który z dwóch typów analizowanych cząstek został wyemitowany z mniejszych (wcześniejszych), a który z większych (późniejszych) obszarów czasowo-przestrzennych. Uzyskane wyniki umożliwiły więc weryfikację stanu wiedzy uzyskanej klasycznymi metodami interferometrii jądrowej (HBT) poszerzając ją o opis źródeł emitujących bariony. Analiza korelacyjna par proton-antyproton skonfrontowana z przewidywaniami modeli uwzgędniających efekty rozpraszania, dowiodła, że mimo identycznych mas cząstek, ich średnie czasy oraz obszary emisji nie są identyczne. Wskutek anihilacji, antyprotony są emitowane średnio później oraz/lub z mniejszych obszarów niż protony.

Poniżej zostają przedstawione aspekty techniczne i fizyczne opisywanych prac.
Część techniczna pracy to:

- Wybór odpowiednich kryteriów selekcji cząstek oraz ich par, aby mierzyć korelacje z jak najmniejszym wpływem efektów detektorowych. W przypadku przeprowadzonej analizy była to eliminacja następujących efektów:

1. zjawiska przykrywania się dwóch śladów cząstek w detektorze (identyfikacja jednego śladu cząstki zamiast dwóch),
2. zjawiska rozszczepiania się śladu jednej cząstki (identyfikacja jednego śladu cząstki jako dwa różne ślady),
3. identyfikacji produktów konwersji kwantów gamma na pary elektron-pozyton, jako pary proton-antyproton.

- Stworzenie oprogramowania umożliwiającego niezbędne korekcje: na błędnie zidentyfikowane cząstki oraz na zmierzone korelacje szczątkowe. Należało także oszacować wpływ skończonej rozdzielczości detektora.

Część fizyczna pracy składa się z następujących elementów:

- Przedstawienie wyników analizy w pełni skorygowanych korelacji trzech kombinacji protonów oraz ich antycząstek. Wszystkie wyniki dla zanalizowanych energii zderzenia oraz ich centralności są ze sobą spójne w zakresie niepewności statystycznych i systematycznych. Oprócz rozmiarów źródeł zbadano sekwencję czasowo-przestrzenną emisji par cząstek nieidentycznych.
- Porównanie wyników eksperymentalnych z przewidywaniami modeli uwzględniających procesy rozproszeń wtórnych (UrQMD). Przedstawiona analiza dowiodła, że wskutek anihilacji antyprotonów z protonami, antyprotony są emitowane wcześniej oraz/lub z mniejszych obszarów niż protony.

Zaprezentowane wyniki wskazują na celowość kontynuacji badań dla par barionowych w innych warunkach eksperymentalnych np. w przygotowywanym obecnie eksperymencie ALICE jaki będzie realizowany na zderzaczu Large Hadron Collider (LHC) w laboratorium CERN.

Abstract

Studies of baryon-baryon correlations in relativistic nuclear collisions registered at the STAR experiment

This work is the part of scientific program of the STAR experiment (Solenoidal Tracker at RHIC) in BNL (Brookhaven National Laboratory) operated with RHIC (Relativistic Heavy Ion Collider). The main goal of the STAR experiment is to measure the properties of extremely hot and dense matter created during heavy-ion collision. STAR complex is described in Chapter 5. It is expected that as a result of collision of gold nuclei at energy $\sqrt{s_{NN}} = 200$ GeV/nucleon a new form of matter - QGP (Quark Gluon Plasma) will be created. Such new state will enable one to measure properties of the smallest matter constituents, which is also predicted to have existed after few micro-second after Big Bang.

Chapter 1 contains the introduction to the heavy-ion collisions; the basics of QCD and phase diagram is presented.

During first years of operations, the results of four RHIC experiments indicate the formation of new state of matter. The results of *jet quenching*, *nuclear modification factor*, collective motions expressed by *elliptic flow* and many others describe a phase transition from ordinary hadron matter to quark matter. However, the QGP was expected to reflect properties of ideal gas. Created matter indicate rather properties of ideal liquid, thus it was called *sQGP* (strongly interaction QGP).

Chapter 2 describes experimental status of QGP research.

Two-particle correlations can also probe matter created during such collisions. The method and the experimental review is described in Chapter 4. The length of homogeneity measured by femtoscopy methods includes the effects of space-momentum correlations. Together with the relations between thermal and collective motions, between chemical and thermal freeze-out, with the effects of resonance production and secondary rescattering the final image of space-time evo-

lution of the system represents a very complex phenomena, whih is difficult to describe quantitatively. A consistent description clearly needs the information coming both from the analysis of light (pions) and heavy (protons) systems.
A detailed analysis performed already for identical mesons: pions and kaons and the pioneer work with the pion-kaon correlations have revealed a lot of unexpected effects commonly known as *RHIC HBT puzzle*. More information was clearly necessary. This work is a step forward to fill this gap and it describes results of correlations for baryonic systems.
The results of this work complement information obtained earlier by the *HBT Physics Working group* of the STAR experiment at BNL.
The following classes of two-particle systems, incident energies and event centralities have been considered in the frame of this work:

- all combinations of two particle systems consisting of protons and antiprotons: ($p-p$), ($\overline{p}-\overline{p}$,$p-\overline{p}$),
- two energies of colliding gold nuclei: 200 GeV and 62 GeV per nucleon pair,
- three classes of event centralities, according to the percentage of the total hadronic cross-section: central (0-10)%, mid-central (10-30)%, peripheral (30-80)%.

The following experimental results (Chapter 7) have been obtained:

- For the first time the analysis of two antiproton correlations has been performed and the sizes of antiproton emission region in relativistic heavy ion collisions has been estimated.
- For the first time the analysis of two-particle correlations for all systems of protons and antiprotons, simultaneously and in the same experimental conditions, has been performed. The obtained quantitative results are consistent within the experimental uncertainties.
- For the first time the asymmetry between space-time parameters of proton and antiproton emission has been analyzed and quantitatively estimated. A small asymmetry has been found, showing that antiprotons are emitted earlier or more close to the edge of the emitting system.

The analysis for all three proton/antiproton systems have been performed in the same way in all energy/centrality classes; the same event selection criteria have been applied; the same corrections have been introduced and the same approach was used to estimate the influence of residual

correlations. Thus the effect of systematic errors was strongly reduced, what is important for the quantitative comparison and for common analysis of all the results obtained in this work.
Chapter 6 present the analysis chain.
In order to obtain the physics results free of experimental distortions, the methodical analysis has been performed.

- A set of cuts have been applied for the registered tracks to eliminate the merging effect which makes that instead of two separate tracks, only one is reconstructed.
- A dedicated analysis of the tracks located very close in the detector space have been performed in order to avoid the splitting effect which causes that instead of one single track, two track are found.
- The contamination of electron - positron pairs have been removed.
- The effect of finite detector resolution has been taken into account as well.
- A special attention has been put to the effect of residual correlations resulting mainly from the contamination of the proton/antiproton sample by the particles (also protons or antiprotons) coming from the week decays of hyperons. This effect is much more pronouced for protons than for pions. Due to kinematics of lambda-hyperon decay, proton practically follows the direction of lambda particle in the detector space and cannot be distinguished experimentally from that coming directly from the interaction point. A detailed procedure has been developed and the decays of lambda and sigma hyperons have been considered, including the decay kinematics. The reflection of FSI correlations in the proton/antiproton hyperon systems, in the studied proton-antiproton correlations have been taken into account. One should mention here that such analysis of correlations was made for the first time for the baryonic systems. This can be important for the comparison of the results obtained here with the other results obtained elsewhere, where the residual correlations have not been taken into account properly.

The following conclusions (Chapter 8 presents discussion) can be drawn:

- The measured vales of proton/anti-proton emission regions are systematically smaller then that of pions and kaons with similar transverse momenta. Considering this result on the base of hydrodynamic approach and taking into account the larger mass of protons with respect to kaons and pions, one can understand it as an interplay of thermal and collective

motion of hot and expanding system. Thus, pairs of lighter particles are on average emitted from the region of larger dispersion.

- The increase of measured sizes with the event centrality reflects the geometry of the colliding systems. This dependence is similar to that for pions and kaons.

- The values of emission sizes obtained for 200GeV are slightly larger than those for 62GeV. More statistics is necessary however to make quantitative conclusion.

- The obtained results are in qualitative agreement with the predictions of theoretical models: UrQMD and EPOS. It is not the case however for the asymmetry results of nonidentical particle correlations (see below).

- A small, but definitively nonzero, asymmetry shift has been found in the analysis of proton-antiproton correlations. One should mention here that a relatively large shift was experimentally found earlier for the pion-kaon system. This result is consistent with the hydrodynamic description, where the mass differences lead to the space-time asymmetries. Such effect cannot be attributed however to the particles with the same masses. The asymmetry shift is also absent in the results of simulations with the EPOS model but is seen in the results of UrQMD simulations. The difference between EPOS and UrQMD, important for the final stage of the interaction dynamics, consistent in the absence of rescattering processes in the EPOS model. One can conclude that the annihilation processes at the last stage of the collision can be responsible for the observed asymmetry. This conclusion is also consistent with the sign of asymmetry effect, showing that antiprotons are emitted earlier or more close to the edge of the emitting system than protons.

The analysis performed here is a step forward in the direction of consistent description of the dynamics of heavy ion collisions, mainly in the part of so called soft processes.
In order to continue such measurements, it is necessary to have more statistics of experimental data. In a natural way it can be achieved in the next generation experiment ALICE being prepared now at CERN. Much larger particle multiplicities and the better detection possibilities makes good perspectives for such measurements.

Acknowledgments

First of all, I would like to thank whole STAR Collaboration at the RHIC community. This research could have never been realized without You. I would like to thank primarily Dr Timothy Hallman for the possibility of taking part in such excellent project as the STAR experiment.
Special thanks to my both supervisors: Professor Barbara Erazmus and Professor Jan Pluta, who inspired me, gave necessary guidance and always supported various ideas. Thanks to You I was able to live through exciting adventure that I never thought could have happened to me. You provided necessary encouragements and warm words. I will never forget that You have been staying with me in the most painful moments as Friends.
I would like to extend my gratitude for support to the whole Heavy-Ion Reaction Group at Faculty of Physics at Warsaw University of Technology and to SUBATECH laboratory- for hospitality during my several stays here.
Valuable discussions with Dr Adam Kisiel and Professor Michael Lisa let me open my mind to many crucial aspects of the femtoscopic measurements. Theoretical input from numerous discussions with Professor Klaus Werner and Dr Richard Lednicky was essential. Many thanks to the all members of GDRE community. This project enables cooperation of many great scientists from West and Central Europe. Common work during numerous workshops in Nantes have been teaching me how to exchange experience.
Many, many thanks go for fruitful discussions to the not mentioned yet STAR HBT Group members: Dr Sergey Panitkin, Dr Fabrice Retiere, Zbyszek Chajecki, Marcin Zawisza, Maciek Jedynak, Michal Bystersky, Peter Chaloupka, Debasish Das, Anneli Bellingeri.
As English is not my native language, I would like to express my deep gratitude to Marek, who had spent his time and help me to improve English in this thesis.
Special thanks to my Parents. You always support me and never let me down. Thank You so much.
Last, but surely not least I would like to express my deep love and thanks to my husband Paweł. You have always been waiting till I come back from various and frequent trips. I love You for

understanding how deep passion Physics is for me, for Your strong and warm arms always when I need You. You are my Love and the best Friend.

Introduction

The 'Big Bang' is a cosmological model of the Universe, whose primary assertion is that the Universe has expanded into its current state from a primordial condition of enormous density and temperature. It has been shown that 'Big Bang' is consistent with general relativity and with the cosmological principle, which states that properties of the Universe should be independent of position or orientation. Observational evidence for the 'Big Bang' includes the analysis of the spectrum of light from galaxies, which reveals a shift towards longer wavelengths proportional to each galaxy's distance in a relationship described by Hubble's law. Combined with the assumption that observers located anywhere in the Universe would make similar observations (the Copernican principle), this suggests that space itself is expanding. The 'Big Bang' is the best model for the origin and evolution of the universe.

Many scientists have intended to build experimental complexes which would enable reproduction of conditions that existed just a few moments after the 'Big Bang'. For many years possibilities of building greater and bigger complexes have been increasing, with maximal reachable energy rising as well. For such reasons, the theory of high-energy physics must have been formed.

Why high-energy physics? Because particle physics deals with the study of elementary constituents of matter. 'Elementary' means here that such particles do not have known structure. In the beginning of the twentieth century, particle beam energies from accelerators only reached a few MeV. Experimental techniques made then possible one to consider protons and neutrons as elementary particles. Nowadays, with advanced experimental complexes, it is possible to measure even the structure of a single nucleon, and other elementary components as well (quarks and leptons). Another reason for high energies is that many of the elementary particles are extremely massive ones, thus ($E = mc^2$) requiring high amounts of energy to be created. The heaviest elementary particle detected so far is the 'top' quark (which has to be created as a pair with their anti-particle), with the mass-energy of $mc^2 \simeq 175$ GeV - almost 200 times more than that of a proton.

Nowadays, the biggest operating accelerator is the Relativistic Heavy Ion Collider (see Chapter

5), with another one, the Large Hadron Collider at CERN, in the final phase of installation. These projects enable one to measure the basic structure of elementary matter. Chapter 1 encloses the basics of heavy-ion collisions. The properties of collision can be deduced by analyzing characteristics of created particles: hadrons, leptons, .. Chapter 2 presents a review of experimental results. First prerequisites about phase transition from ordinary matter to the partonic phase are discussed. RHIC results are divided into sectors of soft processes and hard probes. Chapter 2 reviews an experimental status of known properties of bulk matter. In parallel to experimental observables, theoretical models are presented (Chapter 3), in order to understand better heavy-ion collisions. The method to probe the source of emitting particles is two-particle interferometry. Chapter 4 contains theoretical description of the correlation technique and an experimental review of the most exciting results from last few decades as well. As this work is dedicated to two-baryon femtoscopic measurements, Chapter 4 discusses briefly the most important two-proton correlation results obtained so far. The RHIC complex and its experiments are presented in Chapter 5, which is mainly dedicated to the STAR program. Chapters 6, 7 and 8 present results of proton femtoscopy from the STAR experiment. Chapter 6 describes technical aspects of how to construct a two - proton, two - anti-proton and proton - anti-proton correlation functions properly in STAR. Chapter 8 shows experimental results and Chapter 9 discusses them comparing to the model predictions. The aim of this work is to obtain as global and deep view on baryon correlations as it is possible from experimental and theoretical point of view, in order to learn more about properties of the emission of protons and anti-protons.

Chapter 1

Some base concepts of Heavy-Ion Collision Physics

Heavy-ion collisions at high energies [1, 2] allow one to study the elementary components of matter and the interactions between them. Relativistic heavy-ion collisions give also the possibility to study the behavior of nuclear matter under extremely high pressure and temperature. It is supposed that such conditions were present during first moments after Big Bang [3]. They can be recreated experimentally in heavy-ion collisions at ultra-relativistic energies, using the colliders, such as Relativistic Heavy Ion Collider (RHIC) (more in Section 4.1) and in the near future the Large Hadron Collider (LHC).

1.1 The QCD phase diagram and the QGP

During high-energy collisions (for a more detailed description, see Section 1.2) a hot and dense system of strongly interacting particles is produced. As quarks and gluons are not allowed to exist separately and thus have to be bind in hadrons at low energy densities, with the increasing temperature (heating) and/or increasing baryon density (compression), a phase transition may occur to the state where ordinary hadrons do not exist anymore and where quarks and gluons become the correct degrees of freedom. This extreme state of color-deconfined matter is called Quark-Gluon Plasma (QGP) [4, 5, 6, 7, 8, 9, 10, 11]. The theory describing strong interactions confining quarks into hadrons is a quantum field theory called 'Quantum Chromodynamics' (QCD).

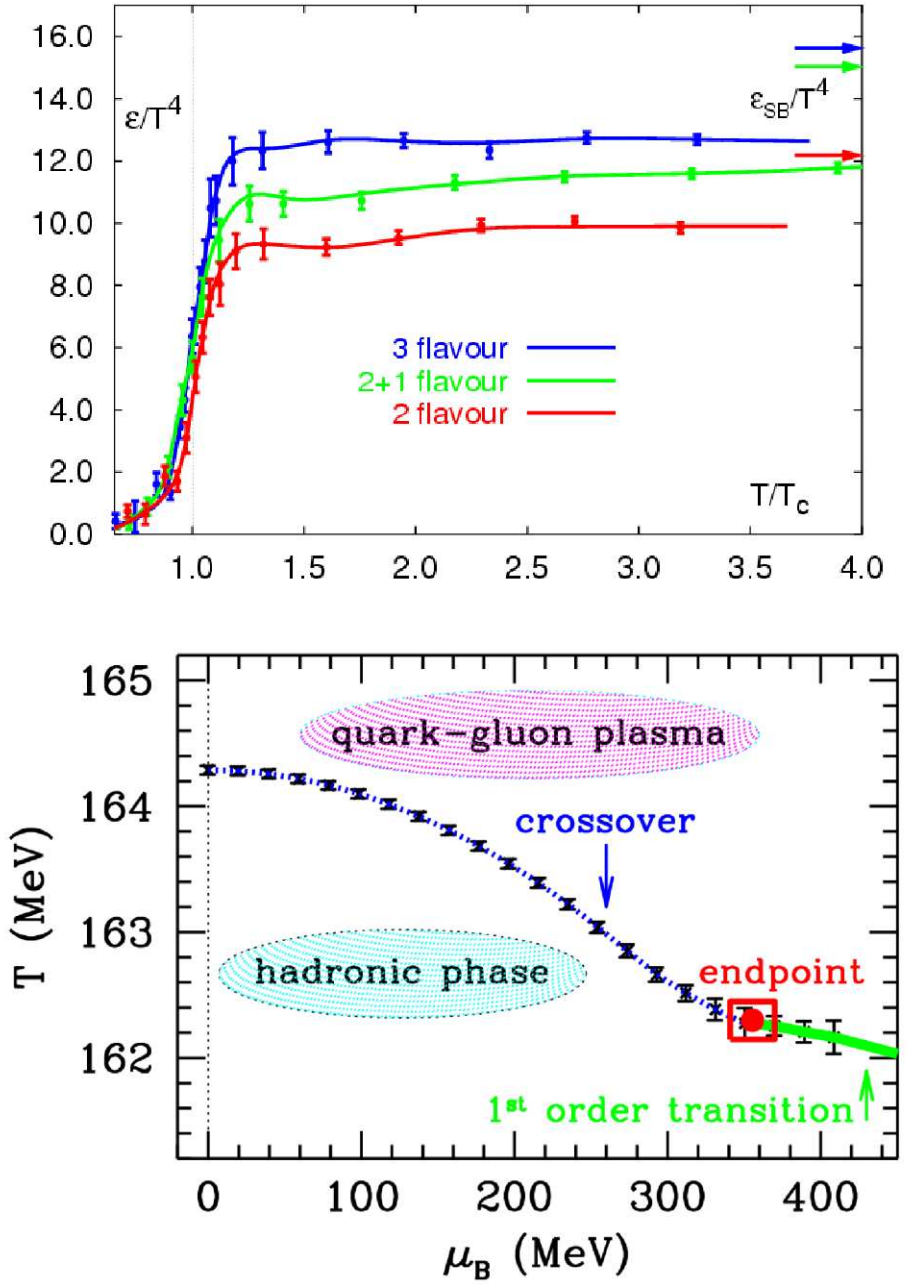

Figure 1.1: Top panel: Lattice QCD (LQCD) predictions for the energy density ϵ/T^4 as a function of temperature T relative to the critical temperature T_c. Flavor dependence is illustrated for the three curves, depicting results on three quarks (u,d,s), 2 light (u,d) plus one heavier (s) quark and 2 light quarks (u,d) as indicated above. The Stefan-Boltzmann values are depicted by the arrows to the right [10]; bottom panel: LQCD calculation results for non-zero chemical potential, suggesting the existence of a critical point well above RHIC chemical potential values. The solid line corresponds to first-order phase transitions, dotted curve indicates crossover transition between hadronic and the QGP phase [11].

QCD is the theory of the strong interaction. It is an important part of the Standard Model of particle physics [12, 13]. The most striking feature of QCD is confinement. At small distances quarks and gluons interact weakly and stronger while increasing the distance between them. The physical concept may be illustrated by a string spanned between quarks while trying to separate them. If the quarks are pulled too far apart, high energy deposited in the string is released, the latter breaks into smaller pieces and as a result a new form of hadrons is produced from these pieces of the initial string. The nuclear forces between baryons and mesons are viewed as a residual forces between quarks and gluons. In the terminology of high energy physics, the QCD confinement scale is:

$$\Lambda^{-1} \simeq (0.2GeV)^{-1} \simeq 1fm \tag{1.1}$$

With increasing temperature T, the strong coupling constant $\alpha_s(T)$ becomes smaller, reducing the binding energy, and the string tension $\sigma(T)$ becomes smaller, increasing the confinement radius and effectively screening the potential:

$$V(r) = \frac{4}{3}\frac{\alpha_s}{r} + \sigma r \rightarrow \frac{4}{3}\frac{\alpha_s}{r}e^{-\mu r} + \sigma\frac{1-e^{\mu r}}{\mu} \tag{1.2}$$

where $\mu = \mu(T) = 1/r_D$ is the Debye-screening (see the Glossary at the end of the thesis) mass and r_D is the Debye screening radius. For $r < 1/\mu = r_D$ quarks are bound but for $r > 1/\mu = r_D$, they are free of potential and effectively deconfined. The most accurate predictions of the phase transition are given by numerical calculations on the lattice. It is a challenge of ultra-relativistic heavy-ion collisions to observe two phase transitions predicted by QCD: discussed 'deconfinement' and 'chiral symmetry restoration'. The notion of chiral symmetry is related to the spin of particle and its 'handeness'. The chirality of a particle is 'right-handed' if the direction of its spin is the same as the direction of its motion. It is 'left-handed' if the directions of spin and motion are opposite (for more description about chirality, see description in the Glossary). Theories with massless fermion fields feature chiral symmetry, i.e., rotating the left-handed and the right-handed components independently makes no difference to the theory; on the other hand massive fermions do not exhibit chiral symmetry. The mass spontaneously breaks chiral symmetry. Therefore, chiral symmetry introduced here is a symmetry of light quark flavors due to their small masses and it is spontaneously broken. The theory says that at high temperatures and densities it should be restored.

Figure 1.1 (top panel) shows result of numerical calculations [10] of the energy density ϵ of colored matter as its temperature T is increased. The ratio ε/T^4 is related to the number of degrees of freedom which describe the system. The rapid rise of this quantity signals the onset of decon-

finement above some critical temperature T_c. A relatively sharp deconfinement transition occurs at a temperature of approximately 175 MeV in 2-flavor QCD and below this temperature quarks and gluons are confined inside hadrons, so only protons and neutrons can be taken into account to describe system. At higher temperatures more degrees of freedom have to be considered.
The most familiar example of phase transitions is the 'phase diagram' of water, where controlled parameters are temperature T and pressure p. Water is commonly described as having three phases: gas, liquid, and solid. There, a dependence $p(T)$ describes the transition from one phase to another (solid to liquid and liquid to gas), which transition depends on pressure and temperature.
Two energy regimes are discussed for the QGP state and phase transitions: at lower energies, $\sqrt{s_{NN}} \simeq 5 - 20$ GeV, typical for the AGS (BNL) and SPS (CERN) programs, the nuclei are expected to stop each other, leading to baryon-rich systems; this is the regime of maximum baryon density. At higher energies, $\sqrt{s_{NN}} \geq 100 - 200$ GeV, nuclei become more transparent and nuclear fragments are better separated from the central region of particle production at mid-rapidity. This regime (baryon chemical potential $\mu_B = 0$) is expected to be baryon-free, or QGP (pure QGP regime); high-energy experiments consider it as a region of "less-baryon density".
In the bottom panel of Figure 1.1 a schematic phase diagram is shown. The phase of matter describes the system in given regions of temperature T and μ_B. Low temperatures and $\mu_B \simeq 940$ MeV characterize ordinary nuclear matter. As the temperature and energy density are increased further, transitions to deconfinement phases of quarks and gluons are expected to occur; these are indicated by the lines in the plot.
A phase transition is characterized by its 'order', corresponding to the order of the derivative of the thermodynamical potential:

$$\Omega(E, T, S, \mu_c, N) = E - T \cdot S - \mu_c \cdot N \tag{1.3}$$

where E means energy, T is the temperature, S is entropy, μ_c is chemical potential and N is the number of particles. For the system in question, the formula 1.3 is rewritten in the form:

$$\Omega(E, T, S, \mu_B, B) = E - T \cdot S - \mu_B \cdot B \tag{1.4}$$

where μ_B is defined as the chemical baryon potential and B is the baryon number. Thermodynamic equilibrium is reached where Ω has a minimum. The phase transitions were labeled by the lowest derivative of the free energy that is discontinuous at the transition. 'First-order' phase transitions exhibit a discontinuity in the first derivative of the free energy with a thermodynamic

variable. The various solid/liquid/gas transitions are classified as first-order transitions because they involve a discontinuous change in density (which is the first derivative of the free energy with respect to chemical potential.) 'Second-order' phase transitions have a discontinuity in a second derivative of the free energy. These include the ferromagnetic phase transition in materials such as iron, where the magnetization, which is the first derivative of the free energy with the applied magnetic field strength, increases continuously from zero as the temperature is lowered below the Curie temperature. The magnetic susceptibility, the second derivative of the free energy with the field, changes discontinuously. Under the Ehrenfest classification scheme, there could in principle be third, fourth, and higher-order phase transitions. In this case there is no discontinuity and no rapid phase transition, but a 'cross-over'. The solid line in Figure 1.1 indicates a first-order phase transition at larger values of chemical potential $\mu_B \geq 360 \pm 40$ MeV with a critical 'endpoint' indicated by the small square, followed a smooth crossover for $\mu_B \leq 360$MeV. As we know from the top panel of Figure 1.1, lattice QCD predicts a phase transition around the critical temperature $T_c = 175 \pm 15$ MeV. The order of the transition of the QGP phase is not known. If gluons were the only degrees of freedom, the transition would be first-order. With the addition of two or three quarks, the transition can be of second-order. At high temperature and high baryon potential, lattice QCD results seem to indicate that the transition is a smooth 'cross-over'. Furthermore, there might be a second-order transition at high density, as shown in Figure 1.1 (top panel). In the early universe, the QGP is thought to have existed $10^{-4} - 10^{-5}$ s after the Big Bang.

1.2 Relativistic heavy-ion collisions

As discussed in the previous section, collisions of heavy ions, like S, Au or Pb at relativistic energies can produce a large and hot system where the QGP can be created. A pictorial view of relativistic heavy-ion collisions is presented in Figure 1.2. In the center-of-mass system of a symmetric nucleus-nucleus collision, two Lorenz-contracted nuclei of radius R hit each other along the beam axis with impact parameter $|\overrightarrow{b}| = b$ (where $\overrightarrow{b}$ is perpendicular to the beam direction the vector connecting centers of colliding nuclei). In the region of overlapping, the 'participating' nucleons interact with each other, while in non-overlapping region, the 'spectator' nucleons continue along their trajectories (but they can interact electromagnetically only). The degree of overlap is called 'centrality of the collision', with $b \sim 0$ fm for the most central collisions (total overlapping of two nucleons) and $b \sim 2R$ for the most peripheral collisions (no overlapping area). The maximum time of overlapping is determined as $\tau_0 = 2R/\gamma c$, where γ is

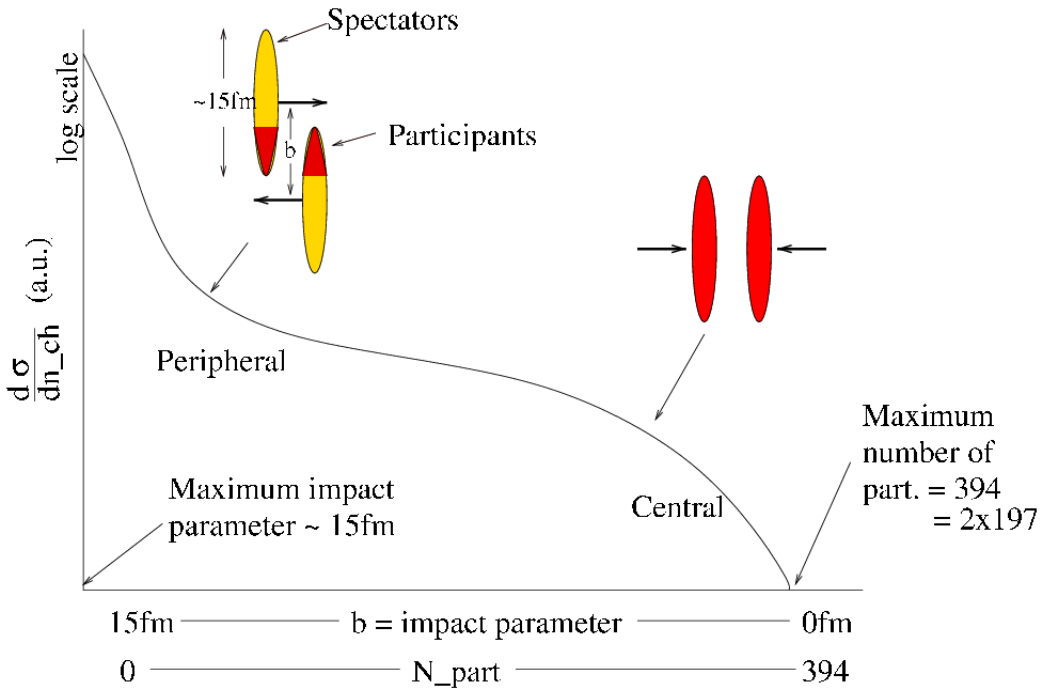

Figure 1.2: The scheme of $Au + Au$ heavy-ion collision with radius R and the impact parameter b. The curve represents the relative probability of charge particle multiplicity n_{ch}, which is proportional to the number of participating nucleons N_{part}[2].

the Lorenz factor if the colliding nuclei.

The impact parameter of a collision in the case of gold nuclei is directly related to the number of participants N_{part}, where in the most central collisions it can reach up to 394 nucleons and in the most peripheral collisions the number of participants can be very small. The beam axis and the direction of impact the impact parameter define a reaction plane.

The colliding nuclear matter loses a substantial fraction of its energy in the collision process, a phenomenon referred to by the therm 'nuclear stopping power' introduced by Busza and Goldhaber [14]. The loss of kinetic energy incident nuclear matter is accompanied by the production of a large number of particles, mostly pions. Therefore, in high-energy collisions, a large fraction of the longitudinal energy is converted into the energy of hadronic matter produced in the neighborhood of the center of mass of the colliding system.

The dynamics of a heavy-ion collision can be viewed in Figure 1.3 as a space-time diagram with the longitudinal coordinate z and and the time coordinate t. The collision takes place at the point $(z, t) = (0, 0)$. The space-time scenario proposed by Bjorken [15], distinguishes five sub-sequent

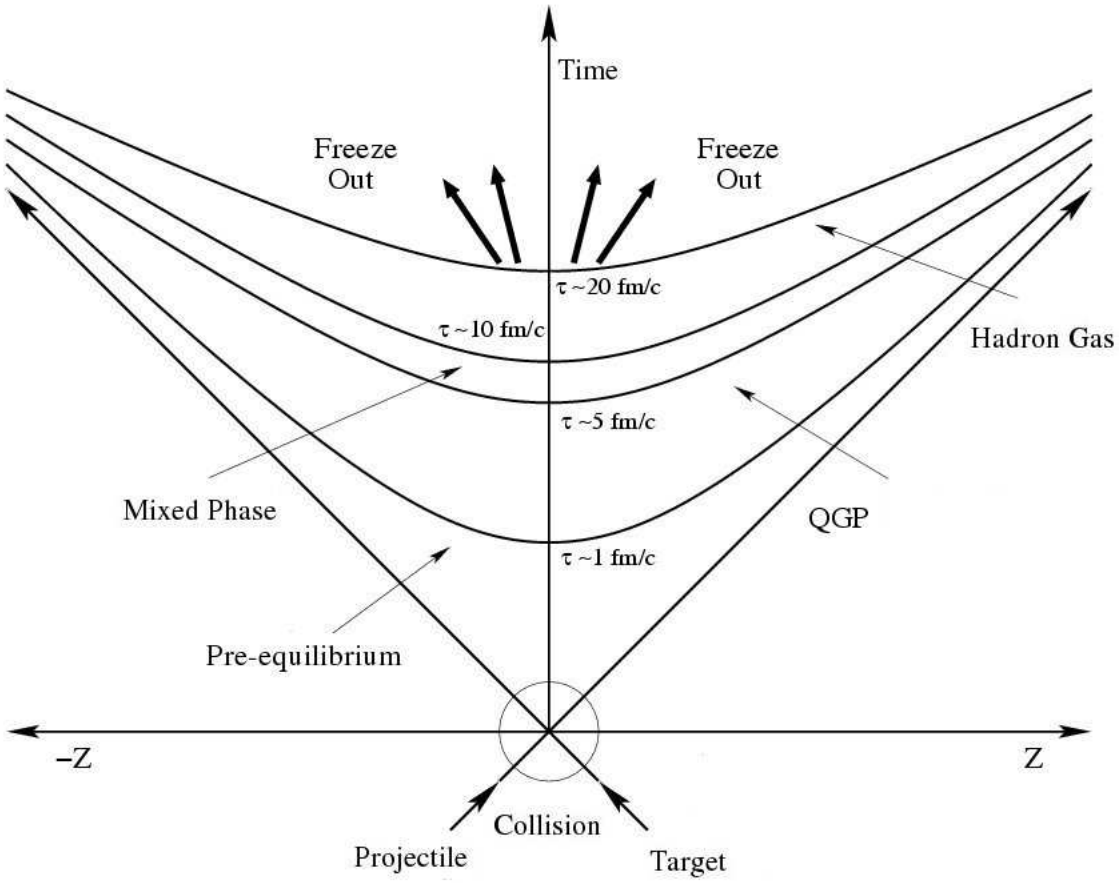

Figure 1.3: The scheme of heavy-ion collision [16].

phases:

- "Pre-equilibrium" (when formation of elementary constituents takes place): nucleons pass through each other and parton-parton interactions occur, where a parton is defined as a quark or a gluon. Due to high energy density, the released partons can re-scattered multiple times, losing part of their initial energy in the interaction region. A 'fire-ball' of interacting quarks and gluons expands and the baryon chemical potentials vanishes at mid-rapidity $y = 0$ (see the Glossary for a definition), while forward and backwards regions, $y \neq 0$, are relatively rich in baryons corresponding to the remnants of the colliding nuclei. At this stage hard partons are scattered.

- "Chemical and thermal equilibrium": the nuclear matter reaches equilibrium at the proper time τ_0 (just before QGP formation) through parton re-scattering in the medium. The energy density obtained in the collisions at RHIC is above the critical value, so when the

interacting medium is thermalized, the QGP might be produced.

- The ”QGP phase”, evolving according to the laws of hydrodynamics.
- The ”Mixed phase” of QGP and a Hadron Gas (HG)
- “Hadronization and freeze-out”: The expanding QGP cools down fast and quickly reaches the transition temperature. It evolves into the phase of hadron gas, finally reaching the state known as ‘chemical freeze-out’. The resulting hadronic gas continues to expand, cooling down the interaction rate between the hadrons. Then the system evolves to the thermal equilibrium; this state is known as ‘thermal freeze-out’. After this moment, hadrons fly freely.

Information about the QGP or the hadron gas at thermal equilibrium must be inferred from the properties of the particles remaining after the thermal freeze-out (hadrons, leptons, direct photons). Some signatures described in Section 2 can give information about what happened before the freeze-out.

Chapter 2

Properties of bulk matter - review of experimental results

The RHIC facility (more in Chapter 5) enables probing the highest-energy region of phase space, where many processes are subjects of our interest. The processes detected in the RHIC energy domain can be selected according to many criteria, one of them being dividing experimental observables into the 'soft' and 'hard' sector of processes. Particle production in the central rapidity region of ultra-relativistic heavy-ion collisions can be treated as a combination of perturbative (hard and semi-hard) parton production and non-perturbative (soft) particle production. By 'hard' one usually means clearly perturbative processes with momentum or mass scale of the order of tens of GeV. The resulting hard partons can fragment into jets. Hadronic jets are observed in $p+p$ collisions at the p_T from around 5 GeV to more than 400 GeV. The term 'Semi-hard' processes refers to such QCD process where partons with transverse momenta of few GeV are produced. 'Soft' process refers, to ones which produce low transverse momenta partons or hadrons.

2.1 Soft processes

2.1.1 Inclusive and semi-inclusive particle production - thermal equilibrium signatures

Single particle distributions are used to look into particle production mechanisms and deduce information concerning system evolution. Measurements in the left panel of Figure 2.1 are pre-

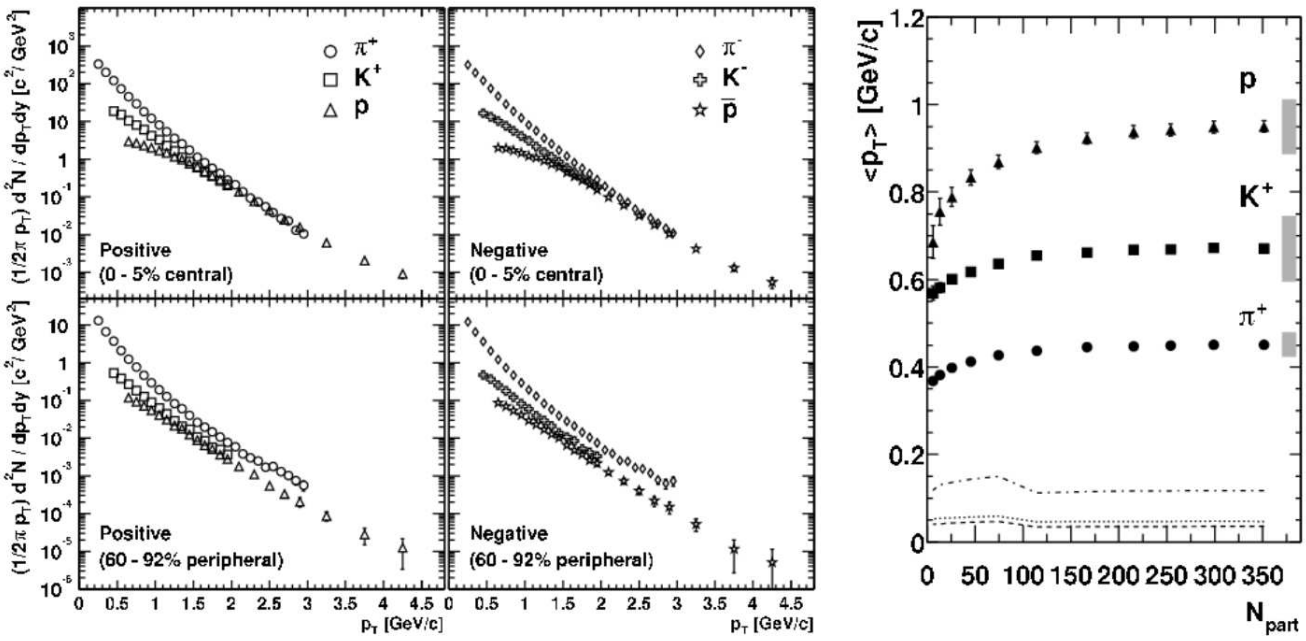

Figure 2.1: a) Semi-inclusive invariant p_T spectra for pions, kaons and protons in $Au + Au$ collisions at $\sqrt{s_{NN}} = 200$ GeV. Left column contains positive hadrons and right one negative particle species. Top row shows the sample of the most central collisions (up to 5% of the total hadronic cross-section of the collision) and the bottom row indicates the most peripheral collisions (from 60 to 92% of the cross-section). b) mean transverse momentum of positive particles as a function of centrality [17].

sented in terms of Lorentz invariant single particle inclusive differential cross-section (or Yield per event in the class of semi-inclusive):

$$\frac{Ed^3\sigma}{dp^3} = \frac{d^3\sigma}{p_T dp_T dy d\phi} = \frac{1}{2\pi} f(p_T, y) \tag{2.1}$$

where y is rapidity (see Glossary for a definition), p_T is transverse component of the momentum vector $\overrightarrow{p}$, (while p_L is the longitudinal component of momentum), σ is the cross section of a reaction and ϕ is the azimuthal angle of the particle.

The plot exhibits some differences between distributions (of pions, kaons and protons) for various centralities (mainly in the number of produced particles of a given type), however their shapes do not differ significantly. The distributions are usually used to estimates the temperature

of thermal freeze-out, as:

$$\frac{d^2\sigma}{dp_L p_T dp_T} = \frac{d^2\sigma}{dp_L m_T dm_T} = \frac{1}{e^{E/T} \pm 1} \sim e^{-E/T} \tag{2.2}$$

The slope of the m_T (or p_T) distribution at mid-rapidity represents temperature of the system. Particles (or partons) which travel with transverse flow velocity $\beta_t = \frac{v_t}{c}$ acquire kinetic energy in addition to thermal energy, so the slope should increase with the rest mass: $T \rightarrow T_0 + \gamma_T m_0$. The average transverse momentum $< p_T >$ of positive pions, kaons and protons (see right panel of Figure 2.1) increases according to their respective masses. The rise of mean transverse momentum of hadrons from peripheral to central collisions is expected for thermal distributions.

2.1.2 Chemical equilibrium signatures

One of the most crucial questions is whether thermal and chemical equilibrium is achieved at some stage of the collision. Applying a statistical model [18, 19] which assumes equilibrium, and testing the experimental data against model predictions is one way to verify if the equilibrium state was reached during systems evolution. The statistical model is based on the use of a grand canonical ensemble to describe the partition function and hence the density of the particles in a equilibrated fireball:

$$n_i = \frac{g_i}{2\pi^2} \int_0^\infty \frac{p^2 dp}{e^{(E_i(p)-\mu_i)/T} \pm 1} \tag{2.3}$$

with particle density n_i, spin degeneracy g_i, $\hbar = c = 1$, momentum p, total energy E and chemical potential $\mu_i = \mu_B B_i - \mu_S S_i \mu_{I_3} I_i^3$. i denotes particle type. The quantities B_i, S_i and I_i^3 are the baryon number, strangeness and three-component of the isospin quantum number. The temperature T and baryon-chemical potential of chemical freezeout are the two independent parameters of the model, while the volume of the fireball V, the strangeness chemical potential μ_S and the isospin chemical potential μ_{I_3} are fixed by the three conservation laws:

$$V \sum_i n_i B_i = Z + N \tag{2.4}$$

$$V \sum_i n_i S = 0 \tag{2.5}$$

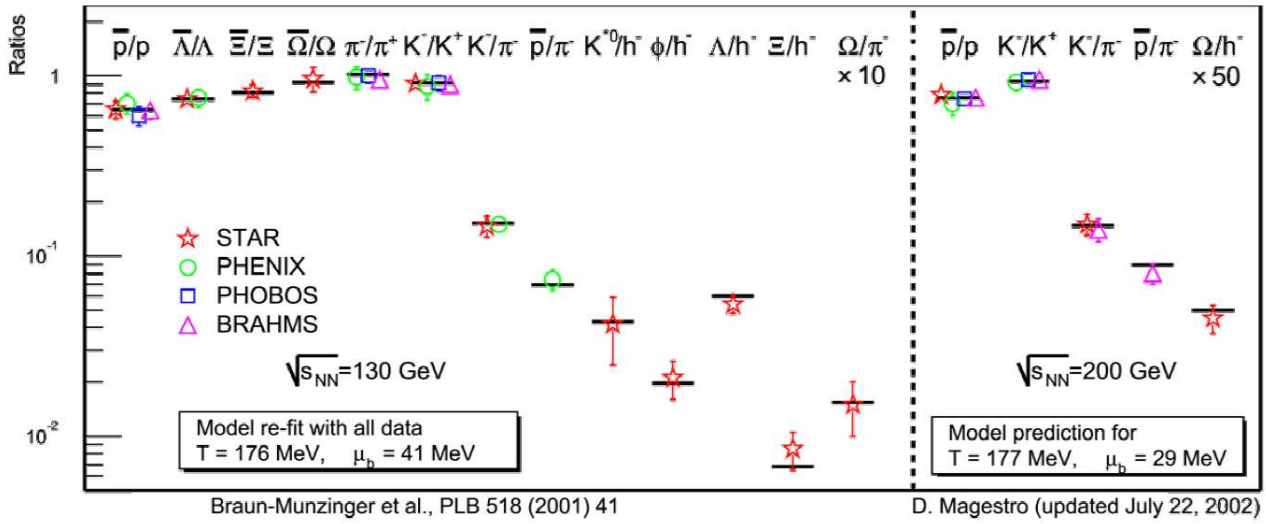

Figure 2.2: Particle ratios for RHIC energies: 130 GeV (left) and 200 GeV (right) together with results of statistical fits. Data are compiled as a result of all RHIC experiments [19].

$$V \sum_i n_i I_i^3 = \frac{Z-N}{2} \tag{2.6}$$

Z and N are the proton and neutron numbers of the colliding nuclei.

The ratios of particle abundances, dominated by low transverse momenta, are even for strange and multi-strange particles well described by fits to a thermal distribution taking into account the baryon chemical potential (μ_B) for non-strange particles and strange chemical potential (μ_S) for strange particles.

The formula for non-strange (e.g protons and anti-protons) particles can be expressed as follows:

$$\frac{d^2\sigma}{dp_L p_T dp_T} \sim e^{-(E-\mu)/T} \rightarrow \frac{\overline{p}}{p} = \frac{e^{-(E+\mu_B)/T}}{e^{-(E-\mu_B)/T}} = e^{-(2\mu_B)/T} \tag{2.7}$$

where p and $\overline{p}$ are the mean numbers of protons and anti-protons, respectively.
For strange (e.g lambdas and anti-lambdas) particles:

$$\frac{d^2\sigma}{dp_L p_T dp_T} \sim e^{-(E-\mu)/T} \rightarrow \frac{\overline{\Lambda}}{\Lambda} = \frac{e^{-(E+\mu_S)/T}}{e^{-(E-\mu_S)/T}} = e^{-(2\mu_S)/T} \tag{2.8}$$

where Λ and $\overline{\Lambda}$ correspond to the yields of lambdas and anti-lambda respectively. Fitted model

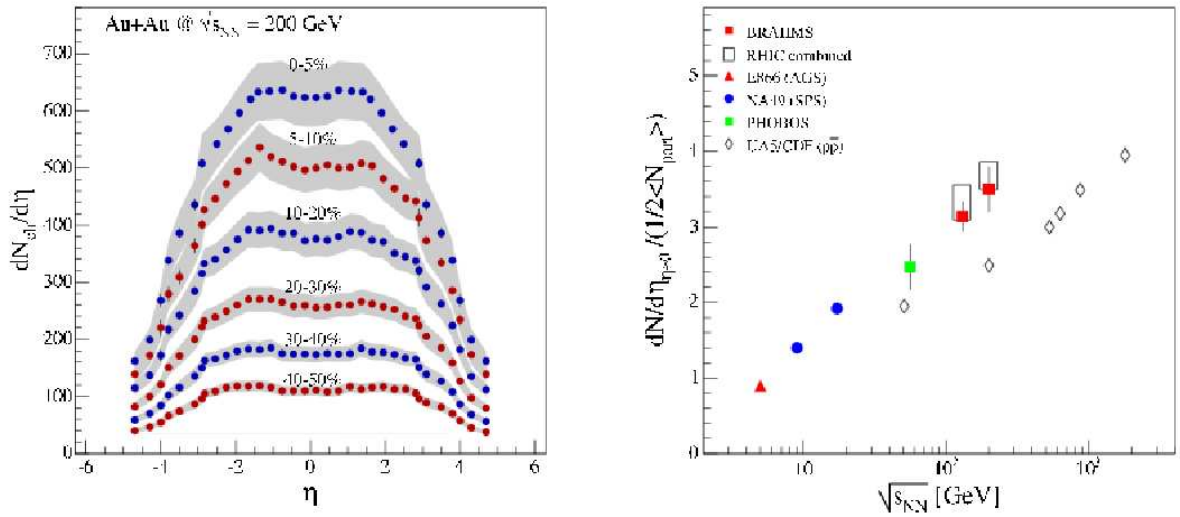

Figure 2.3: a) pseudorapidity distributions for $Au + Au$ at 200 GeV for different collision centralities; b) multiplicity of charged particles per participant pair around midrapidity as a function of collision energy. Particle production in $Au + Au$ collision at top RHIC energies around $\eta = 0$ exceeds that seen in $p + p$ collisions by $40 - 50\%$ [20].

parameters (temperature, baryon potential of the chemical freezeout) from the thermal distribution are displayed in Figure 2.2. For $\sqrt{s_{NN}} = 130$ GeV, the temperature is $T = 176$ MeV and the chemical potential- $\mu_B = 41$ MeV, for $\sqrt{s_{NN}} = 200$ GeV, $T = 177$ MeV and $\mu_B = 29$ MeV. These calculations are done to estimate in which region of the phase diagram the analyzed system is located. These predictions agree with QCD calculations and confirm the fact that RHIC experiments access the region located very close to the boundary of the phase transition.

2.1.3 The (pseudo-)rapidity density

The reference frame of the detectors at RHIC is designed to be a nucleon-nucleon center of mass (c.m.) system. The colliding nucleons approach each other with the energy $\sqrt{s_{NN}}/2$. The rapidity of the nucleon-nucleon center of mass - mid-rapidity - is $y^{cm} = y_{NN} = 0$. The projectile's and target's rapidities are equal (in absolute magnitude), but have opposite signs:

$$y^{proj} = -y^{target} = cosh^{-1}(\frac{\sqrt{s_{NN}}}{2m_N}) = y^{beam}/2 \tag{2.9}$$

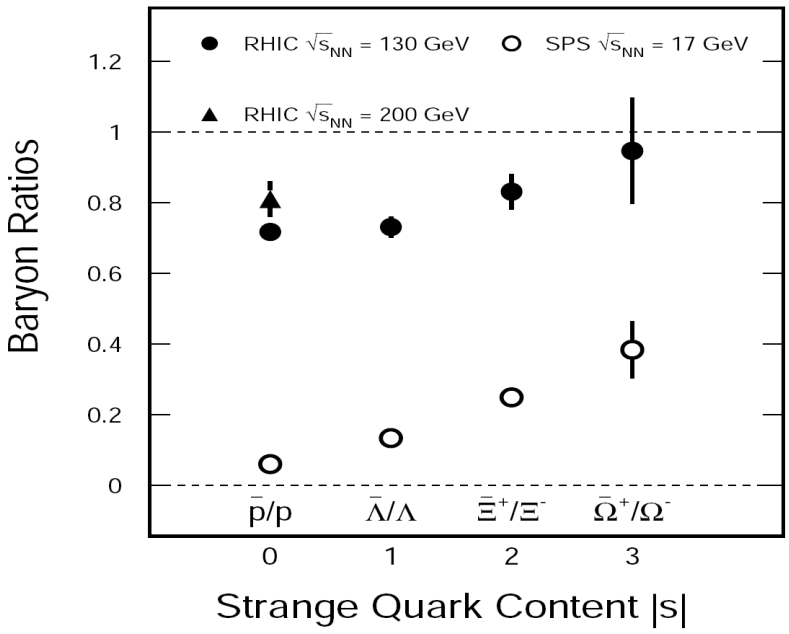

Figure 2.4: Baryon ratios for RHIC and SPS energies showing the net baryon density for some baryon species at given collision energy. Open symbols are for the energy of SPS, closed symbols show RHIC results [18].

where m_N=0.931 GeV is the mass of nucleon and y^{beam} means the beam rapidity. The shape and evolution of charged-particle density in rapidity y and pseudorapidity ($\eta = -ln[tan(0.5\theta)]$, where θ is the angle of particle with respect to the beam axis) in $A + A$ collisions (see Figure 2.3) follow a similar trend. Pseudorapidity is calculated in the case where rapidity cannot be measured directly, for the central-rapidity region rapidity and pseudorapidity distributions follow very similar trends. For more central data, higher multiplicities of particles are registered. The event multiplicity is collision energy-dependent as well (right-hand side of Figure 2.3). Universal scaling of pseudo-rapidity divided by the number of collision participants versus collision energy is observed.

2.1.4 "Net" baryon density

The anti-baryon/baryon ratios have been measured at the SPS and RHIC Displayed in Figure 2.4 are the ratios for SPS (open symbols) and RHIC energies (closed symbols) slightly increase with increasing the content of strange quark of the observed anti-baryon/baryon ratios. Obviously, there is a large increase of baryon ratios from lower to higher energies due to much higher baryon density for higher energy (at lower energies production of anti-baryons was limited). The

tendency for both energies are similar. The slight increase of ratios (such exists in collisions of two nuclei) for both energies is a result of an increase of strange quark content (see the next sub-section for more details about strangeness production). This measurement indicates that baryon-rich density is strange quark content-dependent.

2.1.5 Strangeness Recombination

Strangeness enhancement was one of the first proposed signals for the possible QGP formation [21]. The strangeness content of the colliding nuclei is negligible, consequently all measured strange particles must have been produced during collision. The strange quark s has a much larger mass than lighter quarks (u, d), as described in Appendix 1. The production of particles containing the s quark through hadronic channels usually should not be enhanced. As $m_s < T_c$, an $(s\overline{s})$ pair would be in chemical and thermal equilibrium in the QGP phase. Strange quarks would hadronize, resulting in an enhancement of production of strange particles (containing at least one strange quark or anti-quark). Hyperon production (where hyperon is a baryon with at least one strange or anti-strange quark) in a collision of hadron is expected to be more difficult for multi-strange species (Ξ, Ω), which usually result from a long cascade of reactions, e.g: $\pi + N \rightarrow K + \Lambda$, $\pi + \Lambda \rightarrow \Xi + K$, $\pi + \Xi \rightarrow \Omega + K$. (See also [22]).

In this section, two experimental results are presented: the dependence of strange particle production as a function of the the s quark content in a hyperon and the relation of strange quarks to non-strange light ones (u, d).

It is expected that more hyperons may be detected when a QGP phase is created than in the case of a pure-hadronic system. This effect should increase with the strangeness content of the baryon. The SPS experiment NA57 [23] has measured the yields of $\Lambda, \overline{\Lambda}$,$\Xi^{\pm}, \Omega^{\pm}$ in $p + A$ and $A + A$ collisions. These results are compared as a function of the number of participating or wounded nucleons. Figure 2.5 presents the ratio of (anti)-hyperon yield in nucleus-nucleus ($A + A$) collisions to the $p + Be$ and $p + p$ ones, versus the number of participants (centrality) measured at SPS conditions and extended to the RHIC energy domain. If the yields were simply scaling with the number of participants then all points should be distributed on a flat line. This figure indicates an enhancement of production of (anti)-hyperons with the centrality of the collision. The second important point here is the hierarchy of enhancement- it is higher for multi-strange baryons (Ω, Ξ) than for single strange baryons (Λ) leading to the conclusion than if the s quark content in a particle is higher, then the production of such hadron increases.

As the strangeness content in hadronic matter and in QGP is different, information about pro-

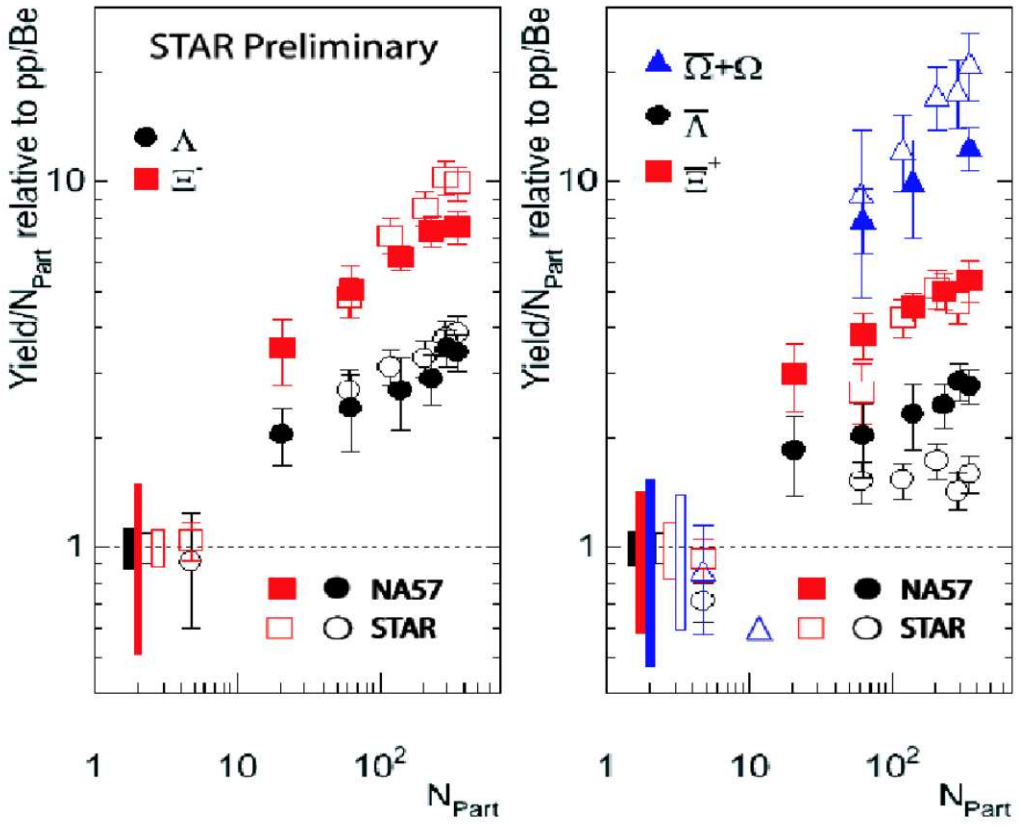

Figure 2.5: Ratio of yields of (anti)-hyperons versus centrality measured for $A + A$ collisions with respect to $p + p$ (STAR) and $p + Be$ (NA57) at SPS (closed symbols) and RHIC (opened symbols). Lambda hyperons are marked by black circles, sigma particles are shown by red squares and omegas are plotted as blue triangles [24].

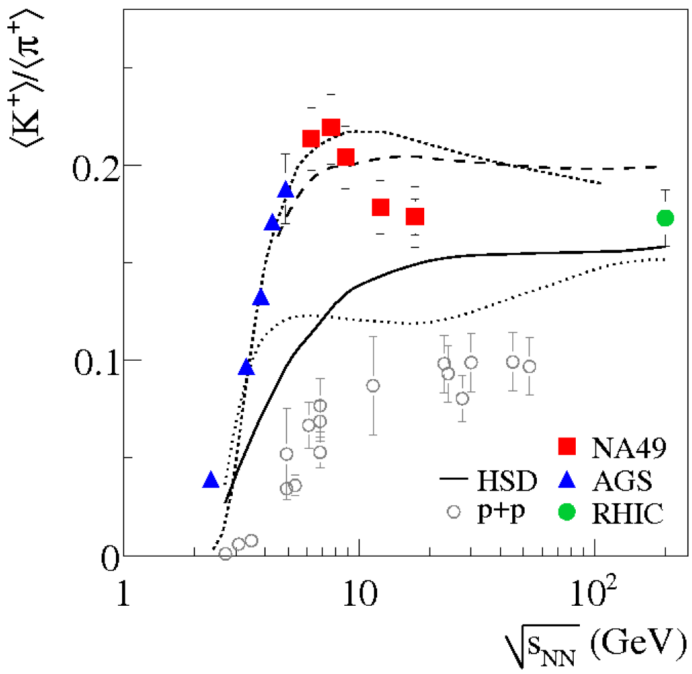

Figure 2.6: Top panel shows K/π ratios for positive and negative meson combination species for $Pb+Pb$ and $Au+Au$ collisions (full symbols) compared to the corresponding results from $p+p$ results (open symbols). The curves in the Figure show predictions of various models: dotted line (UrQMD), dashed line (RQMD) and straight line (HDS). [26].

duced strange quarks can be derived from the ratio K^+/π^+ [25, 26], as it is directly translated to the ratio of strange quarks (formed) to the non-strange (possibly formed at mid-rapidity region):

$$\frac{< s > + < \overline{s} >}{< u > + < \overline{u} > + < d > + < \overline{d} >} \approx \frac{< K^+ >}{< \pi^+ >} \tag{2.10}$$

Figure 2.6 shows increased strangeness production around energy 8 GeV, which can be interpreted as a signature of the phase transition. Results are compared to the predictions of several models, for $Pb+Pb$ and $Au+Au$ collisions neither UrQMD nor RQMD reproduce such strong evidence of the phase transition (above the critical point), for $p+p$ collisions no model follows the experimental results. Such comparisons show that so far the measured transition is not described by these models, more detailed studies of the origin of this phenomenon is required; however, experimentalists from NA49 [27] claim that this observable indicates such a transition.

2.1.6 Flow

The flow phenomenon is a distinguishing feature of a nucleus-nucleus collision compared to the simpler ones: proton-proton or proton-nucleus [28, 29, 30]. This effect is seen at many collision energies. Flow is a collective effect of a bulk matter which obviously cannot be produced as a result of superposition of independent nucleon-nucleon collisions. There can be isotropic or non-isotropic expansion, depending on the class of the collision centrality. Depending on the collision energy, flow does reflect different collective aspects of the interacting medium. At low energies, where relatively few new particles are formed, the flow effect is mostly caused by nucleons from the incoming nuclei. At higher energies, the number of newly produced particles is so large that they dominate the observed flow effect; the primordial nucleons are expected to make only minor contribution, in particular in the region of mid-rapidity.

- Radial flow
  In central collisions between spherical nuclei, the initial state is symmetric in azimuth and the overlapping region is circular (not 'almond-shape' in the transverse direction); this implies that the azimuthal distribution of the final state particles is isotropic as well. Under such conditions, any pressure gradient causes azimuthally symmetric collective flow of the outgoing particles, which is called 'radial flow'. The relevant observables to study such effects are the transverse momentum distributions for various particle species. For a given particle type, the random thermal motion is superimposed onto the collective radial flow velocity.

- Anisotropic flow
  Here non-central collisions are discussed, where the pressure gradient is not azimuthally symmetric. The pressure gradient establishes a correlation between momentum and position points. The initial anisotropy in the transverse space configuration translates into an anisotropy of the transverse momentum distributions of outgoing particles, which is refereed to as 'anisotropic flow'. It depends on collision energy, location in phase space (rapidity, transverse momentum) and the particle species. The dominating flow pattern at low energies arises from colliding nuclei. In such a case, the flow from the projectile nuclei must have its maximum in the reaction plane. Furthermore, the flow of particles originating from the target is characterized by the same magnitude, than the flow of the projectile remnants from opposite direction. The collective motion is called 'directed flow' and it can be large at low energies. The velocity of incoming nuclei at ultra-relativistic energies

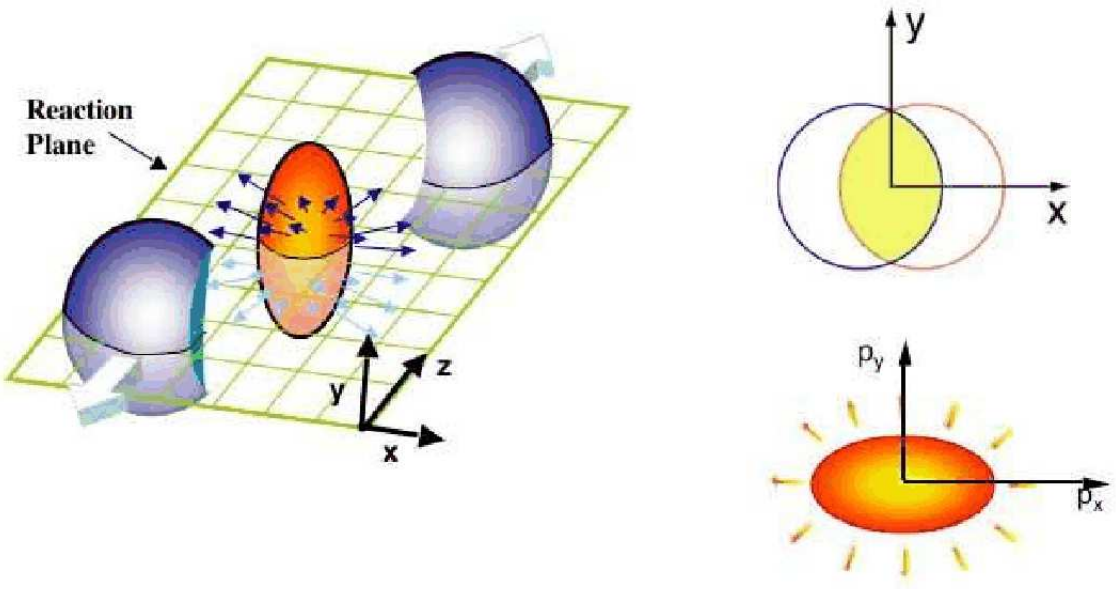

Figure 2.7: a) almond shaped overlap region just after nucleus-nucleus collision, where the nuclei move along z axis, the reaction plane is defined by the z and x axis (defined by the impact parameter vector); b) The view of the collision and momentum distribution just after collision [2].

is the biggest in the longitudinal direction, so the flow exists rather in this direction than in the transverse plane. As a result, the directed flow is significantly reduced at high energies. As most particles are produced in the interaction volume, they can exhibit additional flow patterns. The momentum of these particles can be viewed in the transverse plane as an ellipse with the principal axes parallel and perpendicular to the reaction plane. The corresponding dominant flow is called 'elliptic flow'.

The overlap region in nucleus-nucleus collisions is defined by the nuclear geometry and is almond shaped. The single particle spectrum is modified by an expansion of the particle with respect to the reaction plane $\phi - \Phi_R$, where ϕ is the azimuth of the particle, and Φ_R is the angle of the reaction plane defined along the impact parameter vector (x axis in Figure 2.7):

$$\frac{Ed^3N}{dp^3} = \frac{d^3N}{p_T dp_T dy d\phi} = \frac{d^3N}{2\pi p_T dp_T dy}\left[1 + 2\upsilon_1 cos(\phi - \Phi_R) + 2\upsilon_2 cos2(\phi - \Phi_R) + ...\right] \quad (2.11)$$

The coefficient υ_1 reflects the 'directed flow' and υ_2- the 'elliptic flow'. If the thermal equilibrium is reached, the pressure gradient is directed mainly along the direction of the impact parameter vector and collective flow develops along this direction.

In order to discuss the elliptic flow phenomenon in terms of collision centrality, the eccentricity parameter is defined:

$$\epsilon = \frac{R_y^2 - R_x^2}{R_y^2 + R_x^2} \simeq \frac{R_y - R_x}{R_y + R_x} \tag{2.12}$$

where $R_x = \sqrt{< x^2 >}$ and $R_y = \sqrt{< y^2 >}$. Since the eccentricity is much larger for peripheral than for central collisions, the dependence of v_2 on centrality at RHIC exhibits a characteristic shape (left-hand side of the top panel of Figure 2.8), which slightly deviates from hydrodynamical expectations for peripheral collisions (the lowest numbers of participants). If the system does not thermalize rapidly, the flow tends to vanish due to eccentricity reducing as the system expands.

As the flow phenomenon is caused by soft processes, it follows hydrodynamical predictions for particles with lower transverse momentum (up to 1.5 GeV/c) for centrality $0 - 50\%$, then the plateau is observed for higher p_T region and the experiment does not follow hydrodynamical calculations (right-hand side of the top panel of the Figure 2.8).

The hydrodynamical model excellently reproduces experimental measurements of pions, kaons and protons flow up to $p_T = 1$ GeV (bottom panel of Figure 2.8). Only saturation of elliptic flow for larger transverse momentum values (above 2 GeV/c) is not reproduced by hydrodynamical calculations.

Elliptic flow exhibits similar properties for all mesons (including light ones and heavier as well). The v_2 for all baryon sector is similar as well. If one scales the elliptic flow by the number of coalescence quarks (NCQ), then the v_2 for all hadrons is presented according to the same curve (see left-hand side of Fig. 2.8). It produces copious mesons and baryons with flow properties that suggest their formation via coalescence of valence quarks from a hot, thermal bath. Such behavior indicates that the system behaves as a liquid (see more in Section 2.3).

All these experimental observables describe soft processes. The following section contains results for the hard sector.

2.2 Hard processes

The hard probes, associated with hard scattering or hard processes, are experimental observables which provide tools to study the partonic structure of hadrons with high transverse momentum. For the first time in relativistic heavy-ion collisions, hard scattering observables are used at RHIC to probe the medium through which hard-scattered partons propagate. In order to investigate

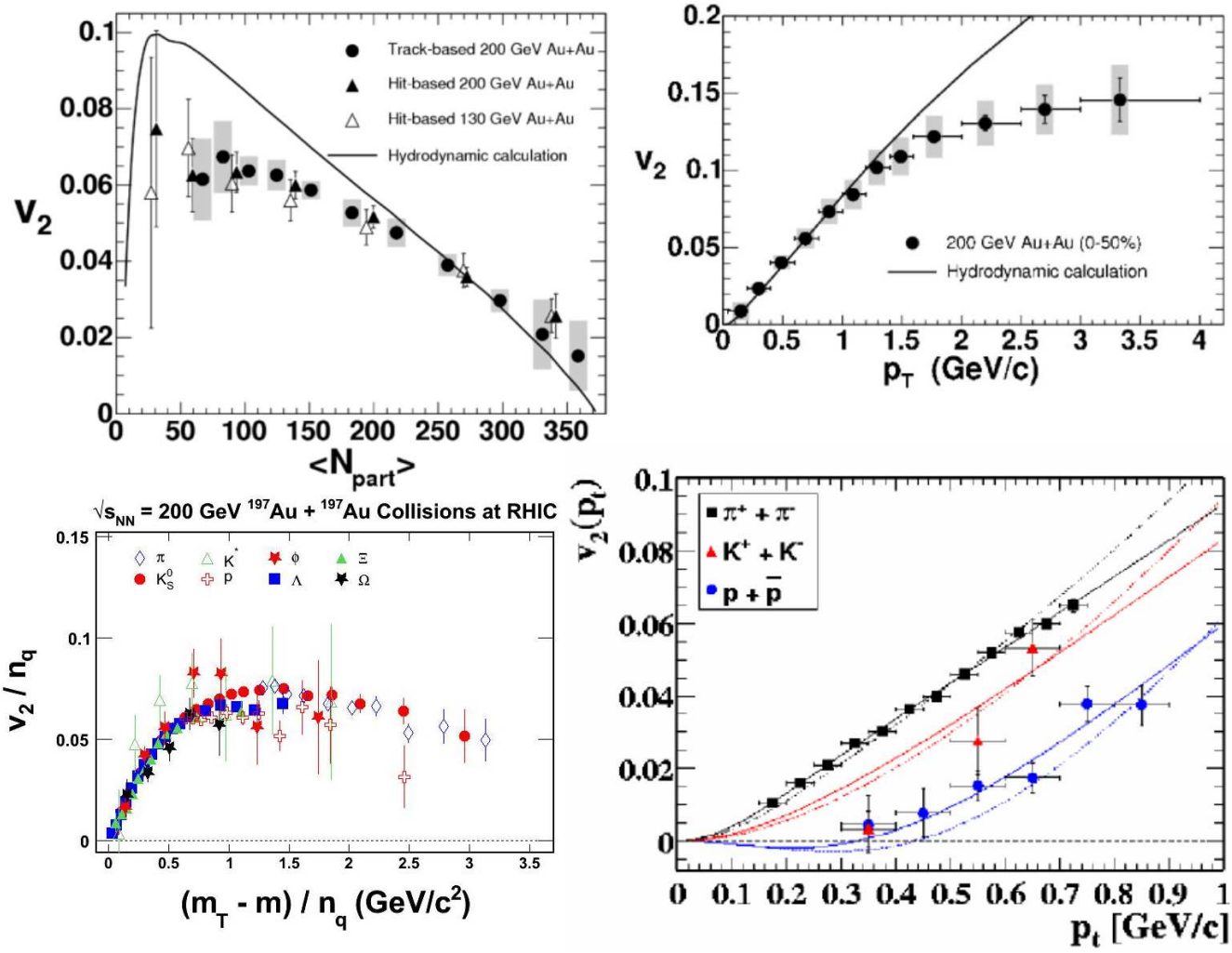

Figure 2.8: Top-left: elliptic flow of charged particles near midrapidity ($|\eta| < 1$) as a function of centrality in $Au + Au$ collisions at $\sqrt{s_{NN}} = 200$ GeV, with systematic errors; smooth curve corresponds to the hydrodynamical predictions close to the calculation with fixed $\upsilon_2/\varepsilon = 0.25$ [31]. Top-right: elliptic flow of charged particles for midrapidity region in 50% of the most central collisions [31]; bottom right: transverse momentum dependence of elliptic flow for pions, kaons and protons measured by STAR, together with hydrodynamical calculations [29], bottom-left: elliptic flow scaled by NCQ for mesons and baryons [32].

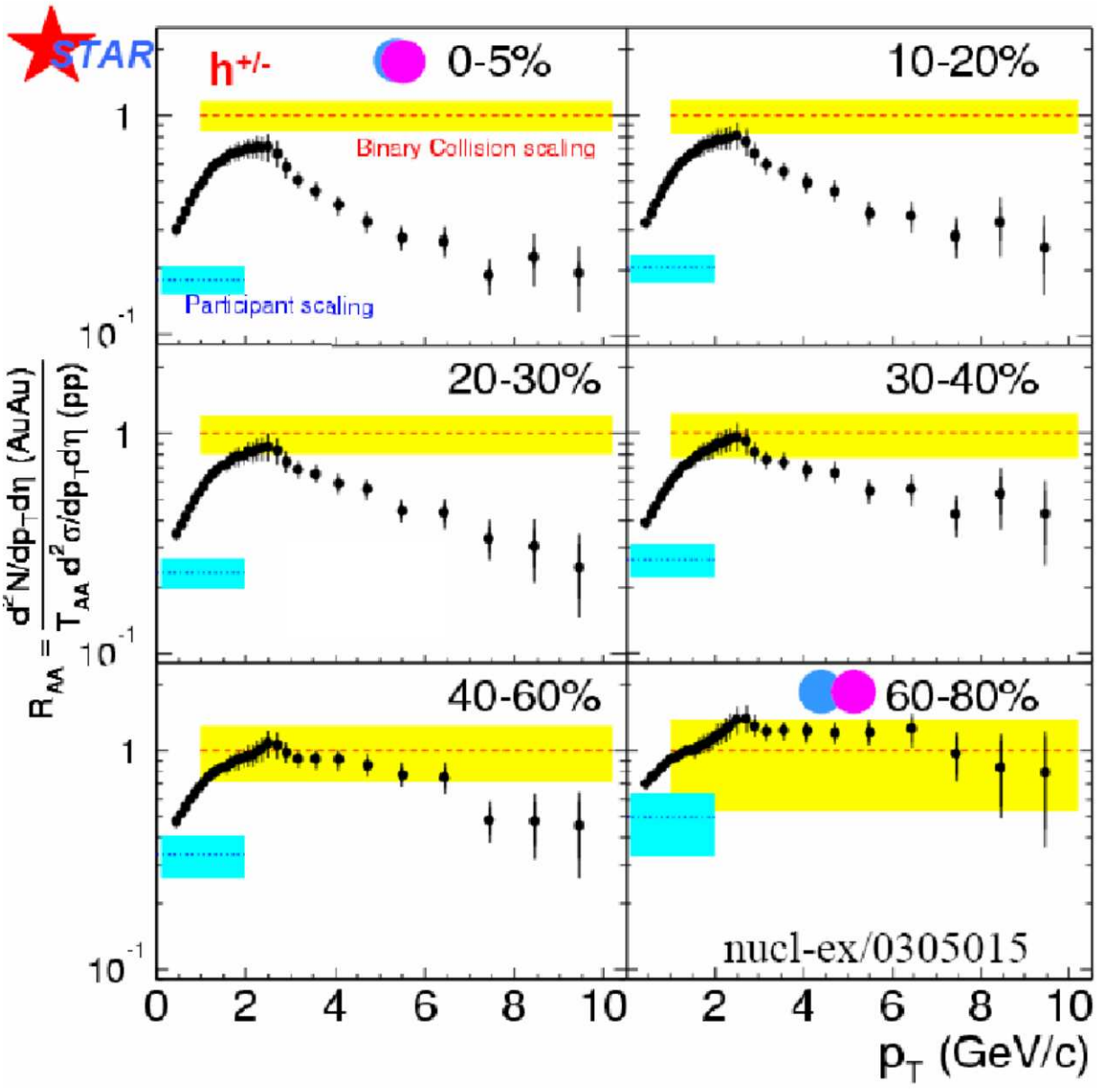

Figure 2.9: Nuclear modification factor for different centralities of $Au + Au$ collisions [33].

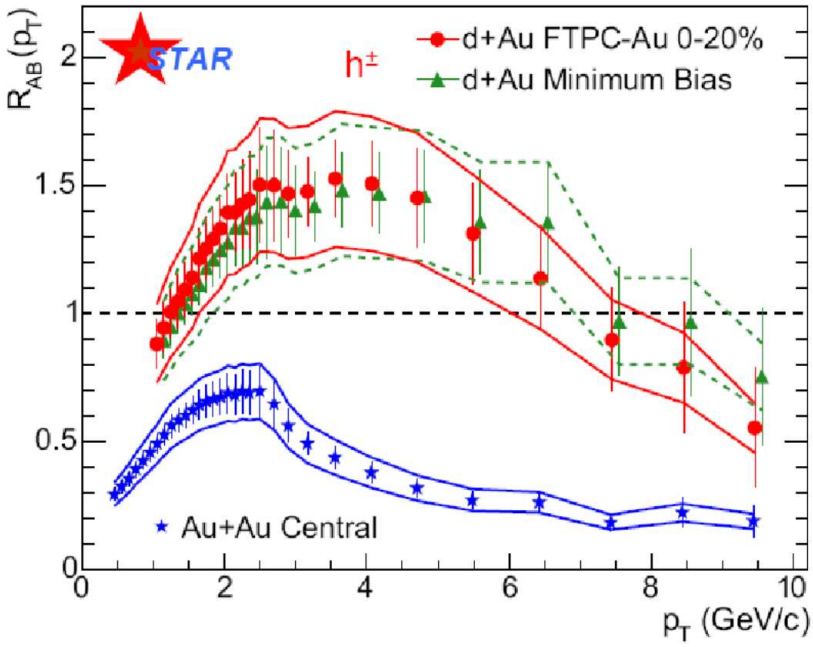

Figure 2.10: Nuclear modification factor for central $Au + Au$ collisions. $d + Au$ data is shown as well [33].

parton energy loss, the RHIC experiments measure hadron spectra and azimuthal correlations of particles with high p_T.

2.2.1 Jet quenching

Jet quenching was proposed as a signature of QGP in the RHIC energy domain. It is expected to be stronger in higher energy collisions of heavy-ions (e.g. in ALICE experiment at the LHC accelerator). In the initial collision of two nuclei, hard scatterings can occur which produce pairs of outgoing particles with high momentum. If the medium is dense, which takes place often in the case of nucleus-nucleus collision, where large numbers of particles are produced, partons lose their energy, which leads to the reduction of their p_T. In other words, when partons move through dense medium, they lose their energy as a result of gluon radiation.This phenomenon is called 'jet quenching'.
In order to compare various colliding systems one can calculate the 'nuclear modification factor' using $p + p$ as a reference to $A + A$:

$$R_{AA}(p_T) = \left(\frac{d^2N_{AA}}{dydp_T}\right) / \left(\frac{N_{coll}d^2N_{pp}}{dydp_T}\right) \tag{2.13}$$

where N_{coll} is the number of binary collisions in the heavy-ion system, N_{AA} and N_{pp} are the average numbers of particles produced in, respectively $A + A$ (nucleus-nucleus, e.g. $Au + Au$) and $p + p$ collisions, y is the rapidity. Sometimes, the nuclear modification factor is expressed in terms:

$$R_{CP}(p_T) = \left(N_{coll}^{peripheral} \frac{d^2 N_{AA}^{central}}{dy dp_T} \right) / \left(N_{coll}^{central} \frac{d^2 N_{AA}^{peripheral}}{dy dp_T} \right) \tag{2.14}$$

where $N_{coll}^{peripheral}$ and $N_{coll}^{central}$ are the numbers of collisions, and $N_{AA}^{central}$ and $N_{AA}^{peripheral}$ are the average numbers of produced particles, respectively in central and peripheral collisions.

When $R_{AA} = 1$ such an $A+A$ collision is a superposition of $N-N$ (nucleon-nucleon) collisions corresponding to scaling with the number of binary collisions (binary scaling). Suppression of the hadron spectra is observed by the nuclear modification factor measured in central $Au + Au$ collisions at RHIC. Figure 2.9 depicts R_{AA} as a function of p_T for 6 different centrality classes for $Au + Au$ collisions. The ratios are taken relatively to $p + p$ collisions scaled by the number of binary collisions. The data expresses clear suppression by a factor of 4-5 in the central case at large transverse momenta $p_T > 2$ GeV/c . The distributions for peripheral collisions remain rather flat up to the p_T about 10 GeV/c. As the jet quenching phenomenon is strongly dependent on medium density, it is clearly reflected by the centrality dependence of nuclear modification factor. As in central collisions the produced medium is much denser than in peripheral collisions, jet quenching should appear stronger in central ones. The R_{dAu} are not suppressed (Figure 2.10) what indicates different medium properties than in $Au+Au$ collisions. Figure 2.11 illustrates, the jet quenching effect shown together for four RHIC experiments: left-hand side of the top panel is dedicated to the PHENIX Collaboration, which shows nuclear modification factor for $Au + Au$ collisions for charged hadrons and neutral pions produced separately (not suppressed data); right-hand side of the top panel shows R_{dAu} for two class of collision centrality (not suppressed data as well) by the PHOBOS Collaboration; left-hand side of the bottom panel presents nuclear modification factor for $d + Au$ and $Au + Au$ collisions by BRAHMS experiment ($Au + Au$ data suppressed and $d + Au$ collisions not suppressed).

Another interesting observable of hadron production is two-particle azimuthal correlations. They are calculated according the formula:

$$D(\Delta\phi) = \frac{1}{N_{trig}} \frac{dN}{d(\Delta\phi)} \tag{2.15}$$

where the azimuthal separation is normalized by the number of triggered particles N_{trig}, $\Delta\phi$ represents the azimuthal angle. In order to calculate $\Delta\phi$, one particle is chosen as a trigger and then

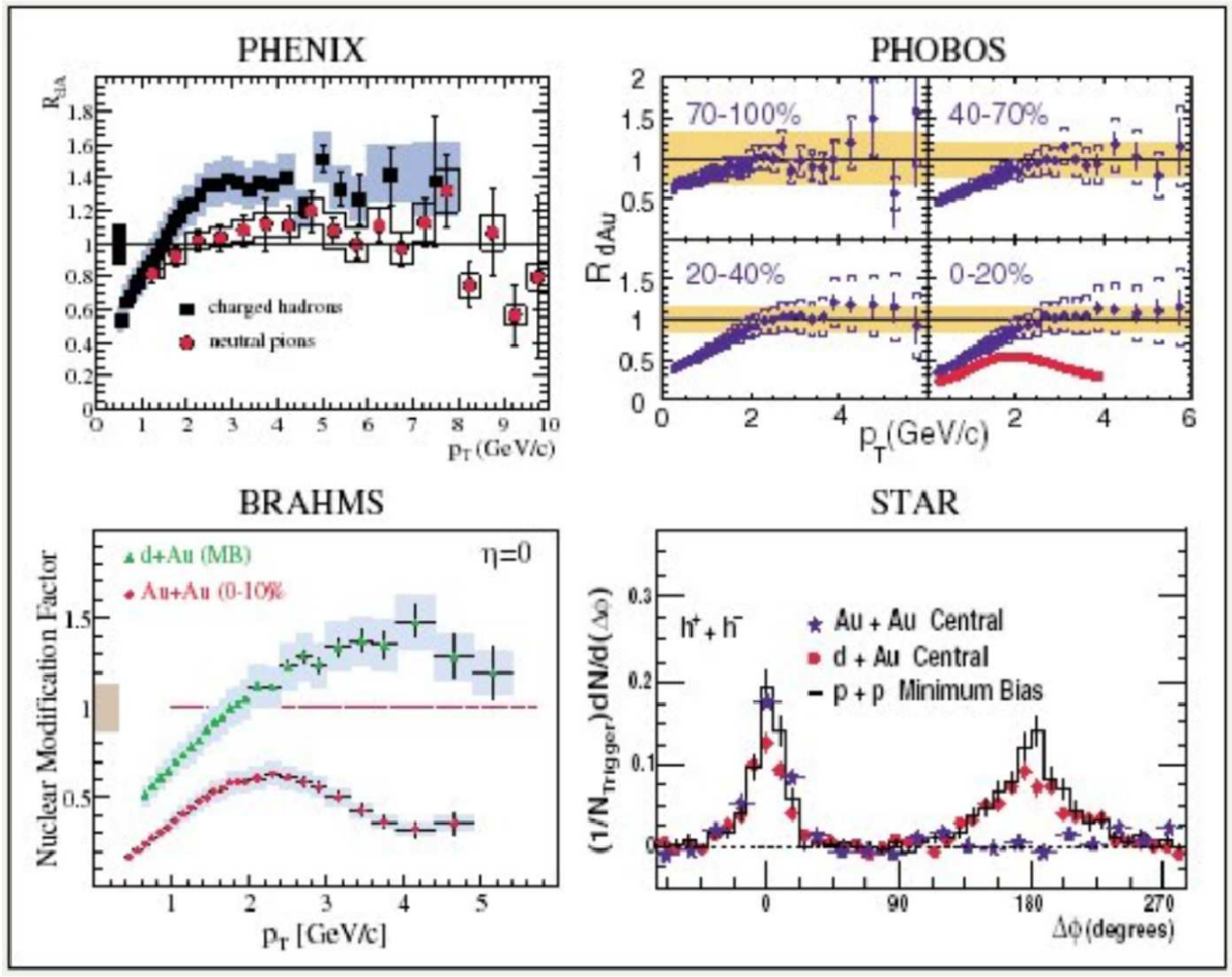

Figure 2.11: Nuclear modification factor measured by PHENIX (left-hand side of the top panel), PHOBOS (right-hand side of the top panel) and BRAHMS experiment (left-hand side of the bottom panel). Di-hadron azimuthal correlations at high transverse momentum. Sub-panel shows correlations for $p + p$, central $d + Au$ and $Au + Au$ from STAR [34]. See more description in the text.

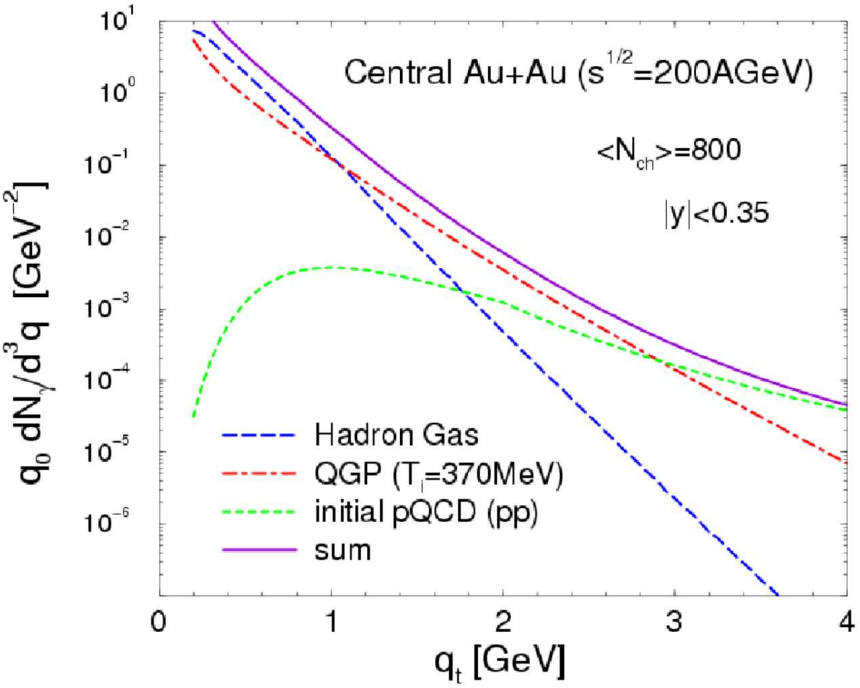

Figure 2.12: Theoretical calculations for the mid-rapidity direct photon yield in central Au+Au collisions at RHIC as a function of transverse momentum, coming from various sources [35].

the angle (around the beam axis) between the trigger particle and any of other ones is calculated separately. In Figure 2.11, right-hand side of the bottom panel shows results demonstrating that in $d+Au$ and $p+p$ collisions there are clear jet peaks for $\Delta\phi = 0$ and somehow lower and wider for $\Delta\phi = \pi$. In central collisions jets at $\Delta\phi = \pi$ are clearly suppressed. For $p+p$ collisions, the medium is not dense enough to suppress jets.

2.2.2 Direct photons

Direct photons are another interesting tool to study the possible QGP. They are directly produced in:

- quark-antiquark annihilation ($q + \overline{q} \rightarrow g + \gamma$) processes;
- quark-gluon Compton scattering ($q + g \rightarrow q + \gamma$) processes.

Direct photons do not come from hadronic decays. Theoretical expectations predict that thermal photons should dominate the direct yield of photons at low transverse momentum. As the yield

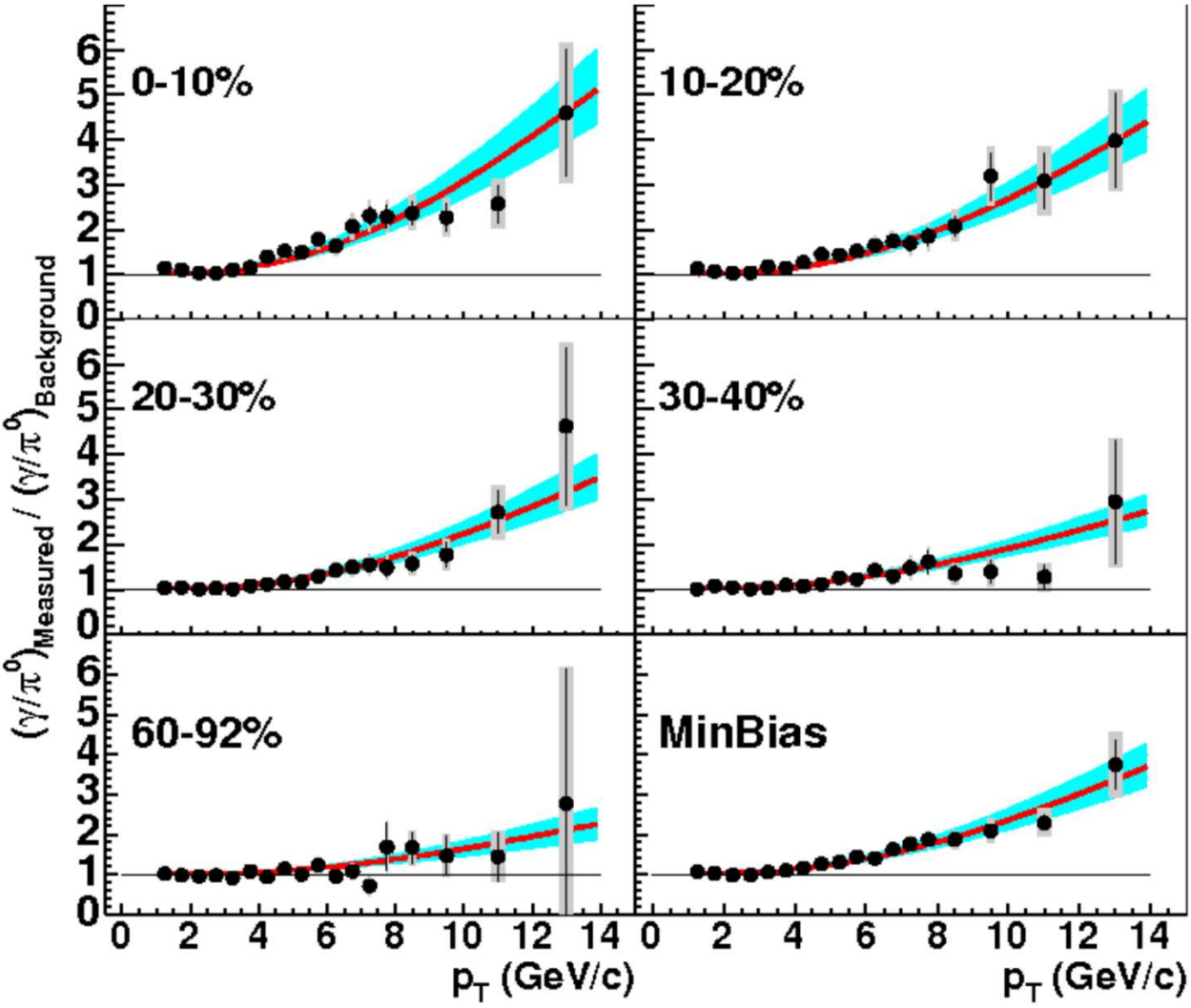

Figure 2.13: The double ratio R as a function of p_T for six various centrality classes. The solid lines indicate a ratio of pQCD predictions to the background photons invariant yields based on the yield on neutral pions for each centrality. The shaded area indicates variations of pQCD calculations, from $p_t/2$ to $2p_t$ [36].

of thermal photons fall off exponentially with transverse momentum, direct photons from the initial hard scattering will dominate the spectrum at higher transverse momentum values (Figure 2.12). In addition, a contribution of photons produced during parton fragmentation is observed. Measurements of thermal photons can provide information about temperature. Measurements of prompt photons allow one to study properties of jets interacting with the medium. They also are interesting in that they could provide background for thermal components.

The production of prompt photons is represented by the nuclear modification factor with yields of hadrons in $A+A$ collisions relative to the scaled reference measured in $p+p$ collisions. Direct photons provide a tool to check the binary collision scaling since their production is not affected by the medium produced in the final stage of the interaction. At RHIC energies it is possible to study direct photons in $Au+Au$, $d+Au$ and $p+p$ collisions. Prompt photons in $p+p$ collisions provide an excellent test of QCD, while results from $d+Au$ collisions may be used to investigate nuclear effects.
In order to determine direct photons, the following formula is calculated:

$$R = \frac{(\gamma/\pi_0)_{measured}}{(\gamma/\pi_0)_{decay}} = 1 + \frac{\gamma_{direct}}{\gamma_{decay}} \tag{2.16}$$

where the numerator corresponds to measured inclusive photon spectrum of the neutral pion spectrum and the denominator reflects the number of simulated decay photons per input pion, shown in Figure 2.13. The contribution of direct photons increases with transverse momentum. It is also collision centrality dependent, for more central data the number of direct photons versus number of decayed ones is bigger indicating that production for central data respectively increases and decreases as collision is described by bigger impact parameter.

2.2.3 Production of heavy flavors

For many years suppression of the J/ψ resonance has been believed, according to lattice calculations, simplificating to be a signature of QGP phase, as J/ψ production in nucleus-nucleus collisions should be suppressed by Debye screening processes. The J/ψ is produced when two gluons interact to create a $(c\bar{c})$ pair, which then form a J/ψ resonance. As in QGP the $(c\bar{c})$ interaction can be screened, its quarks can take part in open-charm production processes (in other words, they can create other hadrons than the J/ψ resonance, e.g. $D_0 = c\bar{u}$, $\overline{D_0} = \bar{c}u$, $B_0 = d\bar{b}$, $\overline{B_0} = \bar{d}b$, $\Upsilon = c\bar{b}$). The NA50 Collaboration [37] has seen a suppression of J/ψ in central $Pb+Pb$ collisions as $\sqrt{s_{NN}} = 17.2$ GeV. The suppression in order of 25% with respect to the

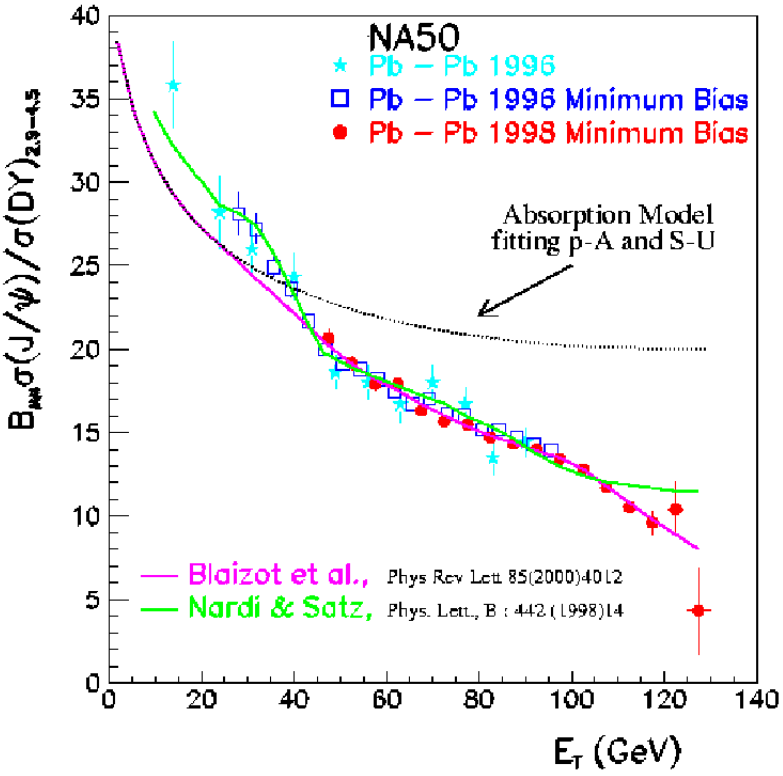

Figure 2.14: The J/Ψ yield normalized by Drell-Yan process versus transverse energy as measured by NA50 in Pb+Pb collisions at SPS. Expectations from models assuming QGP formation are superimposed. Black curve corresponds to the predictions based on lighter systems (from p+p to S+U collisions). Here, a decrease in the order of 25% is observed. [38]

normal suppression in nuclear matter might be interpreted as an evidence for deconfined quarks and gluons. Figure 2.14 shows the yield of J/ψ normalized by Drell-Yan processes. The J/ψ measurements rely on the ratio of observed $J/\psi \rightarrow \mu^+\mu^-$ decays over the number of Drell-Yan processes ($q\bar{q} \rightarrow \mu^+\mu^-$). The ratios obtained experimentally are compared to the prediction of absorption model, and different parts of the whole data sample taken by NA50 Collaboration are consistent with each other.

Due to large production of charmed quarks, the suppression scenario changes at higher energies like those available at RHIC. Experiments at RHIC study the behavior of this possible signature, but from preliminary results at low statistics it cannot be concluded that the ratio of measured to expected of produced J/ψ particle is different than unity. J/Ψ suppression is seen at RHIC energies as well, however its signature as a probe of QGP in lower energies is questionable and cannot be treated as a clear probe of registration the deconfinement stage. In RHIC energy do-

main such suppression occurs for a $\Upsilon = b\bar{b}$ particle. However, because of the small number of bottomium pairs produce at RHIC, Υ formation by coalescence of unrelated pairs is negligible.
Because charm and bottom quarks are massive ones, they are produced almost exclusively in the initial parton-parton interaction in heavy-ion collisions at RHIC energies. In the absence of any nuclear effect, the heavy flavor cross-sections in $A + A$ collisions at RHIC would simply scale with the number of binary collisions. Thus departures from binary scaling for heavy flavor production in $A + A$ collisions provide information about nuclear effects.
The easiest way to measure open heavy flavor yields in heavy-ion collisions at RHIC is through semileptonic decays of D and B mesons. Two very striking and unexpected results have been seen by studying decay electrons from open heavy flavor at RHIC. The first is the observation that the nuclear modification factor for electrons from open heavy flavor decays show very strong suppression in central $Au+Au$ collision [39, 40], similar to that seen for pions. The second striking result is the elliptic flow of electrons from open heavy flavor decays appears to favor charm quark at low p_T [40]. It was expected that heavy quark energy loss would be considerably smaller than that for light quarks due to interference effect. The relatively large v_2 values at low transverse momentum imply at least some degree of charm quark equilibration with the medium. This also imply very strong interactions of charm quarks with the medium at lower p_T.
However it is clear that the RHIC heavy flavor program is now limited by the capabilities of the accelerator and the detectors. The accelerator upgrades planned over the period 2009-2013 to produce a factor of 5 greater luminosity at RHIC II, combined with the detector upgrades will be required for the heavy flavor program at RHIC.

2.3 Perfect Liquid

On one hand, theoretical predictions have assumed that in the case of creation the QGP phase, it should reflect properties of ideal gas. On the other hand, one of the most thrilling of experimental results obtained at RHIC is the 'superstrong' quenching of jets. While quenching was expected and considered by many as a signal of the formation of QGP, it was not expected to be so strong. This fact combined with the robust flow effects observed in the same reactions and which confirmed the hydrodynamical nature of matter lead to the conclusion that the RHIC experiments are very close to the QGP phase, but its behavior does not reflect properties of ideal gas, but of ideal fluid; the observed system is a very strongly interacting one, thus called 'sQGP' [41]. These measurements indicate that hydrodynamics describes heavy-ion collisions, and the following system evolution surprisingly well, even if it fails in describing of many observables

(e.g spectra, HBT- see more in Chapter 5), but reproduces other observables well if earlier thermalization is assumed.
Measurements and comparison with relativistic hydrodynamic models indicate that the matter thermalizes in unexpectedly short time, has an energy density at least 15 times larger than needed for color confinemen, has a temperature about twice the critical temperature predicted by lattice QCD, and appears to exhibit collective motion with ideal hydrodynamical properties- a "perfect liquid" that appears to flow with a near-zero viscosity to entropy ratio- lower than any previously observed fluid nd perhaps close to a universal lower bound. However, a fundamental understanding of the medium seen in heavy-ion collisions at RHIC does not yet exist. The most important scientific challenge for the field in the next decade is the quantitative exploration of the new state of nuclear matter.
The next section contains a description of two models applied successfully in heavy-ion physics in order to compare experimental observables to theoretical predictions.

Chapter 3

Heavy-ion Collision Models

A complicated process of particle production can be described using theoretical models. Nowadays there exist two main descriptions based on: QCD string breaking and QCD parton cascade. In the case of the string decay picture, the nuclei pass through each other and as a result of their collision, color strings are formed. A string can be depicted as a quark - anti-quark pair connected by the color field. In the next step, the string decays producing hadrons, quarks and gluons. Most known descriptions based on string fragmentation are: HIJING (Heavy-Ion Jet Interaction Generator) [42] and URQMD (Ultra Relativistic Quantum Molecular Dynamics) [43, 44, 45]. HIJING includes mini-jet production as well and takes perturbative QCD effects into account. In the URQMD model, a di-quark formed from an initial quark - anti-quark string may collide with nucleons.

The QMD (Quantum Molecular Dynamics) [46] model simulates heavy-ion reaction at intermediate energies on an event-by-event basis, taking into account particle fluctuations inside single event. The advantages of this model are treatment of many-body processes and event-by-event analysis. The RQMD (Relativistic Quantum Molecular Dynamics) model [47] is an extension of QMD description up to relativistic energies (AGS, SPS). One of the main improvements as compared to QMD is an extended collision term with heavy baryons- resonances, strange particles and string excitation for higher energy hadron-hadron interactions. The RQMD describes time evolution of a many-body system using a classical covariant equation of motion. The system propagates in a $8N$- dimensional phase space with $4N$ degrees of freedom representing the space-time coordinates and $4N$ degrees for momentum-energy coordinates. For the highest energies reached today the UrQMD model is used.

In the case of parton-cascade models, the non-perturbative QCD theory is used. The colliding

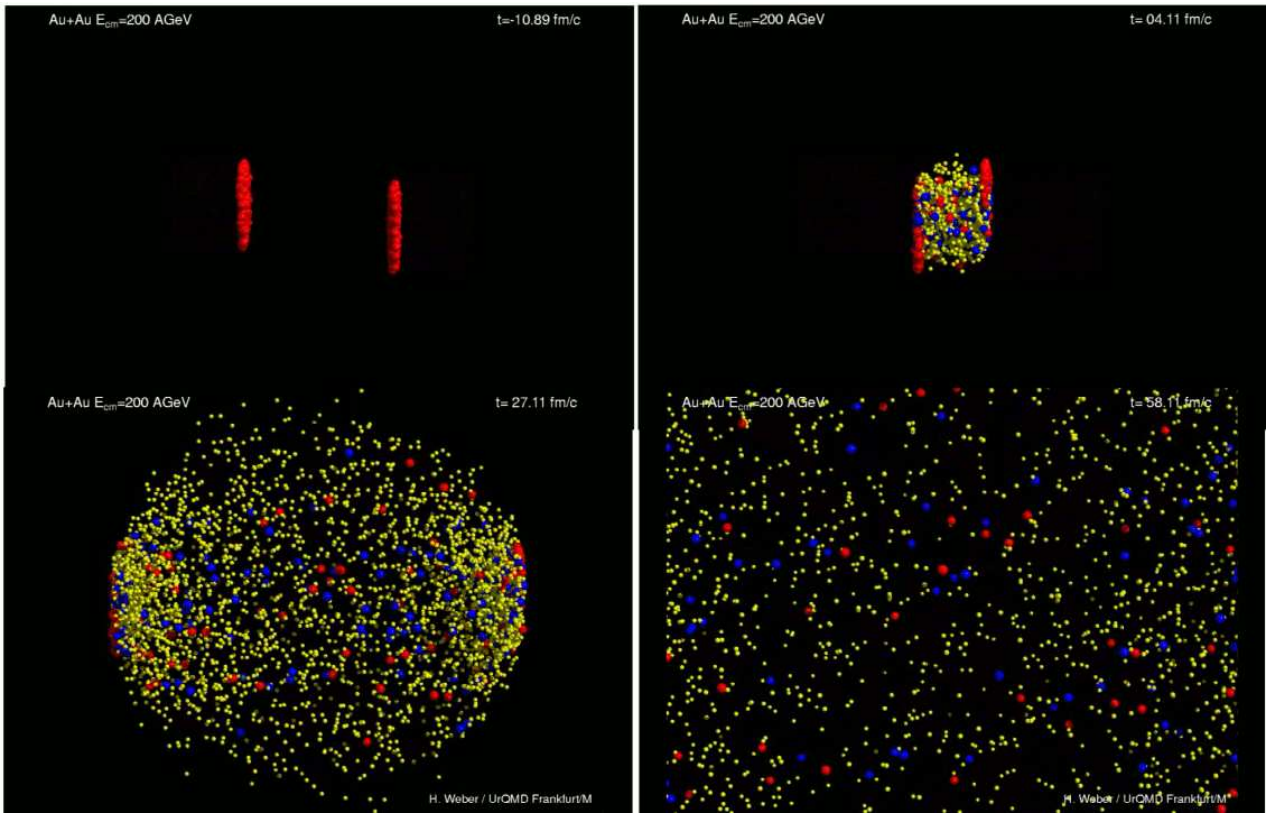

Figure 3.1: The UrQMD simulation of an $Au + Au$ collision performed at 200 GeV collision energy. First picture shows Lorenz-contracted nuclei before the collision, second plot illustrates a stage just after collision, third plot shows newly produced hadrons (mesons in yellow and baryons in blue colors, nuclear remnants are shown in red), and the last plot shows the expanding system at the final stage [43].

nuclei are treated as clouds of quarks and gluons which penetrate each other. An example of a parton model can be EPOS [48].

Unfortunately no model can be used in the whole range of collision energy, because the mechanisms of particle production depend on the specific energy range. The following sub-sections describe the basics of the UrQMD and EPOS approaches. Another sub-section contains a description of hydrodynamical models.

3.1 UrQMD

This model can successfully operate at the relativistic energies available at RHIC ($\sqrt{s_{NN}} = 200\,\text{GeV}$). At the highest energies, a huge number of different particle species can be produced.

The model should allow for subsequent rescatterings. The collision term in the model includes more than fifty baryon species and over thirty different meson species.
All particles can be produced in hadron-hadron collisions and can interact further with each other. The model is a microscopic transport approach. It includes:

- stochastic binary scatterings,
- color string formation,
- resonance decay.

It constitutes a Monte Carlo solution with equations for the time evolution of various phase-space densities, which non-relativistically assumes the Boltzmann form:

$$Stf_i(x,p) = \frac{df_i(x,p)}{dt} = \frac{\partial p}{\partial t}\frac{\partial df_i(x,p)}{\partial p} + \frac{\partial x}{\partial t}\frac{\partial df_i(x,p)}{\partial x} + \frac{\partial df_i(x,p)}{\partial t} \tag{3.1}$$

where x and p are the position and momentum of the particle, respectively, and $Stf_i(x,p)$ corresponds to the collision term of these particle species f_i.
The nucleons are represented by Gaussian shaped density distributions.

The total hadronic cross-section is interpreted geometrically. A collision between two hadrons will occur when $d < \sqrt{\sigma_{tot}/\pi}$, where d and σ_{tot} are the impact parameter of the two hadrons and their total cross-section, respectively.
Concerning input parameters, as it is possible to choose the impact parameter, one can control centrality of the collision. Then, it is necessary to specify the type of the collision (target and projectile), as well as its energy. It is possible to define the equation of state (here the cascade mode is switched on), one can also stop the decay of particles of given types. On the output, the model gives access to many particle properties, however in this studies only the following parameters are used: the counter of the particle, the particle identification number (which allows one to distinguish between pions, kaons, protons and many other implemented types of particles), the momentum four-vector (three components of momentum: p_x,p_y,p_z, and energy E), freeze-out position coordinates (three spatial components: x, y, z, and time t), as well as additional custom-added components: the variable which informs whether the considered particle comes from a decay and if it decays to another particle (or stays stable). Thanks to these, it is possible to deduce the evolution of particles. Further details of the application of the UrQMD model to heavy-ion reactions may be found in [44].

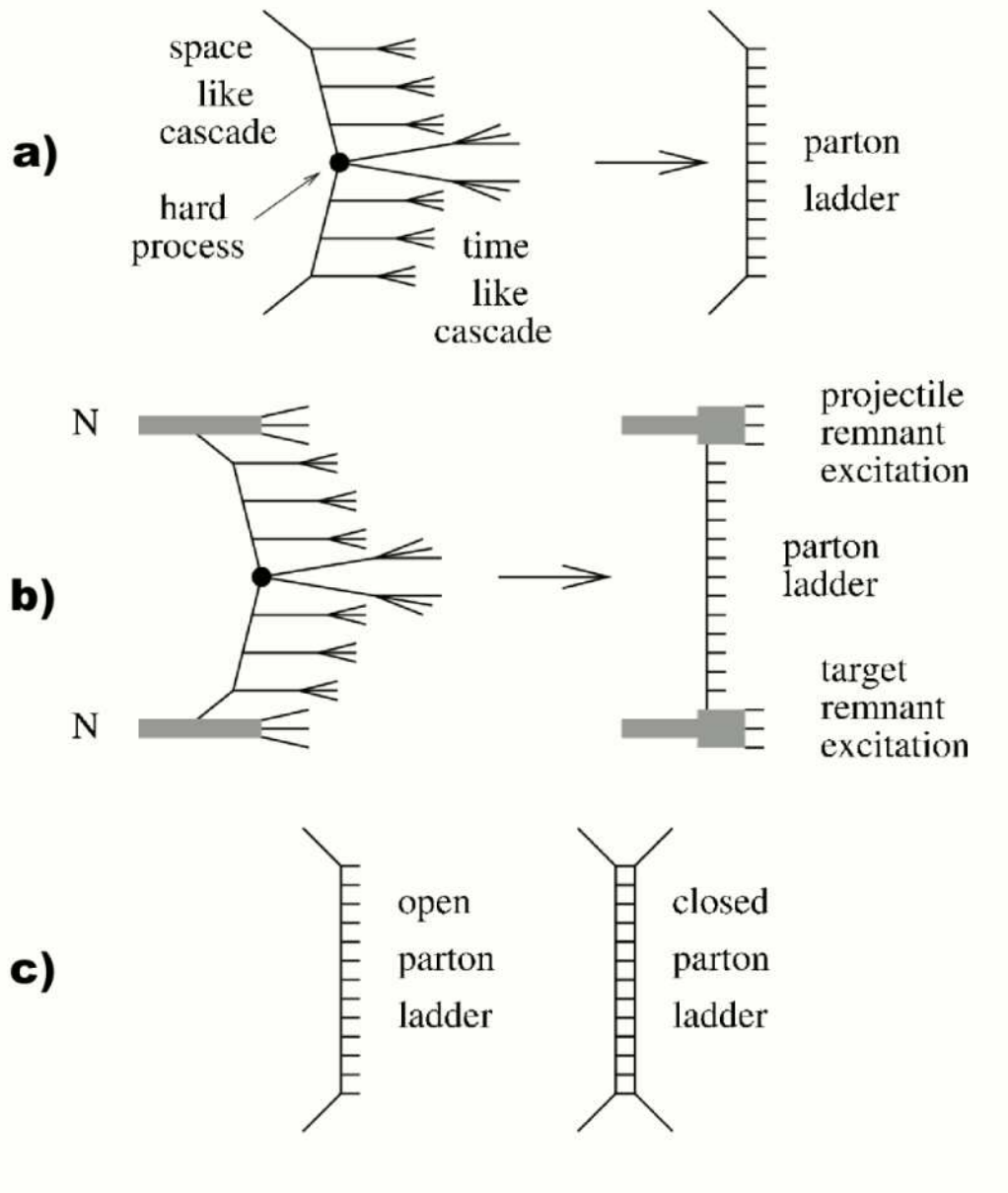

Figure 3.2: a) Elementary parton-parton scattering, the hard part is in the center. The parton ladder is symbolic; b) the complete picture of a parton ladder; c) Open ladder corresponds to inelastic interactions, closed ladder illustrates elastic interactions [48]

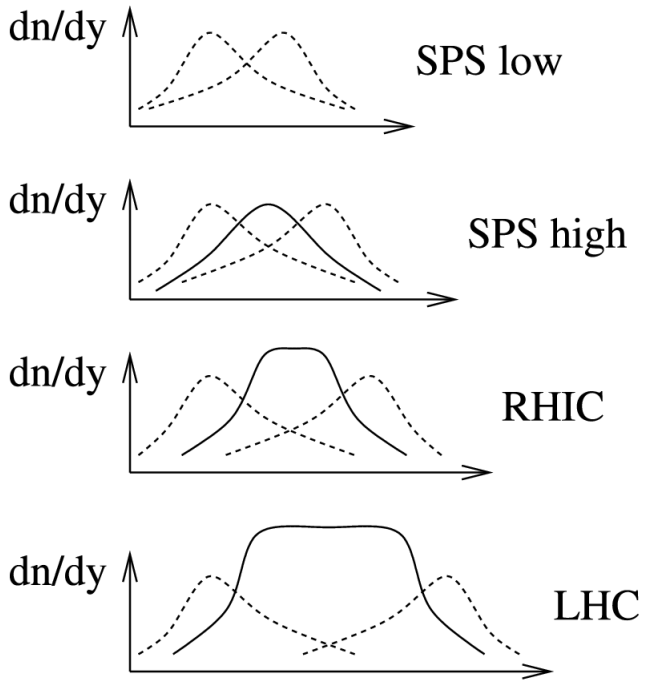

Figure 3.3: Inner and outer contributions at various energies reached by experiments [48]

Figure 3.1 shows a short simulation of an $Au + Au$ collision at 200 GeV. Projectile nucleons: red - target nucleons: red - mesons: yellow - excited baryons: blue.
The model reproduces the total, elastic and inelastic cross-sections of hadronic reactions. The model predicts particle multiplicities (e.g. inclusive cross-sections) and (Lorenz invariant) cross sections as well.

3.2 EPOS

The EPOS model is suited for a broad range of collision energies, it even takes into account predictions for the LHC. In this model many reactions can be simulated, from simple nucleon-nucleon collisions (such as $p + p$), through more complicated nucleon-nucleus systems (e.g. $d+Au$) to the most complicated nucleus-nucleus collisions (e.g. $Au+Au$, $Pb+Pb$, $Cu+Cu$,...). EPOS is an abbreviation, which stands for:

- Energy-conserving quantum mechanical multiple-scattering approach;

- Partons (parton ladders);
- Off-shell remnants;
- Splitting of parton ladders.

Produced partons are generally off-shell ones. They are represented by parton ladders. Each parton ladder is translated into color strings, which fragment into hadrons. A parton ladder consist of two parts: the hard one (discussed above) and the soft one (Figure 3.2, part 1). Two interacting partons, one from the projectile and one from the target, leave remnants as a result of their collision (Figure 3.2, part 2). A remnant can be interpreted as a di-quark with a string.
Open parton ladders correspond to inelastic scattering and closed parton ladders illustrate elastic scattering (Figure 3.2, part 3). There are two, highly significant nuclear "effects": elastic (related to screening and saturation processes) and inelastic (bifurcation) splitting of parton ladders. The idea of "energy-conserving multiple scattering" is simple: in the case of multiple scattering, when one has to calculate the partial cross-section for double, triple, .. scatterings, it is necessary to take care about total energy which have to be shared among individual elementary interactions. A consistent quantum-mechanical formulation requires the consideration of open and closed parton ladders. The closed ladders do not contribute to particle production, but they are significant since they affect the calculations of partial cross section. They lead to large numbers of interfering contributions for the same final state, all of which have to be summed up in order to obtain the corresponding partial cross-section.
The contribution from partons is meant as 'inner contribution' and the one from remnants as 'outer contributions'. In Figure 3.3, it is shown that remnants produce particles mainly in peripheral regions of rapidity and parton ladders- at central rapidities. The inner contribution rises with energy, and it dominates central rapidities at higher energies, whereas outer contributions exist and have a stronger influence at lower energies, where inner contributions may not have conditions to exist. At RHIC energies a significant remnant contribution still exist.
Concerning input parameters, it is necessary to chose the type and energy of the collision. If it is required, it is also possible to stop decays of particles of some types. One can control centrality of the collision by choosing the impact parameter. The model gives access to many particle properties. In these studies only the following characteristics are used: the index of the particle, the particle identification number (which allows to distinguish between pions, kaons, protons and many other implemented types of particles), momentum four-vector (three components of momentum: p_x,p_y,p_z, and energy E), freeze-out position coordinates (three spatial components:

x, y, z, and time t). Freeze-out coordinates were added to model specially for two-particle correlations. Here also another additional components are used: the variable which informs whether considered particle comes from a decay and if it decays to another particle (or stays stable). It is thus possible to reproduce the particle history.

3.3 Hydrodynamics

If the system is macroscopic, then thermodynamics describes the static (temperature, pressure, entropy, ...) and hydrodynamics- the dynamic (directed flow, anisotropic flow, particle production versus transverse momentum, ...) properties of matter. In fact, the observed particle ratios are close to the particle ratios in an ideal gas or fluid at the temperature $T \simeq 165$MeV (while lattice QCD predicts a phase transition at the temperature $T \simeq 175$ MeV). This suggests that the system evolves from a state close to the thermal equilibrium at the phase-transition boundary. On the other hand, the thermal description reproduces hadron ratios in $p+p$ and $e^+ + e^-$ collisions, where the system is small and the thermal equilibrium seems to be impossible. It is important to point out here that as elementary collisions (such $p+p$ and $e^+ + e^-$) do not exhibit hydrodynamical behavior, the excited systems produced as a result of such collisions are not macroscopic ones. Therefore, a thermodynamic (static) description, not taking into account a hydrodynamic (dynamic) one, can probe a macroscopic state. In contrast, experiments with heavy-ion collision programs show evidence for hydrodynamic expansion, as momentum correlations are observed in the energy domains, both SPS and RHIC.
Relativistic hydrodynamics is a set of conservation laws for the energy-momentum tensor $T^{\mu\nu}$ and the current J_i^μ in the case of fluid carrying conserved charges N_i.

$$\partial_\mu T^{\mu\nu} = 0 \tag{3.2}$$

and

$$\partial_\mu J_i^\mu = 0 \tag{3.3}$$

In equilibrium, $T^{\mu\nu}$ and J_i^μ are related to the properties of the fluid by the following relations:

$$T^{\mu\nu} = (e+p)U^\mu U^\nu - pg^{\mu\nu} \tag{3.4}$$

and

$$J_i^\mu = n_i U^\mu \tag{3.5}$$

Here e is energy density, p is pressure, n_i is the number density of corresponding current, $U^\mu = \gamma(1, \upsilon_x, \upsilon_y, \upsilon_z)$ is the proper velocity of the fluid and $J_i^\mu = n_i u^\mu$, where $N_i = \sum_i n_i$, $g = diag(+,-,-,-)$ is the metric tensor. In the case of strong interactions, the conserved currents are: iso-spin (J_I^μ), strangeness (J_S^μ), baryon number (J_B^μ). For the hydrodynamical evolution, iso-spin symmetry is assumed and the net strangeness is zero value, so only baryon current is considered below.

The equations for the dynamics of an ideal fluid are specified by the 'Equation of State' (EoS) for the matter when the condition is set $p = p(\epsilon, n)$. Then, few elements can be specified: the energy $T^{00} = E$, the momentum $T^{0i} = M^i$ and the total charge $N^0 = R$. The equations of motion:

$$\partial_t E + \nabla \cdot (Ev) = -\nabla \cdot (pv) \tag{3.6}$$

$$\partial_t M + \nabla \cdot (Mv) = -\nabla p \tag{3.7}$$

$$\partial_t M + \nabla \cdot (Rv) = 0 \tag{3.8}$$

Solving the EoS enables one to compare many experimental observables with hydrodynamical predictions. Starting from single spectra distributions (calculated by hydrodynamics at given temperature), through directed and anisotropic flow, dependence on impact parameter (transformed often in heavy-ion collisions to the number of charged particles produced in such a collision), momentum correlation: azimuthal and two-particle correlations and many other observables, help to better understand processes and reactions in collisions with a hydrodynamical description. Recent results show that hydro successfully describes single-particle distributions, and momentum spectra, reflects well particle productions versus their transverse momentum and mass; however it fails in reproducing e.g HBT radii. More about hydrodynamical description of heavy-ion collisions can be found in [49, 50].

Chapter 4

Two-particle correlations at small relative velocities

Two-particle correlations at low relative velocities allow one to measure one of the smallest sizes in nature, which corresponds to the size of a nucleon. They also make it possible to deduce space-time properties of the sources. The measured sizes are of the order of 10^{-15}m (1 fm) and therefore such two-particle correlation methods are called 'femtoscopy' [51]. The first such measurement, which can be treated as an introduction to developing the two-particle interferometry method later, was performed in astronomy. R. Hanbury-Brown and R.Q. Twiss have proposed a method (called HBT from their initials) [52] of estimating angular sizes of stellar objects by studying the intensity of electromagnetic signals measured in coincidence. The intensity interferometry for particles has similar origin, but uses particle momentum and is dedicated to measuring space-time extent of the emitting source. Speaking more precisely, it is possible to deduce the particle separation between sources emitting particles using dependencies of their relative momentum. Both the HBT method from astronomy and two-particle interferometry use correlation techniques on one part of the phase space (which can be measured, e.g. photon intensity in astronomy, particle momenta in nuclear collisions) to obtain information about a part of phase space which is not measurable.

4.1 Identical non-interacting unpolarized nucleons and pions

Two identical particles with random polarization are emitted at the space-time points x_1 and x_2, with four-momenta p_1 and p_2 for the first and second particle, respectively (particles are

numbered due to a convention which has to be introduced). In a simpler picture of two spinless bosons, the correlation function is determined by Quantum Statistics (QS) [53] (they are also emitted at the space-time points x_1 and x_2 with their four-momenta p_1 and p_2):

$$R_{\pi\pi}(p_1, p_2) = \frac{1}{2}\left|e^{i(p_1x_1+p_2x_2)} + e^{i(p_1x_2+p_2x_1)}\right|^2 \tag{4.1}$$

The equation takes into account that it is impossible to exclude the scenario when the particle with four-momentum p_1 is emitted from the space-time point x_2 and the particle with four-momentum p_2 is emitted from the space-time point x_1. In the case of non-interacting identical fermions with half spin values, the second factor is subtracted from the first one due to anti-symmetrization of the wave function. In the case of nucleons there are two possible spin states: $S = 0$ (singlet) and $S = 1$ (triplet), with populations of $1/4$ and $3/4$, respectively. The correlation function is determined by QS.

$$R_{nn}(p_1, p_2) = \frac{1}{4}\left[\frac{1}{2}\left|e^{i(p_1x_1+p_2x_2)} + e^{i(p_2x_1+p_1x_2)}\right|^2\right] + \frac{3}{4}\left[\frac{1}{2}\left|e^{i(p_1x_1+p_2x_2)} - e^{i(p_2x_1+p_1x_2)}\right|^2\right] \tag{4.2}$$

The first term corresponds to the singlet (spin-anti-symmetric) state and the second to triplet (spin-symmetric) state. The correlation function (Equation 4.1) can be expressed in the form:

$$R_{\pi\pi}(p_1, p_2) = 1 + \langle cos(qx)\rangle \tag{4.3}$$

where $x \equiv \{t, \overrightarrow{x}\} = x_1 - x_2$ and $q \equiv \{q_0, \overrightarrow{q}\} = p_1 - p_2$. For Equation 4.2:

$$R_{nn}(p_1, p_2) = \frac{1}{4}\left[1 + \langle cos(qx)\rangle\right] + \frac{3}{4}\left[1 - \langle cos(qx)\rangle\right] = 1 - \frac{1}{2}\langle cos(qx)\rangle \tag{4.4}$$

This results were obtained by Kopylov and Podgoretsky [54]. In the case of a Gaussian space-time distribution of emission points:

$$S_i(x_i) \sim exp\left[-\left(\frac{\overrightarrow{x_i}}{\sqrt{2}r_0}\right)^2 - \left(\frac{t_i}{\sqrt{2}\tau_0}\right)^2\right] \tag{4.5}$$

where r_0 and τ_0 are the source's parameters respectively: size and time. Correlation functions take then the form:

$$R_{\pi\pi}(p_1, p_2) = 1 + exp(-\overrightarrow{q^2}r_0^2 - q_0^2\tau_0^2) \tag{4.6}$$

$$R_{nn}(p_1, p_2) = 1 - \frac{1}{2}exp(-\overrightarrow{q^2}r_0^2 - q_0^2\tau_0^2) \tag{4.7}$$

for non-spin (e.g. identical pions) and spin dependencies (e.g. identical nucleons) respectively.

4.2 Identical non-interacting polarized nucleons

Nucleons (as the are baryons) interact through strong forces. In the case of populations of singlet (ρ_0) and triplet (ρ_1) states dependent on the polarization vector, $\overrightarrow{P}$ following terms are considered: [55]

$$\rho_0 = \frac{1}{4}(1 - \overrightarrow{P_n^2}) \tag{4.8}$$

$$\rho_1 = \frac{1}{4}(3 + \overrightarrow{P_n^2}) \tag{4.9}$$

Then, the correlation function is given as:

$$R_{nn}(p_1, p_2) = 1 - \frac{1 + \overrightarrow{P_n^2}}{2} \langle cos(qx) \rangle \tag{4.10}$$

4.3 Non-identical interacting nucleons (neutron - proton)

Below consideration may be applied to non-identical systems like proton - anti-proton but there Coulomb interactions has to be taken into account additionally.
Due to interaction between particles, the plane-wave in the previous example is replaced by the Bethe-Salpeter amplitude [56]:

$$e^{i(p_1x_1+p_2x_2)} \rightarrow \psi^{(S)}_{p_1p_2}(x_1, x_2) = e^{i(p_1x_1+p_2x_2)} + \varphi^{(S)}_{p_1p_2}(x_1, x_2) \tag{4.11}$$

where $\varphi^{(S)}_{p_1p_2}(x_1, x_2)$ is the scattered wave. In this case, the correlation function takes the form:

$$R_{np}(p_1, p_2) = \rho_0 \left\langle \left| \psi^{(0)}_{p_1p_2}(x) \right| \right\rangle^2 + \rho_1 \left\langle \left| \psi^{(1)}_{p_1p_2}(x) \right| \right\rangle^2 \tag{4.12}$$

Here $\psi^{(S)}_{p_1p_2}(x)$ is obtained from the Bethe-Salpeter amplitude after separation of the c.m.s motion:

$$\psi^{(S)}_{p_1p_2}(x_1, x_2) = e^{iPX} \psi^{(S)}_{p_1p_2}(x) \tag{4.13}$$

where $P = p_1 + p_2$, $X = [(p_1P)x_1 + (p_2P)x_2]/P^2 = \{X_0, \overrightarrow{R}\}$ is the two-particle c.m.s four-coordinate.

The populations of singlet and triplet states are:

$$\rho_0 = \frac{1}{4}(1 - \overrightarrow{P_n}\overrightarrow{P_p}) \tag{4.14}$$

$$\rho_1 = \frac{1}{4}(3 + \overrightarrow{P_n}\overrightarrow{P_p}) \tag{4.15}$$

Now, $x^* = (\overrightarrow{r^*}, t^*)$ in the c.m.s of the pair is defined. The amplitude $\psi^{(S)}_{p_1p_2}(x_1, x_2)$ is replaced by the wave function $\psi^{(S)(+)}_{-\overrightarrow{k^*}}(\overrightarrow{r^*})$ describing the relative motion of particles with asymptotic $(r^* \to \infty)$ of a superposition of the plane and diverging spherical wave:

$$\psi^{(S)(+)}_{-\overrightarrow{k^*}}(\overrightarrow{r^*}) \to e^{i\overrightarrow{k^*}\overrightarrow{r^*}} + f^{(S)}(\overrightarrow{k^*})\frac{e^{i\overrightarrow{k^*}\overrightarrow{r^*}}}{r^*} \tag{4.16}$$

where $k^* = \sqrt{-q^2}/2$.

4.4 Identical interacting particles

Replacing the plane waves with Bethe-Salpeter amplitudes, the formula is:

$$R_{nn}(p_1, p_2) = \frac{1}{4}(1-\overrightarrow{P_n^2}) \left\langle \left| \frac{1}{\sqrt{2}} \left(\psi^{(0)}_{p_1p_2}(x) + \psi^{(0)}_{p_2p_1}(x)\right) \right|^2 \right\rangle + \frac{1}{4}(3+\overrightarrow{P_n^2}) \left\langle \left| \frac{1}{\sqrt{2}} \left(\psi^{(0)}_{p_1p_2}(x) + \psi^{(0)}_{p_2p_1}(x)\right) \right|^2 \right\rangle \tag{4.17}$$

4.5 Deuteron formation rate

Assuming that deuteron formation is dominated by the FSI between emitted protons and neutron, it is possible to form a deuteron state. The cross-section for a creation of such a system is given by the formula:

$$\sigma^{(1)}_d(P_d) = (2\pi)^3\gamma\rho_1 \left\langle \left|\psi^{(1)}_b(x)\right|^2 \right\rangle \tilde{\sigma_{np}}(\frac{1}{2}P_d, \frac{1}{2}P_d) \tag{4.18}$$

where γ is the Lorenz factor, $\psi^{(1)}_b(x)$ is the Bethe-Salpeter amplitude describing the bound triplet state of neutron and proton. $\tilde{\sigma_{np}}(\frac{1}{2}P_d, \frac{1}{2}P_d) \simeq \tilde{\sigma_{np}}(p_1, p_2)$ is the production cross-section of uncorrelated (n, p) pairs. It is related to the measured (n, p) production cross-section $\sigma_{np}(p_1, p_2)$

through the correlation function:

$$\sigma_{np}(p_1, p_2) = R_{np}(p_1, p_2)\tilde{\sigma_{np}}(p_1, p_2) \tag{4.19}$$

The deuteron formation cross-section is related to the emission is (p, n) pairs with nearby momenta.

4.6 The treatment of Coulomb Interaction

In the case of charged particles, long-range Coulomb FSI are observed. The pair wave function is described then:

$$\Psi^{(S)}_{\overrightarrow{k*}}(\overrightarrow{r*}) = \sqrt{A_C^{\pm}}\exp(i\delta_0^C)F(-i\eta, 1, i\xi) \tag{4.20}$$

where A_C is the Gamow factor.

$$A_C^{\pm}(k^*) = \pm(2\pi/k^* a_C)\frac{1}{\exp[\pm(2\pi/k^* a_C)] - 1} \tag{4.21}$$

the sign $+(-)$ corresponds to repulsion (attraction), k^* is the momentum of one particle in the PRF (Pair Rest Frame reference), $a_C = \frac{2\left(\frac{h}{2\pi}\right)^2}{me^2}$ is the Bohr radius for particles with unit charges (for protons $a_C = 57.5fm$), $\delta_o^C = \arg\Gamma(1 + i/k^* a_C)$ is the Coulomb s-wave phase shift, $F(-i\eta, 1, i\xi)$ is the confluent hypergeometrical function where $\eta = 1/(k^* a_c)$, $\xi = qr^* + \overrightarrow{q}\overrightarrow{r^*} = qr^*(1 + cos\theta^*)$ and θ^* is the angle between particle relative momentum $\overrightarrow{q}$ and the initial separation $\overrightarrow{r^*}$.

4.7 Combining Strong and Coulomb interaction

Systems which requires combining both of FSI are first of all combinations of baryons (strong interactions dominate in baryon systems in smaller sources), then combinations of two mesons and mesons with baryons. The Coulomb interaction is a modification of the wave-function of the pair and of both incoming plane waves, including the scattered wave. The scattering amplitude becomes then:

$$f(\overrightarrow{k^*}) = \left[\frac{1}{f_0} + \frac{1}{2}d_0 k^{*2} - \frac{2}{a_c}h(k^* a_c) - ik^* A_c(k^*)\right]^{-1} \tag{4.22}$$

In the case of proton-proton interaction $f_0 = 7.77$fm and $d_0 = 2.77$fm. The function $h(x)$ has the following form:

$$h(x) = \frac{1}{x^2} \sum_{n=1}^{\infty} \frac{1}{n(n^2 + x^{-2})} - C + ln|x| \tag{4.23}$$

where C is constant.

4.8 Parametrization of correlation function of identical pions

Very often, the source is assumed to be a three-dimensional sphere described by a Gaussian density distribution in space-time. The $\overrightarrow{q}$ vector can be decomposed into three components, the parametrization of the correlation function was proposed by Kopylov and Podgoretsky [57] (K-P parametrization) and by Bertsch-Pratt (Bertsch-Pratt decompositions) [58] (Figure 4.1). The longitudinal component q_{long} is parallel to the beam axis (the z-axis), the outward component q_{out} is parallel to the transverse momentum of the pair ($\overrightarrow{K_T}$) and the sideward component q_{side} is perpendicular to both of them. More details can be found in the caption of the figure. In this case, one can obtain the following parametrization of the correlation function [1] determined by QS (it is assumed that the cross-terms vanish due to symmetry reasons):

$$C(q_{out}, q_{side}, q_{long}, \lambda) = 1 + \lambda exp\left(-q_{out}^2 r_{out}^2 - q_{side}^2 r_{side}^2 - q_{long}^2 r_{long}^2\right) \tag{4.24}$$

where r_{out}, r_{side} and r_{long} are the size of the source in the out, $side$ and $long$ direction, respectively; the λ parameter indicates the strength of the correlation and is a number in the range $[0.0, 1.0]$. Values of λ lower than 1.0 are observed experimentally and are attributed to several reasons: the admixture of misidentified particles, the inclusion of non-correlated pairs and detector inefficiencies. Frequently, the correlation function is also analyzed as a function of only one variable - the value of relative momentum in the pair rest frame, Q_{inv}:

$$C(Q_{inv}; r_0, \lambda) = 1 + \lambda exp\left(-Q_{inv}^2 r_0^2\right) \tag{4.25}$$

The correlation function fitted by one of above formulas provides the source size - the Gaussian radius of the source r_0 in the case of 1-dimensional correlation functions, or three radii: r_{out}, r_{side}, r_{long} in the case of 3-dimensional correlation functions.
Very often the correlation function is measured for particles which interact by Coulomb and/or

[1] The correlation function is denoted by C, however very often different notations are used as well: CF, R

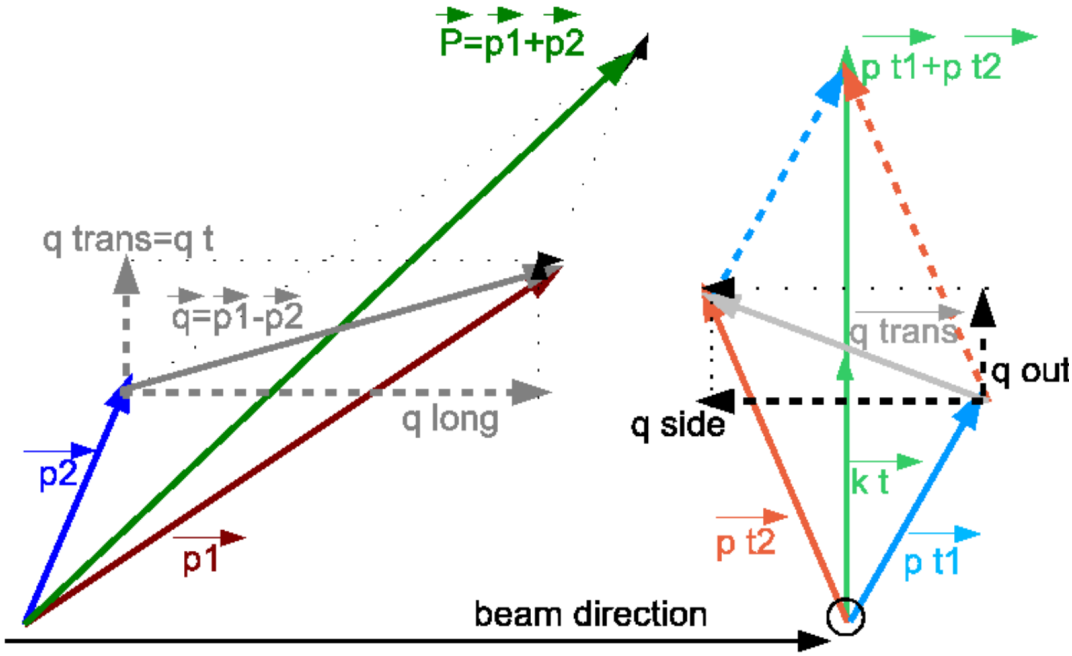

Figure 4.1: Kinematic relations for a two-particle system. Left-hand side of the plot shows decomposition of the q vector into transverse q_{trans} and longitudinal q_{long} components. The q vector is the difference of particle momenta $p_1$and p_2. The q_{long} component has direction of beam axis. The right-hand side of the plot show decomposition of q_{trans} onto q_{out} and q_{side} components. q_{out} is described by the direction of transverse pair momentum, the q_{side} component is perpendicular to q_{long} and q_{out} components. The figure contains as well the k_T vector which is the half of total pair transverse momentum.

strong forces. Such interactions have to be taken into account when trying to deduce the source size.

4.9 Theoretical predictions for $\pi - \pi$, $p - p$ and $p - \overline{p}$ systems

The top panel of Figure 4.2 shows theoretical predictions for $\pi^+\pi^+$ system for a number of source sizes: 3fm, 5fm, 10fm and 20fm. Only sources with $\lambda = 1$ are considered ($\lambda = 1$ is assumed). For each source size complete calculations including QS and Final State Interactions (FSI) [59, 60] have been performed. The figure also contains calculations for the QS effect only (3 and 20 fm). In this case, the correlation function reaches the value of 2.0 for $Q_{inv} = 0$ GeV/c. In the case of a bigger source (20fm), the correlation effect decreases faster. (The finite size of bins causes the first point of correlation does not reach 2.0). For small Q_{inv}, the correlation function goes to zero due to Coulomb repulsion. The strength of correlation increases with decreasing source-size.
The bottom panel of Figure 4.2 shows theoretical predictions for the ($p-p$) system. Calculations for many source sizes are presented. The correlation effect for the case of identical fermions such as $p-p$ and $\overline{p}-\overline{p}$ is driven by anti-symmetrization of the wave function determined by QS. Two FSI exist in this system as well: protons are repelled by Coulomb forces and they strongly interact. For smaller sources, the correlation has a peak for $Q_{inv} = 40$ MeV due to interplay of all types of correlation effects. Coulomb FSI repulsion causes that the correlation function for $Q_{inv} \rightarrow 0$GeV/c. The correlation strength depends directly on the source size, it decreases with increasing the source size. In Figure 4.3, theoretical predictions for proton-proton ($p - p$) and proton- anti-proton ($p - \overline{p}$) correlations are shown. The second part of the plot is dedicated to $p - \overline{p}$ interactions. Proton - anti-proton combinations have not been measured so far due to not sufficient statistic. However, the description of the strong interaction between proton and its anti-particle has not been estimated with a high accuracy. Theorists needed experimental measurements in order to improve the scattering calculations for such system. In $p - \overline{p}$ correlations, only FSI occur. Here the characteristic, wide band below unity corresponding to annihilation processes between particles and their anti-particles appears. Even if, the assumed $p-p$ and $p-\overline{p}$ source sizes are the same (here 3fm), it does not lead to the same range of interactions: the $p-\overline{p}$ correlation can be twice as wide as for $p-p$. Depending on the source size, the correlation function can have a different shape, as strong interactions are more dominant on smaller distances. These two simulations were prepared assuming Gaussian source distributions with the radius of

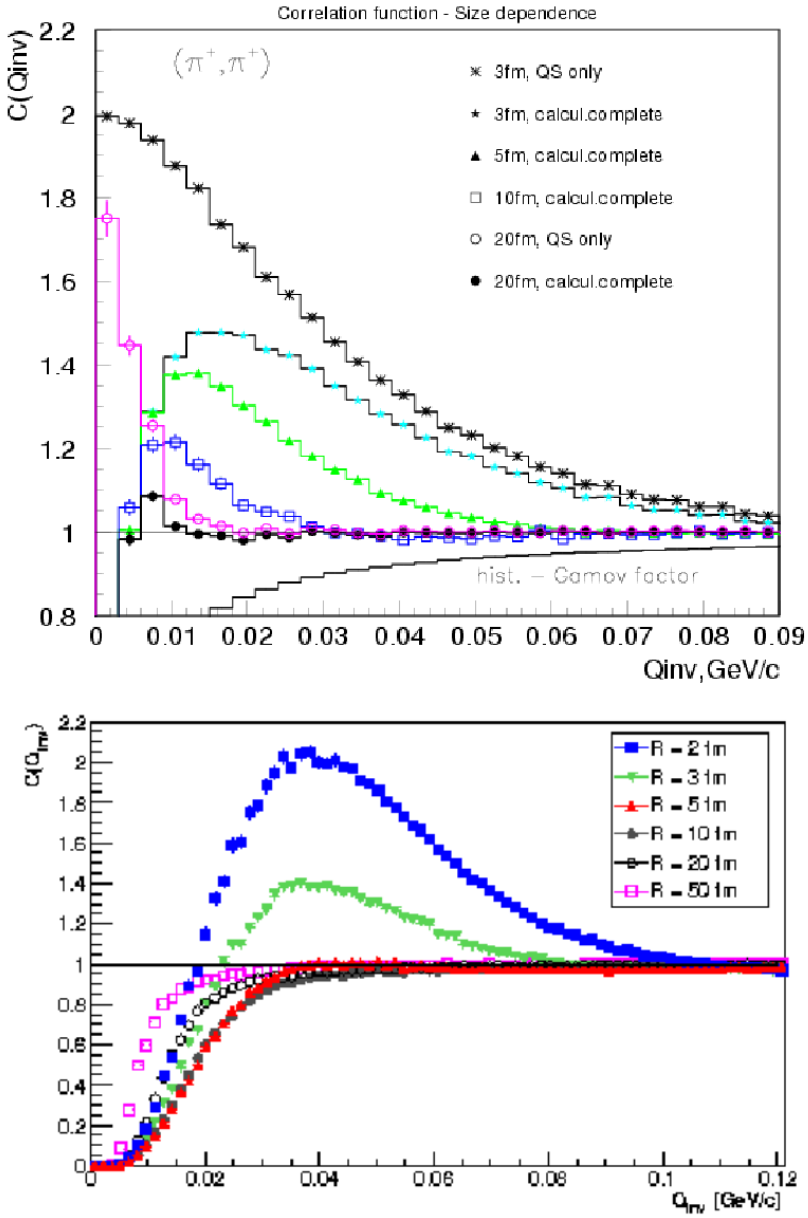

Figure 4.2: Top panel: pion - pion correlation functions for assumed source sizes: 3 fm including QS only (black stars) and for QS and FSI (bright blue points); 5 fm QS + FSI (green triangles); 10 fm for complete calculations (blue squares); 20 fm for QS only (pink open circles) and for QS + FSI (black circles). Bottom panel: proton - proton correlation functions for 6 different source sizes: 2 fm (dark blue squares), 3fm (green triangles), 5fm (red triangles), 10fm (gray closed circles), 20fm (black open circles) and 50 fm (pink open squares) [61].

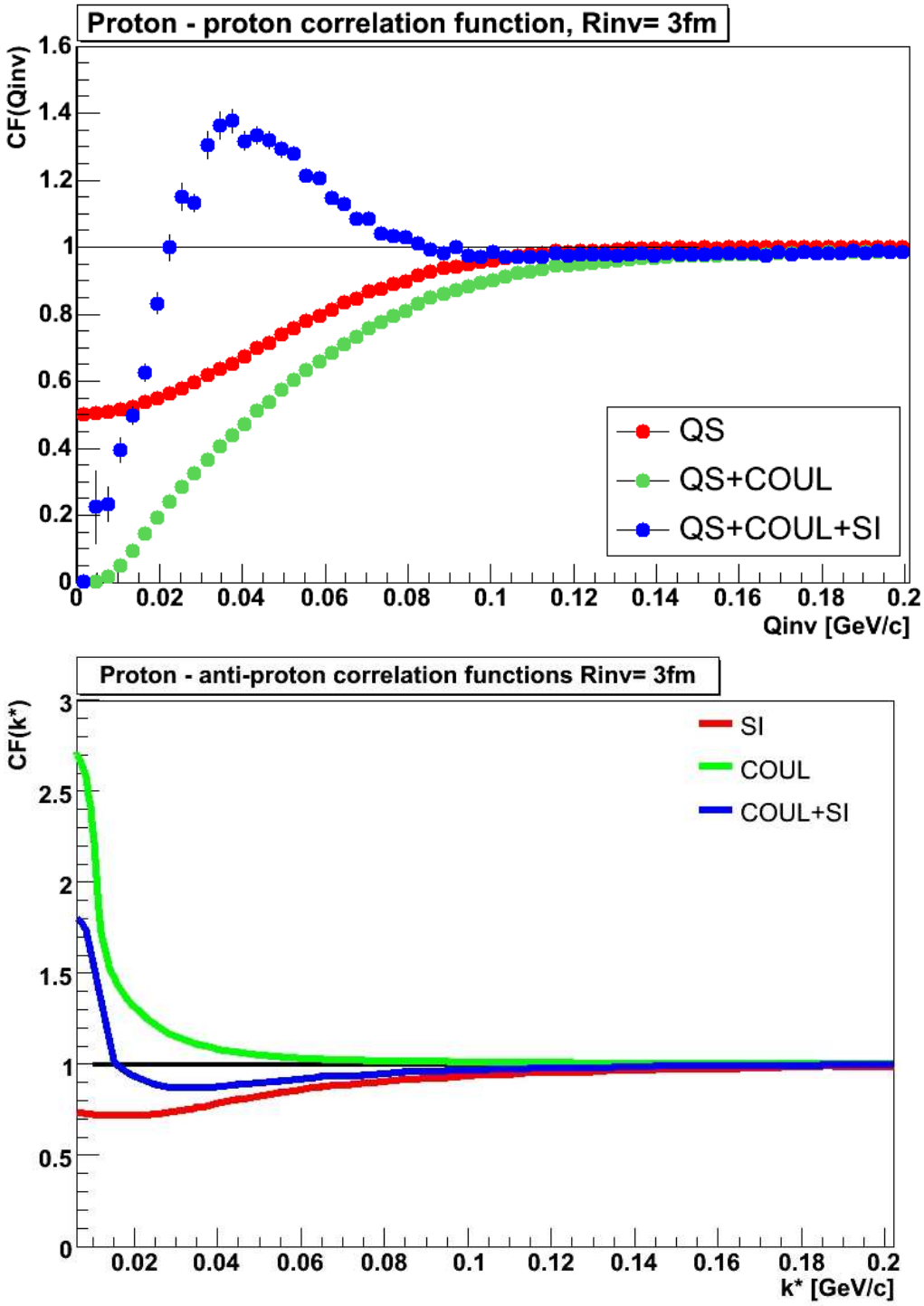

Figure 4.3: $p-p$ and $p-\overline{p}$ correlation functions for the source size of 3 fm. Top panel presents identical proton combinations: QS (red curve), QS+COUL (green curve), QS+COUL+SI (red curve). Bottom panel illustrates non-identical proton combinations: COUL (green curve), SI (red curve), COUL+SI (blue curve).

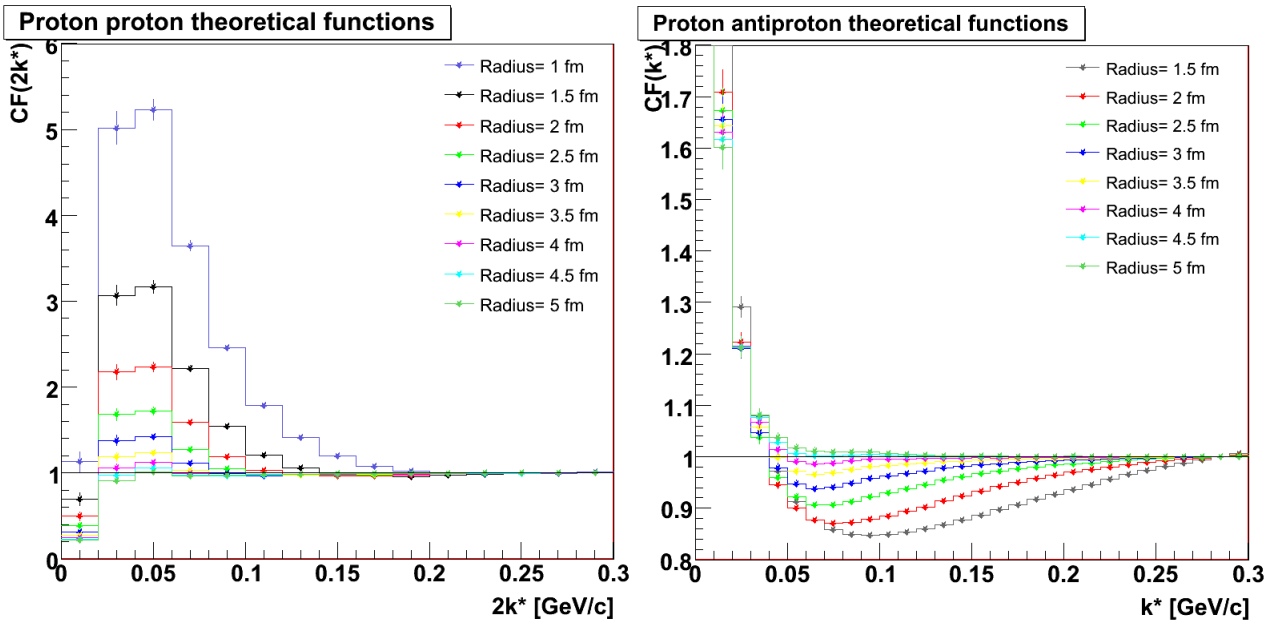

Figure 4.4: $p-p$ and $p-\overline{p}$ correlation functions for various source sizes.

3 fm.

Figure 4.4 shows theoretical calculations for $p-p$ and $p-\overline{p}$ combinations for the source sizes approximately achieved at the STAR experiment. For the source sizes bigger than 4 fm, measuring the size of $p-p$ sources becomes more difficult. In all simulations, no time delay between particles has been assumed.

4.10 Theoretical basics of non-identical particle correlations

Non-identical particle correlation analysis [62] allows one to study space-time asymmetries in the emission of two types of particles (e.g. pions and kaons, protons and anti-protons). The technique is explained on the pion - kaon example, which can be easily extended to the proton - anti-proton system. The correlation region due to Coulomb and, for baryon systems, nuclear interactions depends on whether the two particles move towards each other or away from each other in the Pair Rest Frame (PRF) reference. See Figure 4.5 for the illustration. One has to consider two possible asymmetries: time and spatial ones. In the case (I), when pion (proton) is emitted secondly and/or closer to the center of the system:

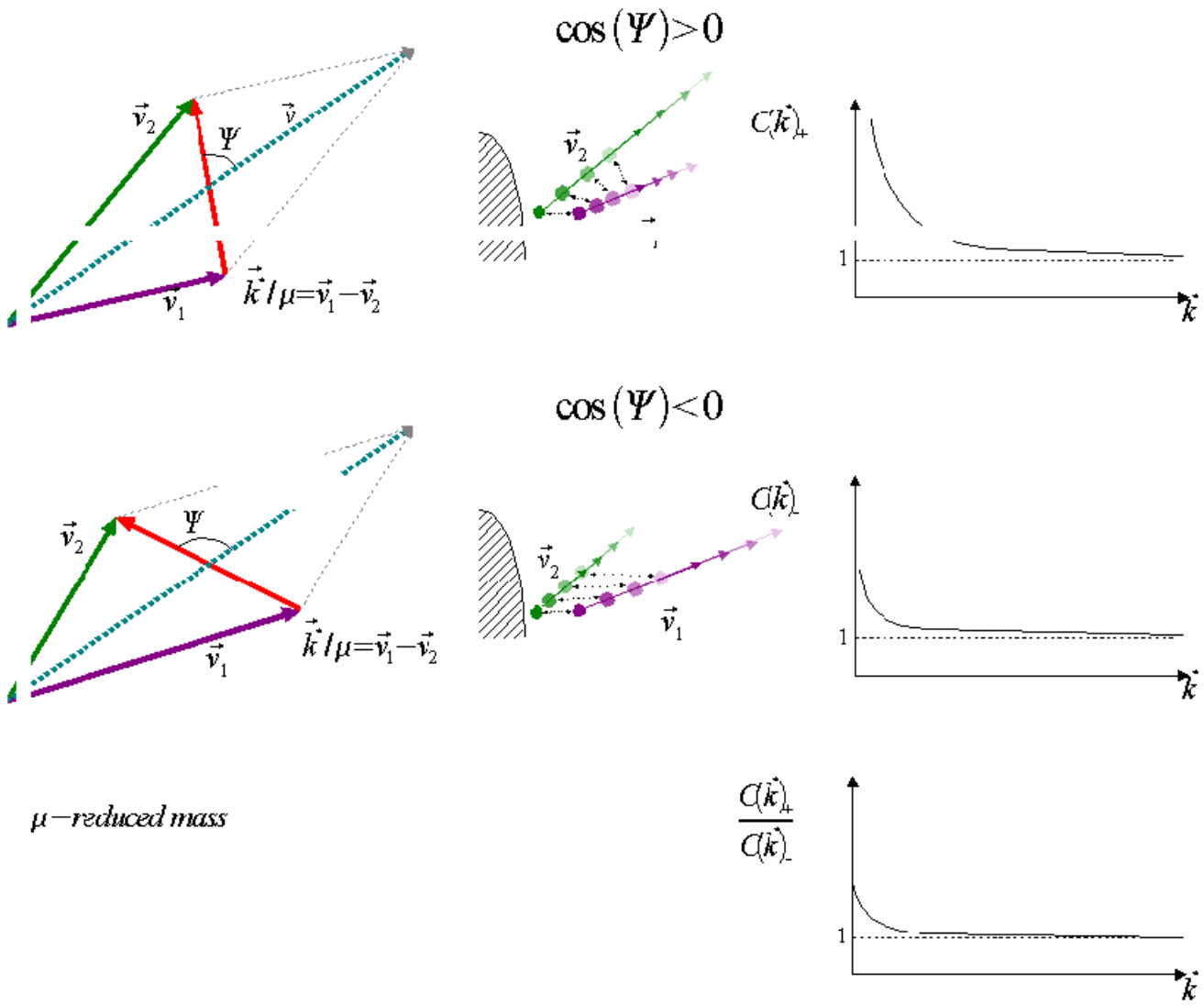

Figure 4.5: Asymmetry in space-time emission seen by non-identical particle correlations. v_1 and v_2 correspond to the first and the second particle velocity, respectively. The first row corresponds to the scenario when particle emitted first is slower and the particle emitted second catches up with it, corresponding correlation function is shown as well. The second row corresponds to the scenario when the particle emitted first is faster and moves away from the particle emitted later. In this case, the effective interaction time is shorter and the interaction is weaker. Below is the 'double - ratio'- the result of dividing the two correlation functions shown above. If it deviates from unity, then possible differences in emission between two types of non-identical particles are observed [63].

- Time asymmetry (particles are assumed to be emitted from the same positions); the kaon (anti-proton) is considered as emitted first, the pion (proton) second

- Spatial asymmetry (particles are assumed to be emitted at the same time); the pion (proton) is assumed to be emitted closer to the center of system and kaon (anti-proton) is considered as emitted further from the system center

  - A) the pion (proton) is faster than the kaon (anti-proton); the pion (proton) catches up with the kaon (anti-proton)

  - B) the pion (proton) is slower than the kaon (anti-proton); the kaon (anti-proton) moves away

In both A cases the correlation effect is stronger and the duration of interaction is longer than in B cases. Such stronger correlation functions are marked by $C_+(k^*_{out})$, and the weaker ones by $C_-(k^*_{out})$.

It is also possible to consider the opposite scenario, case (II): the pion (proton) is emitted first and/or closer to the edge of the system:

- Time asymmetry (particles are assumed to be emitted from the same positions); the pion (proton) is considered as emitted first, the kaon (anti-proton) second

- Spatial asymmetry (particles are assumed to be emitted at the same time); the pion (proton) is assumed to be emitted closer to the edge of the system and the kaon (anti-proton) is considered as emitted further to the edge of the system

  - A) the kaon (anti-proton) is faster than the pion (proton); the kaon (anti-proton) catches up with the pion (proton)

– B) the kaon (anti-proton) is slower than the pion (proton); the pion (proton) moves away

Again, in both A cases the correlation effect is stronger and the duration of interaction is longer than in B cases. Such stronger correlation functions are marked by $C_+(k^*_{out})$, and the weaker ones by $C_-(k^*_{out})$.

In our analysis the convention (I) is assumed; for $k^*_{out} > 0$, the pion (proton) is faster and for $k^*_{out} < 0$ the pion (proton) is slower. By studying the ratio of functions for positive and negative values of $k^*_{out} < 0$, the information about space-time asymmetry is deduced as a deviation from unity. One can study asymmetries in different directions by analyzing the correlations dependent on negative and positive components of k^* projections in three directions: the out, $side$, and $long$ components. In STAR, due to azimuthal symmetry and symmetry at midrapidity, the mean differences: $< r^*_{side} >=< r^*_{long} >= 0$. The asymmetry can be seen for the out projection and it is a mixture of two components: $< r^*_{out} >=< r_{out} > -\beta_t < t >$[64].

4.11 The experimental approach

In the experimental case, the correlation function is defined as a ratio of the probability of registering two particles simultaneously (in the same event) to the product of registering probabilities of such particles independently (in different events). It can be therefore obtained by dividing two-particle distribution by two single-particle distributions:

$$C(p_1, p_2) = \frac{P(p_1, p_2)}{P(p_1)P(p_2)} \tag{4.26}$$

This formula can be also expressed in the formalism of cross-sections:

$$C(p_1, p_2) \propto \left(\frac{d^6\sigma}{d^3p_1 d^3p_2}\right) \Big/ \left(\frac{d^3\sigma}{d^3p_1}\frac{d^3\sigma}{d^3p_2}\right) \tag{4.27}$$

Usually, the correlation function is analyzed as a function of pair relative momentum $\overrightarrow{q}$, considered in the frame, the pair's center-of-mass is at the rest, the Pair Rest Frame (PRF).
Constructing the correlation function in the experiment, one has put pairs of particles coming from the same event into numerator (particles are correlated) and pairs of particles from different

events (non-correlated, as a the reference):

$$C(p_1, p_2) = \frac{A(p_1, p_2)}{B(p_1, p_2)} \tag{4.28}$$

4.12 An experimental review of identical and non-identical particle correlations

Below is a short experimental review of the most significant results concerning identical particle correlations: excitation functions showing source-size dependencies for various values of collision energy, centrality dependencies versus transverse mass of pion source sizes and multiplicity scaling of radii.

Excitation function

Figure 4.6 shows HBT parameters (source sizes: R_{out},R_{side}, R_{long} and λ parameter) vs. collision energy for midrapidity. The data for central $Au + Au$, $Pb + Pb$ and $Pb + Au$ collisions describes $\pi^-\pi^-$ correlations at low transverse momenta. The large source sizes and/or lifitimes were suggested as potential signatures of the QGP state formation. An increase of $\sim 10\%$ (but not more) in the transverse radii R_o and R_s is observed. In the case of R_s, the increase might correspond to the large freeze-out volume for a larger pion multiplicity. R_l is slightly increasing for higher energies. The increase predicted by hydrodynamics in the ratio of R_o/R_s as a probe of QGP formation, is not observed. R_o/R_s is correlated with the emission duration. Hydrodynamical models typically calculate this value approximately equal to 1.5 and moderately dependent on k_T range. The R_o/R_s versus collision energy reflects flat dependence and is equal approximately to the unity, what indicates shorter than predicted by hydrodynamics emission duration. The differences between radii for $\sqrt{s_{NN}} = 200$ GeV (open and closed symbols) occur due to different methods of Coulomb correction [66, 67] applied in these two analysis, respectively. Smaller λ parameter, R_o and R_s values can be explained by applying different criteria in particle selections. This plot illustrates that the collision energy is not a scaling variable for HBT radii. Such behavior is known as $HBT\ puzzle$. As it was expected- for higher energies there should occur an increase of the radii (for out component specially), however the excitation function presents that the region showing this signature of the phase transition has not been achieved yet.

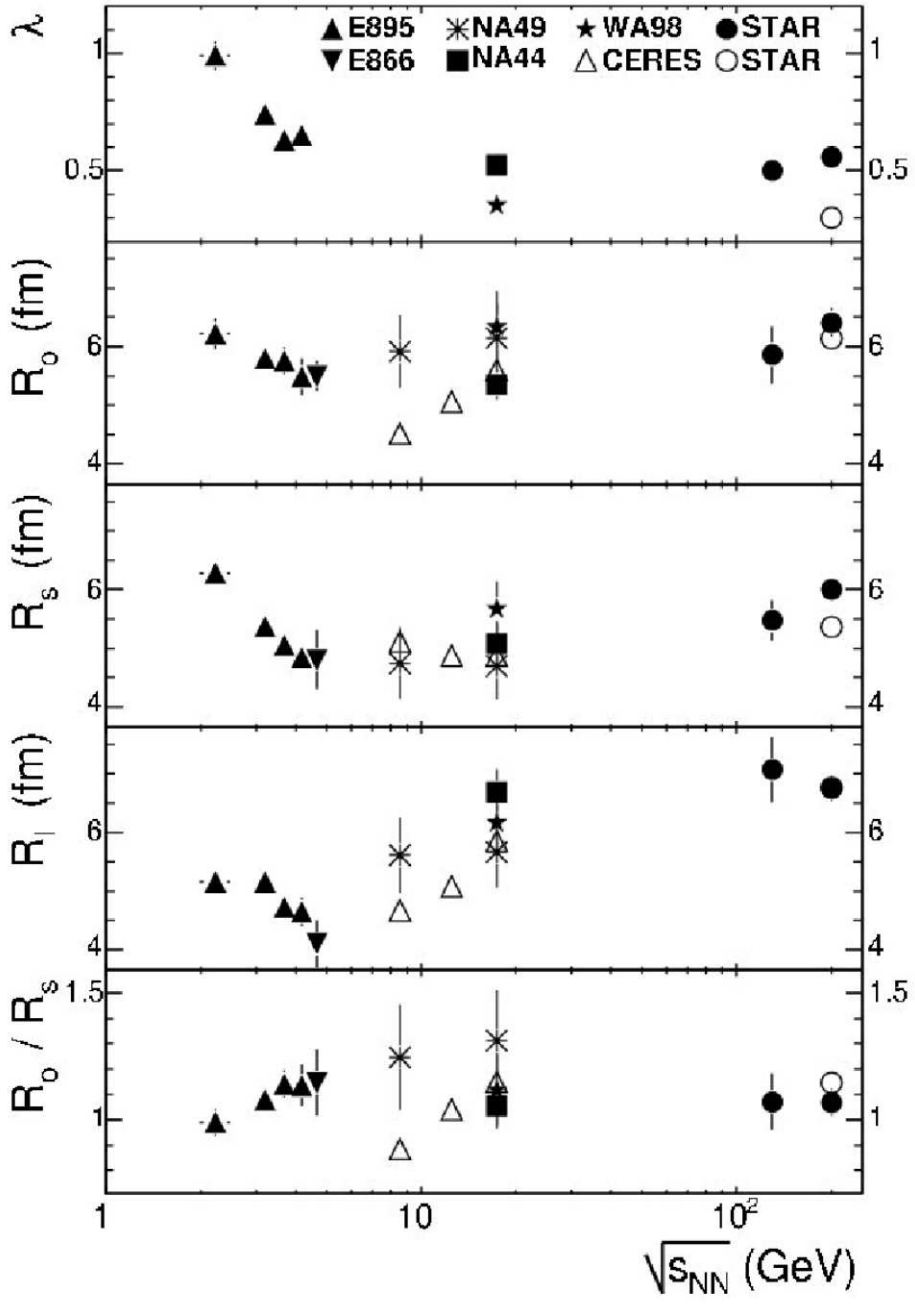

Figure 4.6: Energy dependence of HBT radii for central nucleus-nucleus collisions (Au+Au, Pb+Pb, Pb+Au) at midrapidity region for mean k_T value 0.2 GeV. Error bars on NA44, NA49, CERES and STAR results include systematic uncertainties, other error bars include statistical uncertainties only [65].

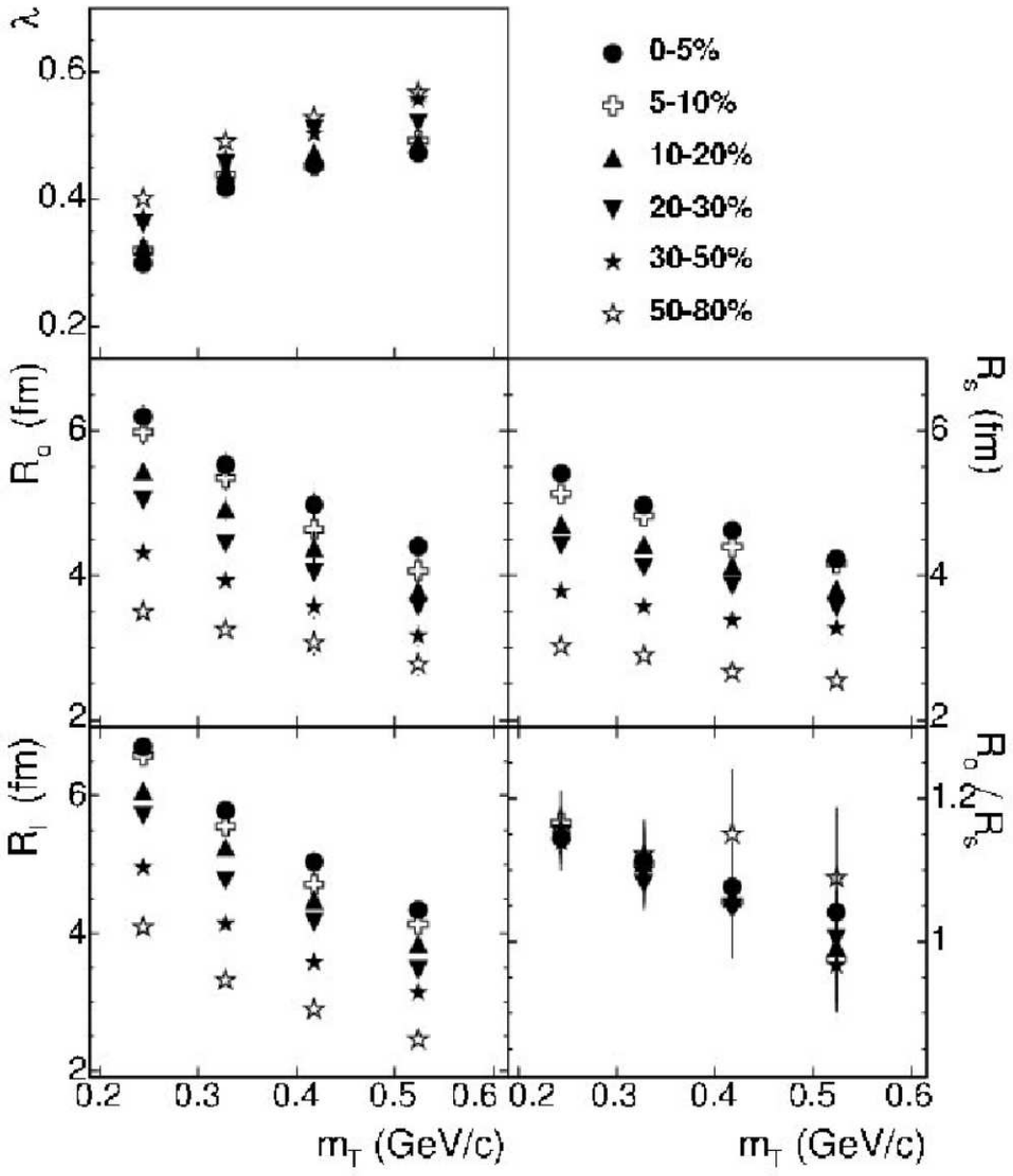

Figure 4.7: HBT parameters from measurements of pions vs. m_T for 6 various centralities. Data come from $Au+Au$ collisions at $sqrts_{NN} = 200$ GeV. Error bars cover systematic and statistical uncertainties [65].

Centrality and m_T dependence of source sizes

The centrality dependence of the pion source parameters are shown in Figure 4.7 as a function of $m_T = \sqrt{m_\pi^2 + k_T^2}$, for six different centralities. HBT radii increase with centrality, which is consistent with initial source size and can be attributed to the initial geometrical overlap of the two nuclei. The increasing m_T for radii confirm flow; R_o and R_s reflect transverse properties of collective motion and R_l is attributed to the longitudinal component. The λ parameter slightly increases with decreasing centrality. R_o/R_s approaches unity for all centralities, which does not signal QGP formation.

Multiplicity scaling

Figure 4.8 shows the radii dependence (R_{out},R_{side},R_{long}) on $(dN_{ch}/d\eta)^{1/3}$ (N_{ch} is the number of charged particles) for different colliding systems at different collision energies. These studies were done in order to check whether any relation exists at freeze-out time between final state geometry and particle density. All STAR results for $p + p$, $d + Au$, $Cu + Cu$ and $Au + Au$ collisions are combined on the left panel and confirm scaling with multiplicity. On the right hand panel there are STAR radii for different k_T ranges plotted together with the results from AGS/SPS/RHIC. The radius parameter for the $side$ and $long$ directions follows the same curve for different collisions, the same can be said of most of the radii for the out direction. The multiplicity $(dN_{ch}/d\eta)^{1/3}$ is a scaling variable driving HBT radius parameters. R_{out} is a mixture of space and time information, it is unclear whether it is reasonable to expect following the tendency of this projection as well. Scaling of sideward and longitudinal radii is determined by multiplicity only and is independent of collision energy, colliding system or the impact parameter. Scaling breaks down at lower energies while baryons constitute a significant fraction of the freeze-out system.
More about the most important femtoscopic measurements can be found in [69].

Proton femtoscopy from lower energies

One of the first attempts in two-proton correlations was the theoretical work performed by S. Koonin [70]. Two-proton correlations were intensively measured in low energy domains: starting from low beam energies of order of a few tens of MeV e.g. in National Superconducting

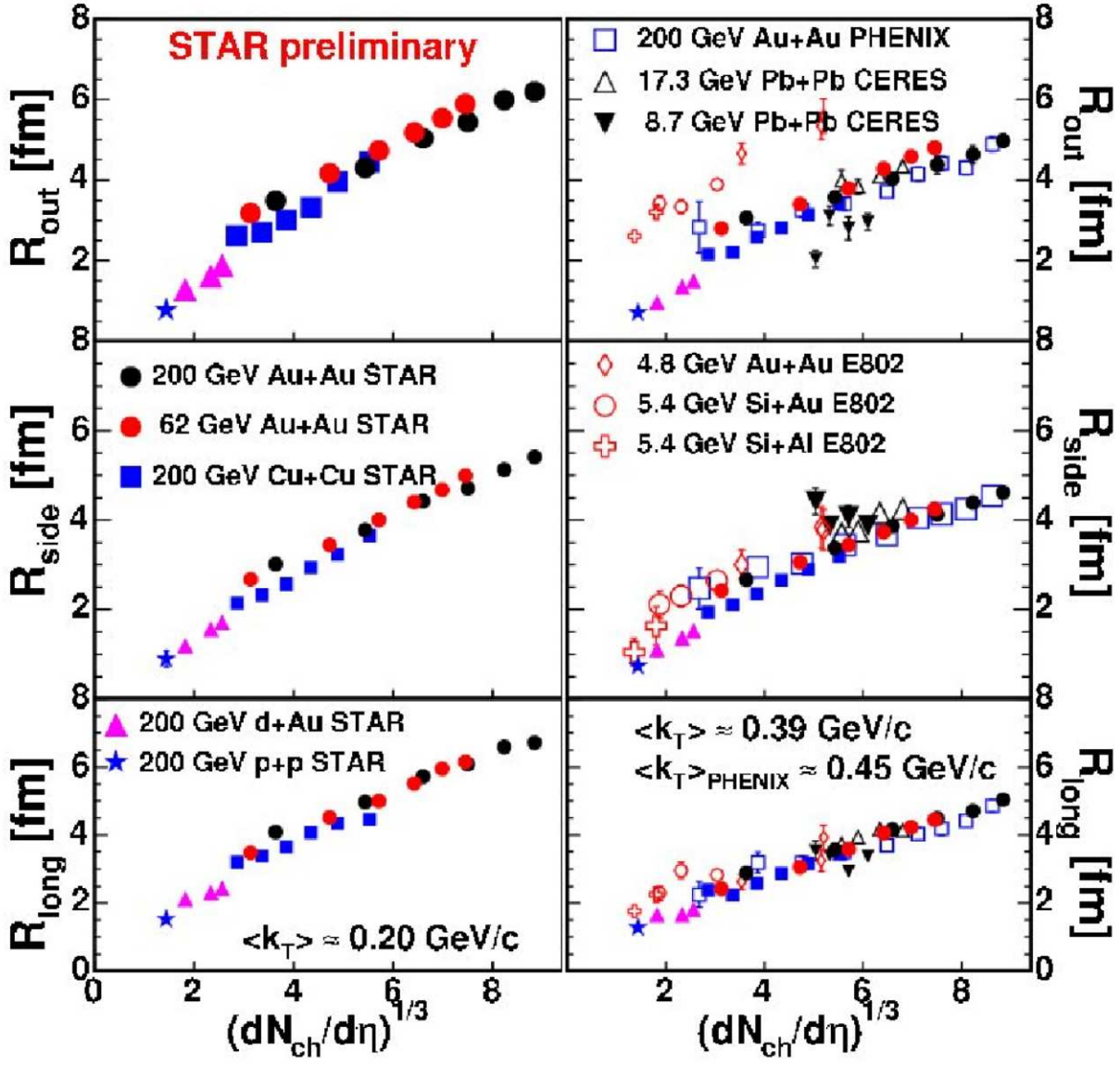

Figure 4.8: Femtoscopic radii dependence on the number of charged particles [68]

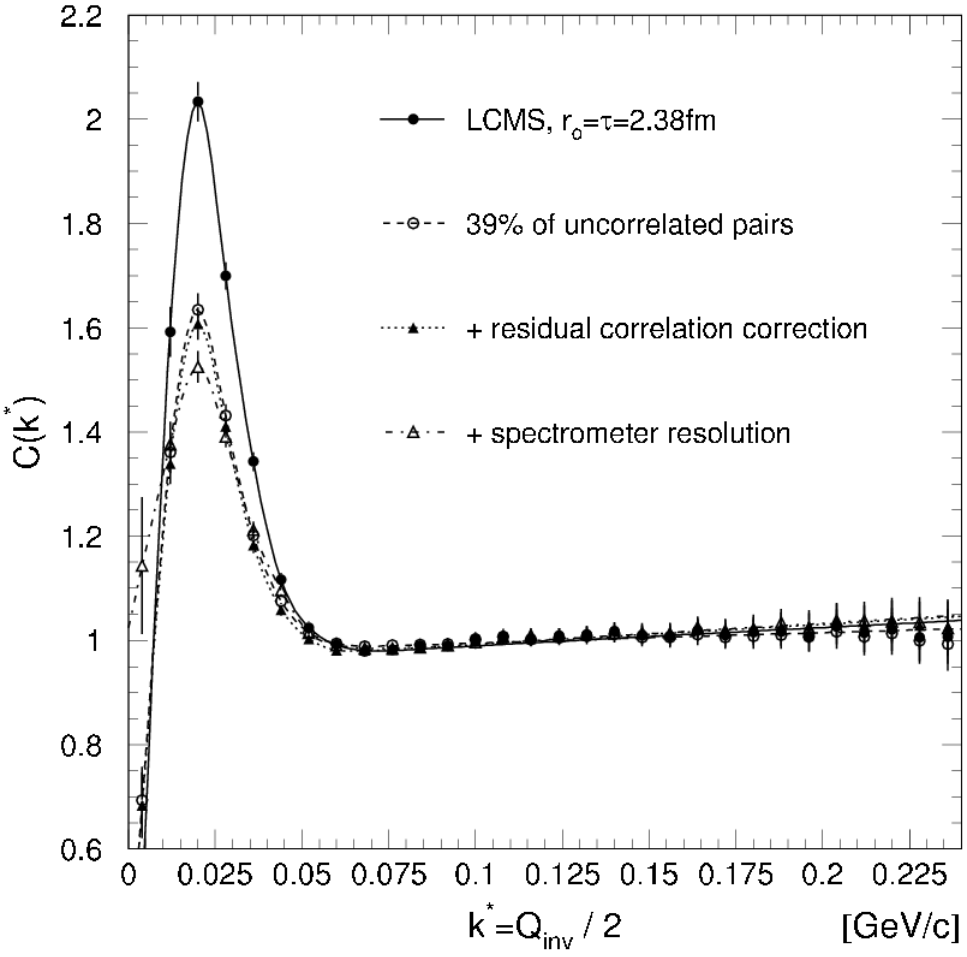

Figure 4.9: The influence of different experimental factors on the form of the measured correlation function. The example is for a Gaussian source with $r_0 = 2.38$ fm., where each effect has been added cumulatively [75].

Cyclotron Laboratory, at Michigan State University, through higher energy domain in SIS complex (FOPI Collaboration) [71, 72], AGS domain (E814 [73] and E877 [74] Collaborations) and SPS energies (NA44 [75], NA49 [76] Collaborations), in Dubna as well. Proton femtoscopy has been studied as proton particles dominate the measured sample of hadrons. Now, due to large hadron multiplicities produced at RHIC, it is possible to extend previous measurements, as experiments performed at lower energies operated with protons from the colliding nuclei.
The NA44 Collaboration was interested in $p + Pb$, $S + Pb$ and $Pb + Pb$ collisions at 450 GeV/c and 200 AGeV/c, respectively. They took into account three particularly important methodical factors at their studies: the admixture of indirect protons coming from hyperons (mainly products of lambda hyperon decay) leading to 'residual correlations' arising as a result of not excluding non-primary protons from the sample, the acceptance and the resolution of the experiment. Weak decays of baryons are a significant source of protons and contribute to the yield measured in the spectrometer. The influence of admixture of indirect protons on the shape of the correlation function has been studied using data from RQMD and Venus event generators combined with a detailed simulation (GEANT) of the detector. Two models gave similar results: about 22% of protons measured in the spectrometer came from weak decays of lambda hyperons in both collisions: $p + Pb$, $S + Pb$ and cannot be distinguished from direct protons. In order to take into account this non-correlated contribution to coincident pairs, a fraction of 22% of "decay" protons is included giving the 39% of un-correlated pairs in two-particle sample. This contribution significantly reduces the magnitude of the observed correlation effect but does not change the general shape of the function. Another issue taken into account was detector resolution, which smears particles and influences most pairs for lower $k*$ values. All these three effects were included in the simulation procedure and are present in Figure 4.9, which demonstrates separately the relative significance of each contribution. The NA44 Collaboration assumed that the effects of uncorrelated pairs and residual correlation would deplete the correlation function and the resolution smearing would shift the points. Figure 4.10 shows centrality dependence of $p - p$ correlations. The observed peak is much more pronounced for the $p + Pb$ data than for $S + Pb$, indicating that protons are emitted from a smaller source in the case of $p + Pb$ collisions. All functions are plotted with the associated source size from the Gaussian model. In the case of centrality selection for central collisions the correlation is the weakest, indicating the biggest source size and for peripheral data the strongest correlation is observed indicating the smallest source size. Even for lower energies, in the order of few hundreds of MeV, it is possible to compare different observables, versus e.g. colliding systems or collision energies. The lowest of presented here energies show that comparing various correlation, makes it possi-

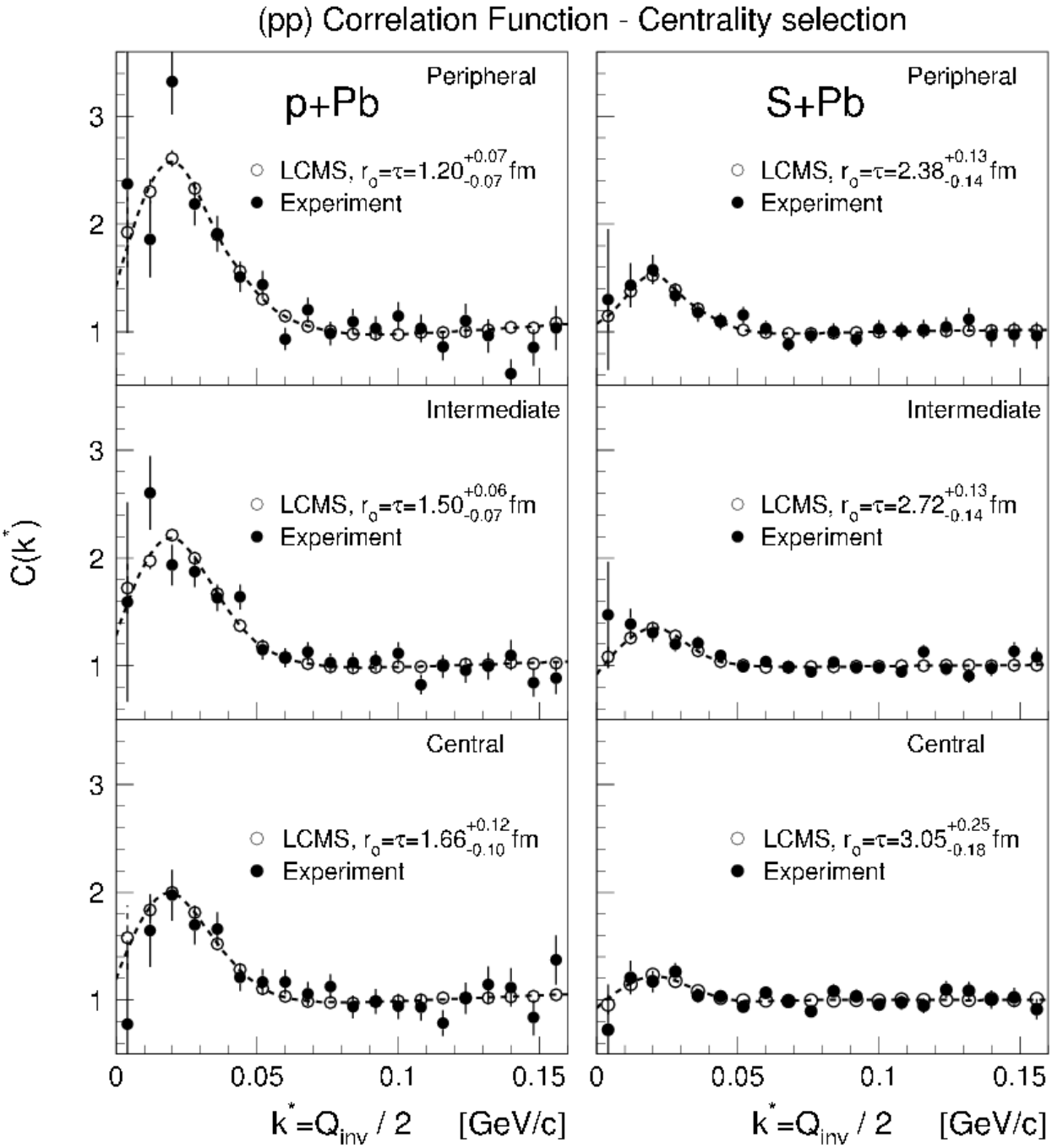

Figure 4.10: The left column is for $p + Si$ collisions, the right one for $S + Pb$. First row: no centrality selection, the rows exhibit data divided according to centrality: peripheral data (first row), mid-central data (second row), central data (third row). All functions have theoretical fits assuming for longitudinally co-moving Gaussian sources [75].

ble to conclude about the system evolution. Higher energies reached at the AGS complex enable one to compare correlation functions for two colliding systems applying the same experimental requirements on the registered particles and later pairs. At the AGS it is possible to divide the data sample according to centrality (two classes checked) or even the reaction plane. The SPS complex allows one to study proton femtoscopy with even higher accuracy. NA44 compares two different, non-symmetric reactions. The data has been divided into three centrality classes and enable one to observe the shape and magnitude of correlation function depending on impact parameter. The NA44 Collaboration notices the fact that the proton sample is contaminated by weak decay products and tries to estimate the effect of residual correlations, taking into account other uncorrelated pairs and the effect of detector resolution. It is worth to emphasize that at SPS first attempts have been made in order to remove Residual Correlations (RCs) of particles coming from weak decays. Also the other experiment from SPS- NA49 worked with proton femtoscopy and did first step to estimate the impact of RCs [76]. Now, the STAR Collaboration provides more precise estimations (see Chapter 7).

Non-identical particle combinations

Figure 4.11 shows an example of pion-kaon correlation functions. The top panel introduces the correlation functions for different combinations of pion-kaon pairs. The consistency between like-sign (π^+K^+ and π^-K^-) and unlike-sign (π^+K^- and π^-K^+) pairs is very good. The middle and bottom panel show the ratios of C^+/C^- for all pair combinations. C^+/C^- with respect to the sign k^*_{side} and k^*_{long} is unity within statistical uncertainties. However, C^+/C^- correlation with respect to k^*_{out} is larger than unity for small k^*_{out} for unlike-sign pair combinations (when the correlation is positive) and smaller than unity for small k^*_{out} for like-sign pair combinations (when the correlation is negative). For both sign orientations, the correlation for $k^*_{out} > 0$ is stronger than for $k^*_{out} < 0$. Assuming the convention (I), as described in Section 4.10, these results indicate that pions and kaons are not emitted on average at the same radius and/or time. Using the Blast Wave [77] model, these results can be interpreted as pions are on average emitted closer to the center and/or later than kaons. An explanation of such a conclusion is introduced below.

Figure 4.12 presents simulations for two temperatures, which correspond to two different transverse velocity β_t. The average emission points of pions $< r_\pi >$ and kaons $< r_K >$ are different. If a system with ideal flow is produced, this implies a zero temperature in Blast Wave, which leads to the phenomenon where all particles are emitted along the radial direction. In such a

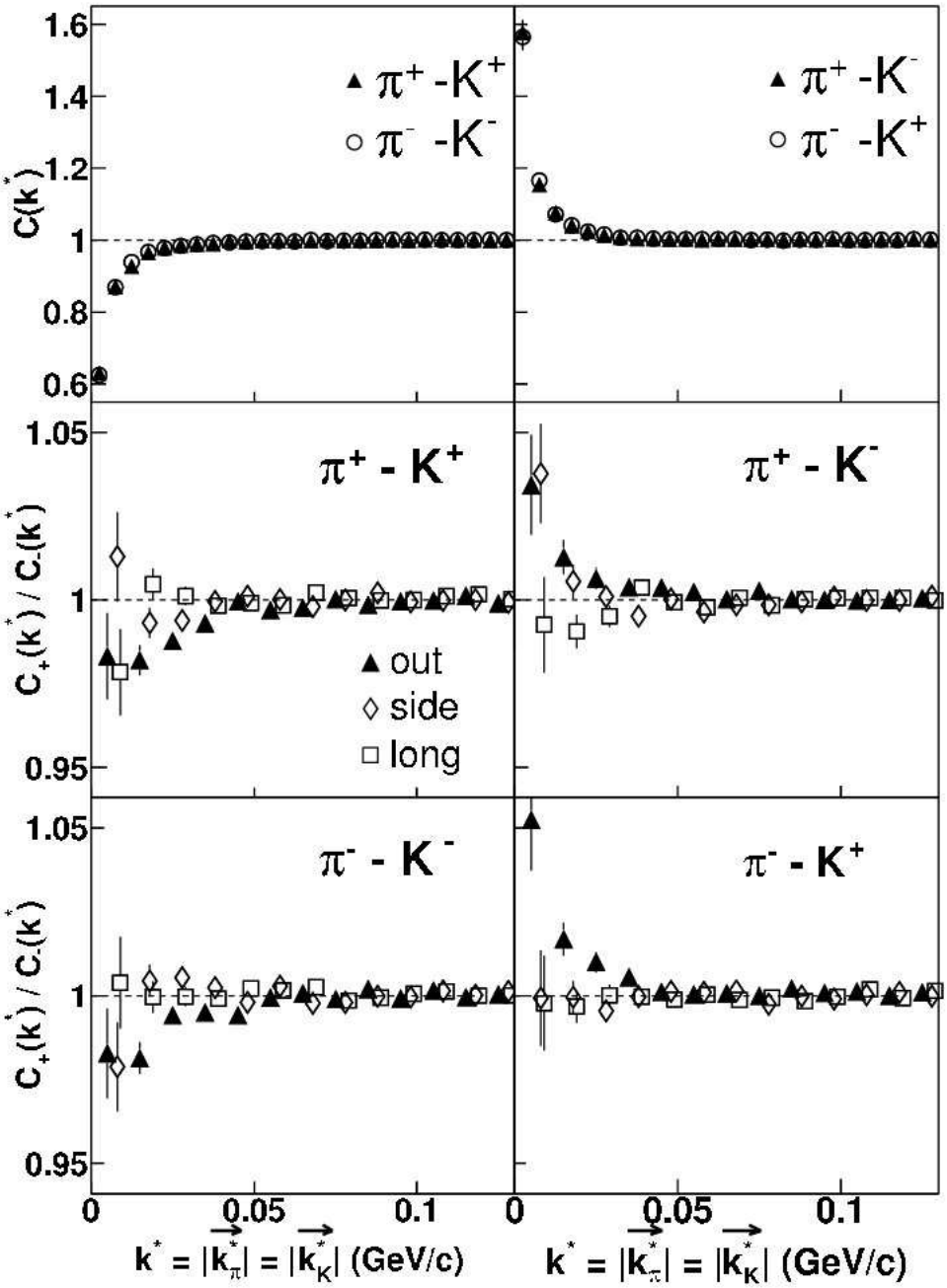

Figure 4.11: Pion-kaon correlation functions for $Au+Au$ collisions of 200 GeV, registered by the STAR experiment at RHIC. Top panels show pion-kaon correlation functions $C(k^*)$, the average of $C_+(k^*)$ and $C_-(k^*)$. Middle and bottom panels introduce the ratios of $C_+(k^*)$ and $C_-(k^*)$ defined by the signs of projections k^*_{out}, k^*_{side} and k^*_{long}. Error bars are statistical only [64].

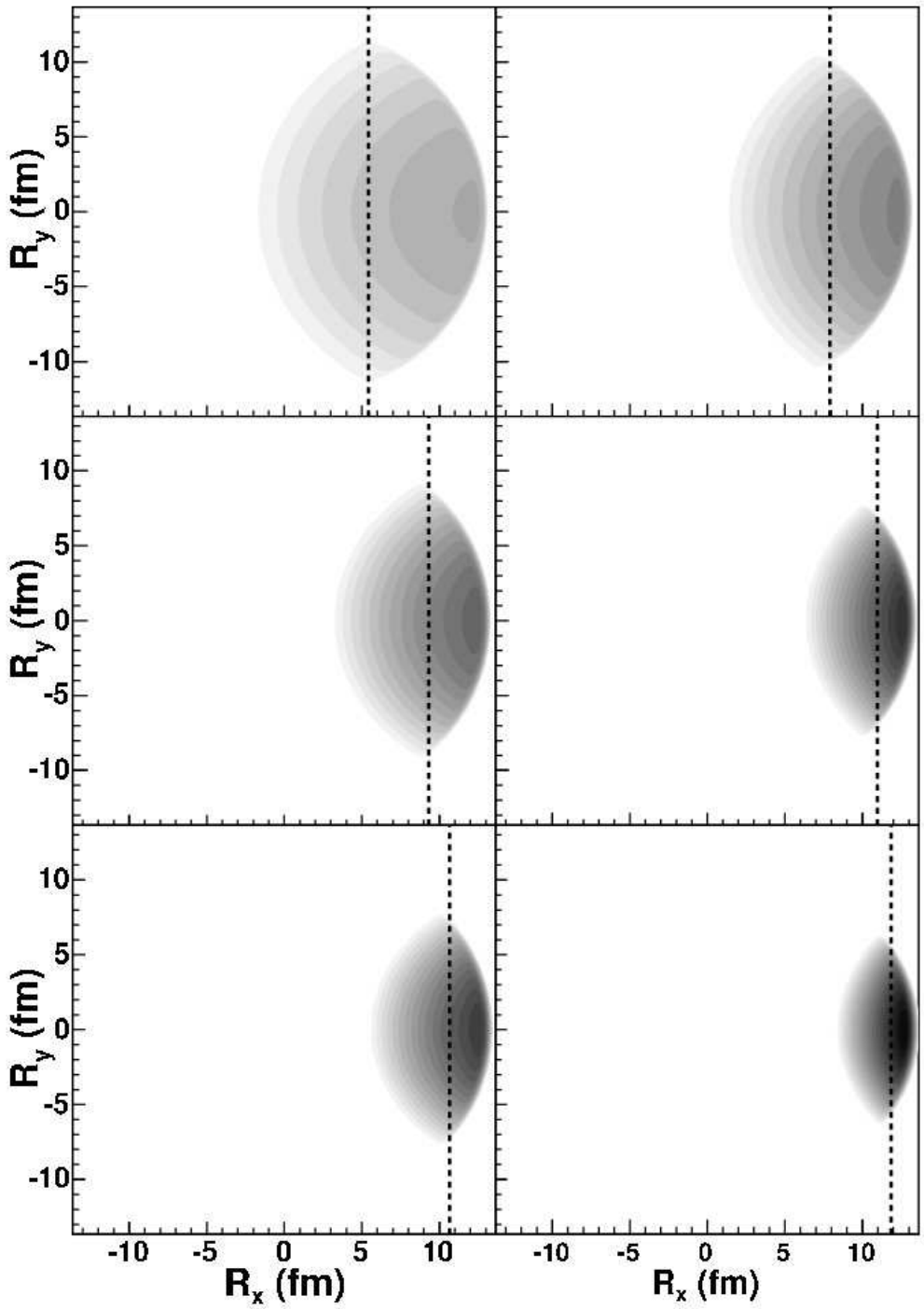

Figure 4.12: Distributions of emission points in the transverse plane, for different particle species at the same velocity. Top panels introduce pions, middle one- kaons, bottom ones- protons. Left panels show simulations where velocity is assumed to $\beta_t = 0.907$ and right panels correspond to the estimation of $\beta_t = 0.974$. Dashed curves show Blast-wave predictions [77].

profile, all particles are emitted from the same space-time point, independly on their mass. However, in Blast Wave, a particle velocity is sum of the flow velocity β_f (which does not depend on mass; it is determined by the flow field and a thermal velocity β_t. In the case of non-identical particles (with different masses) particles with the same β_f and β_t, thus identical momenta are produced, but their velocities are not identical. For particles with smaller masses, the average β_t is relatively larger, indicating the spread of the emission point is larger for lighter particles (here, pions). This is the reason why the average emission point of pions is closer to the center that in the case of kaons. This effect is also dependent on temperature, as higher temperature provides stronger flow. This leads to the conclusion that on average, pions and kaons are emitted from different areas.

4.13 Baryonic systems

Strong flow occurring in $Au + Au$ collisions at $\sqrt{s_{NN}} = 200$ GeV causes that from correlations smaller sizes of emitting areas at given temperature are given. The results on baryon femtoscopy comply with the ones from meson interferometry and confirm such a hypothesis of flow.
On one hand, the $p - \Lambda$ and $\overline{p} - \overline{\Lambda}$ interaction potentials are relatively well known; on the other $p-\overline{\Lambda}$ and $\overline{p}-\Lambda$ interaction potentials have been estimated by the STAR Collaboration for the first time. Constraining baryon - anti-baryon potentials, the information determines $p - \overline{\Lambda}$ and $\overline{p} - \Lambda$ annihilation cross sections. Figure 4.13 presents combined $p-\overline{\Lambda} \oplus \overline{p}-\Lambda$ and $p-\overline{\Lambda} \oplus \overline{p}-\Lambda$ correlation functions. The symbol $\oplus$ means that the numerators and denominators of the systems have been added to build a combine correlation function. In both functions, the curves correspond to the fit carried out using the Lednicky - Lyuboshits formalism [78]. The radii extracted from like-sign ($r_0 = 3.09 \pm 0.34^{+0.17}_{-0.25} \pm 0.2 fm$) and unlike-sign ($r_0 = 1.50 \pm 0.05^{+0.10}_{-0.12} \pm 0.3 fm$) [79] correlations are significantly different. The error bars include both statistical and systematic uncertainties. This difference was unexpected. Correlation functions shown here are corrected with the best estimate of purity, however not taking into account any RCs. Their effect to strange baryon combinations is expected to be significant (more about estimating the residual correlations in proton and anti-proton femtoscopy in Section 6). In the case of poor knowledge of strong interactions between two particles in such exotic systems as (M=meson) $M\Lambda$ and $\Lambda\Lambda$ the correlation measurement of scattering lengths might be highly useful. In heavy-ion collisions, the effective radius r_0 of the emission region should be considered much larger than the range of strong interaction potential. At small k^* the FSI contribution to the correlation function is determined by s-wave scattering amplitude $f^s(k^*)$. In the case of $|f^s| > r_0$, the contribution is

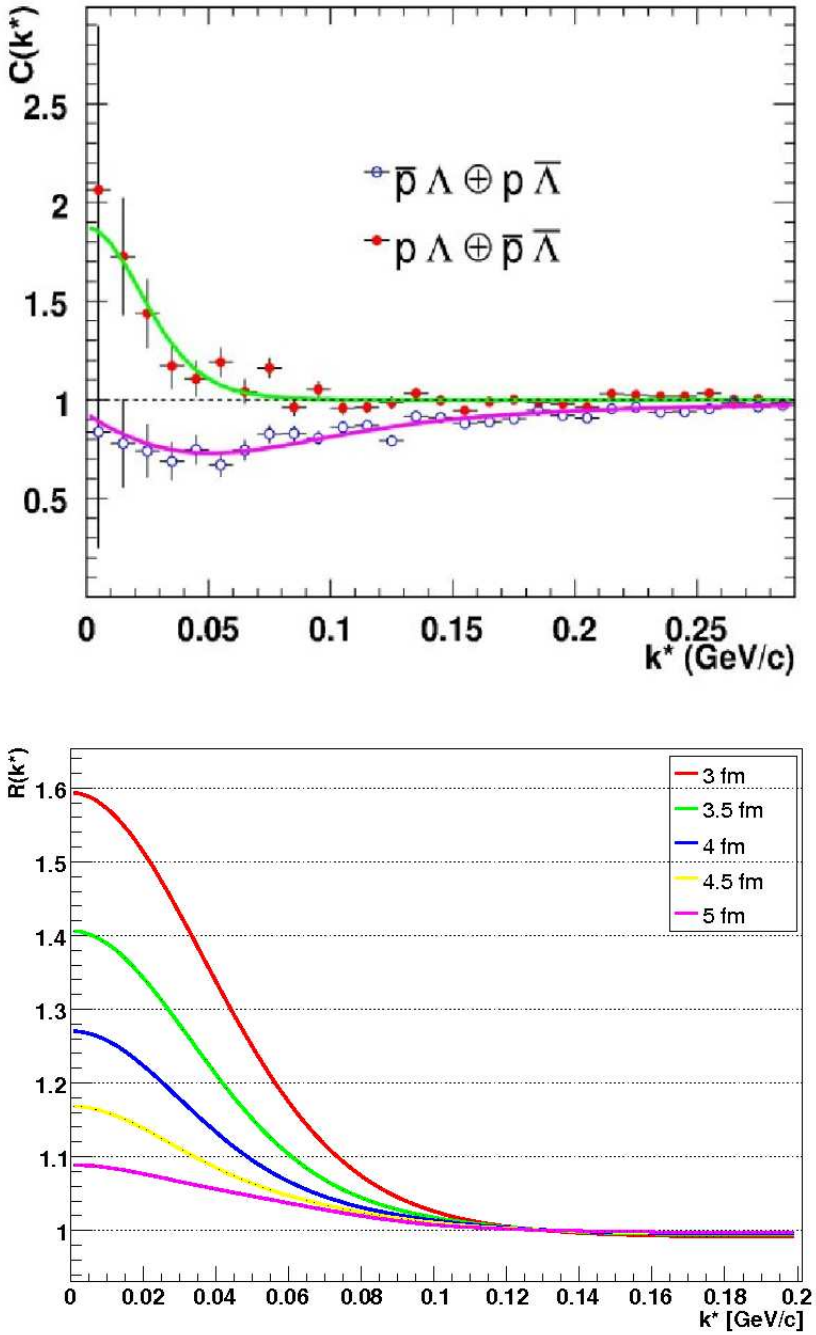

Figure 4.13: Top panel: $p-\overline{\Lambda} \oplus \overline{p}-\Lambda$ and $p-\overline{\Lambda} \oplus \overline{p}-\Lambda$ correlation functions corrected for purity and momentum resolution. Curves corresponds to fits done using the Lednicky & Lyuboshitz analytical model [79]; bottom panel illustrates the correlation function for $\Lambda\Lambda$ system for few source-sizes.

of the order of $|f_0/r_0|^2$ and dominates the effect of QS (in identical particle correlation), in the opposite case the sensitivity of the correlation function to the scattering amplitude is determined by the linear expression f^s/r_0. Theoretical predictions of the $\Lambda\Lambda$ system are presented in Figure 4.13.

Chapter 5 describes experimental complexes of RHIC accelerator, Chapter 6 contains a detailed description of the whole data analysis and encloses complex results concerning proton femtoscopy. and Chapter 7 contains results for proton femtoscopy performed at RHIC.

Chapter 5

The STAR experiment

In this chapter the STAR experiment is presented. During seven years of operation, STAR has collected an impressive amount of data, which is used to calculate two-proton femtoscopy presented in Sections 6 and 7. First, the RHIC complex is introduced, then four experiments operating at the facility are described. STAR is one of them.

5.1 RHIC

The scientific program of the Relativistic Heavy-Ion Collider (RHIC) [80] is mainly dedicated to studying the properties of matter under extreme conditions created as a result of relativistic heavy-ion collisions. The collider is located at the Brookhaven National Laboratory (BNL) in Upton, New York in the United States of America. Its construction began in 1991 and was completed in 2000. The collider, which consists of two rings of 1740 superconducting magnets, was constructed in a tunnel of c.a. 3.8 km circumference. It offers an impressive combination of energy, luminosity and polarization. It accelerates ions up to the energy of 100 GeV per nucleon; therefore, the maximum center-of-mass energy for beam-beam collisions is $\sqrt{s_{NN}} = 200$ GeV. Each collision produces a large number of particles; for example, in a central $Au + Au$ collision few hundreds of primary particles per unit of pseudo-rapidity are produced. The average transverse momentum is about 500 MeV/c. Each collision also produces a high number of secondary particles that exist due to interactions of primary particles with the material in the detector and the decay of short-lived primaries. RHIC demands a highly advanced environment to operate with heavy-ion collisions. A diagram of the RHIC complex with various facilities used to produce and pre-accelerate the beams of heavy-ions and nucleons is shown in Figure 5.1.

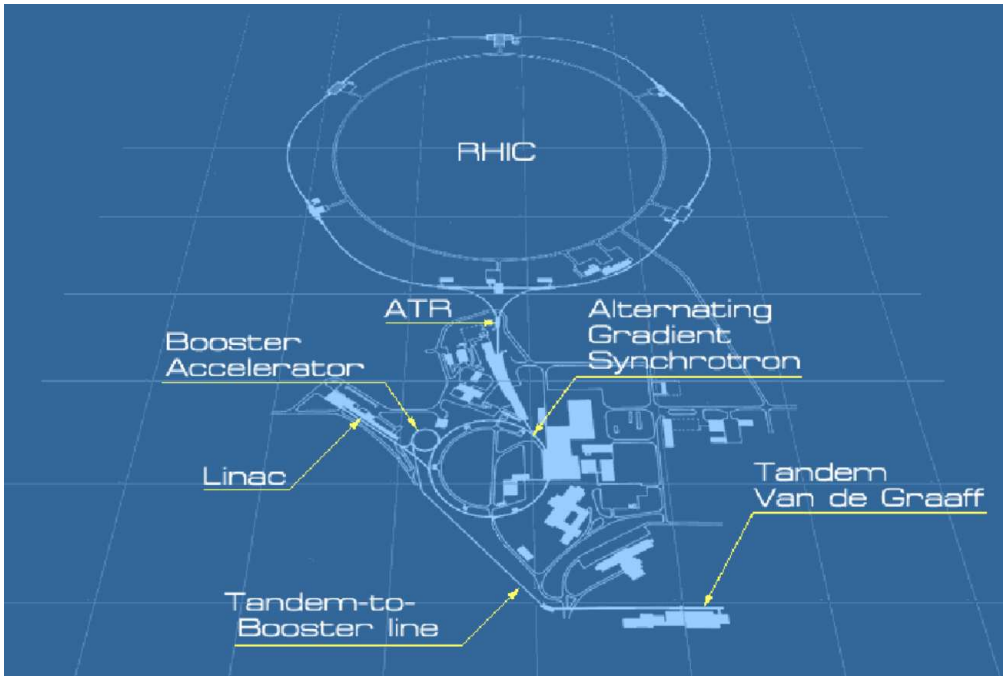

Figure 5.1: RHIC complex [80].

RHIC is also able to accelerate beams of polarized protons up to 250 GeV/nucleon. The RHIC program consist of one part dedicated to heavy-ion collisions (which intends to find possible signatures of the QGP) and another one for nucleons (which intends to learn about nucleon structure and its properties). The RHIC facility is composed of several parts. The main elements are as follows:

- Tandem Van de Graaf
  The Tandem Van de Graaf at RHIC was completed in 1970. For many years it was the largest electrostatic accelerator. It can provide beams of more than 40 different types of ions from hydrogen to uranium. The facility consists of two electrostatic accelerators, each 24 meters long. Inside tandem, due to ionizations the atoms are eventually stripped of remaining electrons and then accelerated to the kinetic energy of 1MeV/nucleon.

- Heavy-ion Transfer Line (HITL)
  In order to study heavy-ion collisions at high energies, a 700 meter-long tunnel and beam transport system called HITL were completed in 1986. It allows the delivery of heavy ions from the Tandem Van de Graaf to the Booster for further acceleration.

- Linear Accelerator (LINAC)

For the study of $p+p$ or $p+A$ collisions at the experiments, the LINAC supplies energetic protons. LINAC was designed and built in 1960 in order to upgrade the Alternating Gradient Synchrotron (AGS) complex. The major components of LINAC are the ion sources. The LINAC is able to produce up to a 35 miliampere proton beam at energies up to 200 MeV, for injection into the AGS Booster.

- Booster
  The Alternating Gradient Synchrotron Booster is less than one quarter the size of the AGS. It is used to pre-accelerate particles entering the AGS ring and it plays a highly important role in the operation of RHIC collider by accepting heavy-ions from the Tandem Van de Graaf facility via the heavy-ion Transfer Line and protons from Linac. The Booster delivers ions to the AGS for further acceleration.

- AGS
  Since 1960, the Alternating Gradient Synchrotron has been one of the major particle accelerators and play an important role in studies of relativistic heavy-ion collisions in the last decades. The name AGS is derived from the concept of alternating-gradient focusing, in which the field gradients of magnets are alternated inward and outward allowing ions to be focused in both horizontal and vertical planes at the same time. Nowadays, AGS is used as a major injector of accelerated ions into the RHIC ring. AGS was capable to accelerate ions up to silicon, with the atomic mass of 28; together with RHIC, the AGS is able to work with ions up to Au with the atomic mass number of 197.

- ATR
  The AGS-to-RHIC transfer line sends ions or protons from AGS to RHIC. At the end of this line, there is "fork in the road", where sorting magnets separate ions bunches into two beams. From here, two beams circulate in the RHIC where they are collided at four intersecting points.

RHIC provided the beam for four experiments: BRAHMS, PHOBOS, PHENIX and STAR. Figure 5.2 shows detector layout for each project. A brief description of each experiment is presented below:

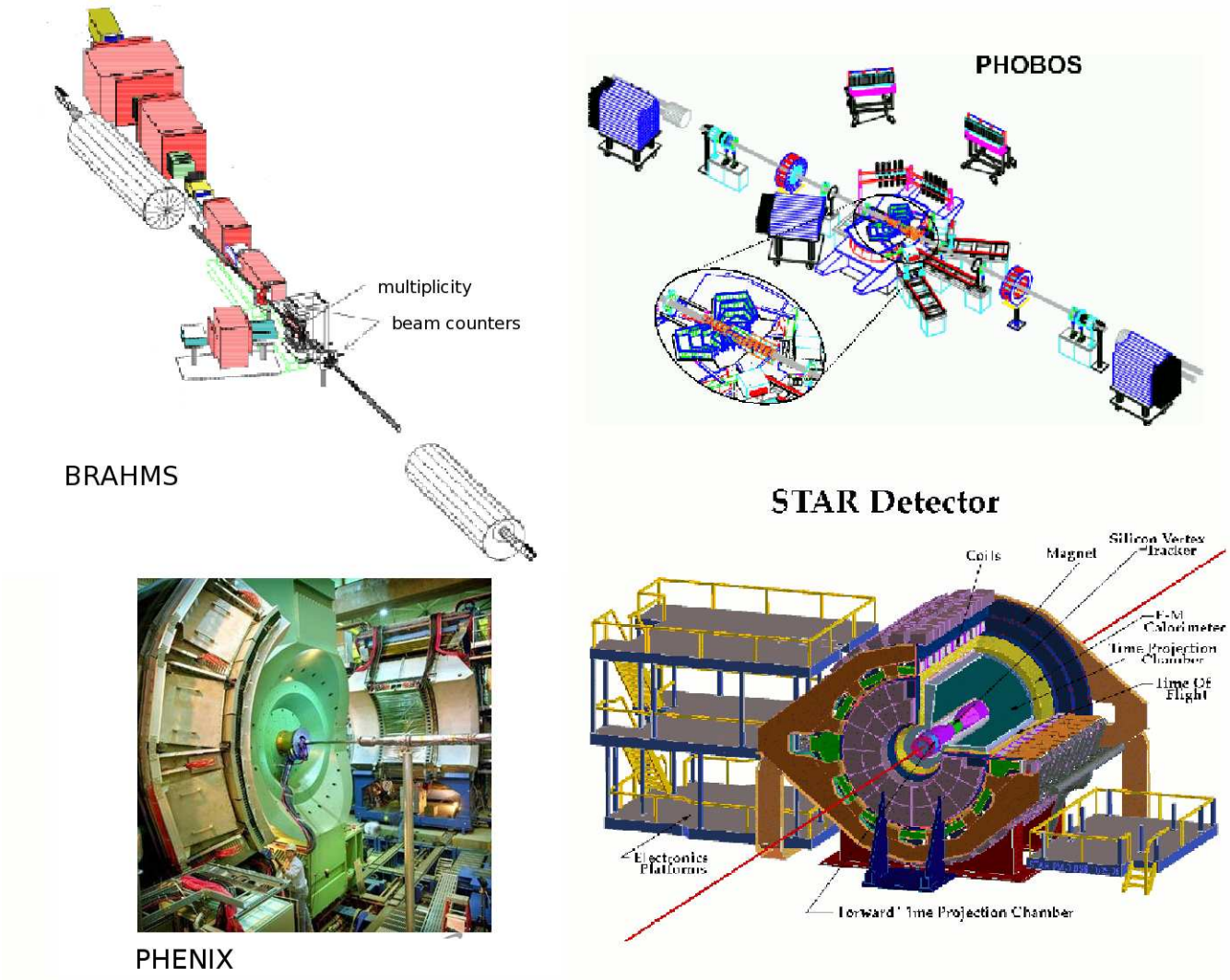

Figure 5.2: Schematic figures of each of four experiments operating at RHIC: Brahms (left-hand side of the top part), Phobos (right-hand side of the top part), PHENIX (left-hand side of the bottom part) and STAR (right-hand side of the bottom part). More details can be found in the text [81, 82, 83, 84]

BRAHMS

The Broad Range Hadron Spectrometer experiment [81], designed to measure charged hadrons over a wide range of rapidity and transverse momentum for all beams and energies available at RHIC is already accomplished. The detector requirements at midrapidity and forward angles are different and the experiment uses two movable spectrometers for these two regions (Figure 5.2). The mid-rapidity spectrometer covers the pseudorapidity range $0 < \eta < 1.3$ and the forward spectrometer covers $1.3 < \eta < 4.0$ range. There are four dipole magnets, three time projection chambers (TPC) and drift chambers. Particle identification is possible via time-of-flight hodoscopes and Cerenkov counter. The mid-rapidity spectrometer was designed to record charged particles below momenta of 5 GeV/c.

PHOBOS

This detector [82] was designed to measure as many produced particles as possible and to allow the detection of particles with lower transverse momenta (Figure 5.2). The experiment is already accomplished. The detector is composed of two parts: a multiplicity detector covering almost the entire pseudorapidity range ($-5.4 < \eta < 5.4$) measuring total charged particle multiplicity $\frac{dN_{ch}}{d\eta}$ over entire phase-space, and a two-arm spectrometer at mid-rapidity region. For about 1% of the produced particles, information about momentum and particle identification is done via the spectrometer. Each of the two arms covers about 0.4 rad in azimuth and one unit of pseudorapidity in the range of $0 < \eta < 2$.

PHENIX

This experiment [83] is dedicated to measuring electrons, muons, hadrons and photons. Its experimental abilities reach the highest event rates, even up to ten times of RHIC design luminosities. The goal is to collect rare signals such as the J/ψ decays into muons and electrons, high transverse momentum π^0's, direct photons and many others. The detector is composed of four spectrometer arms, two central have a small angle coverage at central rapidity region. Each is built up from a silicon vertex detector, a drift chamber, a pixel pad chamber, a ring-imaging Cerenkov counter, a time-expansion chamber, a time-of-flight and an electromagnetic calorimeter. These detectors enable identification of electrons over a broad range of momenta in order to measure low- and high-mass vector mesons. The other two spectrometers are used for muon

detection, and are built up from cathode strip chambers. The PHENIX experimental setup is presented in Figure 5.2.

STAR

The Solenoidal Tracker At RHIC (STAR) [84] is another of the four experiments at the RHIC accelerator. STAR has been design to investigate the behavior of strongly interacting matter at high energies and to search for signatures of QGP formation. Its goal is to understand fundamental properties of hadronic matter and its interactions.

5.2 The STAR detector

The STAR layout is shown in Figures 5.2, 5.3. The data collecting is performed in the magnetic field of up to 0.5T. The main detector used to measure charged hadrons is the Time Projection Chamber (TPC). It is located at a radial distance of 50 to 200cm from the beam axis. The TPC is 4.2m long and has 4m of diameter. TPC is filled with the $P10$ drift gas (10% methane, 90% argon) regulated at 2mbar above atmospheric pressure. The main property of the $P10$ gas is its fast drift velocity in low electric field. The drift velocity is stable and insensitive to small variations in temperature and pressure. The uniform low electric field is 135V/cm. The paths of primary ionizing particles passing through the gas volume are reconstructed with high precision from released secondary electrons, which drift to the readout end caps. Electric field uniformity is critical to the order of mm and electron drift paths are up to 2m long.
In order to increase the TPC acceptance, the tracking is extended to the forward region using two radial-drift TPCs. The combination of the TPC and the tag two FTPC covers $-1.8 < \eta < 1.8$ with complete azimuthal symmetry ($\Delta\phi = 2\pi$), over the full range of multiplicities. The TPC records tracks of particles, measures their momentum and identifies the particles by estimating their ionization loss (dE/dx)- (see more details in Chapter 5.3). Particles are best identified in their momentum range of 100 MeV/c to 1GeV. Momenta without particle identification can be measured up even to 30 GeV/c.
Charged particles produced close to the interaction region are identified via sub-detectors: the Silicon Vertex Tracker (SVT) and the Silicon Strip Detector (SSD). The silicon detectors cover the pseudo-rapidity range of $-1 < \eta < 1$ with complete azimuthal symmetry ($\Delta\phi = 2\pi$) and they can find secondary vertices from weak decays of hyperons, e.g. Λ, Ξ, Ω. In order to extend

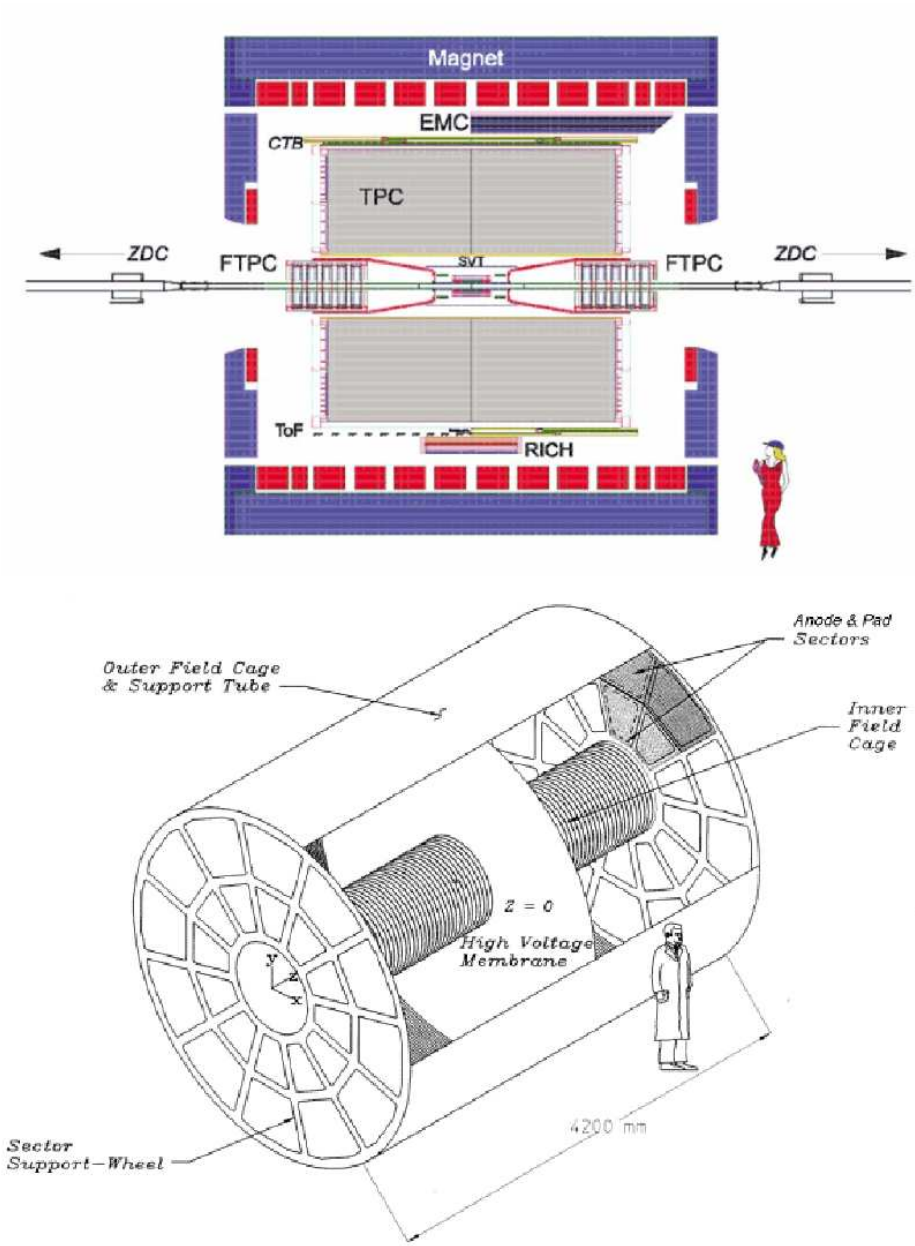

Figure 5.3: Top panel: a complex view of the STAR detector. The whole detector is surrounded by a magnet. It is composed of several sub-detectors: Silicon Vertex Tracker (SVT) in the center, then the Time Projection Chamber (TPC) above SVT, the Silicon Strip Detector (SSD) between SVT and TPC, then Forward TPCs (FTPC) and Zero-Degree Calorimeters (ZDC). Other components are: Central Trigger Barrel (CTB), Electro-Magnetic Calorimeter (EMC), Time of Flight (TOF) and Ring Imaging Cerenkov RICH. Bottom panel: STAR TPC overview [84]

the particle identification to larger momenta for identified single-particle spectra at midrapidity, a ring imaging Cerenkov detector covering $-0.3 < \eta < 0.3$ and $\Delta\phi = 0.11\pi$ and Time-Of-Flight (TOF) with coverage $-1.0 < \eta < 1.0$ and $\Delta\phi = 0.04\pi$ were installed. STAR has the ability to detect hadrons in large detector acceptance, it is also able to measure event-by-event fluctuations and jets.

5.3 Performance of TPC

The STAR detector uses the TPC as its primary tracking device. All results of data analysis presented in this work use data reconstructed by the TPC detector only. The STAR TPC is presented in Figure 5.3 (bottom panel).
The track of a finite momentum particle passes through the TPC and can reach up to 45 pad-rows. A finite momentum track rarely crosses all rows, it depends on the radius of curvature of the track, the track pseudorapidity, cuts nearby sector boundaries and few more other details about particle trajectory. While the wire chamber is sensitive to almost 100% of the secondary electrons, the overall tracking efficiency is lower (80-90%) due to cuts, track merging, bad pads and dead channels. There is a few percent of dead channels in any run cycle.
The track of a primary particle passing through the TPC is reconstructed by finding ionization clusters along the track. The clusters are found separately in x, y and z directions. The local x axis is along the direction of the pad-row, the local y axis extends from beam-line outward through the middle of an perpendicular to the pad-rows, the local z axis lies along the beam axis. These clusters are split using an algorithm then looks for peaks with a valley between them and then ionization is divided between the two tracks. Below, experimental details concerning the track reconstruction and its imperfections are explained.

Distortions

The position of a secondary electron in a pad can be distorted by non-uniformities in the electric and magnetic field of the TPC. The non-uniformities in the field lead to non-uniform drift. In the STAR TPC, the electric and magnetic fields are parallel and nearly uniform in r and z. The deviations from these ideal conditions are small and a typical distortion along the pad row is ≤ 1 mm before applying a correction. The magnitude of different distortion corrections are presented in the Table 5.1.

Table 5.1: The distortion corrections applied to STAR data, their cause and the magnitude of their effect on the data

Cause of the Distortion	Magnitude of the Imperfection	Magnitude of the Correction
Non-uniform B field	$\pm$0.004 T	.. leads to $\sim$0.1 cm
Geometrical effect between the inner and outer sub-sectors	Exact calculation based on geometry	0.005
The angular offset between E and B field	0.2 mr	0.03 cm
TPC endcaps - non-flat shape and tilt	0.1 cm	0.03 cm

Two-hit resolution

The efficiency of two-hit resolution is the ratio of the distributions of the distance separating 2 hits from the same event and 2 hits from different events. Two hits can be completely resolved when they are separated in the pad-row direction by at least 0.8 cm in the inner sector and 1.3 cm in the outer sector. Similarly, two hits are completely resolved when they are separated in the drift direction by 2.7cm in the inner sector and 3.2cm in the outer one.

Tracking efficiency

The tracking software performs two distinct tasks: the algorithms associate space-points to form tracks and fit the points on a track with a track model to extract information such as the momentum of particle. The track model is a helix. Second-order effects include the energy lost in the gas which causes a particle trajectory to deviate slightly from the helix.
The tracking efficiency depends on the acceptance of the detector and the two-hit separation capability of the system. The acceptance is 96% for high-momentum tracks traveling perpendicular the beam. The 4% inefficiency is caused by the spaces between sectors which have to exist due to the wires on the sectors. The software also ignores any space-points that fall on the last 2 pad-rows. This cut is applied to avoid position errors that result from tracks not having symmetric pad coverage on both sides of the track. It also allows to avoid local distortions in the drift field, so the total acceptance is 94 %.
The detection efficiency of the electronics is almost 100% except for dead channels (they count

below 1% of the total amount). However, the system cannot always distinguish one hit from two hits and this merging reduces tracking efficiency. In order to estimate the tracking efficiency, simulated tracks are embedded inside real events and then the number of simulated tracks that are in the data after track reconstruction are counted. This technique allows to account for detector effects and especially for the losses related to a high density of tracks. The simulated tracks are very similar to the real tracks and simulator tries to take into account all the processes that lead to the detection of particles including: ionization, electron drift, gas gain, signal collection, electronic amplification, electronic noise and dead channels. The results of embedding studies indicate that systematic error on the tracking efficiency is about 6%.

Vertex resolution

The primary vertex can be used to improve the momentum resolution of tracks and to distinguish secondary vertices from the primary ones. It is also possible to improve the momentum resolution of secondary vertices as well, however the vertex resolution has to be good enough. Many strange particles produced in heavy-ion collisions can be identified this way. The primary vertex is found by considering all of the tracks reconstructed in the TPC and the extrapolating them back to the origin. The global average corresponds to the the vertex position. The primary vertex resolution is calculated by comparing the position of the vertices that are reconstructed using each side of TPC separately. As expected, the resolution decreases as the square root of the number of tracks used in calculations. A resolution of 350μm is achieved when more than 1000 tracks exist.

Momentum resolution

The transverse momentum p_T of a track is measured by fitting a circle through the x, y coordinates of the vertex and the points along the track. The total momentum is calculated using this radius of track curvature and the angle of the tracks with respect to the z- axis of the TPC. This procedure works for all primary particles coming from the vertex, but for secondary decays, such a Λ or K^0_s, the circle must be done without reference to the primary vertex first. In order to estimate the momentum resolution, it is necessary to apply the embedding technique. A track simulator is used to create a track with known momentum, then the track is embedded in real event in order to simulate the momentum smearing effects. There are two regions of low resolution: lower-p_T domain: for e.g. pions - for $p_T < 400$ MeV/c, for anti-protons - $p_T < 600$ MeV/c,

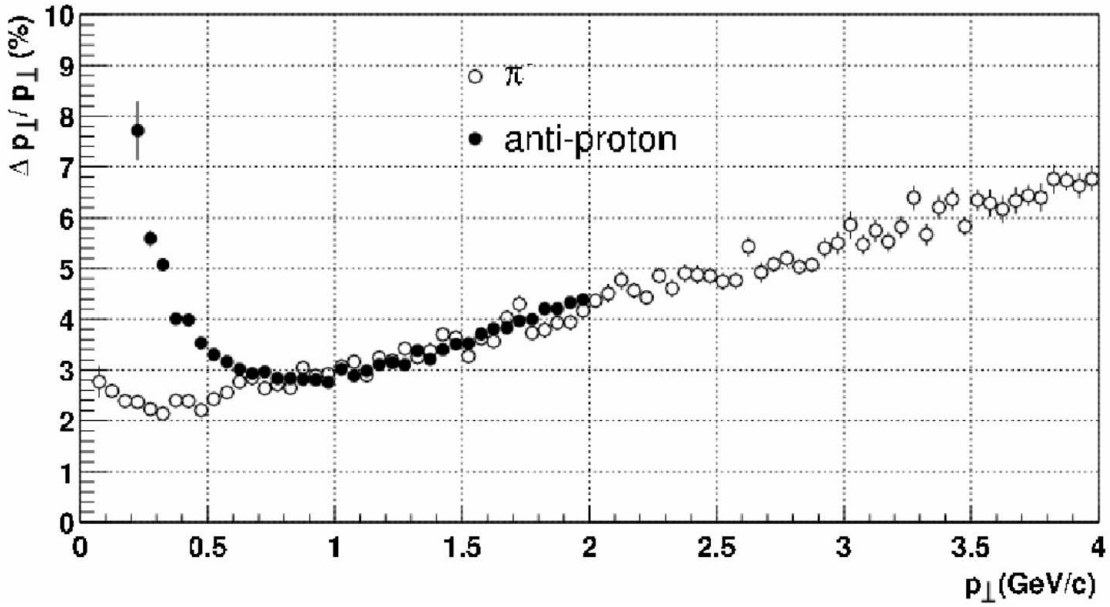

Figure 5.4: Transverse momentum resolution of the STAR TPC for negative pions and anti-protons in the magnetic field 0.25T. Tracks are required to be built up from more than 15 hits. Tracks are embedded in minimum bias events [84].

and higher-p_T domain where the momentum is limited by the strength of the magnetic field and the TPC spatial resolution (see Figure 5.4).

Particle identification using dE/dx

Energy loss in the TPC is a valuable tool to identify particle species. It works especially well for low momentum particles but as the particle energy increases, the energy loss becomes less mass dependent and it is highly difficult to separate particles with their momenta above several GeV/c. STAR is able to separate pions, kaons and protons with a very good accuracy up to 1.2 GeV/c. Above this region, the accuracy is much lower, but separation is still possible, up to the momentum above 10 GeV. The best separation requires a relative momentum resolution of the order of 7%. The dE/dx loss is extracted from the energy loss measured on up to 45 pad-rows. The procedure to get particle characteristics (momentum, energy, ..) is the offline analysis which consists of several parts:

- Digital and analog signals (hits) are read from the detector clusters. Using known calibration constants, any signal is converted into space-time coordinates of a given cluster

(x,y,z,t).

- Tracks are assembled from read clusters.

- A global track can be formed from several segments (tracks) of the analyzed part of the detector.

- With a global track present, it is extrapolated to the primary vertex. A fit to the primary vertex can be done using the values of the magnetic field.

- The velocity coordinates are specified and when the mass of particle which left a track at that moment is known- the momentum coordinates are given as well.

- In the case of non-primordial particles (decayed from other particle), the reconstruction of secondary vertices and other particle daughters can be found.

- The Bethe-Bloch formula on energy loss is given:

$$-\frac{dE}{dx} = \frac{4\pi}{m_e c^2}\frac{nz^2}{\beta^2}(\frac{e^2}{4\pi\epsilon_0})^2[\ln\frac{2m_e c^2\beta^2}{I(1-\beta^2)} - \beta^2] \tag{5.1}$$

  where E is the energy, x is the distance unit where the energy is losses; $\beta = \frac{v}{c}$ (v is the particle velocity, c is the speed of light); m_e is the mass of electron e; z is the charge of particle; n is the density of electrons inside the medium $n = \frac{N_A Z\rho}{A}$ (N_A is Avogadro's number; A, Z corresponds to the atomic properties of the element which the medium is built of; ρ is the density of the medium); $I = (10\text{eV})Z$ is the ionization potential of the medium.

The measured dE/dx resolution depends on the gas gain which itself depends on the pressure in the TPC. Since the TPC is kept at a constant value of 2 mbar above atmospheric pressure, the TPC pressure varies with time. There are small variations between pads and groups of pads, due to the different response of each readout board.
The length over which the particle energy loss is measured (depending on: pad length, crossing and dip-angle) is too short to average out ionizations fluctuations. Indeed, particles lose the energy in collision with the gas. It is not possible to measure accurately the average of dE/dx,

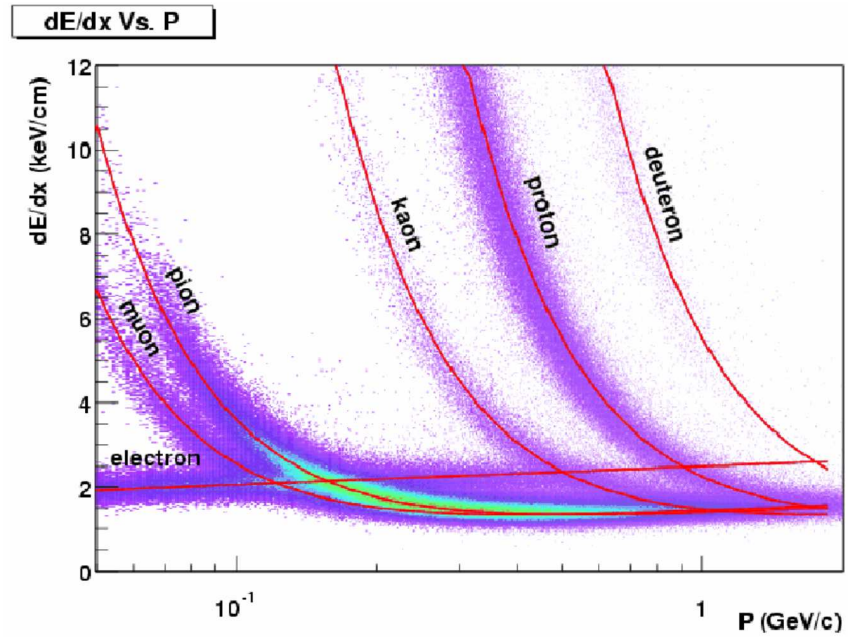

Figure 5.5: The energy loss distribution in the STAR TPC as a function of transverse momentum. The magnetic field is 0.25T. The resolution of 8% of a track that crosses 40 pad-rows. Both primary and secondary particles are included. Pions, kaons, protons can be separated from each other up to 1GeV/c. The electron band contaminates mostly sample of pions, kaons and protons for higher momenta [84].

so the mean energy losses are distinguished. They are parametrized according to the Landau distribution. The energy is measured for multiple points of the track, then the energy losses $\frac{dE}{dx}$ can be calculated (truncated mean). Figure 5.5 shows the energy loss for particles in the TPC detector.

More about the main STAR detector TPC can be found in [85].

Experimental details related to proton femtoscopy analysis are described in the next Section 6.

Chapter 6

Analysis of two-baryon correlations

6.1 Construction of two-particle correlation function

In order to build up any correlation function, a proper selection of correlated particles must be applied. Collection of correlation function constituents is done on three different levels:

- events,
- particles,
- pairs.

Proper event selection is highly important for correct background construction. A correlation function is usually calculated by dividing two-particle distributions coming from the same event (in numerator) and from different events (in denominator), where the latter- the background sample should be a "perfect reference", reflecting an ideal scenario of non-correlated particles. On the other hand, this sample should preserve some geometrical correlations resulting e.g. from the collision geometry (physics) and detector configuration (measurement). It is not enough to mix particles from any different events- they should exhibit similar properties concerning position as the vertex in the detector along the beam axis, as well as multiplicity (events should be characterized by comparable centrality of the collision). A commonly used, simple-to-calculate variable which enables estimation of the centrality class is a percentage of total hadronic cross-section of the collision. For this analysis, 20 million minimum-bias events have been selected with the collision vertex position within ± 30 cm measured along the beam axis from the center of TPC.

Three different centrality ranges are considered here: 0-10% (central) and 10-30% (mid-central), 30-80% (peripheral) of the total hadronic cross-section of the collision. In the experiment, collision centrality is specified according to the number of charged particles registered in the given event (one collision). After counting charged particles in many events as a reference, it is possible to transform such an observable into collision centrality. Is not possible to access the impact parameter in the experiment, however the number of charged particles registered in the TPC detector allows estimation basing on Glauber's calculations [86], of the number of binary collisions and wounded nucleons.

Then correct particle selection must be done. First of all, one has to select properly-identified particles using dE/dx distributions, as mentioned in Section 5.3. Particles are distinguished using specific gas ionization in the TPC. They are plotted in two-dimensional Bethe-Bloch histograms according to their transverse momentum and energy loss. The two-dimensional Gaussian distribution is fitted to each histogram cell, projected along the momentum axis. Only particles which are located within two standard deviations of the mean of Gaussian can be taken into analysis. It is also mandatory to select only tracks reconstructed using at least 20 of all 45 pad-rows in the detector. To reduce the significant contribution from non-primary (decayed) protons and anti-protons, a cut of 3 cm is applied to each track on the Distance of Closest Approach (DCA) of the track to the primary vertex. As the TPC is able to identify particles with low transverse momentum and for higher p_T values particles of different types are almost indistinguishable (here, protons and electrons), only protons and anti-protons with transverse momentum not higher than 0.8 GeV/c are taken into account. On the other hand, due to their high mass, the transverse momentum cannot be lower than 0.4 GeV/c. The total momentum can reach up to 0.9 GeV/c. As STAR has the best acceptance at mid-rapidity, selected particles have to be characterized by $|y| < 0.5$.

The third level of correlation function construction pertains to pair selection. Three main factors resulting from limitations of detecting devices are discussed and all these artificial effects are removed:

- track splitting,
- track merging,
- misidentification of electrons as protons.

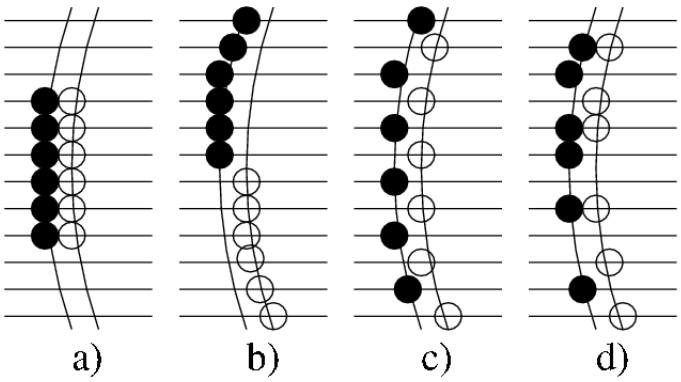

Figure 6.1: Distribution of the same number of hits in two tracks for four possible cases. Closed circles are hits assigned in one track, open circles are assigned to the other. a) SL=-0.5 (clearly two tracks), b) and c) SL=1 (possible split track), d) SL=0.6 (likely two tracks)[65].

6.1.1 Track splitting

Track splitting causes an enhancement of pairs at low relative pair momentum k^*. This enhancement is created by a single track reconstructed as two tracks, with similar momenta. Track splitting mostly affects identical particle combinations (here, $p-p$ and $\overline{p}-\overline{p}$), as one track may leave a hit in a single pad-row. Due to shifts of pad-rows, it can be registered twice. In order to remove split tracks, a comparison of the location of the hits for each track in the pair along the pad-rows in the TPC is made. The following formula is applied to each pair:

$$SL = \frac{\sum_i S_i}{Nhits_1 + Nhits_2} \tag{6.1}$$

where $S_i = +1$ if one track leaves a hit on the pad-row i, -1 if both tracks leave a hit there and 0 if none of them do; $Nhits_1$ and $Nhits_2$ are the total number of hits associated with each track in the pair. After the sum is done, it is divided by the sum of all hits (from both tracks). The SL value is between -0.5 (both tracks have hits in the same pad-rows) and 1.0, when neither pad-row is shared by both tracks. All pairs with $SL < 0.6$ were rejected. See Figure 6.1 for an illustration.

6.1.2 Track merging

Track merging causes a depletion of pairs at low relative momentum and appears when two tracks are registered as a single one. The merging effect affects mostly non-identical particle

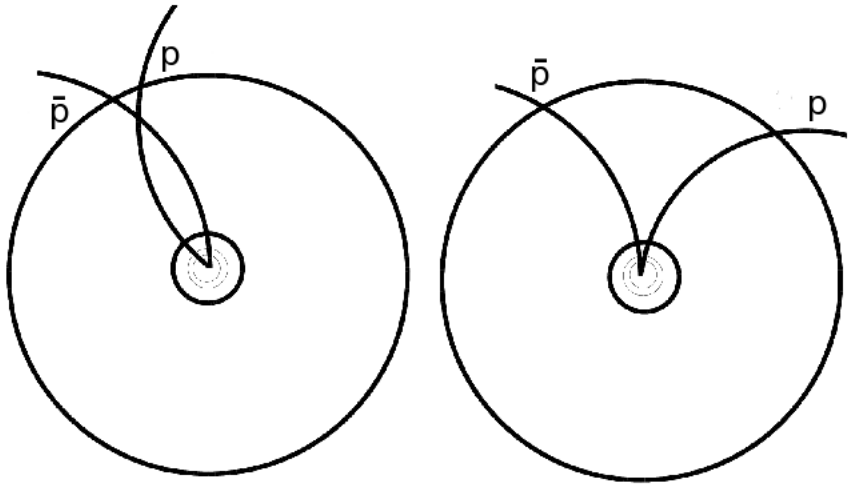

Figure 6.2: Two cases for oppositely-charged particles, in the scenario where they cross each other an merging effect can occur.

combinations with opposite charges: due to presence of the magnetic field their curves go in opposite directions and if the angle between tracks is too small, they are treated as a single track. In order to eliminate this effect it is necessary to remove such pairs composed of merged tracks from both, the numerator and denominator of the correlation function. Track merging is estimated by counting how many single hits with respect to all are reconstructed instead of separate two tracks. The algorithm is as follows:

- The hits from reconstructed helices (two tracks) are taken;
- For each hit the distance $\delta r(i)$ between the hits coming from the first and the second track is calculated;
- If the distance $\delta r(i)$ is less than the mean TPC distance separation, the hits are "marked" as merged;
- The percentage of all merged hits comparing with numbers of all hits are counted;
- The maximal value (the percentage) when pair is accepted is specified;
- If the percentage of merged hits is more than the specified value, pair is removed from the analysis.

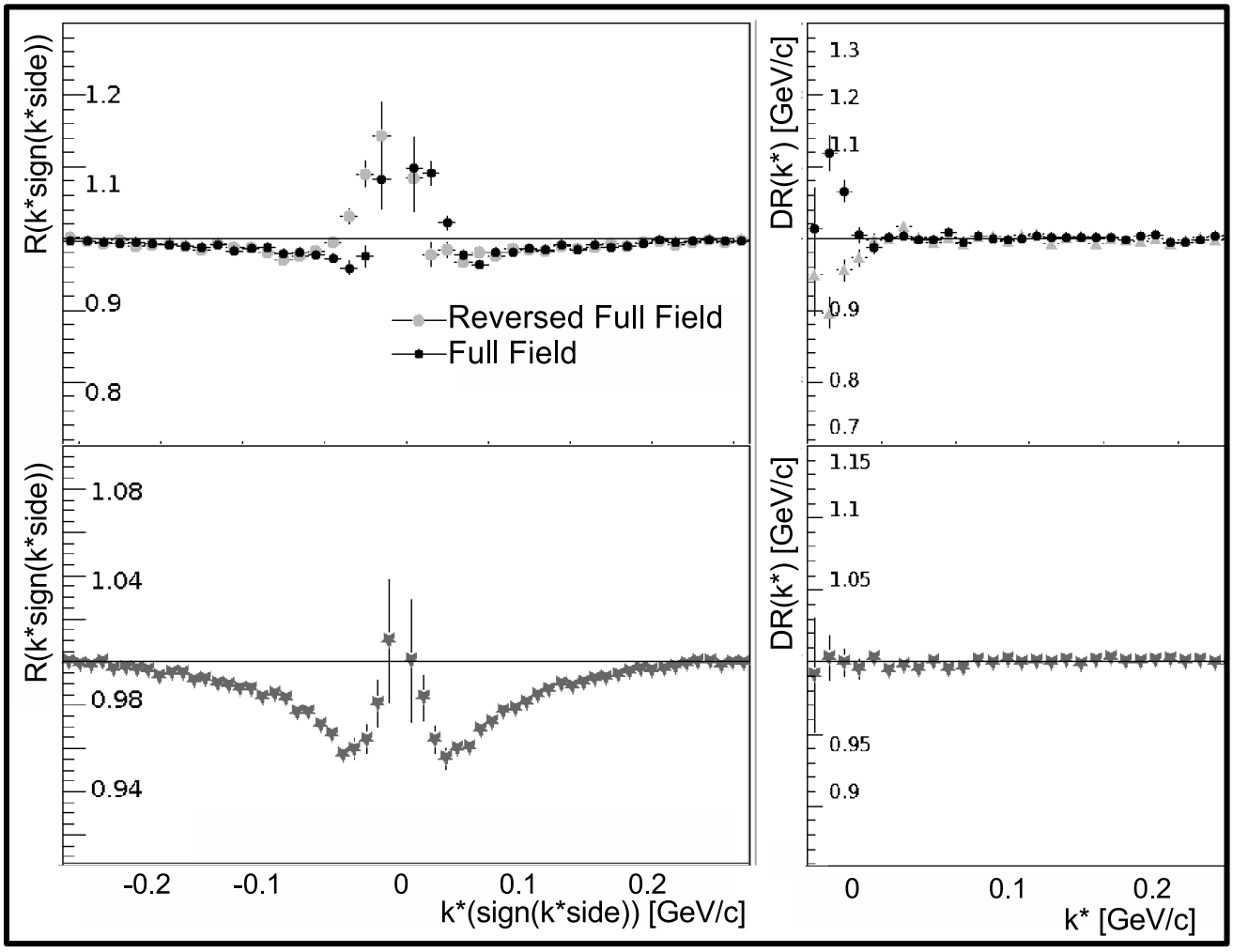

Figure 6.3: Proton - anti-proton correlation functions influenced by e^+e^- pairs (top panel) and after removing them (bottom panel).

Then, a percentage of merged hits is determined. The best compromise between reduction of too many suspected pairs and removing no pair is discarding from the numerator and the denominator of the correlation function, the pair candidates which have the fraction of merged tracks higher than 10% of all hits.

6.1.3 Gamma conversion into electron-positron pairs

Pairs of electrons and positrons (e^+e^-) constitute a significant contribution to non-identical unlike-charge two-particle correlation function. Fortunately such pairs may be distinguished from other pairs and cut out from the analysis. Since the photon is massless, conversion prod-

ucts will have momentum only along the straight line, determined by the gamma momentum before conversion. Within the scope of this analysis such pairs primary originating from gamma conversion are present in the material of the detector. If conversion takes place in the presence of a magnetic field, trajectories of the electron and the positron are bent in opposite directions, leaving tracks in detector. However, 'at the moment of conversion', both the electron and the positron have parallel momentum vectors (these are parallel to the gamma momentum). Removing a significant fraction of e^+e^- pairs improves the measurements a lot, as contamination with e^+e^- pairs is the most significant artificial effect occurring in proton femtoscopy. Figure 6.3 presents one dimensional proton - anti-proton correlations multiplied by sign of $side$ direction. Due to azimuthal symmetry the result of division of two functions for different sign of k^*_{side} should be equal to the unity. No deviation is expected. The top panel shows functions for two various orientation of the magnetic field and it clearly shows that before removing e^+e^- pairs, the function is strongly distorted; the double ratio emphasizes the magnitude of deviation. After removing false pair candidates, the correlation function is much improved (bottom panel).

6.2 Corrections

There are two significant sources of systematic impurities: particle misidentification (when a simple track is treated as a one of other type) and a misinterpretation of the particle origin (when it is treated as a primary one while it is a product of weak decay of other particle). Another correction is related to finite detector resolution- resolution smearing correction.

6.2.1 Purity correction

The formula for single particle purity correction is as follows:

$$Part\,pur(p_T) = Pid(p_T) * Fp(p_T) \tag{6.2}$$

where $Part\,pur(p_T)$ is particle purity, $Pid(p_T)$ is particle identification probability and $Fp(p_T)$ is the probability of being a primary particle. $Pid(p_T)$ is a number experimentally available from dE/dx analysis (here the probability of correct proton and anti-proton identification is in the range greater than 0.8 and it is smaller for the lowest transverse momenta). $Fp(p_T)$ is an estimated probability of 0.5 , that the selected proton is a primary particle [79] (50% of protons do not come from decay of Λ or Σ^* hyperon, thus they are considered as primordial (primary)

protons). The calculation is based on HIJING predictions [42] for transverse momenta $[0.4, 0.8]$ GeV/c (as the highest proper proton and anti-proton identification probabilities are estimated in this interval). In the terms of a pair:

$$Pair\ pur(k^*) = Part\ pur_1(p_{T1}) * Part\ pur_2(p_{T2}) \tag{6.3}$$

where $Pair\ pur(k^*)$ is a pair purity product of multiplying separate probabilities for single particles $part_1$ and $part_2$. $Pair\ pur(k^*)$ is a histogram which depends on many combinations of p_{T1} and p_{T2}. In the terms of a pair, the probability that a pair is composed of primordial particles is 0.25 (not taking into account the track misidentification). Corrected correlation functions are calculated according to the formula:

$$C_{corr}(k^*) = \frac{C_{meas}(k^*) - 1}{Pair\ pur(k^*)} + 1 \tag{6.4}$$

6.2.2 Resolution smearing correction

Momentum resolution is parametrized in the following way:

$$\frac{\triangle p_i}{p_i} = a_{p,i} + b_{p,i} p_i^{\alpha_i} + c_{p,i} p_i \tag{6.5}$$

$$\triangle \phi_i = a_{\phi,i} + b_{\phi,i} \phi_i^{\alpha_i} \tag{6.6}$$

$$\triangle \theta = a_{\theta,i} + b_{\theta,i} \theta_i^{\alpha_i} \tag{6.7}$$

where i denotes a particle type. For each particle, basing on its momentum p and angles ϕ and θ (the azimuthal angle with respect to the horizontal plane and the polar angle between the track and beam axis, respectively), corresponding smeared sigmas $\sigma \triangle p$, $\sigma \triangle \phi$ and $\sigma \triangle \theta$ are found. Then, momentum resolution smears ∂p, $\partial \phi$ and $\partial \theta$ are generated, from Gaussian distributions with zero mean values and corresponding sigmas; new, smeared momenta are calculated:

$$p_x^{smear} = p_x^{meas} + \partial p_x \tag{6.8}$$

$$p_y^{smear} = p_y^{meas} + \partial p_y \tag{6.9}$$

$$p_z^{smear} = p_z^{meas} + \partial p_z \tag{6.10}$$

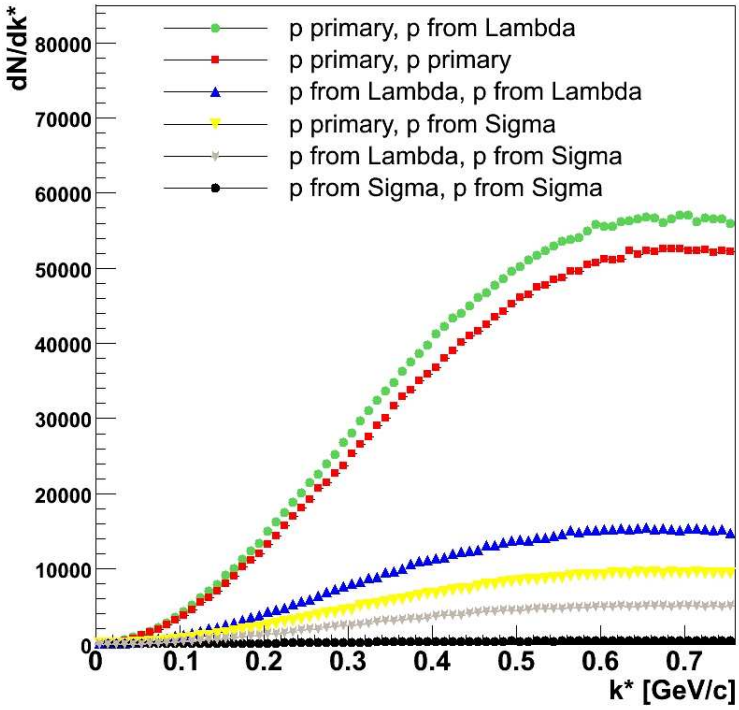

Figure 6.4: Two-proton distributions of momentum differences in the Pair Rest Frame (PRF) for central ($0-10\%$) Therminator data

where ∂p_x, ∂p_y and ∂p_z are the functions dependent on angles ϕ and θ and, respectively p_x, p_y and p_z.

6.2.3 Residual correlation correction

This correction allows one to estimate the impact of contamination originating from hyperon decays to the experimental $p-p$, $\overline{p}-\overline{p}$, $p-\overline{p}$ correlation functions. A detailed description of the technique is presented in the following section.

6.3 Residual correlations

6.3.1 Basics of residual correlation effects

The motivation of these studies is that preliminary results on proton femtoscopy indicated two source sizes: one for identical particles and the other one for non-identical particle species. The radii for $p-p$ and $\overline{p}-\overline{p}$ are consistent within each centrality bin, however the source size for $p-\overline{p}$ is considerably smaller. These observables agree for two collision energies: 62 and 200 GeV. Then again, these results are obtained without taking into account the effect of residual correlations arising due to baryons decaying into protons and anti-protons.
From the experimental point of view, many secondary protons and anti-protons are indistinguishable from primordial particles, as their parent particles are not detected. Neglecting this fact leads to misinterpretation of the results, where instead of $p-p$ interactions, correlations between other particles (which decayed finally into proton) are observed. Two main weak decay channels are the most important:

$$\Lambda \rightarrow p + \pi^{-} \tag{6.11}$$

$$\Sigma^{+} \rightarrow p + \pi^{0} \tag{6.12}$$

In fact, all Residual Correlations (RCs) arising from decay channels which lead to proton (anti-proton) through hyperons are considered. In order to evaluate the effect of RCs occurring in proton femtoscopy, this analysis uses the Therminator (THERMal heavy-ion GenerATOR) Monte Carlo event generator [87, 88], a generator designed to study particle production at SPS, RHIC and LHC energies. This program implements a thermal model of particle production with a single freeze-out. The geometry of the freeze-out hypersurface is chosen according to the Cracow model [89, 90] and the space-time emission point, as well as parent information is stored for each particle. These studies are centrality dependent, which means that for each centrality class, a separate sample of Therminator events is generated. Figures 6.4-6.7 present the results for central events.

6.3.2 Combining contributions from several sources

The experimentally measured proton - proton (and anti-proton - anti-proton) correlations are described by the Equation 6.13. It includes all pair combinations, taking into account both (ex-

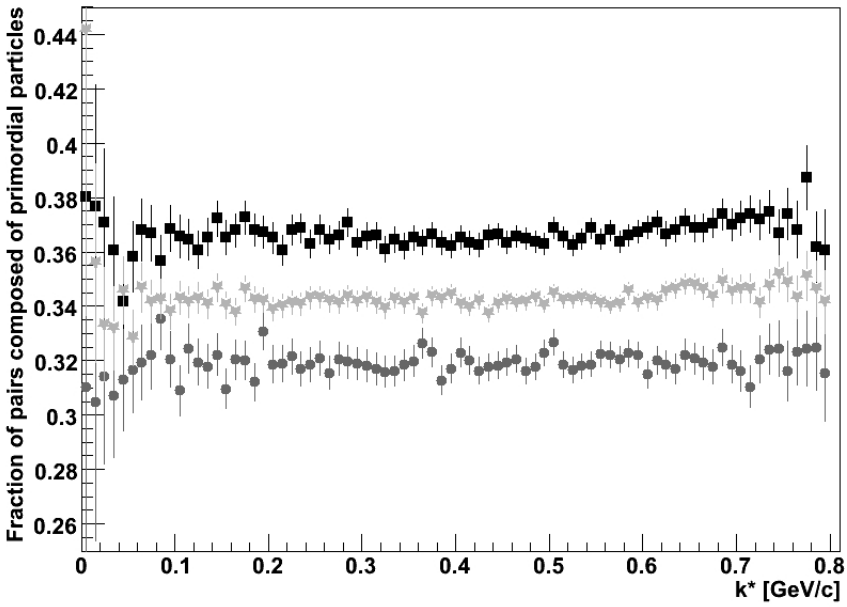

Figure 6.5: The fraction of pairs composed of primordial particles: proton - proton (black squares), anti-proton - anti-proton (dark gray circles), and proton - anti-proton (bright stars) for central ($0-10\%$) Therminator collisions

pressions 6.11 and 6.12) decay channels:

$$C_{true}(k^*) = C_{p-p}(k^*)F_{p-p}(k^*) + C_{p-\Lambda}(k^*)F_{p-\Lambda}(k^*) + C_{\Lambda-\Lambda}(k^*)F_{\Lambda-\Lambda}(k^*) + C_{p-\Sigma}(k^*)F_{p-\Sigma}(k^*) + C_{\Sigma-\Sigma}(k^*)F_{\Sigma-\Sigma}(k^*) + C_{\Lambda-\Sigma}(k^*)F_{\Lambda-\Sigma}(k^*) \tag{6.13}$$

where $F_{x-y}(k^*)$ represents the fraction of measured $p-p$ pairs, where most primary parents were x and y. In order to evaluate the fractions $F_{x-y}(k^*)$ of each type of correlation, all protons are divided into three groups: primordial particles, protons coming from Λ hyperons and ones coming from decays of Σ^+ baryons. It is calculated as the number of $x-y$ pairs (dependent on k^*) with respect to all pairs (e.g if x, y mean primary protons, then $F_{p-p}(k^*)$ is calculated as a number of all $p-p$ pairs, where both particles are primary ones and their number is scaled by the number of all $p-p$ pairs, where the origin of first and second proton does not matter). For all two-proton combinations, k^* distributions are computed (Figure 6.4). The dominant contribution for all k^* values, comes from $p-\Lambda$ pairs, indicating that $p-\Lambda$ residual interaction strongly affects measured $p-p$ correlation. The presence of other types of residual correlations

is much less significant. $C_{x-y}(k^*)$ means the residual contribution of $x-y$ correlation (explained in the next sub-section). $C_{true}(k^*)$ is the experimentally measured correlation function corrected for particle identification probability (PID) purity. The aim of this study is to estimate the pure $p-p$ correlation ($C_{p-p}(k^*)$ from Equation 6.13) after removing the residual ones. The fraction of pure correlation is slightly k^*- dependent function, with the mean value from 0.31 (for the $\overline{p}-\overline{p}$ system) to 0.38 (for the $p-p$ system), due to $\overline{p}/p$ ratio smaller than $\overline{\Lambda}/\Lambda$ ratio. These numbers correspond to central events. The main weak-decay channels of protons and anti-protons are lambda and anti-lambda ones. The fractions of pure correlations are shown in Figure 6.5.
The formula for the $p-\overline{p}$ system is a little more complicated as it contains all combinations of protons and anti-protons from 6 different groups. The mechanism of calculating the RCs existing in $p-\overline{p}$ systems is not described here as it is similar to the one for identical proton femtoscopy.

6.3.3 Convolution of decay kinematics

The $p-\Lambda$ correlation function is measured by STAR [79] as a function of $k^*_{p-\Lambda}$. However the argument of $C_{p-\Lambda}$ in Equation 6.13 is k^*_{p-p}, the relative momentum between two protons; in this case, one of the protons is the decay daughter of Λ. To calculate the $p-\Lambda$ contribution to the measured $p-p$ correlation function, the $p-\Lambda$ correlation function must be convoluted with Λ-decay kinematics. Figure 6.6 shows regions of $k^*_{p-\Lambda}$, where the $p-\Lambda$ RC affect some ranges of k^*_{p-p}. This figure presents results for central collisions. For each value of k^*_{p-p}, the influence of the $p-\Lambda$ correlation is computed (Equation 6.14) as a sum over all $k^*_{p-\Lambda}$ bins, of experimentally measured $p-\Lambda$ correlations scaled by the factors from the $W(k^*_{p-p}, k^*_{p-\Lambda})$ histogram.

$$C_{p-\Lambda}(k^*_{p-p}) = \sum_{k^*_{p-\Lambda}} C^{meas}_{p-\Lambda}(k^*_{p-\Lambda}) W(k^*_{p-p}, k^*_{p-\Lambda}) \tag{6.14}$$

The $p-\Lambda$ correlation should not be corrected for purity, as it contains residual correlations derived from higher-order decays. For mid-central and peripheral collisions $p-\Lambda$ (and $\overline{p}-\Lambda$) correlation functions are analytically calculated using the Lednicky & Lyuboshitz model [78], assuming scaling of $p-\Lambda$ (and $\overline{p}-\Lambda$) radii according to scaling of $p-p$ (and $p-\overline{p}$) source sizes before applying RC corrections. RCs from $p-\Sigma^+$ and $\Sigma^+-\Sigma^+$ channels are assumed to arise only from Coulomb interactions for all systems, in addition to QS for $\Sigma^+-\Sigma^+$. The (k^*_{p-p} and $k^*_{p-\Sigma^+}$), (k^*_{p-p} and $k_{\Sigma^+-\Sigma^+}$) kinematic dependencies of decay of Σ^+ hyperons are considered separately. In the case of $\Lambda-\Lambda$ and $\Lambda-\Sigma^+$ interactions no correlation is assumed, therefore for each k^* value a flat distribution is equal to unity. In these systems strong FSI occur (and

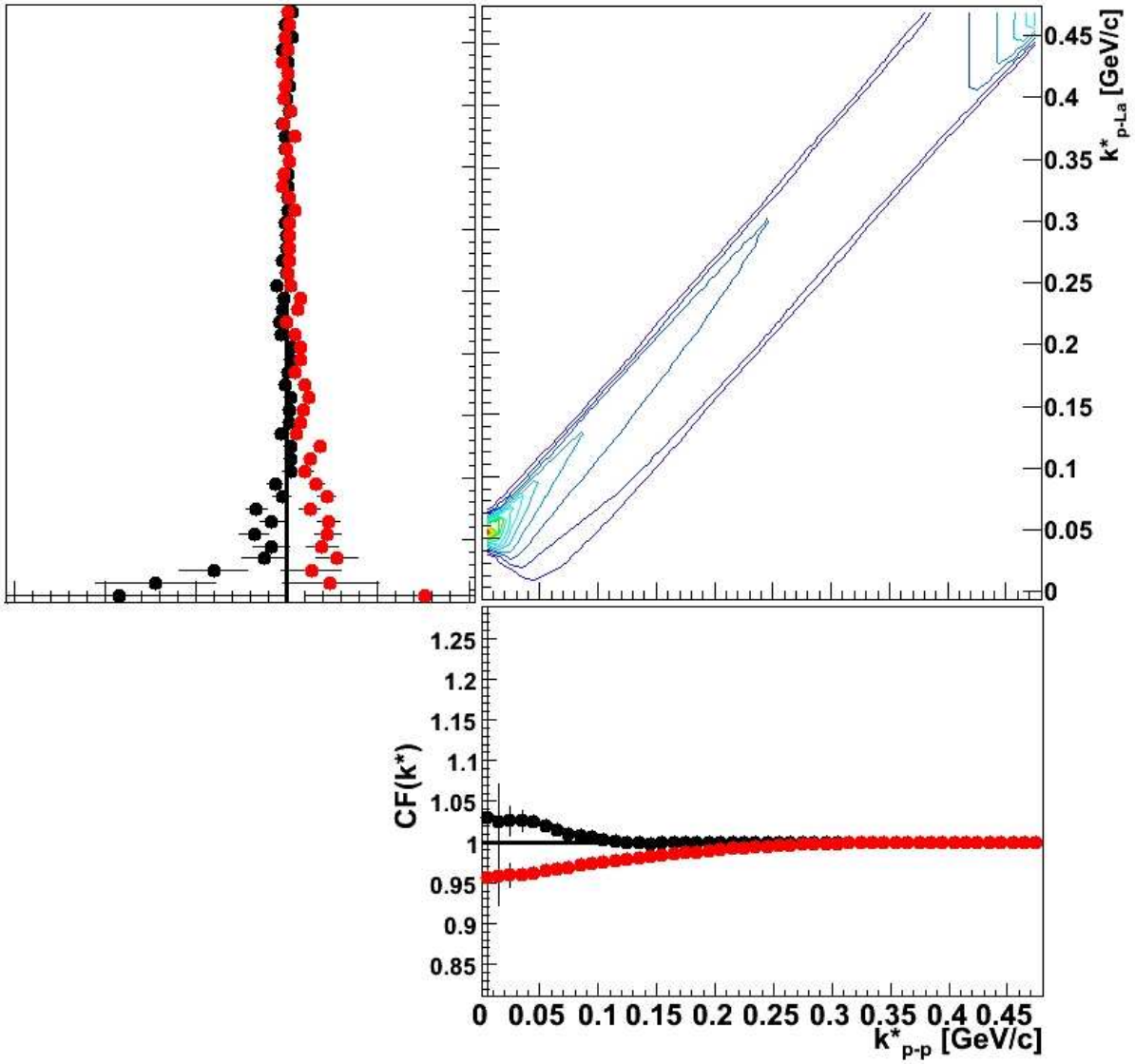

Figure 6.6: Top-left panel: experimentally measured $p-\Lambda$ (black marker) and $\bar{p}-\Lambda$ (red marker) correlation functions for central collisions. Top-right panel: kinematic dependencies $W(k^*_{p-p}, k^*_{p-\Lambda})$of lambda decays, k* of $p-\Lambda$ pairs versus k* of $p-p$ pairs. Bottom-right panel: $p-\Lambda$ and $\overline{p}-\Lambda$ residual correlations reflected in correlation functions for $p-p$, $\overline{p}-\overline{p}$ (black circles) and $p-\overline{p}$ (red circles). All results for central $(0-10\%)$ collisions.

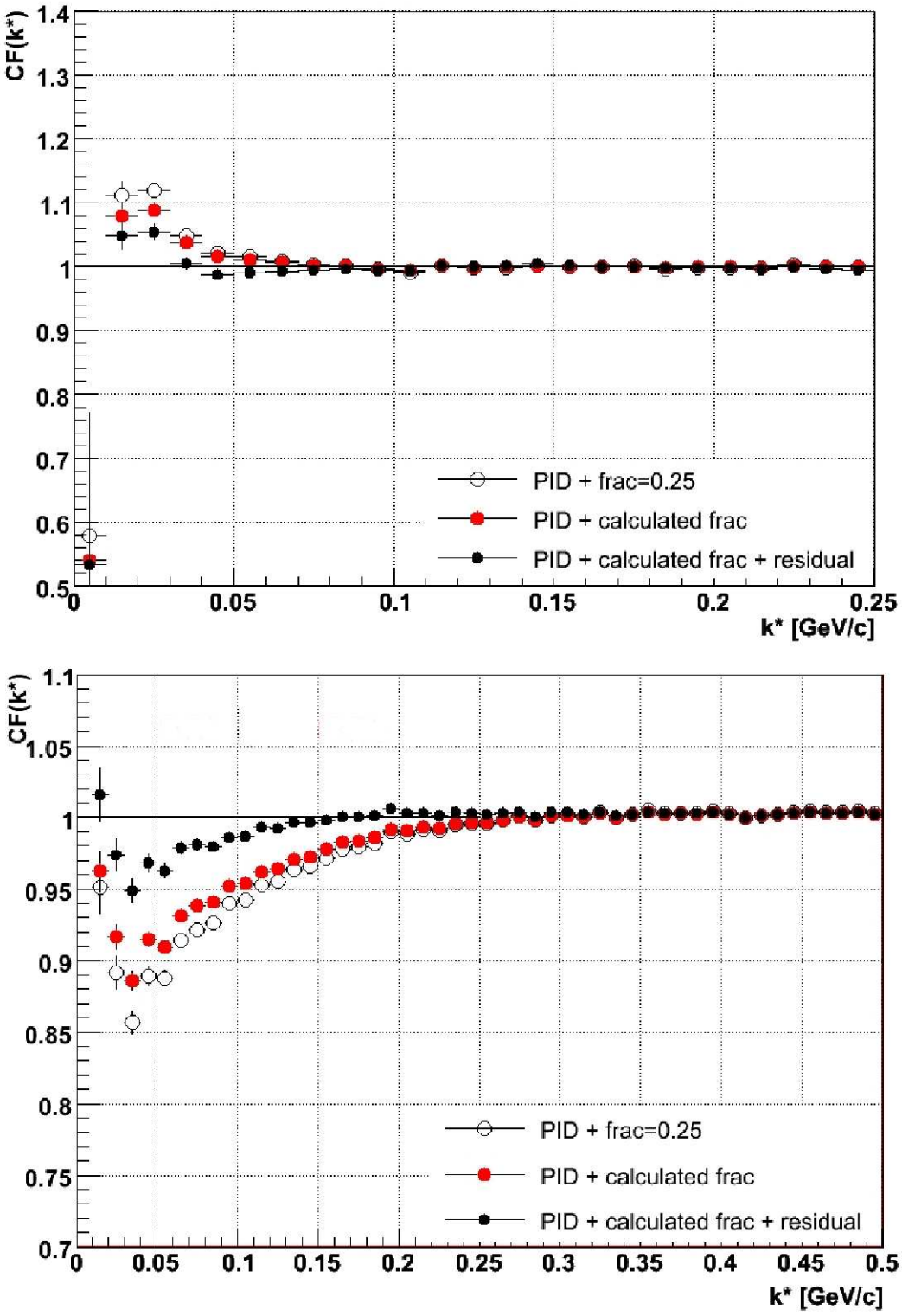

Figure 6.7: Residual correlations in proton - proton (top panel) and proton - anti-proton (bottom panel) system for central collisions (0-10%). The differences between red (uncorrected) and black circles (corrected for residual correlations) show the importance of residual correlation correction.

QS in $\Lambda - \Lambda$ system as well); their existing theoretical descriptions are not confirmed so far by any experiment, thus should not be taken into account. On the other hand, the impact of RCs coming from these combinations do not contribute to the pure $p-p$ correlation such significantly as $p - \Lambda$ system, so assuming no correlation for these cases is much appropriate than assuming some correlation. If such correlation would be predicted (if $\Lambda - \Lambda$ correlation would be known), one should consider proper source size. At the moment it is not clear how to estimate the shape of $\Lambda - \Lambda$ correlations correctly.
In these studies only $p-\Lambda$ (and $\overline{p}-\Lambda$) are taken from experiment. Correlating processes for other systems are estimated if the calculation of QS and Coulomb interaction is possible to perform. Estimation of strong-interaction parameters for systems like: $\Lambda-\Lambda$, $(\Lambda-\overline{\Lambda})$, $\Sigma^+-\Sigma^+$ $(\Sigma^+-\overline{\Sigma^+})$, and $\Lambda - \Sigma$ $(\Lambda - \overline{\Sigma^+})$ is highly non-trivial and is not included in these studies; however, it does not add significant discrepancies as fractions of such RCs are not large (see Figure 6.4).

6.3.4 Effects on extracted length scales

The net effect of the purity and RC corrections is shown in Figure 6.5. All correlation functions are corrected for Particle IDentification (PID) effects (more in Section 7). Here, the first estimate of the fraction of primary-primary proton pairs was 0.25 (i.e. fraction of of primary protons 0.5); the correlation function corrected for this purity is shown by open circles in Figure 6.5 for $p - p$ (top panel) and $p - \overline{p}$ (bottom panel). A better calculation of pair purity (fraction $F_{p-p}(k^*)$ from Equation 6.13) is shown by correlation functions marked by red circles. Finally, the extracted correlation is further reduced when RCs are also corrected for (black circles).
Since the $\overline{p} - \Lambda$ correlation is much stronger and wider than the $p - \Lambda$ one, the residual effects on the $p - \overline{p}$ system are more significant than those for $p - p$ system. This is clear in Figure 6.7, where the effects of various corrections on $p - \overline{p}$ are shown.

Chapter 7

Experimental results

The presentation of experimental results is divided into three sub-sections: the first one (7.1) contains results without a precise estimation of the effect of RCs, the second sub-section (7.2) discusses this problem with more details included. Within each part two kinds of corrections are gradually applied: estimation of impurities and resolution smearing effects. The last sub-section (7.3) treats non-identical proton - anti-proton correlations in terms of asymmetry analysis in order to discuss possible differences in the emission process between protons and their anti-particles.

7.1 Two-proton correlations without residual correlation corrections

7.1.1 Raw data

The first step in the analysis of two-particle correlations is to obtain the correlation functions free of experimental distortions. Some experimental effects, as e.g.: track merging, track splitting, contamination with electron - positron pairs coming from photon conversion, can be easily removed at the level of pair selection. However, there are few imperfections which cannot be removed during raw-data analysis: falsely identified tracks of particles, resolution smearing of single tracks, and contamination with non-primary particles. These contaminations are especially important for baryon correlations, as many of them come from weak decays.
Figure 7.1 shows two - proton, two - anti-proton and proton - anti-proton correlation functions without corrections for resolution smearing and purity. As mentioned, the effects of track split-

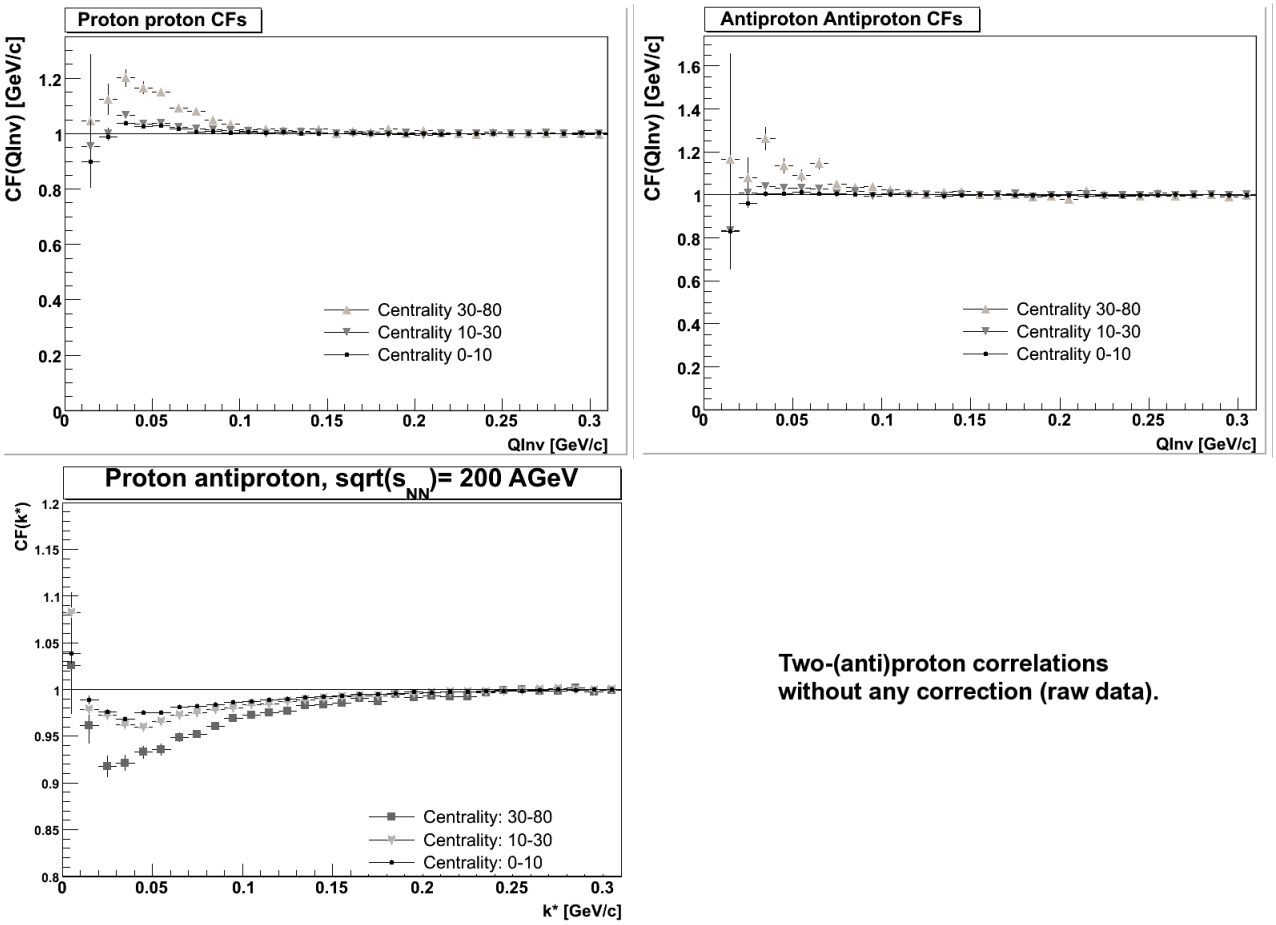

Figure 7.1: Results of proton femtoscopy with no correction applied: proton - proton (top-left panel), anti-proton - anti-proton (top-right panel) and proton - anti-proton (bottom-left panel).

ting, track merging and electron - positron contamination were removed in the course of data analysis. The results for identical particle combinations agree with each other within each centrality bin and follow similar trends, as expected. The correlation functions for central collisions are weaker than for non-central ones, thus their source sizes are bigger. The correlation effect is the strongest while considering more peripheral collisions. The top-left panel illustrates proton - proton correlations for three centralities (up to 10%, 10 - 30%, 30 - 80% of the total hadronic cross section of the collision), the top-right panel shows anti-proton - anti-proton correlations and the bottom-left panel presents proton - anti-proton correlation functions. Even if none of the functions are corrected for such impurities, a clear centrality dependence can be observed. In the case of non-identical particle combinations, annihilation processes between particles and their anti-particles are observed as well; this effect can be seen as an anti-correlation (below the value of 1.0). Presented in Figure 7.1 are the raw correlation functions, treated as a base for further corrections. The best source-size fits are not calculated, as the functions need to be scaled according to many correcting factors.

7.1.2 Purity correction

Due to corrections for purity, comparing to the raw correlation functions, the correlation effects become stronger and thus their source sizes are smaller. Including statistical and systematic errors, the results of fit are stored in Table 7.1. The systematic uncertainties are estimated from the discrepancy of correction for purity. Stability of the fit (for 100% of the applied purity correction) is checked by estimation of fitted source sizes while applying from 90% to 110% of the correction.

Table 7.1: Source sizes $[fm]$ for different proton combinations and centralities; with purity corrections applied; reported errors are respectively, statistical and systematic (due to purity correction applied)

	$p-p\,[fm]$	$\overline{p}-\overline{p}\,[fm]$	$p-\overline{p}\,[fm]$
$peripheral$	$2.52^{+0.11-0.05}_{-0.11-0.05}$	$2.53^{+0.13+0.08}_{-0.13-0.07}$	$1.62^{+0.12+0.05}_{-0.12-0.05}$
$mid-central$	$3.59^{+0.09+0.04}_{-0.09-0.04}$	$3.51^{+0.09+0.07}_{-0.09-0.07}$	$2.13^{+0.10+0.03}_{-0.10-0.04}$
$central$	$4.02^{+0.07+0.05}_{-0.07-0.06}$	$4.47^{+0.08+0.07}_{-0.08-0.06}$	$2.61^{+0.09+0.03}_{-0.09-0.03}$

An agreement between identical particle combinations is observed, except for central collisions, where the source size of the anti-proton - anti-proton correlation is half of fm bigger than the source size of the proton - proton correlation. The discrepancy can be explained as an effect of

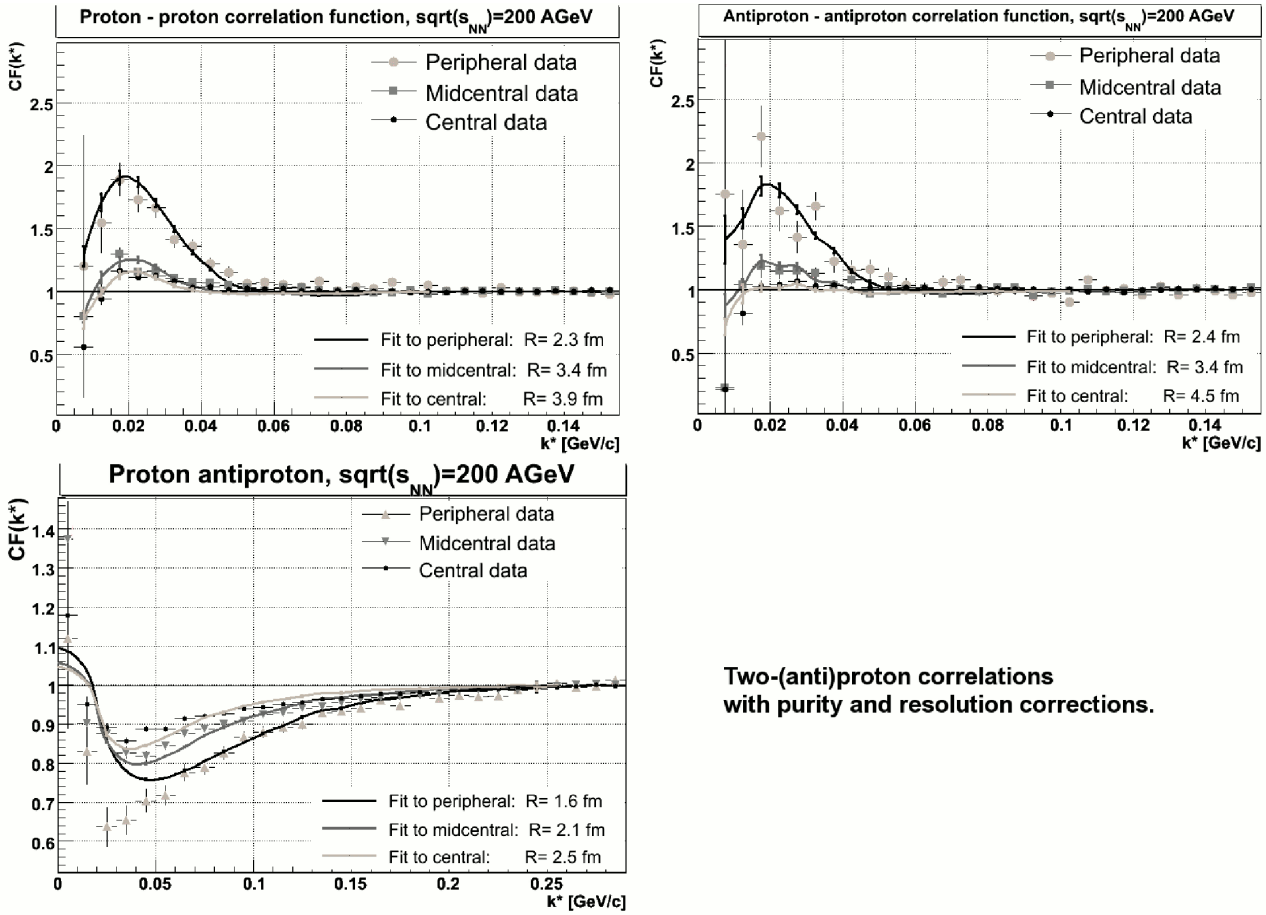

Figure 7.2: Results of proton femtoscopy with purity and resolution corrections: proton - proton , anti-proton - anti-proton and proton - anti-proton (left-hand side of the bottom panel).

the weakness of the signal for central collisions. As the source size becomes larger, the correlation becomes weaker and estimation of the source size of the order of $4-5$fm becomes more difficult. Another interesting difference between the fitted sources is that one between identical and non-identical particle combinations. In results for $p-p$ and $\overline{p}-\overline{p}$, only for a very small difference between protons and anti-protons is detected. For these two systems the same source sizes are expected. The proton - anti-proton system is subject of other mechanisms (e.g. annihilation processes), however smaller source sizes were not expected. The two-particle correlation technique allows one to conclude about size of emission region (ang. *lenght of homeogenity*), which is expected to be of the same size in the case of $p-\overline{p}$ as the source size of $p-p$ and $\overline{p}-\overline{p}$- if both identical combinations have the same radii. FSI measured via correlation technique do not contribute to the emission processes, they are reflected in particle correlations and specify a source size, but they cannot produce differences in source sizes. The conclusion from this part is that an additional source of contamination must be considered in next steps of analysis.

7.1.3 Purity and resolution smearing corrections

In this part, the results of correction of another experimental imperfection are discussed. Comparing the output of fits from previous section to the ones after taking into account the effect of momentum resolution for a single track leads to a conclusion that resolution smearing is not as significant as it could be suspected. In terms of two-particle correlations it causes a decrease of source sizes by a factor of up to 0.2 fm. The results for a combination of purity and resolution-smearing corrections applied are shown in Figure 7.2. Table 7.2 collects values of fits, with their statistical and systematic errors; systematic uncertainties are estimated from the discrepancy between two corrections (purity and resolution smearing). Stability of the fit is checked by estimation of fitted source sizes while applying from 90% to 110% of any correction. The agreement between the fits and the experimental points is quite good except for the proton - anti-proton correlation for peripheral data- other correlation is suspected to exist there. This effect is considered in Section 7.2. Previous results obtained taking into account the purity correction applied simply and the effect of resolution smearing are described in [91].

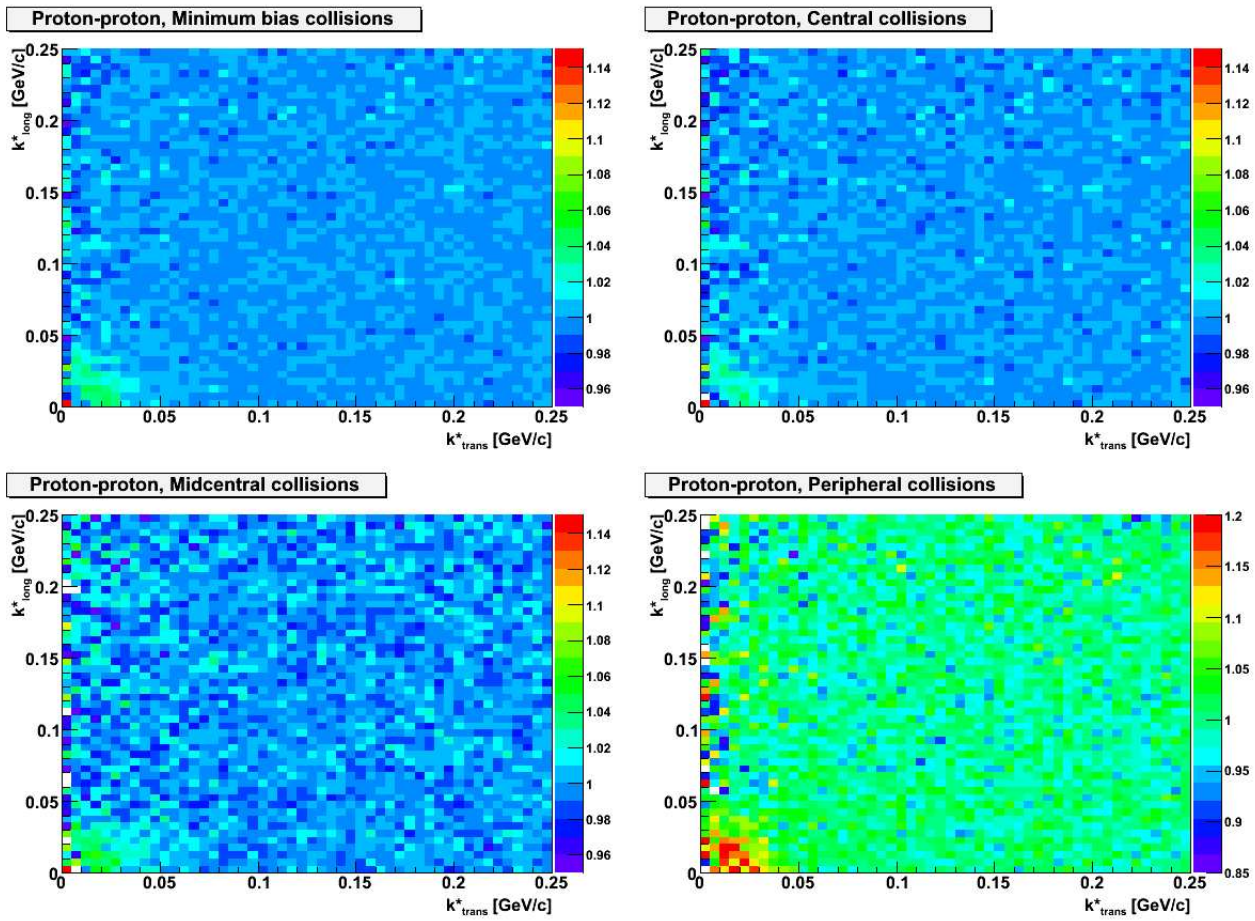

Figure 7.3: Two-dimensional correlation functions for proton - proton combinations (k^*_{long} versus k^*_{trans}). Left-hand side of the top panel shows correlation for minimum-bias events, right-hand side of the top panel illustrates the correlation function for central data, left-hand side of the bottom panel exhibits function for mid-central data and the right-hand side of the bottom panel shows peripheral data.

Table 7.2: Source sizes $[fm]$ for different proton combinations and centralities; purity and resolution smearing corrections applied; reported errors are respectively, statistical and systematic (due to purity and resolution smearing corrections)

	$p-p\,[fm]$	$\overline{p}-\overline{p}\,[fm]$	$p-\overline{p}\,[fm]$
$peripheral$	$2.31^{+0.11+0.05+0.02}_{-0.11-0.05-0.02}$	$2.41^{+0.13+0.08+0.04}_{-0.13-0.07-0.05}$	$1.62^{+0.12+0.05+0.02}_{-0.12-0.05-0.02}$
$mid-central$	$3.41^{+0.09+0.04+0.02}_{-0.09-0.04-0.02}$	$3.52^{+0.09+0.07+0.04}_{-0.09-0.07-0.04}$	$2.14^{+0.10+0.04+0.01}_{-0.10-0.03-0.02}$
$central$	$3.89^{+0.07+0.05+0.03}_{-0.07-0.06-0.03}$	$4.51^{+0.09+0.07+0.04}_{-0.09-0.07-0.04}$	$2.48^{+0.09+0.03+0.02}_{-0.09-0.03-0.02}$

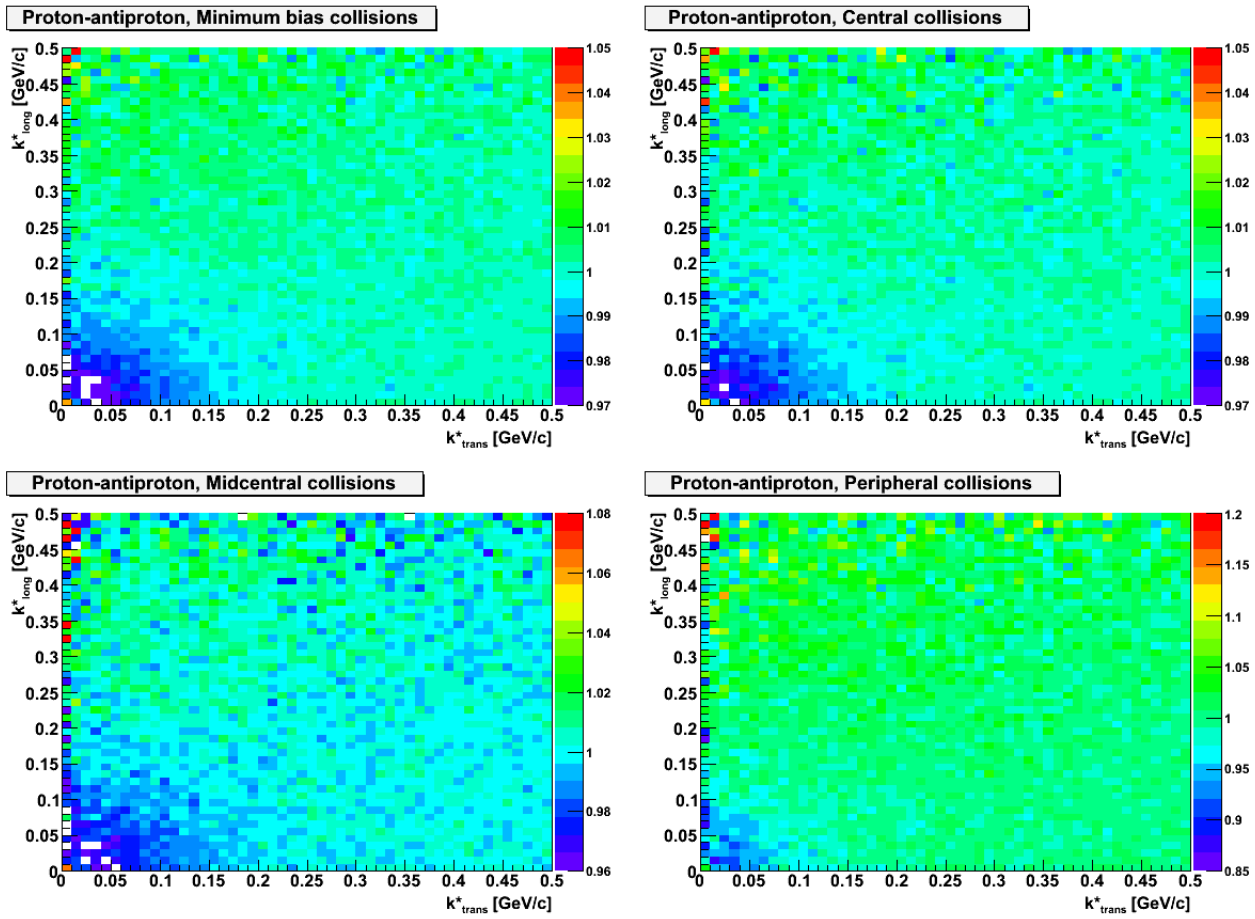

Figure 7.4: Two-dimensional correlation functions of proton - anti-proton combinations (k^*_{long} versus k^*_{trans}). Left-hand side of the top panel shows correlation for minimum-bias events, right-hand side of the top panel illustrates the correlation function for central data, left-hand side of the bottom panel exhibits function for mid-central data and the right-hand side of the bottom panel shows peripheral data.

7.1.4 Two-dimensional correlation functions

As one-dimensional correlation functions are measured with a very good accuracy, two-dimensional correlations can be also estimated. For these studies the same data collections are used. Due to statistical limitations, the quality of such correlation functions is lower than in one-dimensional cases. For one- and two-dimensional analysis the same statistics is considered; even if statistical uncertainties are bigger, some properties of two-dimensional functions can be discussed. Figure 7.3 shows clearly a centrality dependency for two-proton combinations, as expected- the correlation effect is stronger for less central collisions. Two-anti-proton correlations are statistically more limited comparing to two-proton ones, thus they are not shown here. Proton - anti-proton correlations (see Figure 7.4) have the best statistics.
Two-dimensional correlation function data is neither corrected nor fitted, experimental values of PID numbers are not separately available for transverse and longitudinal components of particle momentum. These results indicate a statistical possibility for proton femtoscopy measurements for higher than one-dimensional case. Future experiments (e.g. ALICE [92] that is being prepared to operate at the LHC accelerator), where collisions of heavy-ions will occur at higher energies that those achieved at RHIC, will provide much bigger data collections. then, perhaps studies of proton femtoscopy even for three-dimensional cases will be possible.

7.2 Two-proton correlations with residual correlation corrections

7.2.1 Purity correction

The RCs correction introduced in Section 6.3 was applied for the results discussed in this section. The first consequence which may be observed is the removal of significant discrepancies in source sizes between identical and non-identical proton combinations. The results of the fits (Table 7.3) are much closer to each other than before applying the RC corrections. Statistical and systematic errors are listed in table as well. Systematic uncertainties are estimated from the discrepancy between the two corrections (purity and RCs). The stability of the fit is checked by estimation of fitted source sizes while applying from 90% to 110% of either correction for each point of correlation function.

Table 7.3: Source sizes $[fm]$ for different proton combinations and centralities; purity and RCs corrections applied; reported errors are respectively. statistical and systematic (due to purity and RCs corrections)

	$p-p\,[fm]$	$\overline{p}-\overline{p}\,[fm]$	$p-\overline{p}\,[fm]$
$peripheral$	$2.79^{+0.11+0.05+0.06}_{-0.11-0.05-0.06}$	$2.81^{+0.13+0.08+0.14}_{-0.13-0.07-0.13}$	$2.31^{+0.12+0.05+0.05}_{-0.12-0.05-0.06}$
$mid-central$	$4.01^{+0.09+0.04+0.05}_{-0.09-0.04-0.04}$	$4.22^{+0.09+0.07+0.13}_{-0.09-0.07-0.12}$	$3.39^{+0.10+0.04+0.08}_{-0.10-0.03-0.06}$
$central$	$4.51^{+0.07+0.05+0.07}_{-0.07-0.06-0.10}$	$5.11^{+0.08+0.07+0.10}_{-0.08-0.06-0.11}$	$4.19^{+0.09+0.03+0.05}_{-0.09-0.03-0.06}$

7.2.2 The significance of RC correction

This section complements results shown in Section 6.3 and presents correlation functions for all three systems and centrality bins separately; two collision energies are discussed. As it was mentioned in Section 6.3, RCs affect proton - anti-proton system more than proton - proton one. Figure 7.5 is composed of six panels; each of them presents correlation function before (red points) and after (black points) applying RC correction. For such identical system as $p-p$, the correlation functions after taking into account the influence of RCs do not differ from those before including an RC correlation procedure significantly. For non-identical system as $p-\overline{p}$, the impact of RCs is more dominant. Such dependence occurs as $p-\overline{\Lambda}$ RC observed in $p-\overline{p}$ is stronger than $p-\Lambda$ RC measured with $p-p$ (more details was discussed in Section 6.3). Due to statistical limitations $\overline{p}-\overline{p}$ are not presented. Figure 7.6 shows results for higher collision energy- $\sqrt{s_{NN}}=200$. Conclusions are similar as discussed in Section 6.3: the RCs affect non-identical systems more. The figure complements Figure 6.7 and presents non-central (mid-central: first raw, left column and peripheral: first raw, second column data) results of $p-p$, non-central (mid-central: second raw, left column and peripheral: second raw, right column data) results of $p-\overline{p}$ and three centrality bins for $\overline{p}-\overline{p}$ system (mid-central: third raw, left column, peripheral: third raw, right column, central: fourth raw, left column). Magnitude of RC correction is not centrality dependent, but centrality dependence of $p-\Lambda$ and $\overline{p}-\Lambda$ RCs measured in $p-p$ and $p-\overline{p}$ influence on the magnitude of RC correction.

7.2.3 All corrections applied

This section introduces fully-corrected femtoscopic measurements of proton correlations (as discussed in the previous sections, the additional correction for single track for resolution smearing). The agreement between the results for identical and non-identical particle correlations for collision energy $\sqrt{s_{NN}}=200$ GeV is good, however small discrepancies do remain. They fluctuate

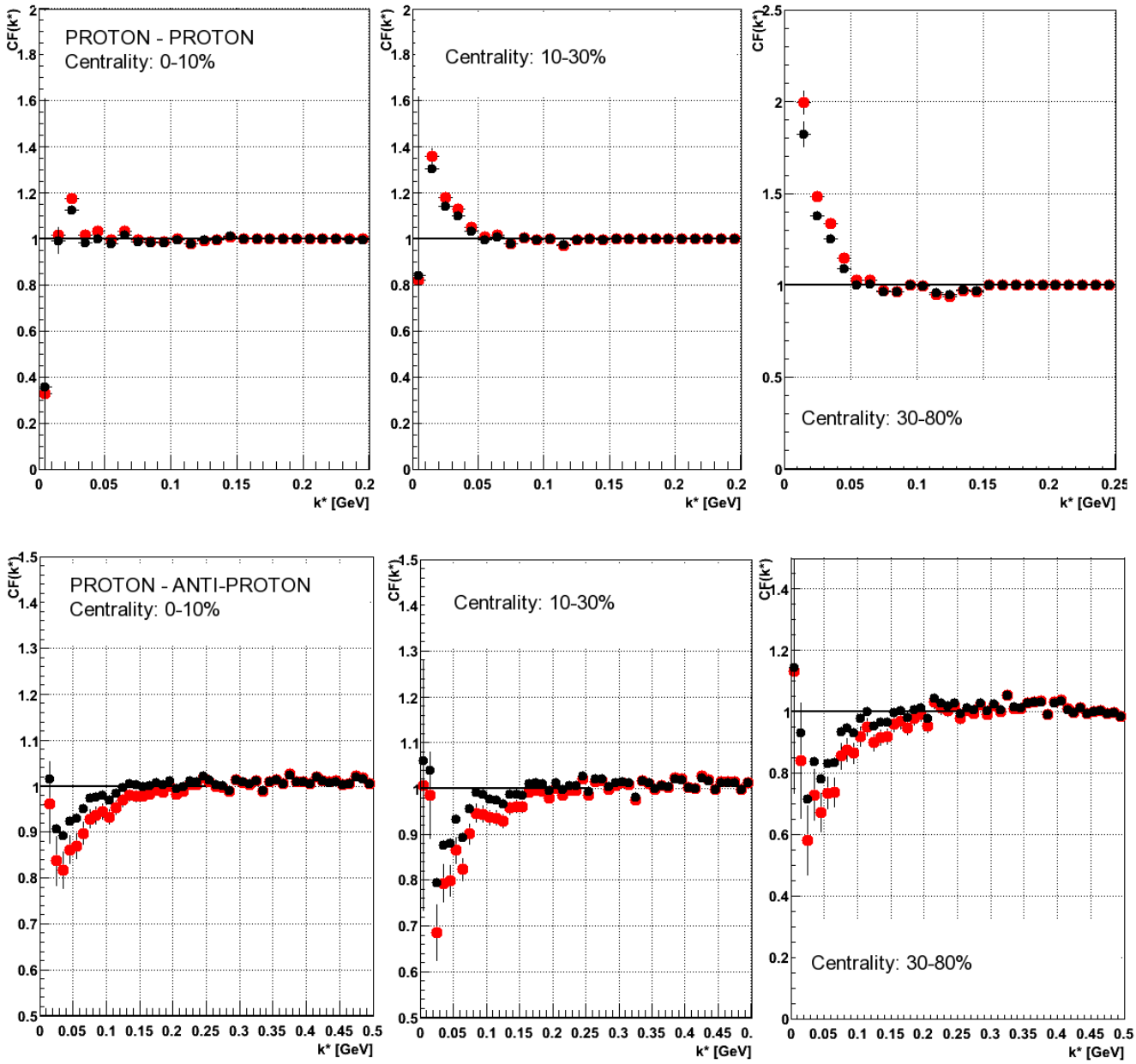

Figure 7.5: Results for proton - proton (top panels) and proton - anti-proton (bottom panels) for collision energy $\sqrt{s_{NN}} = 62$ GeV. Correlation functions before applying RC correction (but corrected for purity and detector resolution effects) are illustrated by red circles; correlations after taking into account effects of RCs are shown by black points.

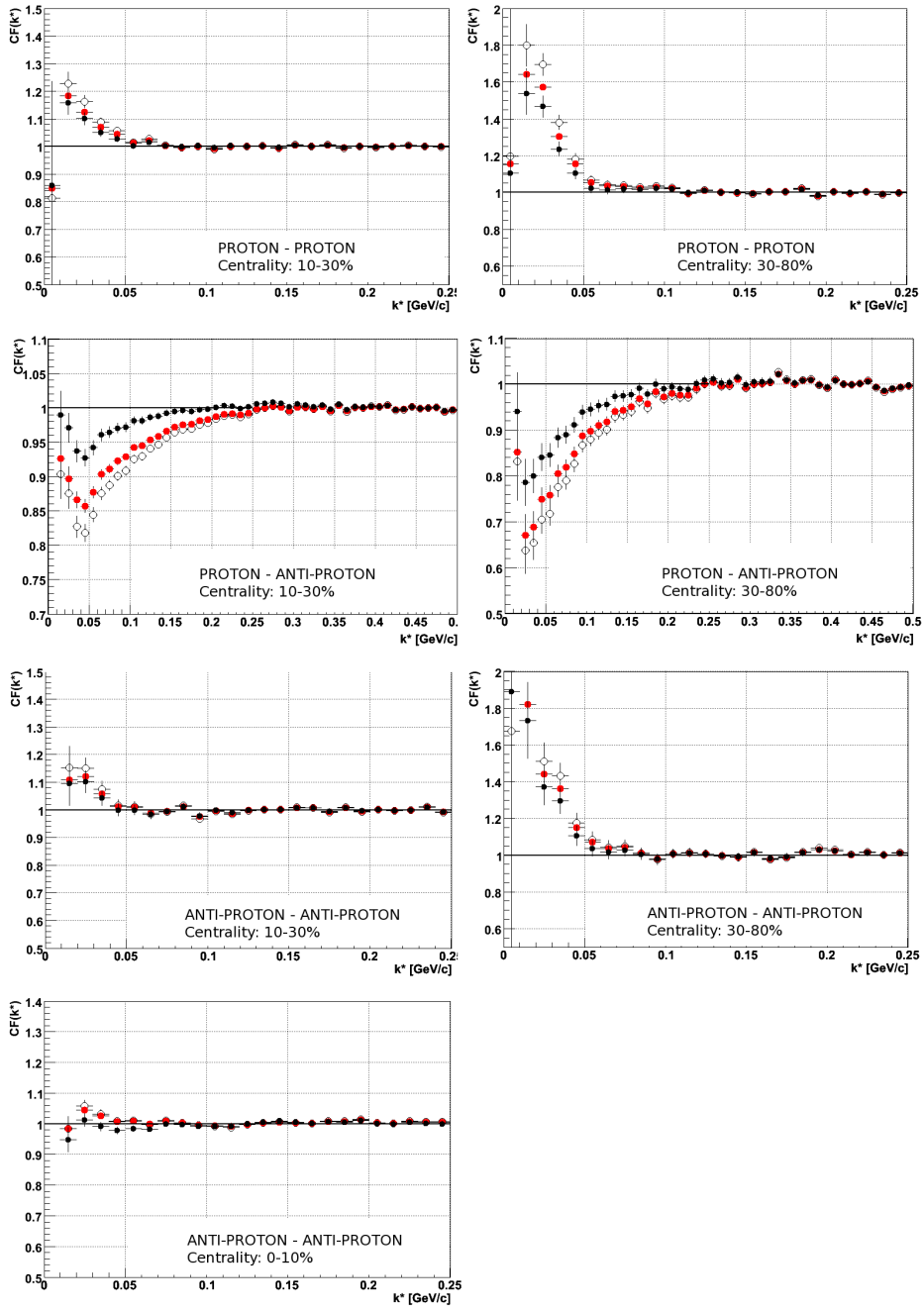

Figure 7.6: Open symbols present correlation functions corrected for PID and fraction of primordial particles to be estimated to 0.25; red circles show functions corrected for PID and calculated fractions of primary particles; black points illustrate fully corrected correlation functions. All functions are corrected for effect of detector resolution. Data for $\sqrt{s_{NN}} = 200$ GeV.

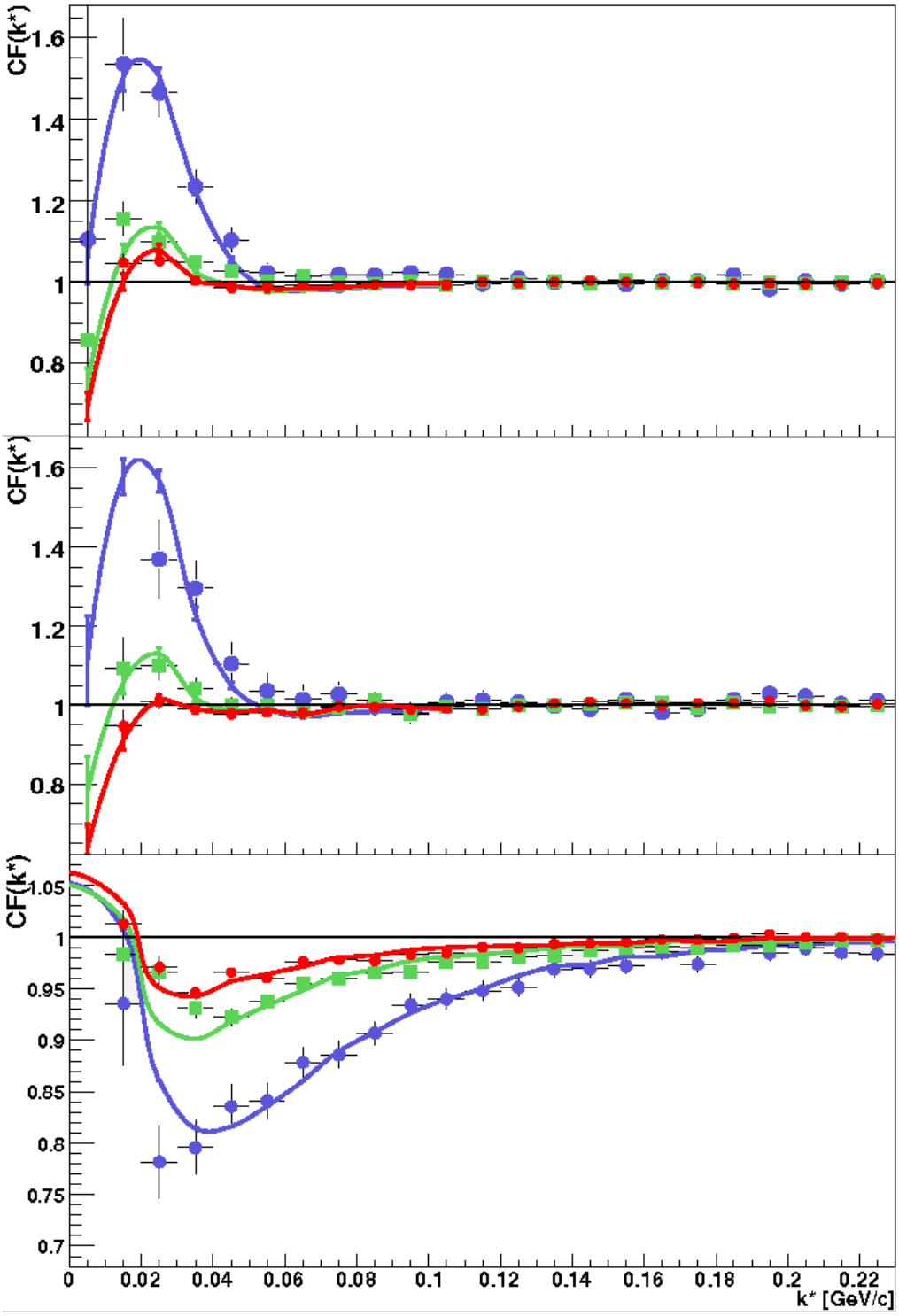

Figure 7.7: Results of proton femtoscopy with all corrections included: proton - proton (top panel) anti-proton - anti-proton (middle panel) and proton - anti-proton (bottom panel). Data for $\sqrt{s_{NN}} = 200$ GeV.

with the systematic error bars- see Table 7.4. Statistical and systematic errors are listed in the table as well. Systematic uncertainties are estimated from the discrepancy between three corrections (purity, resolution smearing and RCs). The stability of the fit is checked by the estimation of fitted source sizes while applying from 90% to 110% of either correction. Results are presented in Figure 7.7. The agreement between peripheral proton - anti-proton data and the fit is much better than before implementing a significant correction.
For lower collision energy, $\sqrt{s_{NN}} = 62$ GeV, correlation functions with the best fits are presented in Figure 7.8; their calculated source sizes are collected in Table 7.5. Data for lower collision energy are statistically limited comparing to the ones for higher collision energy; thus their agreement between experimental points and the best fits is not as good as in the case of collision energy $\sqrt{s_{NN}} = 200$ GeV. For anti-proton - anti-proton system to perform such source size calculation is almost impossible, thus not discussed here. These results indicate that all

Table 7.4: Source sizes $[fm]$ for different proton combinations and centralities; purity, resolution smearing and RCs corrections applied for collision energy $\sqrt{s_{NN}} = 200$; reported errors respectively, statistical and systematic (due to purity, resolution and RCs smearing corrections)

	$p-p\,[fm]$	$\overline{p}-\overline{p}\,[fm]$	$p-\overline{p}\,[fm]$
$peripheral$	$2.71^{+0.11+0.05+0.02+0.06}_{-0.11-0.05-0.02-0.05}$	$2.59^{+0.13+0.08+0.04+0.14}_{-0.13-0.07-0.05-0.13}$	$2.22^{+0.12+0.05+0.02+0.05}_{-0.12-0.05-0.02-0.06}$
$mid-central$	$3.82^{+0.09+0.04+0.02+0.05}_{-0.09-0.04-0.02-0.04}$	$4.02^{+0.09+0.07+0.04+0.13}_{-0.09-0.07-0.04-0.12}$	$3.27^{+0.10+0.04+0.01+0.08}_{-0.10-0.03-0.02-0.06}$
$central$	$4.51^{+0.07+0.05+0.03+0.07}_{-0.07-0.06-0.03-0.10}$	$5.05^{+0.08+0.07+0.05+0.10}_{-0.08-0.06-0.04-0.11}$	$4.08^{+0.09+0.03+0.02+0.05}_{-0.09-0.03-0.01-0.06}$

Table 7.5: Source sizes $[fm]$ for different proton combinations and centralities; purity, resolution smearing and RCs corrections applied for collision energy $\sqrt{s_{NN}} = 62$ GeV; reported errors respectively, statistical and systematic (due to purity, resolution and RCs smearing corrections)

	$p-p\,[fm]$	$p-\overline{p}\,[fm]$
$peripheral$	$2.48^{+0.13+0.06+0.02+0.05}_{-0.13-0.05-0.02-0.05}$	$2.33^{+0.13+0.05+0.02+0.05}_{-0.13-0.05-0.02-0.05}$
$mid-central$	$3.23^{+0.12+0.06+0.02+0.09}_{-0.12-0.05-0.02-0.06}$	$2.72^{+0.13+0.05+0.02+0.04}_{-0.13-0.04-0.02-0.06}$
$central$	$4.17^{+0.11+0.11+0.03+0.09}_{-0.11-0.12-0.03-0.20}$	$3.53^{+0.12+0.04+0.02+0.04}_{-0.12-0.03-0.01-0.05}$

corrections should be applied together. The RC correction is the most essential one, it should be performed with purity correction due to misidentification of particles. RC correction causes all proton femtoscopic measurements to be consistent with each other. In the case of like-signs combinations ($p-p$ and $\overline{p}-\overline{p}$) no asymmetry in emission process between identical particles is expected as their emission properties are identical; however, the production of $p-\overline{p}$ pairs can be different. On the one hand, different strong interactions between identical and non-identical particles should not affect source sizes, as they do not concern FSI, but production mechanisms.

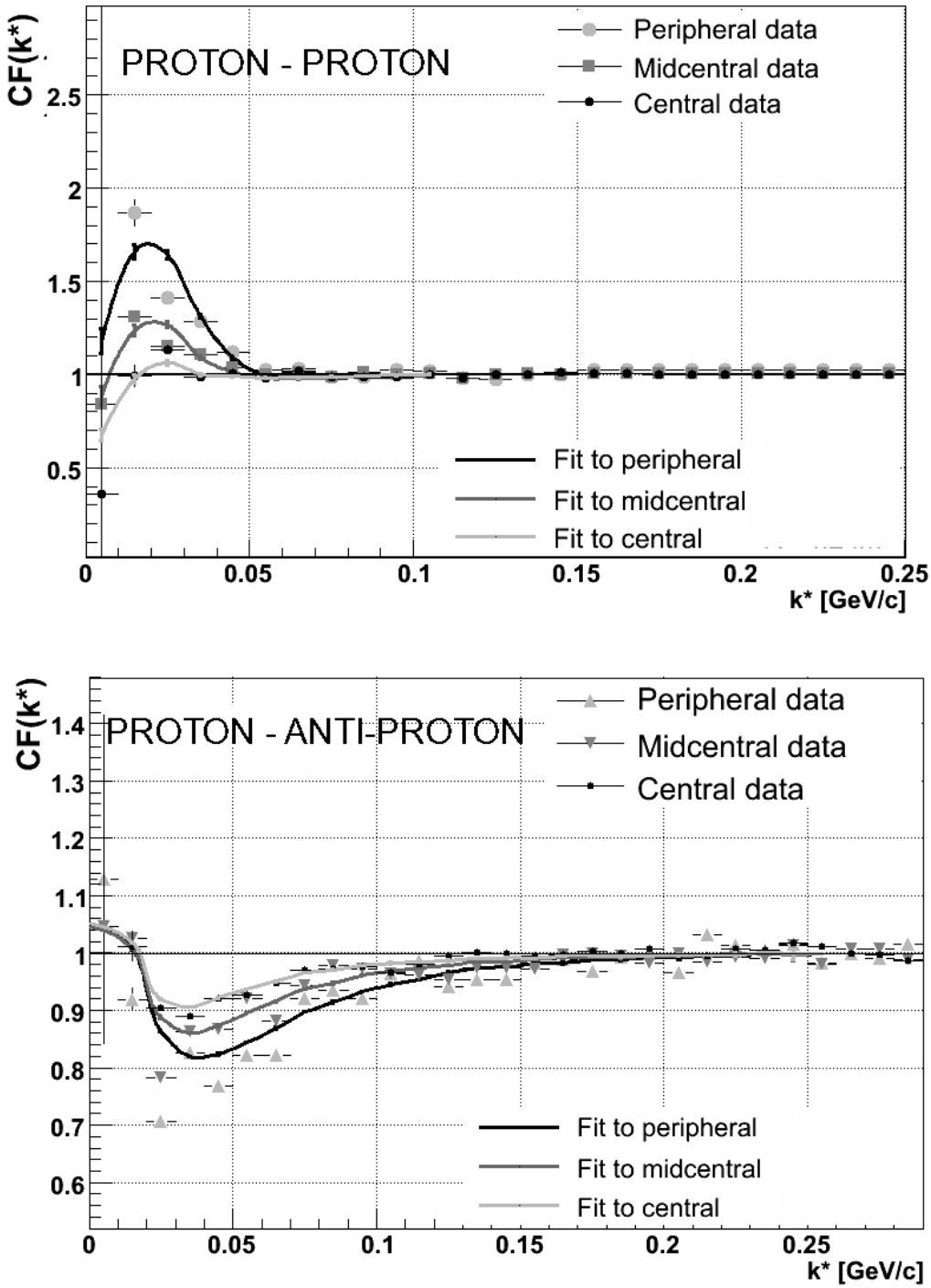

Figure 7.8: Results of proton femtoscopy with all corrections included: proton - proton (top panel) and proton - anti-proton (bottom panel) for collision energy $\sqrt{s_{NN}} = 62$ GeV.

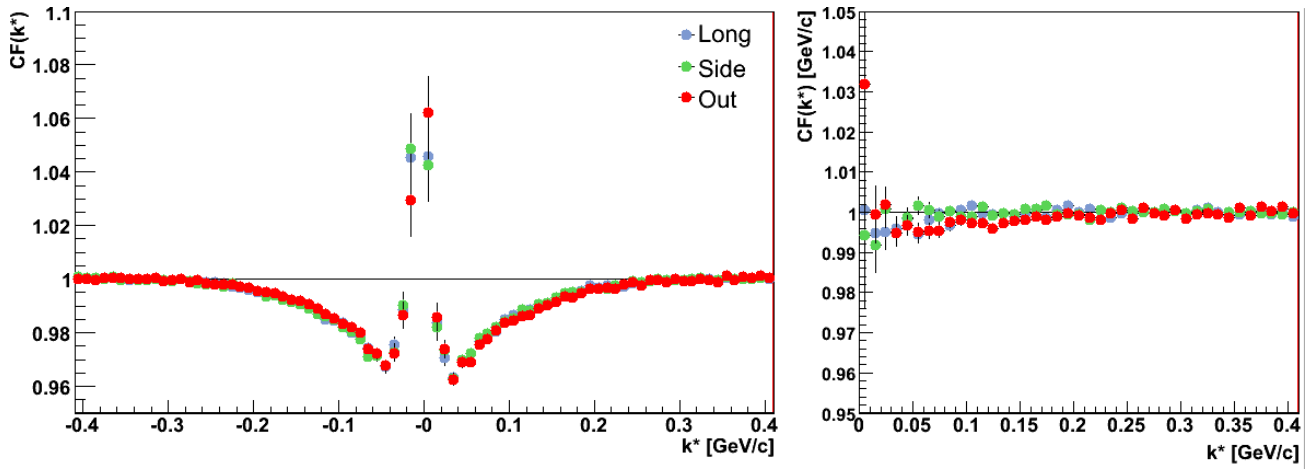

Figure 7.9: Left panel shows correlation functions for k^* multiplied by the sign of k^* for given projection: out, $side$ and $long$; right panel presents their 'double ratios'.

On the other hand, such differences are measured. Thus, observation of other additional correlations, which arise due to existence of residual particles, is concluded. This is the reason why proton and anti-proton studies reflect different source sizes. This problem would not exist in the case of perfect particle detection, where all particles decaying finally into protons or anti-protons would be registered and identified properly. Such results are also described in [93].

7.3 An asymmetry between proton and anti-proton emission

7.3.1 Nonidentical particle correlations

Hydrodynamical models do not predict any space-time asymmetry in emission processes between non-identical particles with the same mass. In these studies protons and anti-protons are considered; the ratio of $\overline{p}/p$ at mid-rapidity is about ~ 0.75 (according to BRAHMS measurements [94]). In the case of non-equal masses, for a given temperature, flow phenomenon causes a space-time shift in the emission. The non-identical particle correlation technique introduced in Section 4.3 allows one to measure possible shifts and it may be applied to any of particle combinations, e.g. proton - anti-proton as well. In order to analyze possible asymmetry, all pairs are divided into two groups, depending on the sign of k^* vector in a given direction: out, $side$, $long$. Then, one-dimensional correlation function is multiplied by the sign of pair in out, $side$ and $long$ projections of k^*. $Long$ and $side$ projections are used as a cross-check, due to symmetry in rapidity and in azimuth in the STAR experiment, no asymmetry can occur in these

two directions. Any discrepancy (except statistical fluctuations) between correlation functions for positive and negative sign for $long$ and $side$ component and any deviations in the division product ('double ratio') of two functions are interpreted as result from impurities in the analyzed sample (e.g. due to contamination with electron-positron pairs, merging effects, ..) and has to be eliminated in order to draw a physical conclusion (see section 4.3). Figure 7.9 shows correlation functions with no correction (raw data) for $k^*(sign(k_x^*))$, where x means out, $side$ and $long$; in the case of minimum bias data for $side$ and $long$ components. Both of correlation functions are similar and their 'double ratios' are flat, however for out projection small deviation from the unity is observed in the division product. The studies of such effect are shown in the following parts. Figure 7.10 demonstrates proton - anti-proton correlation functions for three centrality

Table 7.6: Source sizes $[fm]$ for proton - anti-proton combinations for different centralities (purity and resolution smearing corrections applied) for $\sqrt{s_{NN}} = 200$ GeV; reported errors are respectively, statistical and systematic (due to purity and resolution smearing corrections)

	$R^{\sigma}_{out}\ [fm]$	R^{mean}_{out}
$peripheral$	$3.39^{+0.13+0.05+0.02}_{-0.13-0.05-0.02}$	$-0.40^{+0.13+0.07+0.02}_{-0.13-0.07-0.02}$
$mid-central$	$3.78^{+0.13+0.05+0.02}_{-0.13-0.04-0.02}$	$-0.20^{+0.13+0.07+0.02}_{-0.13-0.07-0.02}$
$central$	$3.97^{+0.12-0.04-0.02}_{-0.12-0.03-0.01}$	$-0.70^{+0.12+0.08+0.02}_{-0.12-0.06-0.02}$

Table 7.7: Source sizes $[fm]$ for proton - anti-proton combinations for different centralities (purity, resolution smearing and residual correlations corrections) for $\sqrt{s_{NN}} = 200$ GeV; reported errors are respectively, statistical and systematic (due to purity, resolution smearing and RCs corrections)

	$R^{\sigma}_{out}\ [fm]$	R^{mean}_{out}
$peripheral$	$2.83^{+0.13+0.05+0.02+0.09}_{-0.13-0.05-0.02-0.06}$	$-0.70^{+0.13+0.07+0.02+0.09}_{-0.13-0.07-0.02-0.09}$
$mid-central$	$3.39^{+0.13+0.05+0.02+0.04}_{-0.13-0.04-0.02-0.06}$	$-0.10^{+0.13+0.07+0.02+0.11}_{-0.13-0.07-0.02-0.11}$
$central$	$3.75^{+0.12+0.04+0.02+0.04}_{-0.12-0.03-0.01-0.06}$	$-0.50^{+0.12+0.08+0.02+0.09}_{-0.12-0.06-0.02-0.09}$

bins for the out projection of the k^* vector before the RC correction and Figure 7.11 exhibits correlation functions after applying RC corrections. Fitted source sizes with their statistical and systematic uncertainties (estimated identically as before), for the case before applying RCs corrections are are stored in Table 7.6. R^{σ}_{out} numbers can be translated into source size. They vary from the source sizes from Table 7.2, as different parametrizations were assumed during these two calculations. In order to estimate just the source size (see Sections 7.1 and 7.2), a simple Gaussian source profile is assumed with no time and space differences in emission processes between both particles (this is a very good reference to compare directly all three types of proton and anti-proton combinations). In the case of possible asymmetry studies, such a delay or

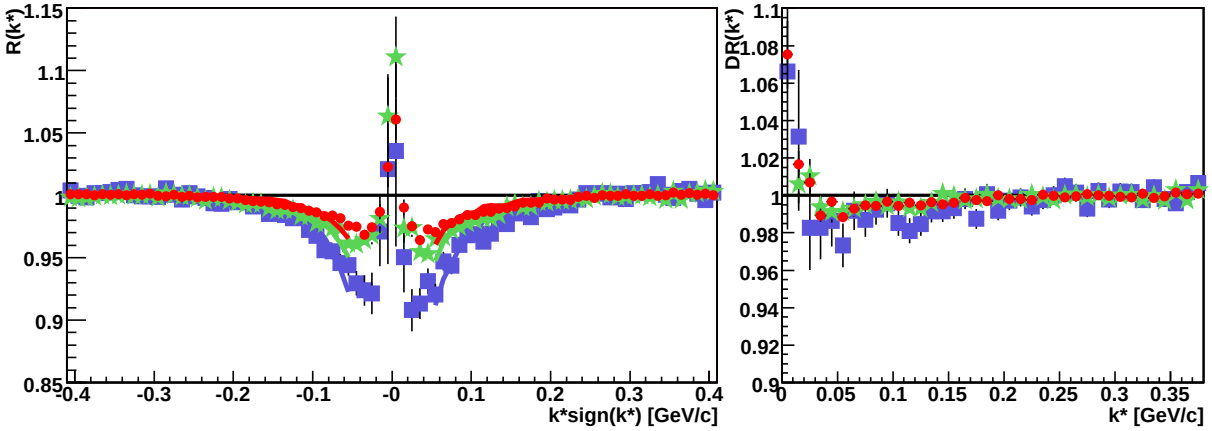

Figure 7.10: Results of proton - anti-proton femtoscopy with purity and resolution smearing corrections for three centrality bins: central (red), mid-central (green), peripheral data (blue) for out projection of k^*.

a spatial difference is calculated, so it might lead to small differences of source sizes between two calculation procedures. On the other hand, if such discrepancies occur they might indicate that assuming no space and/or time differences in emission between protons and anti-protons is an approximation. (However, as possible detected asymmetry is not as significant as in cases of systems with particles of non-equal masses, such approximation of no asymmetry does not disqualify results from Sections 7.1 and 7.2).

The parameter R_{out}^{mean} corresponds to the quantitative asymmetry in emission between non-identical particle species. The same, negative here, sign of R_{out}^{σ} values indicates a similar tendency for all centrality bins. Variations of such parameters for different centrality bins are not monotonic. Table 7.7 present results of fits after applying RC corrections. As the correction is applied identically to the correlation functions of both k_{out}^* signs, it should not affect the mean value of R_{out}. Observed discrepancies are interpreted as systematic uncertainties due to applying the RC correction. Again, for each centrality, the deviation of R_{out}^{mean} value from zero and of 'double ratio' from unity is observed; it is clear in the case of the most central collisions (the numbers vary after applying the correction, however the signal is strong enough to conclude), in the case of semi-peripheral collisions. It is almost impossible to draw a conclusion about centrality dependence of emission asymmetry, where for the most peripheral and central data the signal of asymmetry is strong and for mid-central data almost disappears. In other words, the data indicates no centrality dependence on such asymmetry.

According to the (I) convention described in Chapter 5.10, such studies suggest that the average point of proton emission is closer to the center of the system than in the case of anti-protons. On

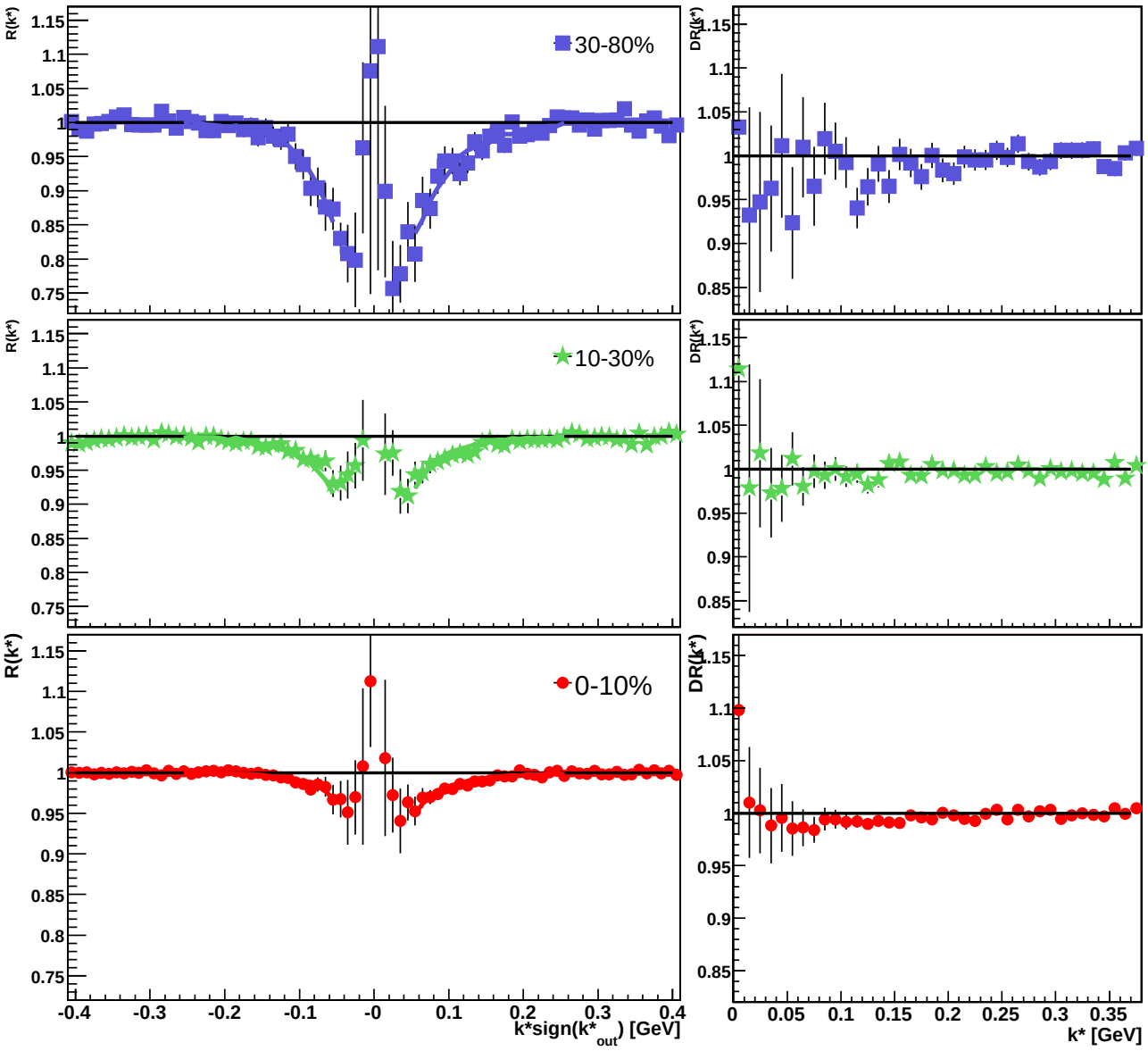

Figure 7.11: Results of proton - anti-proton femtoscopy with all corrections applied.

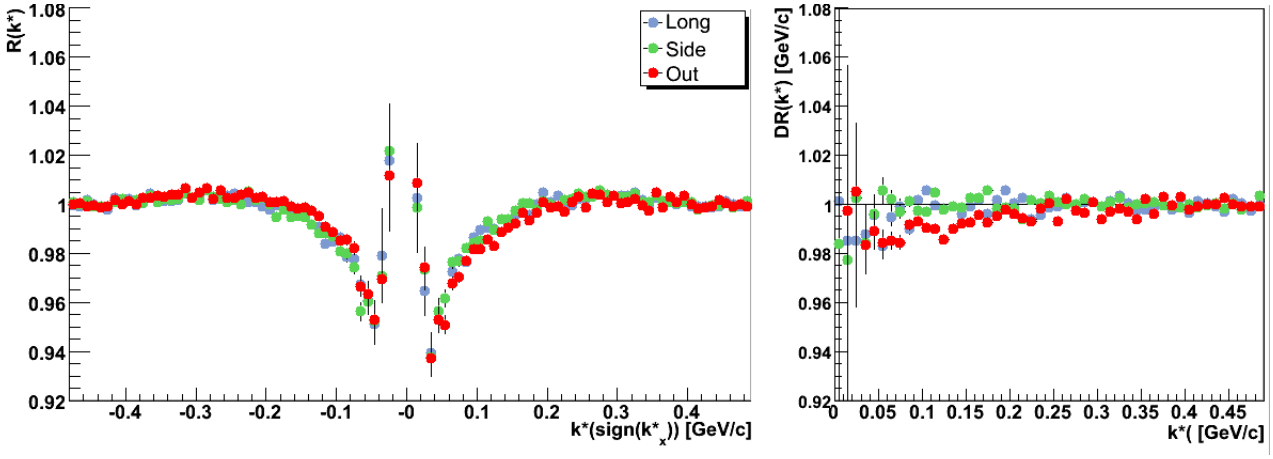

Figure 7.12: Results of proton femtoscopy with all corrections applied for minimum-bias collisions for three different projections of k^*.

the other hand, protons are also considered as emitted later (on average) than anti-protons.
In such case when proton is faster (correlation function for $k^*_{out} > 0$) it catches up to the slower anti-proton, so they stay close to each other longer, their effective interaction time is longer, hence the correlation effect is stronger. When proton is slower (correlation function for $k^*_{out} < 0$), the faster anti-proton flies away fast, the time they spend close to each other is short, hence the effective interaction time is short and the correlation effect is smaller.
Figure 7.12 presents results fully corrected (RC correction included as well) for minimum-bias collisions with the respect to the sign of each component: out, $side$ and $long$. Deviation from unity for the out component is clearly visible, while 'double ratio' for two other ones remains almost flat. In order to try to check whether the asymmetry (and in which centrality) occurs, the new technique of spherical decomposition is studied.

7.3.2 Spherical Harmonics decomposition

Three-dimensional correlation function can be decomposed into three components [95, 96], as shown in Figure 7.13. The spherical coordinates θ, ϕ, Q are related to the Cartesian coordinates as:

$$Q_o = Qsin\theta cos\phi \tag{7.1}$$

$$Q_S = Qsin\theta sin\phi \tag{7.2}$$

$$Q_L = Qcos\theta \tag{7.3}$$

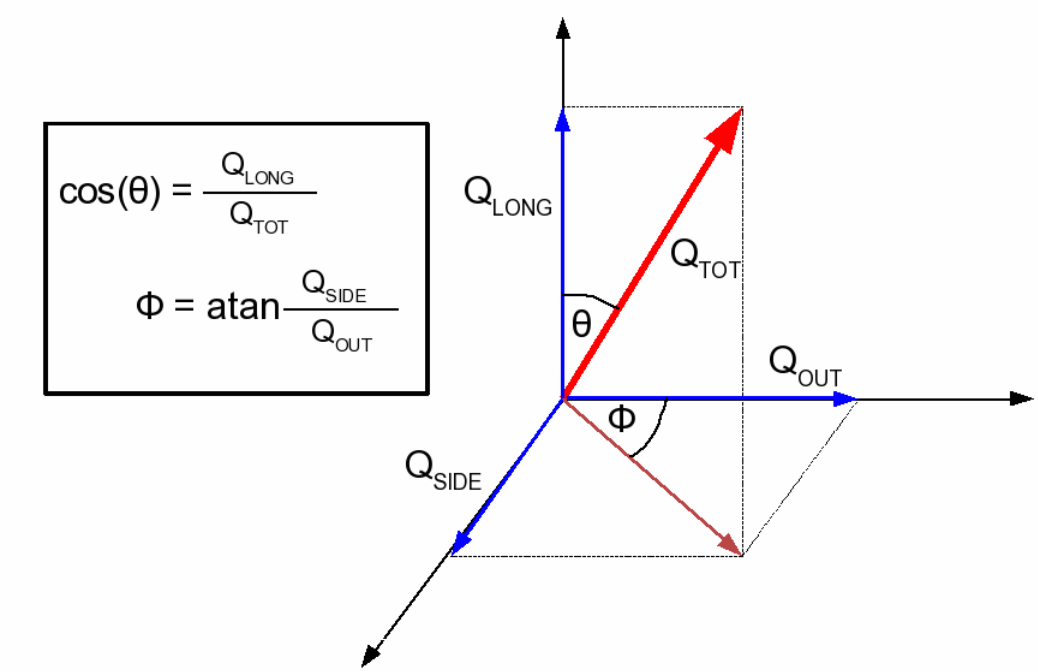

Figure 7.13: Decomposition of the $Q = 2k^*$ vector [97].

The correlation function can be binned in Q, θ and ϕ and represented via its spherical harmonic coefficients, which depend on Q:

$$A_{lm}(Q) = \sum_{i}^{all-bins} C(Q, \theta_i, \phi_i) Y_{lm}(\theta_i, \phi_i) F_{lm}(\theta_i, \triangle_{cos\theta}, \triangle_{\phi}) \tag{7.4}$$

where $F_{l,m}$ represents a numerical factor correcting for finite bin sizes $\triangle_{cos\theta} = \frac{2}{N_{cos\theta}}$ and $\triangle_{\phi} = \frac{2\pi}{N_{\phi}}$; it turns out not to depend on θ_i. $Y_{lm}(\theta_i, \phi_i)$ are the spherical harmonics functions (Legendre functions), $C(Q, \theta_i, \phi_i)$ represent bins of the correlation function.

In proton femtoscopy measured at the STAR experiment, due to statistical limitations and limited acceptance it is not possible to decompose two - proton, two - anti-proton and proton - anti-proton correlation functions perfectly- there are many cases where no pair can be characterized by a given $C(Q, \theta_i, \phi_i)$).

While decomposing spherical harmonics, one obtains many A_{lm} coefficients. All coefficients for odd l should vanish in the case of identical particle combinations. For non-identical particles, the coefficients with odd l lead to the asymmetry in the emission process (coefficient A_{11}). A_{00} has a structure of the one-dimensional correlation function. All imaginary parts should vanish as well. $A_{20} > 0$ occurs when $R_T > R_L$ ($R_T = \sqrt{R_O^2 + R_S^2}$ and R_L are the transverse and longitudinal

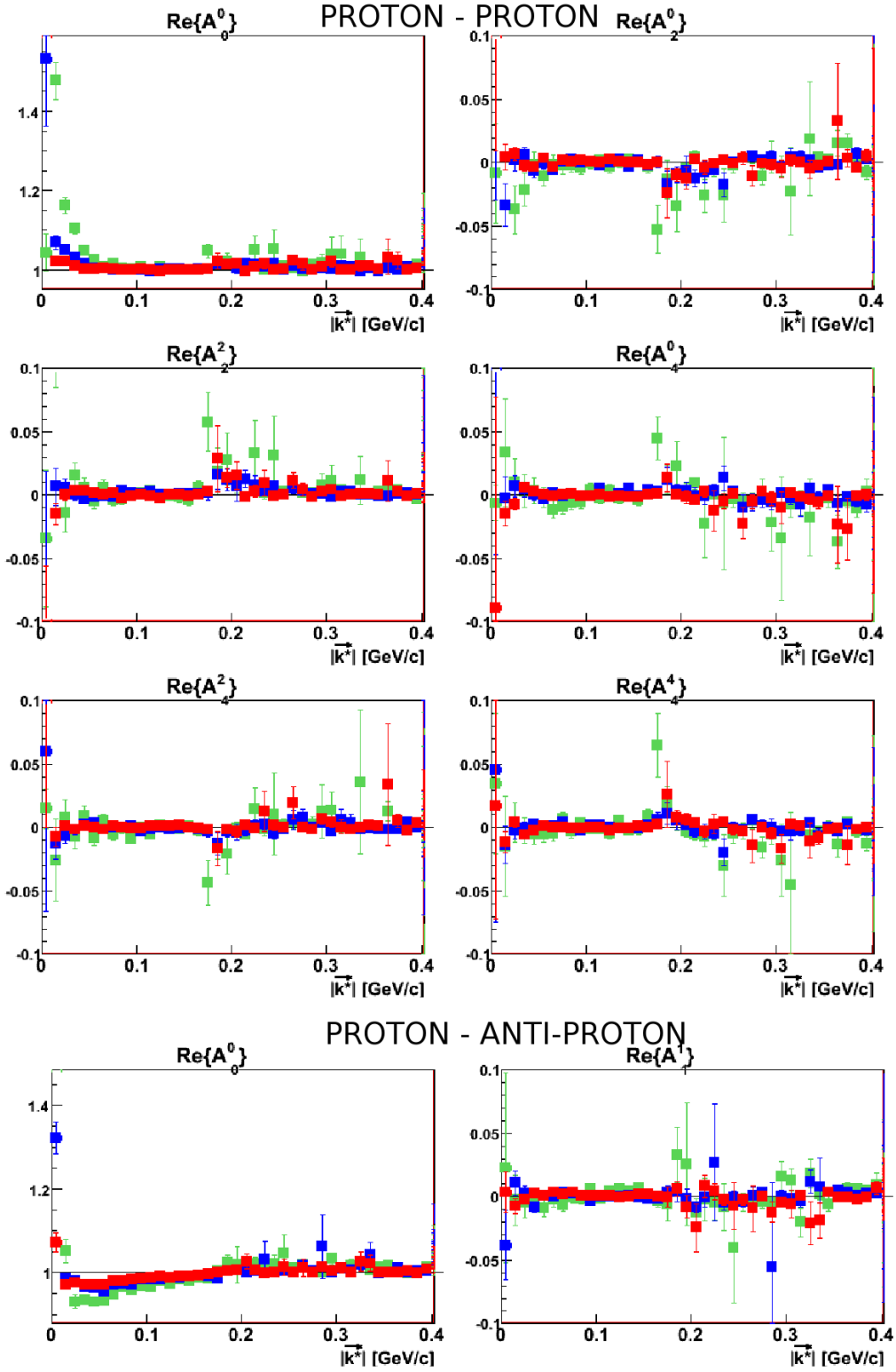

Figure 7.14: Decomposition of three-dimensional proton - proton correlation function (first three rows) and their A_{lm} components: red points show central data, blue marker exhibits mid-central sample and green points are for peripheral data. The last row presents proton - anti-proton results.

components of radii of source respectively), $A_{20} < 0$ otherwise. $A_{22} > 0$ tells if $R_o < R_s$, $A_{22} < 0$ in the opposite scenario. As shown in Figure 7.14 (proton - proton), the source seems to be spherical. In the case on non-identical proton - anti-proton systems (Figure 7.14, bottom part), the most interesting coefficient is $A_{11,}$ which especially for central collisions seems to deviate from zero value. For other centralities, statistical limitations occurs. For each system, centrality dependence is reflected in A_{00} coefficients, which claims propriety of decomposition technique. It is clear that for proton femtoscopy it is very difficult to conclude about source properties basing on spherical harmonics decomposition, due to statistical limitations. However, the results on non-identical particle correlation technique have not been discarded.

Application of the RC correction would not change conclusions as the correction would be identically done on each direction (the same scaling factor within the same k^*). On the other hand, the RC correction would provide an additional source of uncertainty, so drawing any conclusions would be much more difficult than in the case on non-corrected data.

Chapter 8

Discussion

8.1 Importance of residual correlation corrections

Fully corrected correlation functions for $Au + Au$ collisions at $\sqrt{s_{NN}} = 200$ GeV for different centrality bins are shown in Figure 7.7. For lower collision energy- $\sqrt{s_{NN}} = 62$ GeV such corrected correlations (proton - proton and proton - anti-proton systems) are presented in Figure 7.8. For all systems the correlation effect decreases with increasing centrality. The extracted Gaussian radii with their statistical and systematic uncertainties are given in Section 7.2 in the Tables 7.4 and 7.5, for $\sqrt{s_{NN}} = 200$ GeV and $\sqrt{s_{NN}} = 62$ GeV respectively. The approximate consistence for different pair combinations, for all energies and centrality selections, gives confidence in the stability of our results. Comparing results for two collision energies, they are consistent within error-bars, however in the most systems and centralities, the radii deduced for lower collision energy are slightly lower, which is interpreted as a consequence of lower particle multiplicities registered in such collisions (more in Section 8.2). Results not corrected for RCs are shown in Section 7.1. Radii for identical particles vary from non-identical ones as additional correlations measured with $p - p$, $\overline{p} - \overline{p}$ and $p - \overline{p}$ were not taken into account. Neglecting the presence of residual sources of correlations may significantly falsify physical conclusions, thus correct source sizes and their agreement for identical and non-identical protons and anti-protons combinations would not be possible to deduce if the RC correction had not been applied.

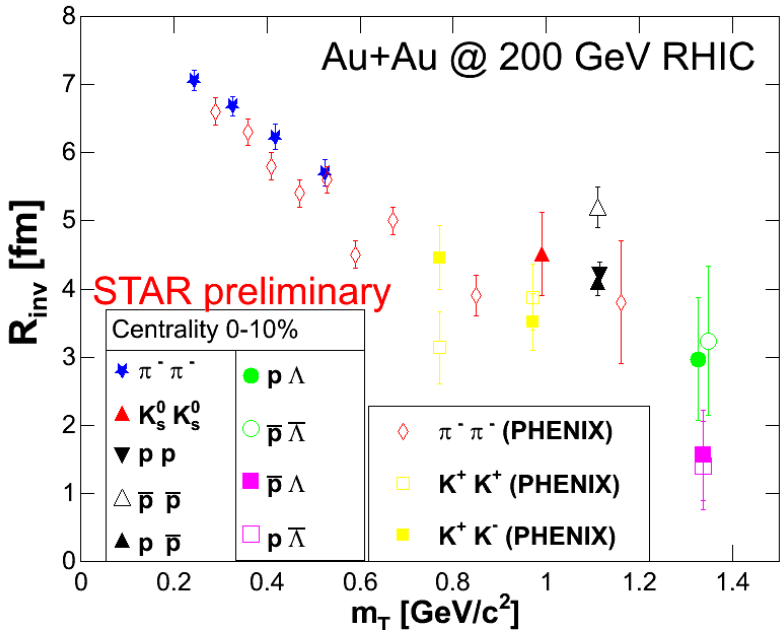

Figure 8.1: R_{inv} values extracted from hadron femtoscopy at $\sqrt{s_{NN}} = 200$ GeV for 10% of central collisions [68].

8.2 Transverse mass dependencies

Extracted radii for central collisions (up to the 10% of the total hadronic cross-section of the collision) confirm the hydrodynamical description of source evolution, where for given temperature and phase-space, heavier particle species are expected to be emitted from smaller areas. The system's collective expansion produces such differences in the length of homogeneity (the size of area emitting particles of a given type) due to thermal motion. Massive particles (e.g. protons) are on average more pushed towards the edge of system than lighter ones (e.g. pions). The explanation of such behavior is described in Section 4.12. In Figure 8.1, the present results are confronted with the "universal" m_T systematics established with other particle species [68]. Proton femtoscopic results complement those for mesons and other, heavier baryon combinations. Black symbols refer to $p-p$, $\overline{p}-\overline{p}$ and $p-\overline{p}$. The radii extracted from $\overline{p}-\overline{p}$ is about 1 fm bigger than the ones for $p-p$ and $p-\overline{p}$. As it is described in Section 4.9 (see Figure 4.4), it is very difficult to distinguish between correlation functions describing source size of 4 and 5 fm. Their shapes and magnitudes of correlations are almost identical, thus due to e.g. statistical and/or systematic uncertainties any difference between them might be indiscernible. As the outcomes of strange baryon femtoscopy ($p-\Lambda$, $\overline{p}-\overline{\Lambda}$, $\overline{p}-\Lambda$, $p-\overline{\Lambda}$) were not corrected for the effects of

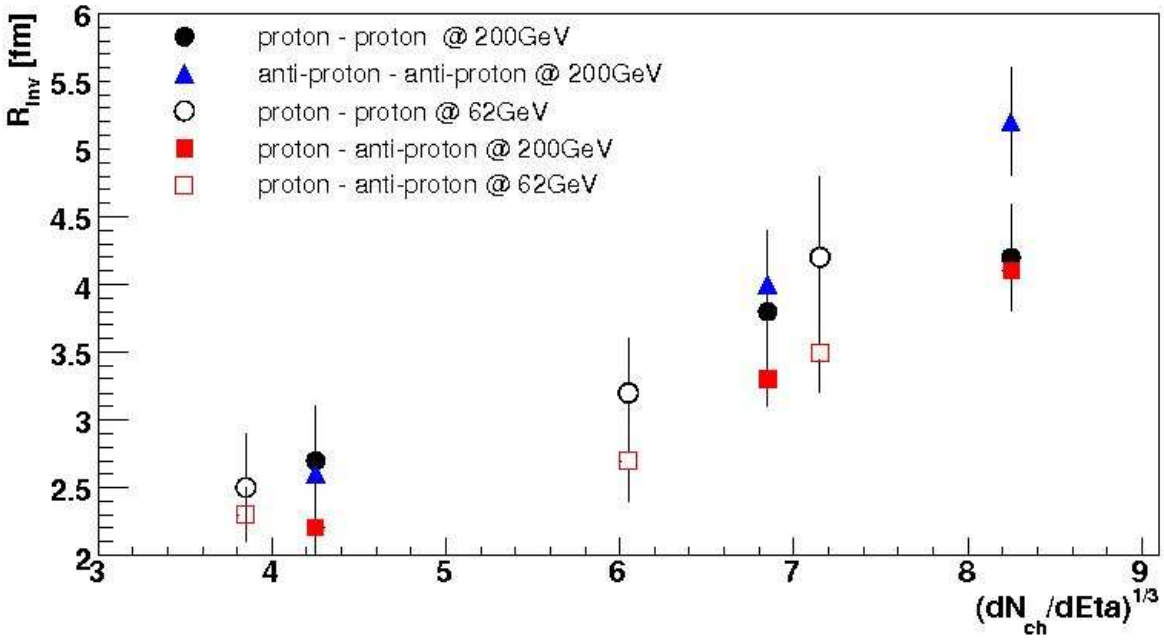

Figure 8.2: $(dN_{ch}/d\eta)^{1/3}$ scaling of source sizes from proton femtoscopy at $\sqrt{s_{NN}} = 62$ GeV and $\sqrt{s_{NN}} = 200$ GeV

RCs, the results of correlation for $\overline{p} - \Lambda$ and $p - \overline{\Lambda}$ are expected to be affected stronger than two other ones by RCs, thus observables indicated by green points are more reliable. In general, the results of proton femtoscopy agree with the other STAR measurement more.

8.3 Multiplicity dependencies

Another experimental result is the nature of the $(dN_{ch}/d\eta)^{1/3}$ scaling (N_{ch}- number of charge particles) of HBT radii, seen in pion interferometry [68]. It is observed also in proton femtoscopy. Studying such relations is motivated by relations of $(dN_{ch}/d\eta)^{1/3}$ dependencies with the final state geometry through particle density at freeze-out. Figure 8.2 presents such scaling for R_{inv} source sizes extracted from $p - p$, $\overline{p} - \overline{p}$ and $p - \overline{p}$ at $\sqrt{s_{NN}} = 62$ GeV and $\sqrt{s_{NN}} = 200$ GeV energies. Errors shown are both statistical and systematic. Comparing to pion measurements, proton ones are smaller by the order of ~ 1 fm. Discrepancies between three systems are shown, however results agree with error-bars. Source sizes monotonically increase with $(dN_{ch}/d\eta)^{1/3}$. Radii fluctuate due to statistical limitations. Such figures for identical pion observables present a linear dependence of $(dN_{ch}/d\eta)^{1/3}$ (multiplicity, which is distinguished via collision central-

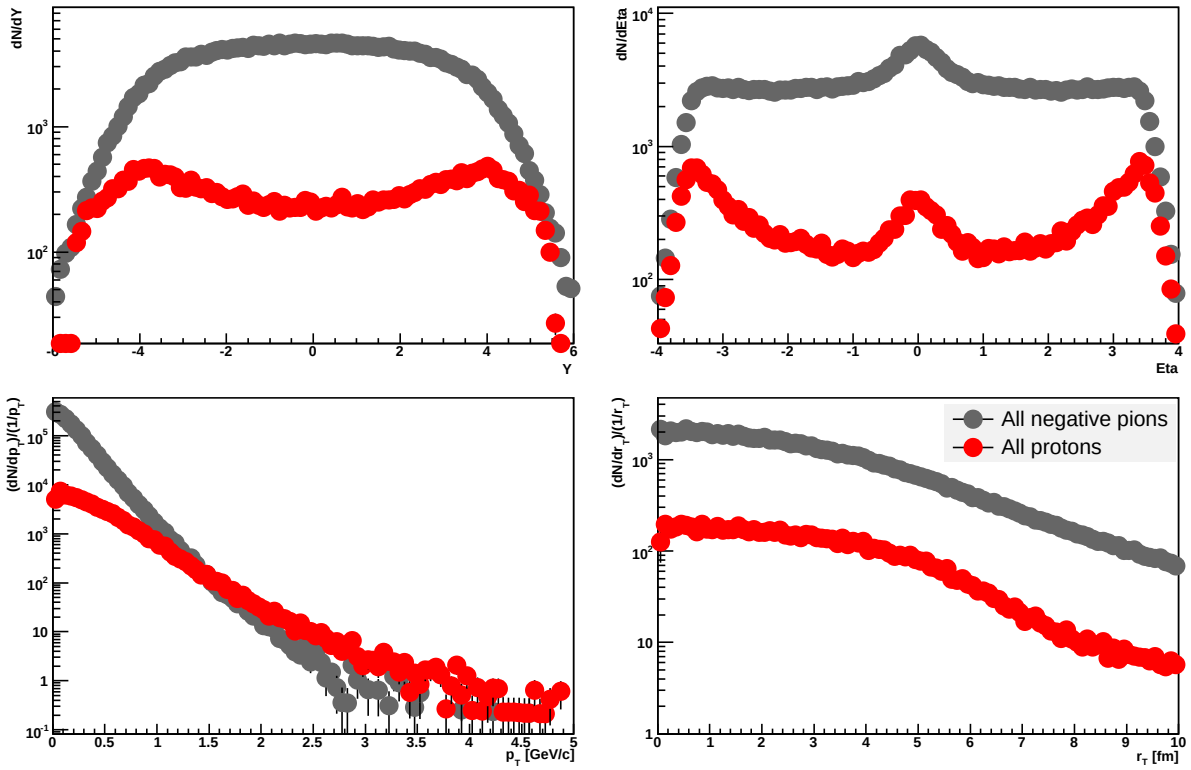

Figure 8.3: Spectra for all negative pions and protons emitted in UrQMD sample. Left-hand side of the top panel shows the rapidity distributions, right-hand side of the top panel reflects pseudorapidity distributions, the left-hand side of the bottom panel illustrates spectrum of transverse momentum and right-hand side of the bottom panel exposes transverse position distributions.

ity). In the case of pions the R_{out}, R_{side} and R_{long} dependencies on $(dN_{ch}/d\eta)^{1/3}$ are checked. These three components follow a linear dependence,so does the product of the freeze-out volume ($V_f \simeq R_{out}R_{side}R_{long} \simeq R^2_{side}R_{long}$). Such studies for pions are performed as the contribution of pions to the particle production significantly rises with increasing beam energy and for RHIC conditions pions dominate the data sample. Thus, the system volume can be approximated by the pions volume. Even if the contribution of protons is not as significant as in the case of pions, it is still interesting to see how their source sizes scale with multiplicity. Protons enable one to see the scaling tendency as well, however as they reflect some part of the phase space only, one cannot expect that all proton sources would scale as linearly as pions do.

8.4 Comparison with model predictions

This subsection presents the results of simulations with two theoretical models: UrQMD and EPOS. First, simple one-particle distributions are discussed: rapidity, pseudorapidity, transverse momentum and freeze-out coordinates. Then, two-particle separation distributions are shown (see Appendix 3 for details). Many systems composed of various particle combinations are checked and compared to each other, but only distributions of protons and anti-protons are shown here; non-identical combinations are also discussed (pions and kaons). The possibility to detect asymmetry in the emission process is checked on experimentally known cases (like and un-like signs combinations of pions and kaons). These studies are treated as a base for deducing possible asymmetry in emission between protons and their antiparticles.

8.4.1 UrQMD

Single-particle distributions

Single-particle distributions allow one to take a look into particle production mechanisms. The UrQMD model was discussed in Section 3.1. Data has been gathered for $Au + Au$ collisions at $\sqrt{s_{NN}} = 200$ GeV. In order to see how the production mechanisms look like, the following distributions are calculated: rapidity, pseudorapidity, transverse momentum: $p_T = \sqrt{p_x^2 + p_y^2}$ and transverse freeze-out position: $r_T = \sqrt{r_x^2 + r_y^2}$. Seen in the Figure 8.3 increased numbers of protons at higher rapidity and pseudorapidity intervals are a result of taking nuclear remnants into account. Higher multiplicities of pions are generated. Due to higher proton mass, more protons with higher transverse momentum are observed as compared to pions. The last plot of Figure 8.3 presents the distribution of r_T. Figure 8.4 shows ratios of particle productions versus rapidity. The ratio of negative to positive pions remains flat through of the rapidity interval, showing that similar amount of negative and positive pions are produced (the production of π^- mesons is slightly increased in higher rapidity ranges). The production of kaons is not identical for positive and negative particle species. In mid-rapidity interval (up to $|y| = 2$) production of K^+ and K^- hadrons is similar; for higher rapidity values, production of positive kaons dominates. For protons, even for mid-rapidity ($|y| < 1$), twice as many protons are produced as their anti-particles. For the highest of ranges of rapidities shown here, the production of anti-protons is highly decreased. Comparing to RHIC measurements (BRAHMS [94]), pion production in UrQMD is similar to measured in the experiment and for mid-peripheral rapidities kaon production looks comparable as well, however for the highest rapidities in UrQMD production of

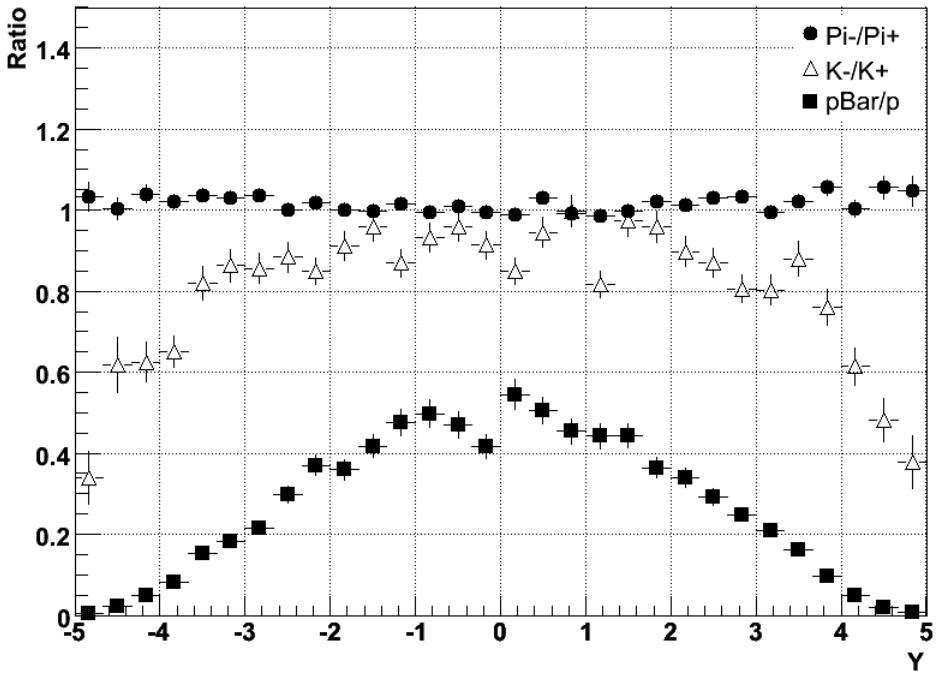

Figure 8.4: Rapidity distributions of ratios of produced particles: π^-/π^+ (black circles), K^-/K^+ (open triangles), $\overline{p}/p$ (closed squares).

negative kaons is decreased. In terms of protons, the ratio $\frac{\overline{p}}{p}$ deviates from the BRAHMS measurements. In experiment, the ratio of anti-protons with respect to protons is not equal to unity indicating the contamination of protons from nuclear remnants (due to conservation of baryon number, the production of anti-protons must be equal to the number of produced protons, any excess of protons come from colliding nuclei- for mid-rapidity $\frac{\overline{p}}{p} \sim 0.8$ [94]).

Two-particle distributions

The formulas for two-particle distributions in this section are given in Appendix 2. Three windows in figures: 8.5-8.7 illustrate the freeze-out separation distribution in the CMS reference frame; the fourth shows the $time$ separation. The analysis of such distributions can provide information about emission processes of such particles. The mean values of $side$ and $long$ distributions should always remain around zero value due to symmetry reasons, while in the case of non-identical particles any possible difference in their emissions should be reflected in out and $time$ components. In other words, for identical particles, all mean values should be close to zero. The differences between distributions for all produced particles (primordial and coming from decays) and such for primordial particles only can be seen in Root Mean Square (RMS)

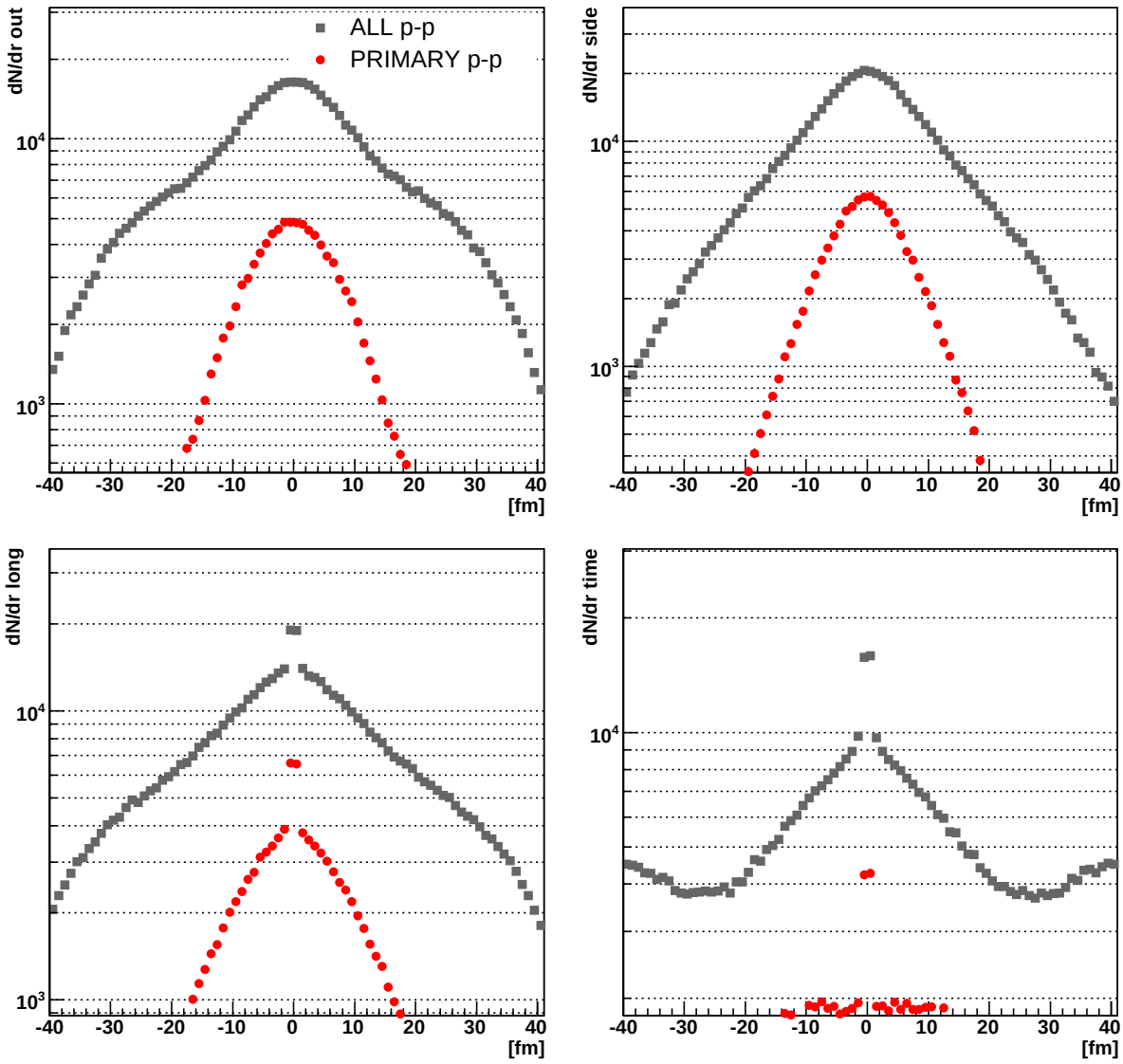

Figure 8.5: Two-proton separation distributions for all particles (gray points) and primordial only (red points) in CMS reference. Top-left panel presents separation for out component, top-right panel illustrates $side$ component separation, bottom-left panel reflects separation distribution for $long$ component and bottom-right panel exhibits time separation.

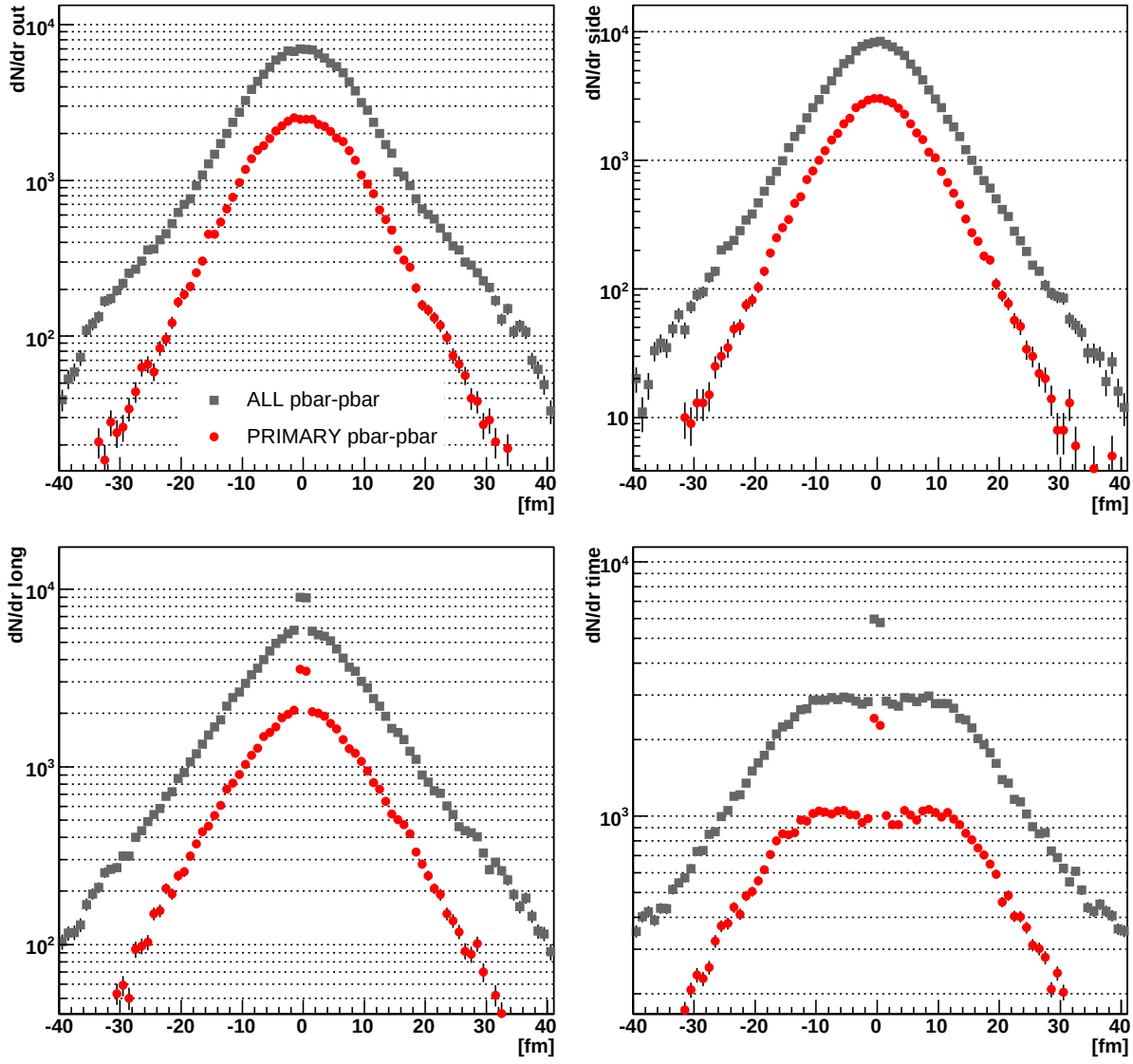

Figure 8.6: Two-anti-protons separation distributions for all particles (gray points) and primordial only (red points) in CMS reference. The figure layout is the same as in 8.5.

values, where the width of distributions can be transformed to the source size emitting particles. By primordial (or primary) proton is meant such particle, which does not come from the weak decay of Λ or Σ^+ hyperons. Primordial (or primary) anti-proton is such particle, which does not come from weak decay of $\overline{\Lambda}$ or $\overline{\Sigma^+}$. Primordial particles come from a smaller area than non-primary particles which might come from much bigger sources. Distributions of all particles are always plotted in gray and those for primordial particle species- in red. Figure 8.5 presents two-proton separation distributions (the peaks in $long$ and $time$ distribution appears as a consequence of taking into account particles lying very close to the z axis in the laboratory frame), Figure 8.6 illustrates two-anti-proton distributions; see Tables 9.10 and 9.11; comparing to two-proton distributions, the scale on the vertical axises are different) and Figure 8.7 presents proton - anti-proton distributions (as a first particle proton is denoted, as a second one- anti-proton). Especially important are those for primordial particles, where the separation distributions for out direction and $time$ remain away from zero, indicating some asymmetry in the emission process (see Table 8.1). For identical particle combinations all values remain close to zero, except the few containing remnants from nuclear matter which might contaminate the analyzed sample (see Figure 8.5 and 8.6). Each distribution does not represent Gaussian shape (which is indicated by the general shape of each distribution- they have 'non-gaussian' tails observed in the logarithmic scale, so a Gaussian can be fitted to the central parts of out and $side$ distributions only), as the model generates tails which cannot be parametrized in this way.

Correlations

As the UrQMD model gives momenta and freeze-out coordinates, it is possible to calculate correlation functions for many particle combinations as long as generated statistics enables estimation of the shape of correlation. In Figure 8.8 correlation functions for identical particles are presented: pion-pion correlation functions, taking into account both QS and Coulomb interactions for all positive pions (gray points) and for primordial particles only (red points). Obviously, the correlation function calculated for primary particles only is stronger and leads to smaller source sizes than in the other cases. The same conclusion comes from proton-proton correlations: gray points illustrate correlation of all protons and red points correspond to the primordial protons only (not taking into account the remnants of colliding nuclei). In order to increase statistics, the correlation functions for anti-proton - anti-proton are calculated as well and then their numerators and denominators respectively were added in order to obtain correlation functions. Besides identical particle combinations, the non-identical ones are considered as well. In the bottom panel of Figure 8.9, correlations for like-signs combinations of pions and kaons are shown. All

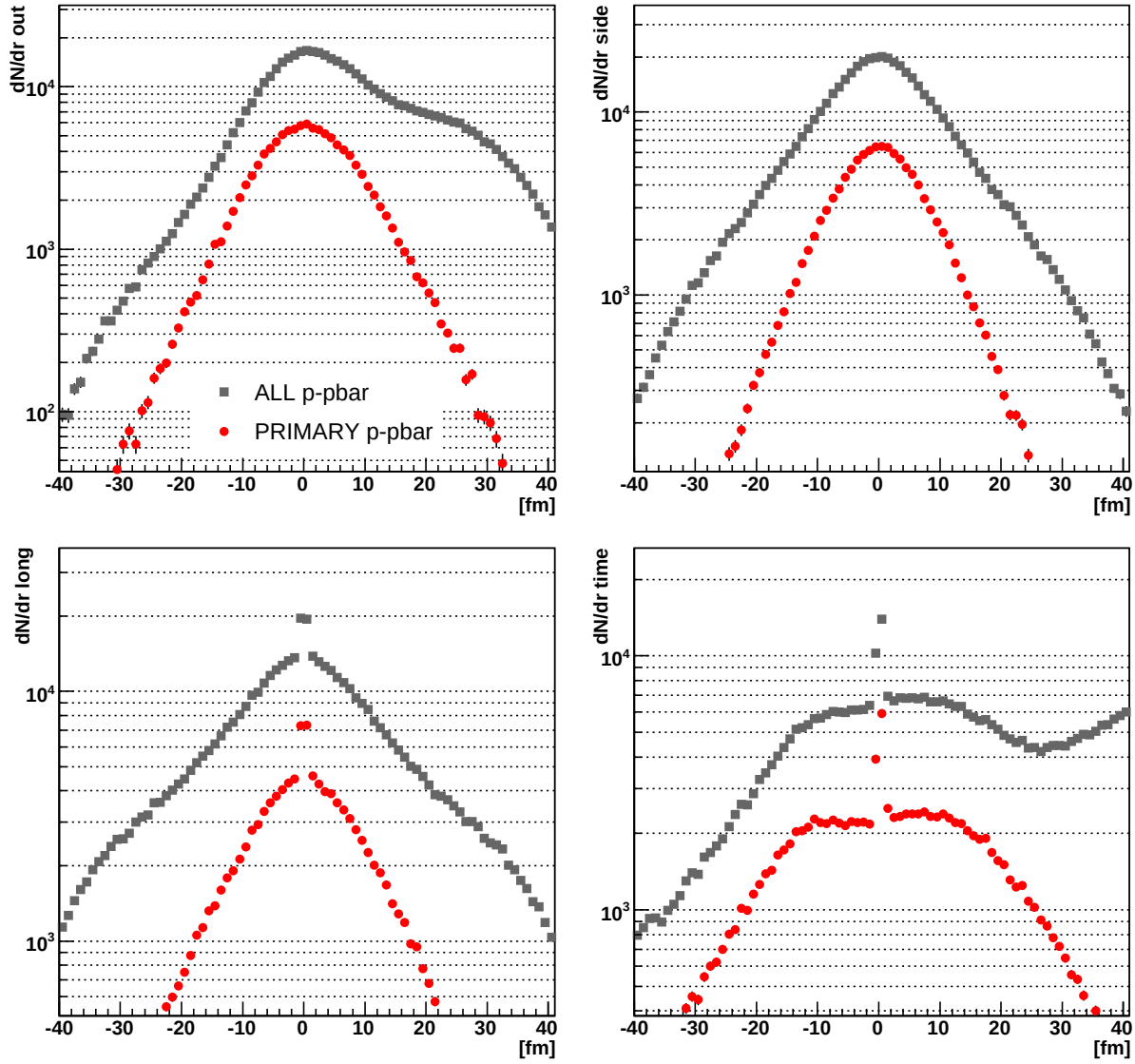

Figure 8.7: Proton-anti-proton separation distributions for all particles (gray points) and primordial only (red points) in CMS reference. The figure layout is the same as in 8.5.

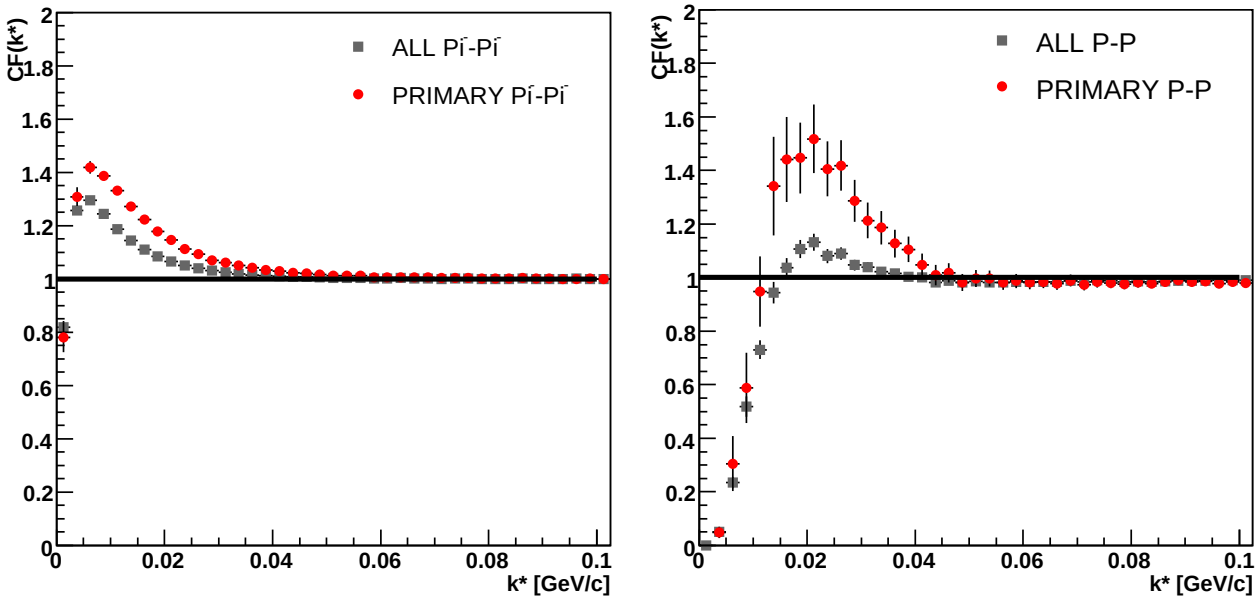

Figure 8.8: Identical two-particle correlations (two-pion and two-proton) from UrQMD.

pairs were divided into two groups (following the same rules of the STAR Collaboration, see Section 5.12). Dividing the correlation for positive sign of k^*_{out} by the one for negative sign, it is possible to detect the differences in the emission, depending on the deviations of 'double ratio' from unity (see the right panel of Figure 8.10 for like-sign combination). The top panel of Figure 8.9 and the left panel of Figure 8.10 present results for unlike-signs. The 'double ratio' for the same signs of particles goes below unity and for opposite signs it rises above unity exactly as observed at STAR, indicating than in the model pions are in average emitted from bigger area (or earlier) than kaons (according to the flow prediction). These correlations are obtained for minimum-bias collisions, where impact parameters indicating the collision centrality is in the wide range $b \in [0; 15]$ fm; therefore the magnitude of detected asymmetry cannot be compared directly to the STAR data.

Figure 8.11 shows proton - anti-proton correlation functions. The correlation effect clearly indicates annihilation of protons and their anti-particles. The first plot in Figure 8.11 shows correlation function with respect to the sign of k^*_{out}, the last plot illustrates one dimensional correlation function; for small k^* values (close to 0 GeV/c), an attraction due to Coulomb forces can be noticed, then an annihilation channel due to strong interactions is present. Two of the 'double ratios' indicate small deviation from the zero value (the tendency is illustrated below unity), which indicates that on average stronger correlation occurs for $k^*_{out} > 0$. These model predictions are consistent with experimental results. The same convection (described in Section

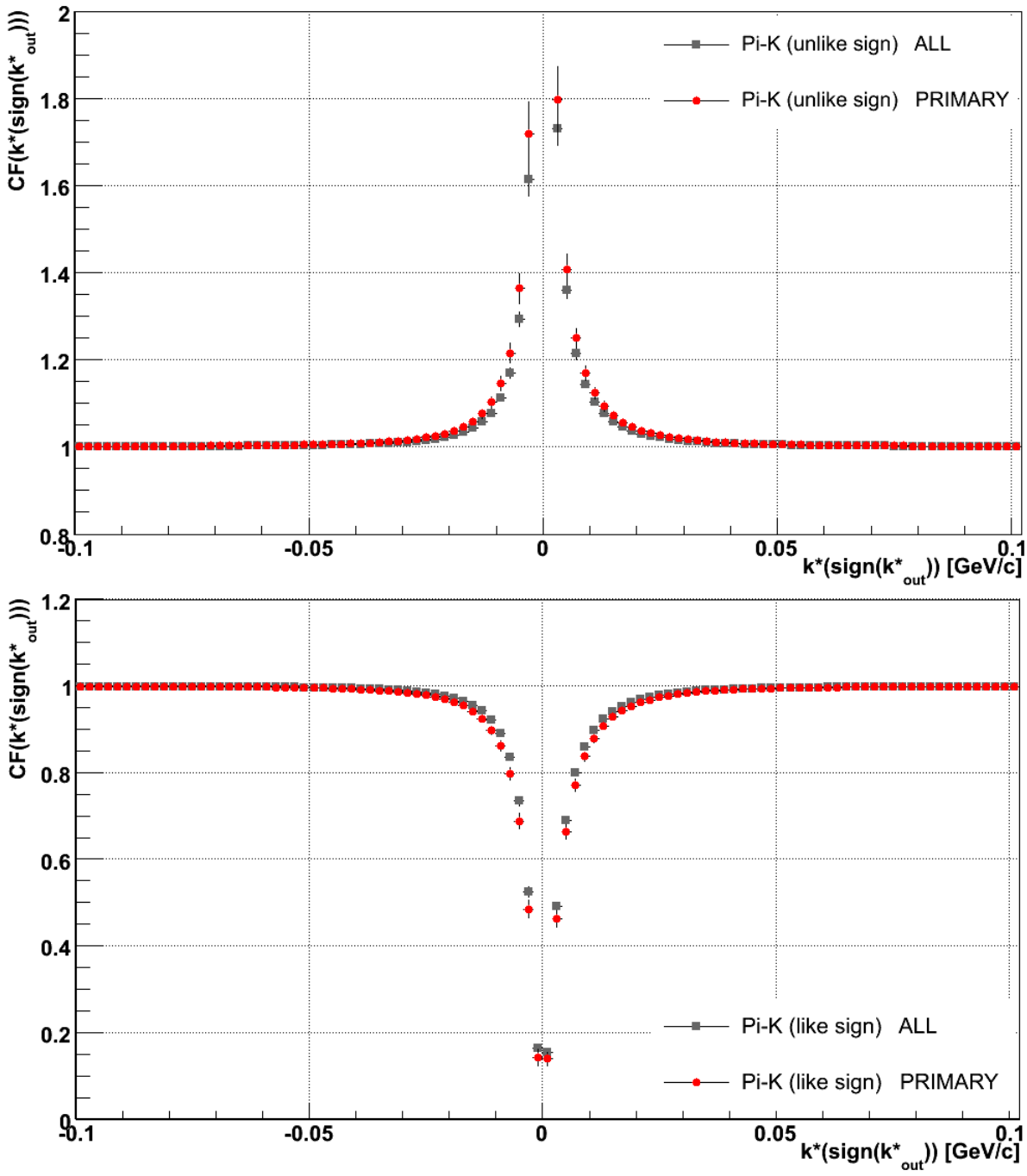

Figure 8.9: Pion-kaon (like signs in bottom panel and un-like signs at top panel) correlation function. Grey marker shows correlation functions calculated for all particles, red marker indicates correlation functions for primordial particles only

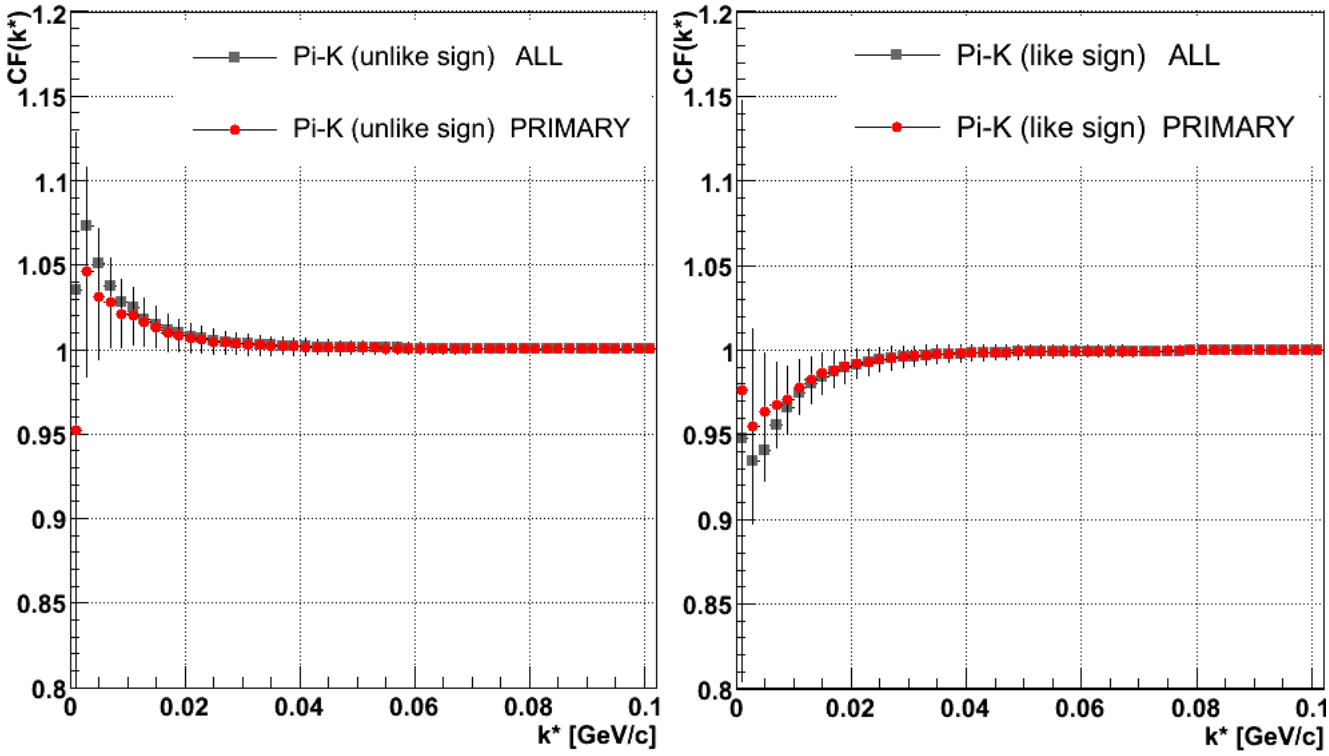

Figure 8.10: Pion-kaon (like sign in right panel and un-like signs at left panel) double ratios. Grey marker shows 'double ratios' calculated for all particles, red marker indicates 'double ratios' for primordial particles only

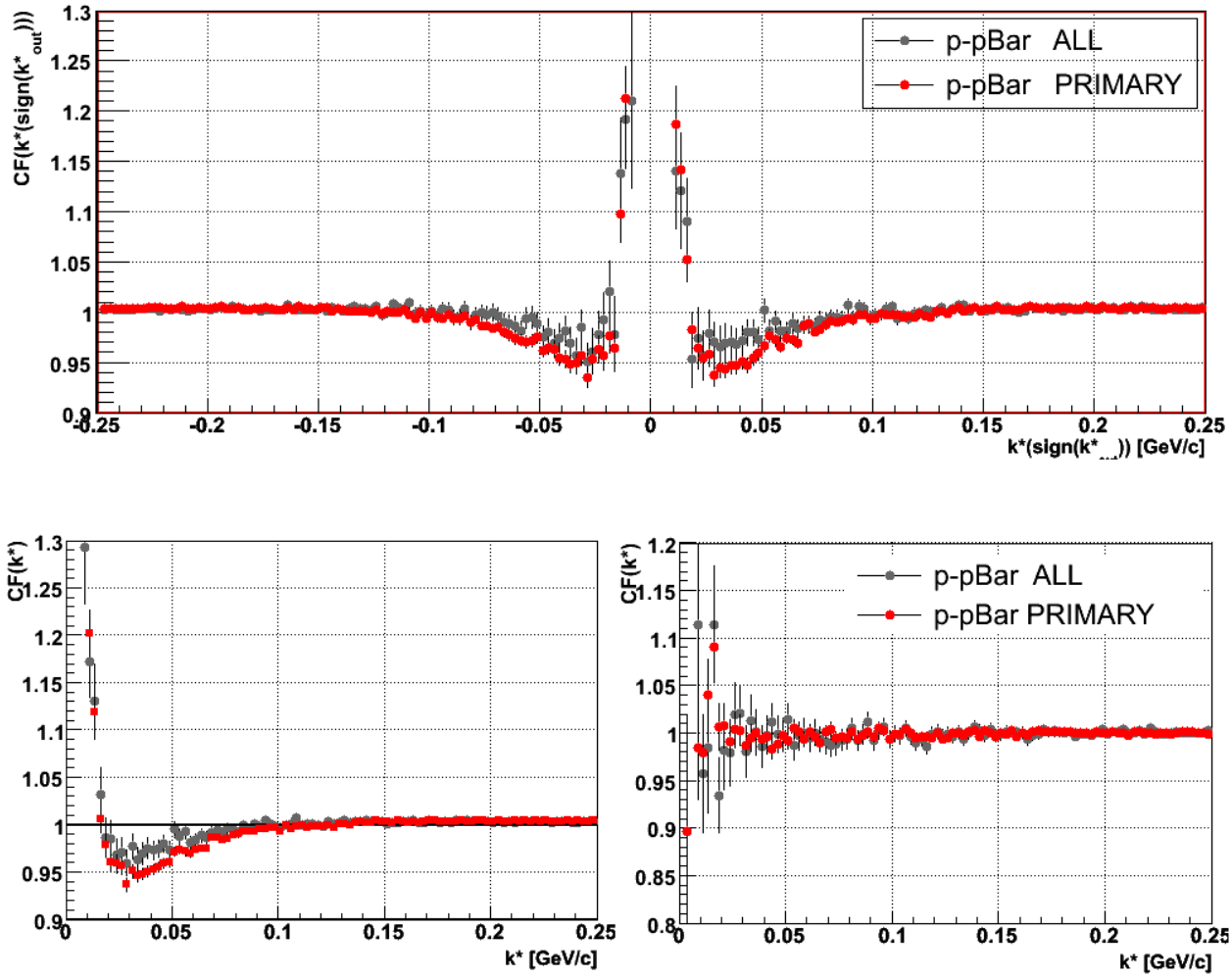

Figure 8.11: Proton - anti-proton correlation functions. Gray points show all particles, red squares only primordial ones. Top panel presents correlation function for positive and negative sign of $k*_{out}$, bottom-left panel shows their 'double ratio', the bottom-right panel presents one-dimensional correlation function.

4.10) as in data analysis is used, so the fact that 'double ratio' is below unity for smaller $k*$ values indicate that in model in average protons are emitted from bigger area and/or earlier than anti-protons.

Asymmetry discussion

As it was mentioned in the previous sections, the asymmetry in emission mechanisms can be detected in non-identical particle combinations. Figure 8.12 shows two-particle separation distributions in the CMS reference, same for primordial protons and anti-protons only, for 3 classes of centrality: central collisions (up to 10% of the total hadronic cross section of the collision), (10-30)% and (30-80)%. The plots and corresponding tables (Table 8.1 for Figure 8.12 and Table 9.12 for Figure 8.7) show that the deviation of the mean value of R_{out} distributions from zero indicates possible spatial asymmetry of emission between protons and anti-protons. There is also an asymmetry in time indicated by time distributions. All these deviations monotonically rise from central to peripheral collisions: for central collisions the deviation of R_{out} separation distribution from zero value is around 0.7 fm, for mid-central- ~ 0.9 fm for peripheral data- ~ 1.2 fm. Such behavior indicates influence of final-state rescattering; non-central collisions seem to be affected more, thus stronger effect in two-particle separation distributions. The mean values and RMS are stored in Table 8.1 (together with results for the EPOS model). Tables 9.8 and 9.9 present the values of separation distributions from pion-kaon distributions (together with results for EPOS).

8.4.2 EPOS

Single-particle distributions

The same single-particle distributions are presented for the EPOS model. Data gathered for $Au+Au$ collisions at $\sqrt{s_{NN}} = 200$ GeV, same as for UrQMD sample, are shown in Section 8.4.1. Figure 8.13 shows rapidity, pseudorapidity, transverse momentum and position spectra. Here, mid-rapidity and mid-pseudorapidity (up to $|y| = 2$ and $|\eta| = 2$) pion and proton distributions are constant, for the other ranges of rapidity and pseudorapidity ($|y| > 2$ and $|\eta| > 2$) they are naturally decreasing. Concerning momentum spectra, as pions have smaller mass, they populate mainly lower momentum intervals. The last plot in Figure 8.13 indicates r_T. Figure 8.14 shows rapidity distributions of particle ratios. For mid-rapidity ($|y| < 2$), ratios: $\frac{\pi^-}{\pi^+}$ and $\frac{K^-}{K^+}$ are flat.

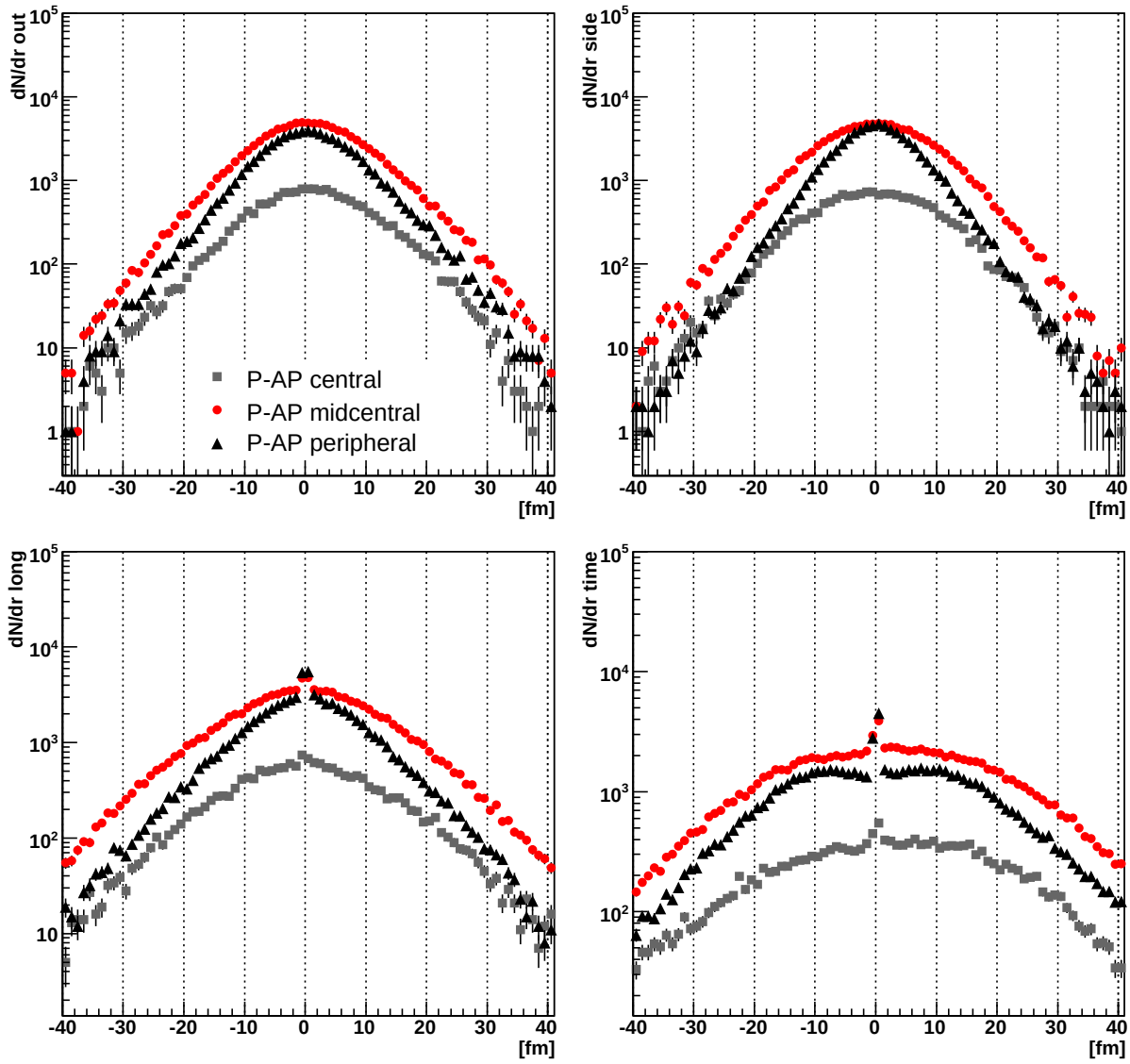

Figure 8.12: Proton -anti-proton (centrality dependencies) separation distributions. Gray points are for central collisions: (0-10)% of the total hadron cross section of the collision, red points are for mid-central collisions (10-30)% and the black points are for peripheral data (30-80)%. The figure layout is the same as in 8.5.

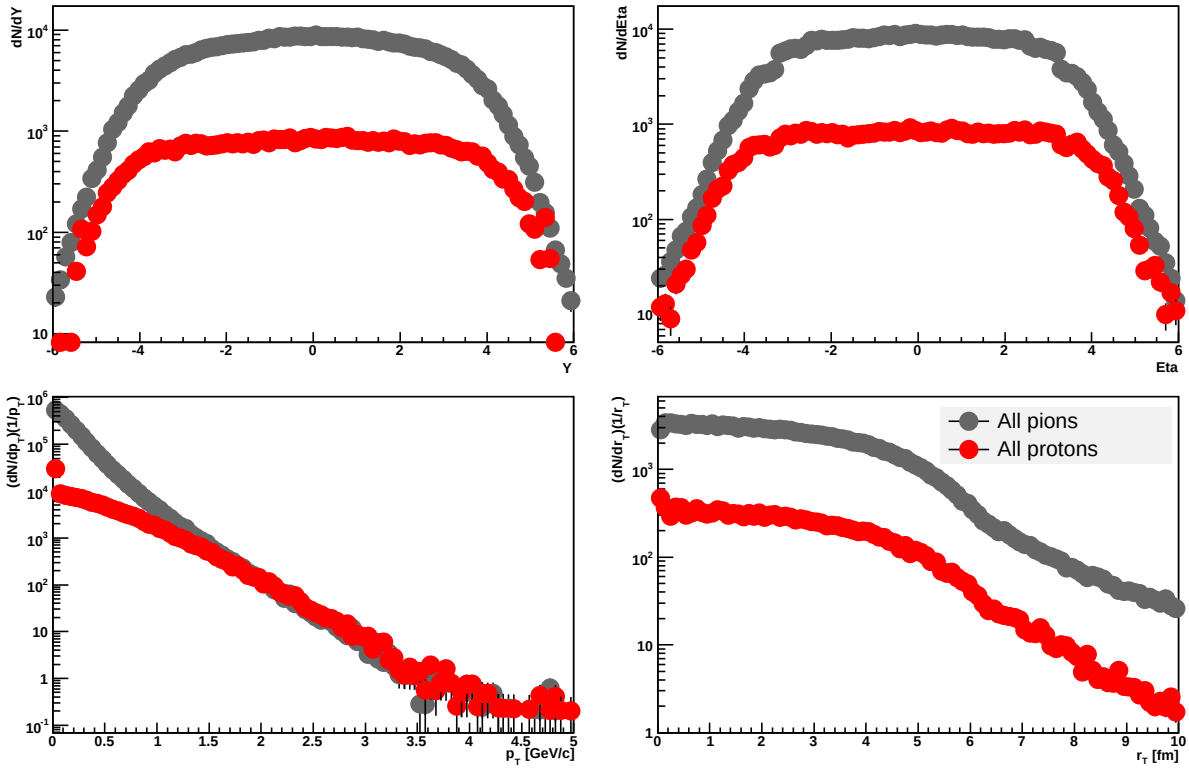

Figure 8.13: Spectra for all negative pions and protons generated in EPOS sample. Top-left panel shows the rapidity distributions, bottom-right panel reflects pseudorapidity distributions, bottom-left panel illustrates spectrum of transverse momentum and bottom-right panel exposes transverse position distributions.

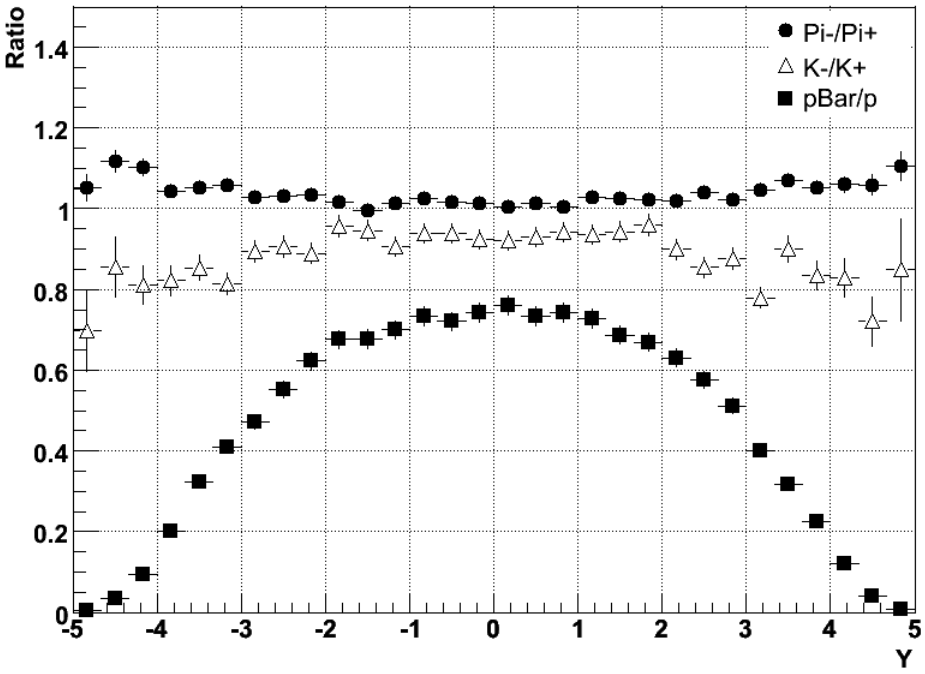

Figure 8.14: Rapidity distributions of ratios of produced particles: π^-/π^+ (black circles), K^-/K^+ (open triangles), $\overline{p}/p$ (closed squares).

Similar number of negative pions is produced as of positive ones, the ratio of kaons is ~ 0.9. For higher values of rapidity intervals the number of negative pions is slightly bigger than that of positive ones. For $|y| < 5$ and $|y| > 2$, the production of negative kaons slightly decreases comparing to mid-rapidity region. In the experiment protons and anti-protons (used in proton femtoscopy) are taken from the mid-rapidity ($|y| < 0.5$).
In EPOS their ratio is $\frac{\overline{p}}{p} \sim 0.7$. It indicates the contamination of nuclear remnants. Figure 8.14 is similar to the BRAHMS [94] one, assuming that particle production in $Au + Au$ collisions for $\sqrt{s_{NN}} = 200$ GeV in EPOS is similar to RHIC observables.

Two-particle distributions

The same distributions as for the UrQMD model are shown. For identical particle combinations (Figure 8.15 for two-proton and Figure 8.16 for two-anti-proton), all mean values remain around zero as expected from theoretical predictions. In the case of non-identical, proton - anti-proton combinations (Figure 8.17), mean values of $side$ and $long$ components equal zero, whereas other distributions indicate some possible asymmetry. In the case of distributions of 'ALL' particles, the contamination of nuclear remnants is reflected by deviations for out and $time$ components

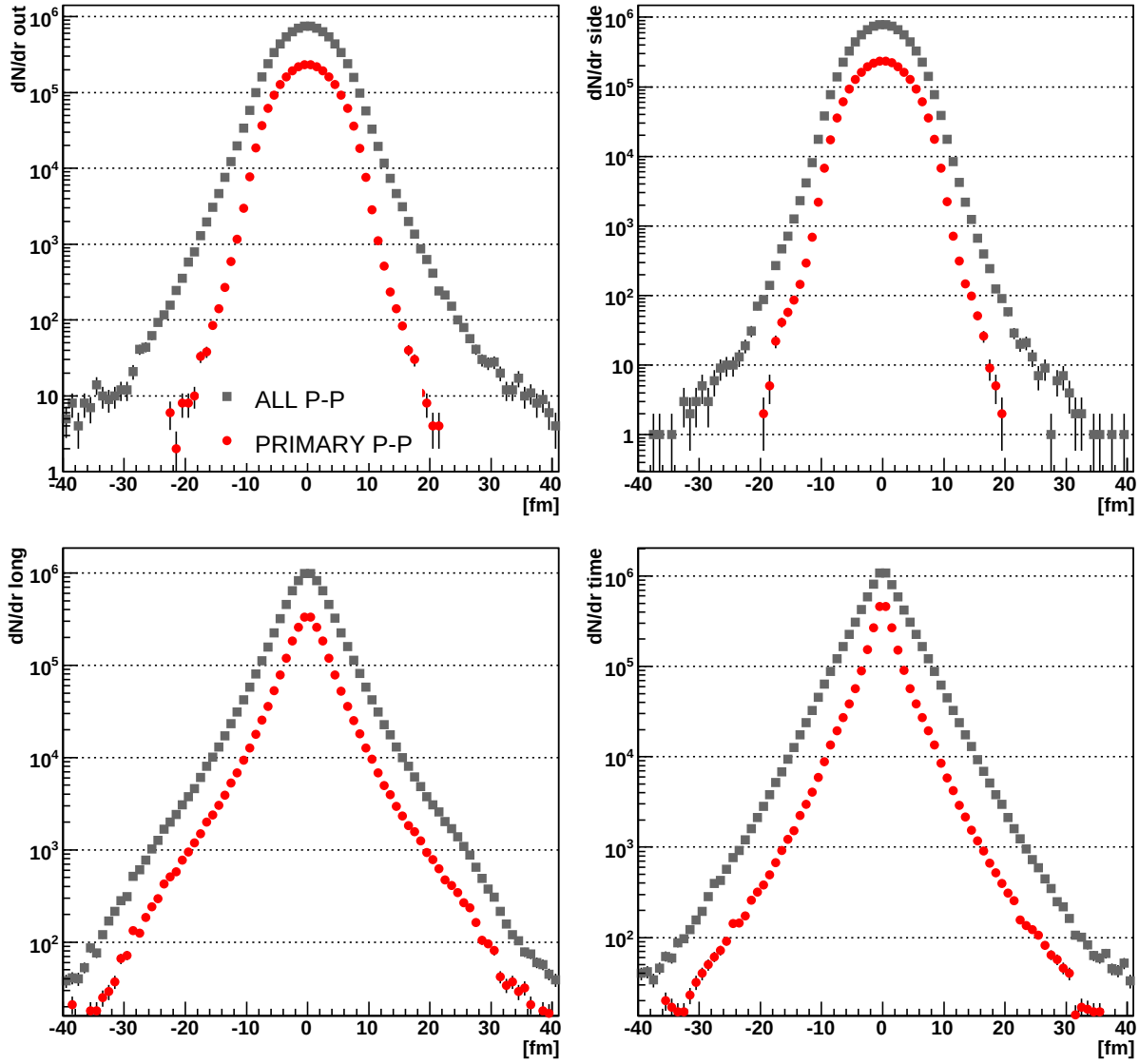

Figure 8.15: Two-proton separation distributions for all particles (gray points) and primordial only (red points) in CMS reference. The figure's layout is the same as in 8.5.

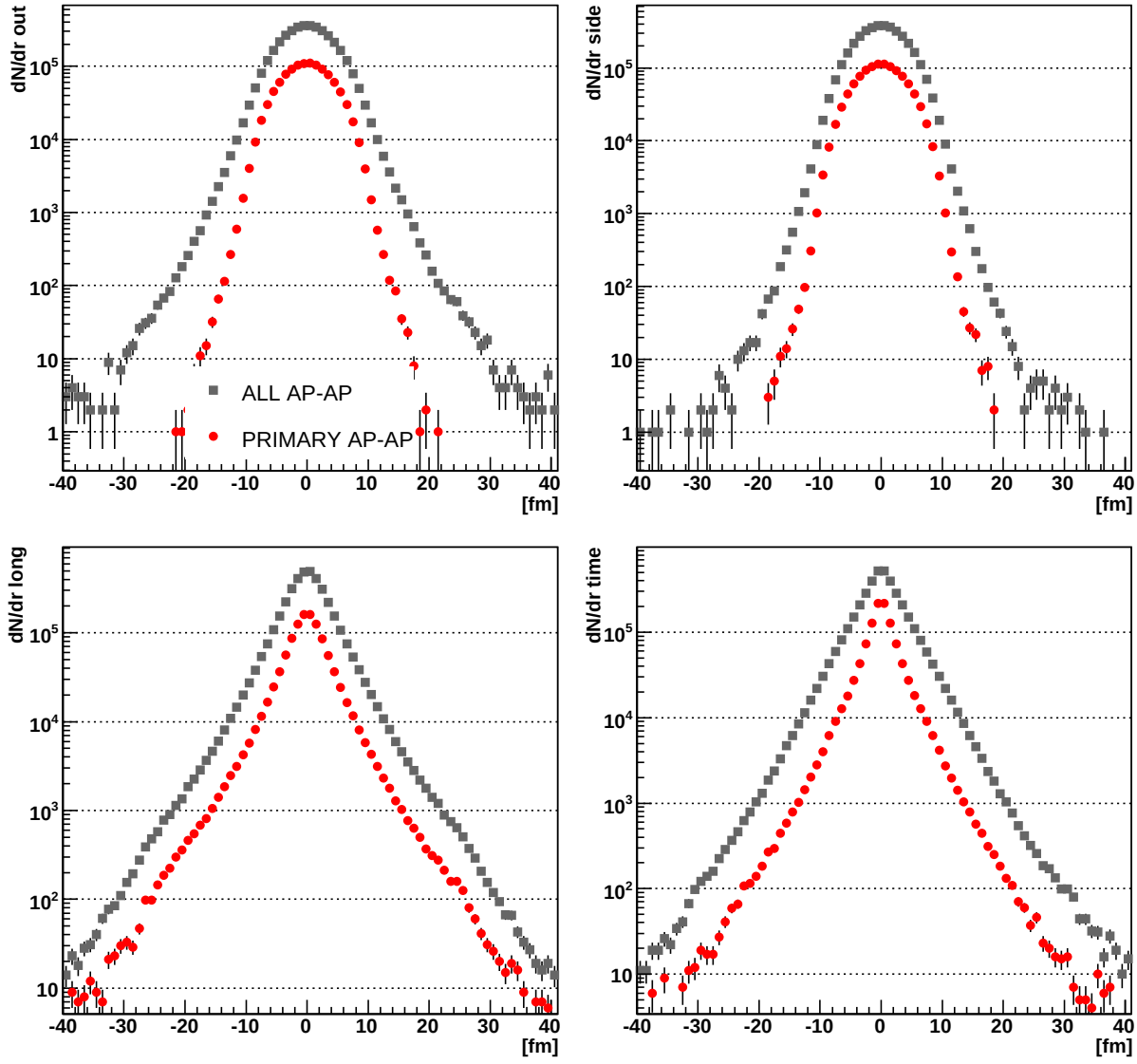

Figure 8.16: Two-anti-protons separation distributions for all particles (gray points) and primordial only (red points) in CMS reference. The figure layout is the same as in 8.5.

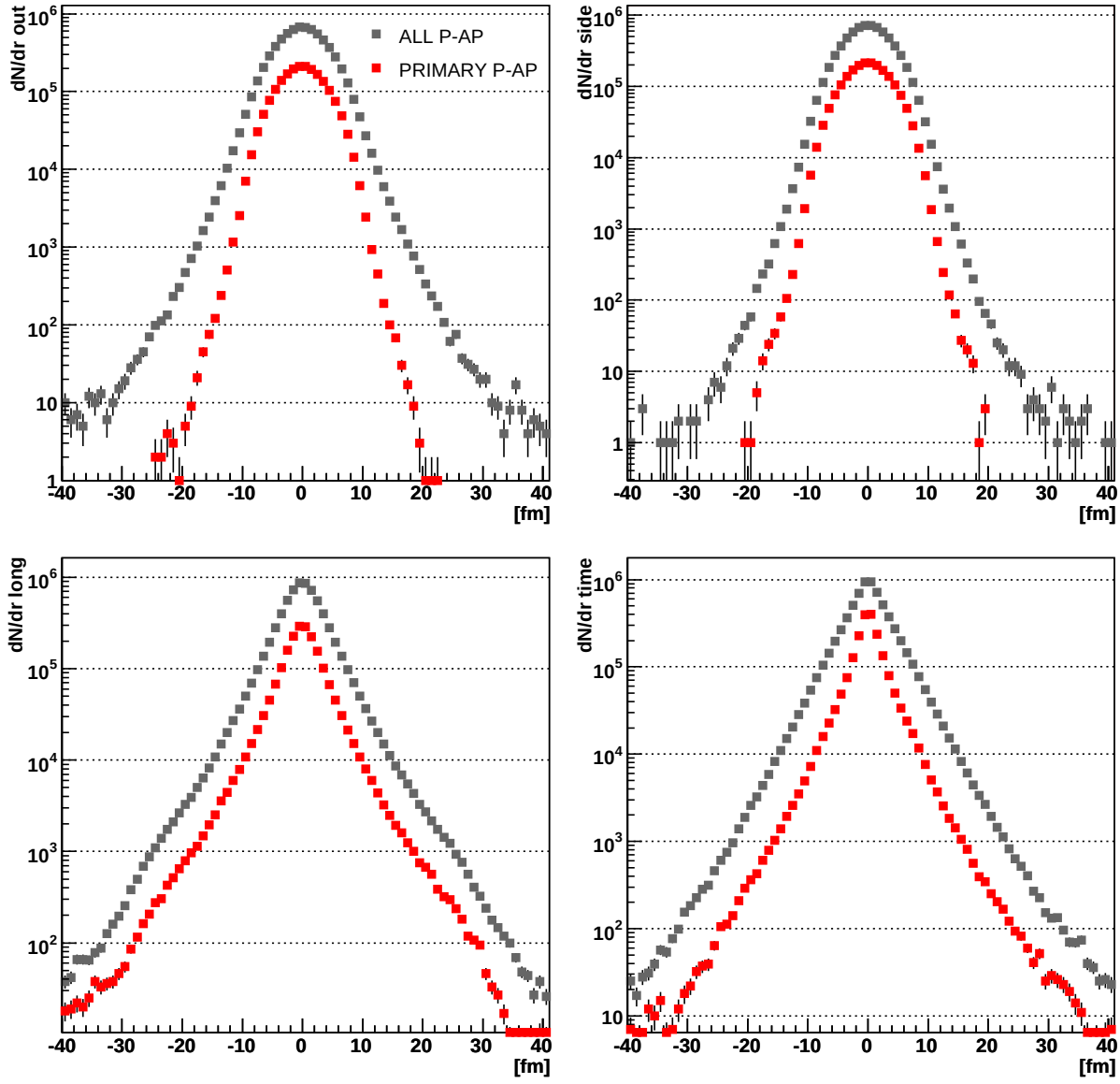

Figure 8.17: Proton-anti-proton separation distributions for all particles (gray points) and primordial only (red points) in CMS reference. The figure's layout is the same as in 8.5.

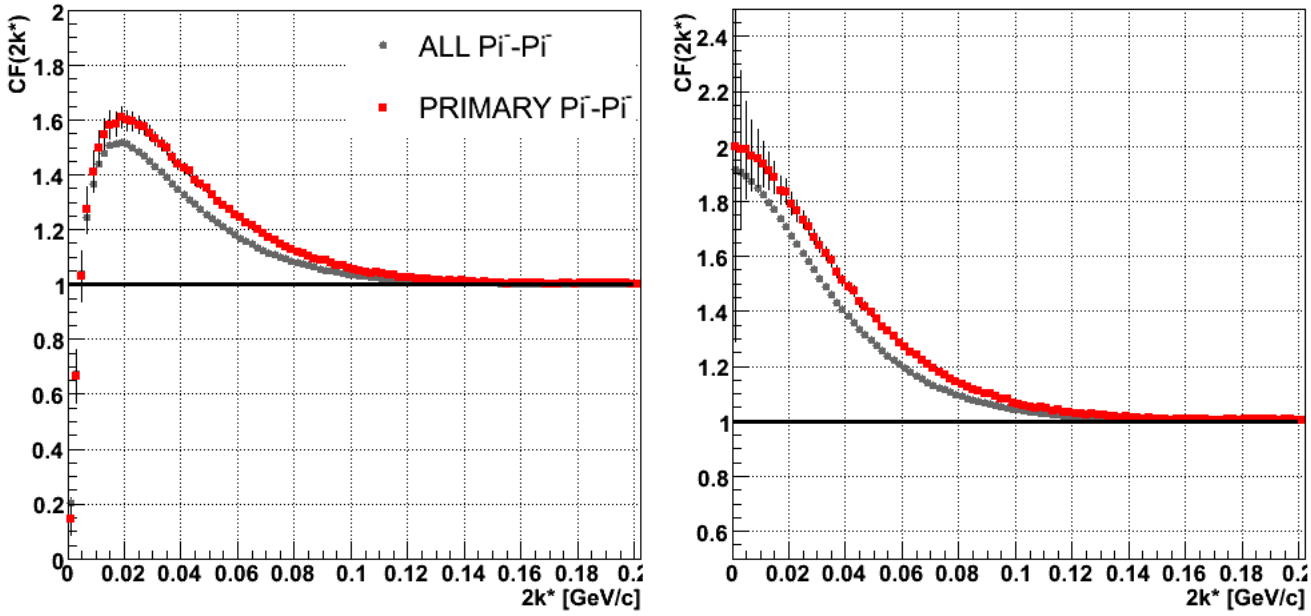

Figure 8.18: Pion-pion correlation function, left panel shows functions for QS and FSI included, right one illustrated correlations for QS only. Grey marker shows correlation functions calculated for all particles, red marker indicates correlation functions for primordial particles only

(for positive values of separation). Each distribution does not represent a Gaussian shape (out and $side$ separations seen in the logarithmic scales- central parts represents Gaussian shape but their tails imply non-Gaussian source distribution), whereas components $long$ and $time$ do not exhibit Gaussian form at all. The distributions for $p-p$ and $p-\overline{p}$ systems are highly contaminated by residual and nuclear remnants.

Correlations

Figure 8.18 shows identical pion correlations for QS calculations only (right panel) and QS+FSI included (left panel), the second plot can be compared to the plot of correlation function calculated for the UrQMD model (Figure 8.8, left panel). This confirms what two-particle separation distributions indicate: EPOS gives smaller source size than UrQMD, therefore the correlation effect is stronger for the EPOS model.

The correlation function for pion-kaon combinations are shown in Figure 8.19; top panel of the figure shows un-like signs combinations and the bottom panel shows like signs particle combinations. Their 'double ratios' are shown in Figure 8.20 (left panel for un-like signs and right panel for like signs). Also in pion-kaon correlations for EPOS, the correlation effect is stronger

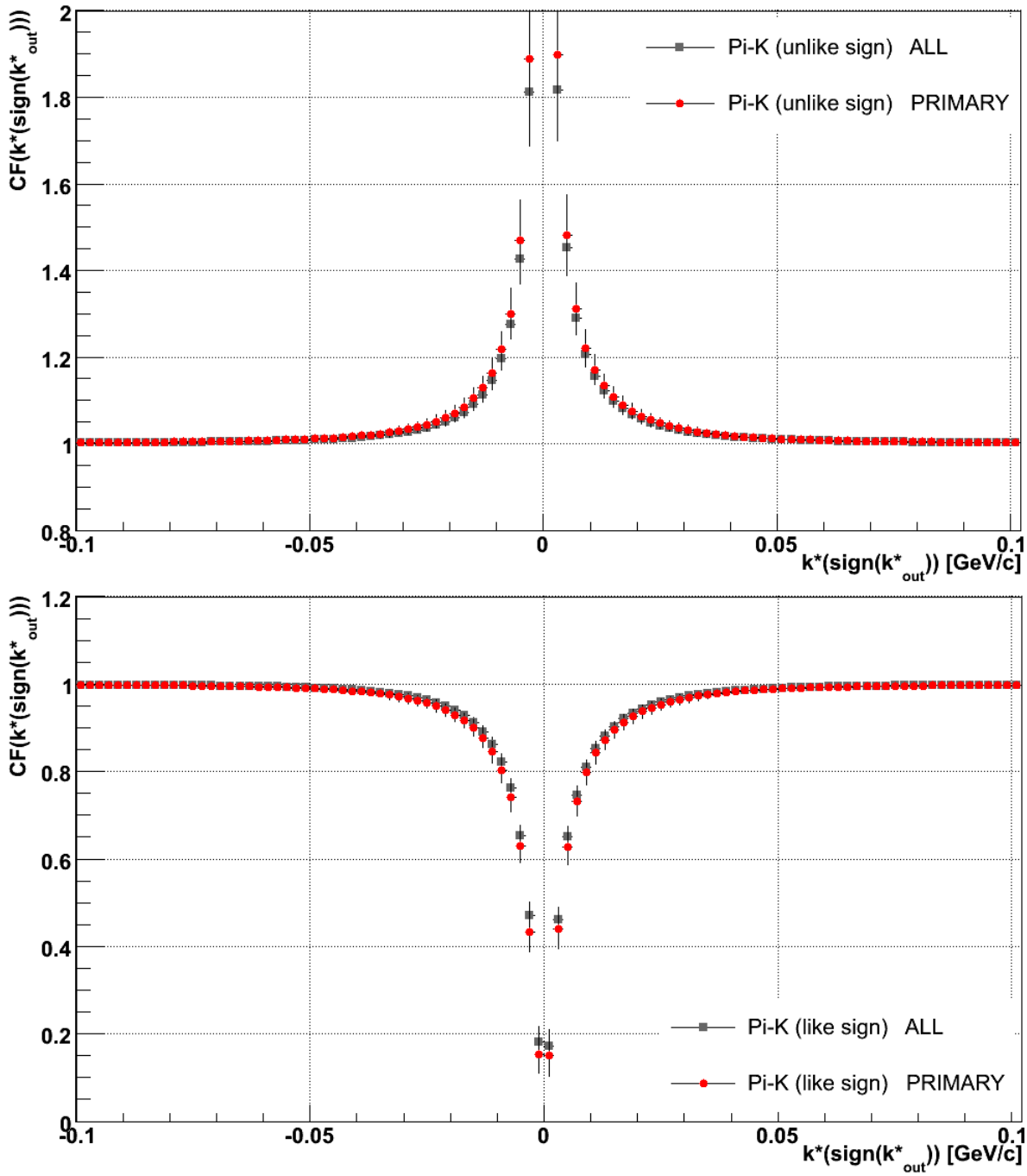

Figure 8.19: Pion-kaon (like signs in bottom panel and un-like signs at top panel) correlation function. Grey marker shows correlation functions calculated for all particles, red marker indicates correlation functions for primordial particles only

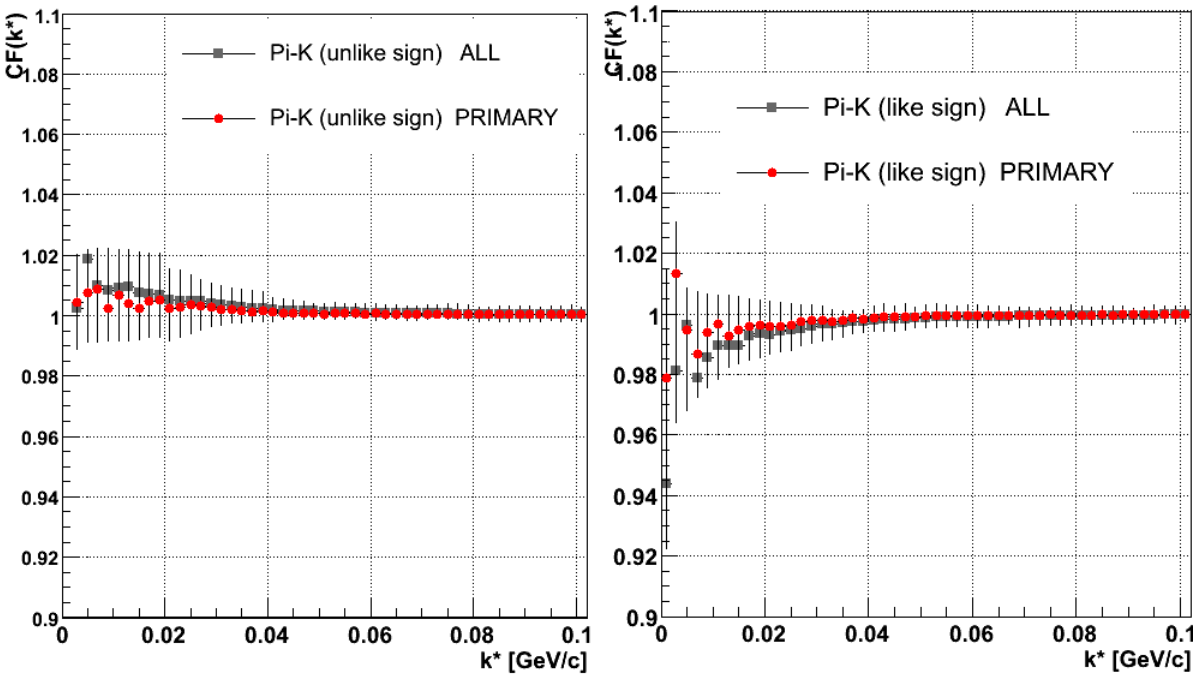

Figure 8.20: Pion-kaon (like signs in right panel and un-like signs at left panel) 'double ratios'. Grey marker shows 'double ratios' calculated for all particles, red marker indicates 'double ratios' for primordial particles only

than in UrQMD, which again indicates smaller source size (as bigger RMS values in two-particle separation distributions). Another issue is the magnitude of asymmetry: in EPOS it is weaker than in UrQMD.

Figure 8.21 shows proton - anti-proton correlation functions. The correlation signal is clearly visible. For pairs composed of primordial particles- the correlation effect is stronger. Top panel presents correlation functions with respect to the sign of k^*_{out}. The left-hand side of the bottom part illustrates their 'double ratios', which fluctuate around unity. As EPOS model does not contain final particle rescattering implemented- the emission of protons and anti-protons seems to be similar to each other.

Asymmetry discussion

This section contains similar distributions as the section dedicated to the asymmetry discussion in UrQMD. Figure 8.22 shows centrality dependence of proton - anti-proton separation distributions in the CMS reference frame for primordial particles only. All mean values for $side$ and $long$ components are close to zero, however small deviation from zero is observed in distributions for out direction and $time$ as well. For peripheral collisions the magnitude of asymmetry seems to be the strongest and for central collisions the weakest. Even if they are reflected in both separation distributions: for out and $time$ components, the deviations from zero are much smaller and weaker than in the UrQMD model; they should not be interpreted as a clear evidence of asymmetry in emission process between protons and anti-protons. Another two distributions can be deduced for pion-kaon combinations from Tables 9.8 and 9.9 confirming what is observed in the experiment and UrQMD model asymmetry in emission process between pions and kaons. Table 9.7 collects results for two-pion system and confirms that in the case of identical particle combinations no asymmetry is expected.

8.4.3 UrQMD and EPOS comparison

In terms of single-particle distributions (Figures 8.3, 8.13 and 8.4, 8.14), the EPOS model predicts observables similar to BRAHMS measurements. For separation distributions, both models do not represent Gaussian shape of any source of particles. The comparison of mean values from separation distribution is collected in Tables: 8.1 and 9.7-9.12.

Table 8.1 stores RMS and mean values for both models for three different centrality classes, Tables 9.7, 9.8 and 9.9 contain these distribution characteristics for pion-pion, pion-kaon (like

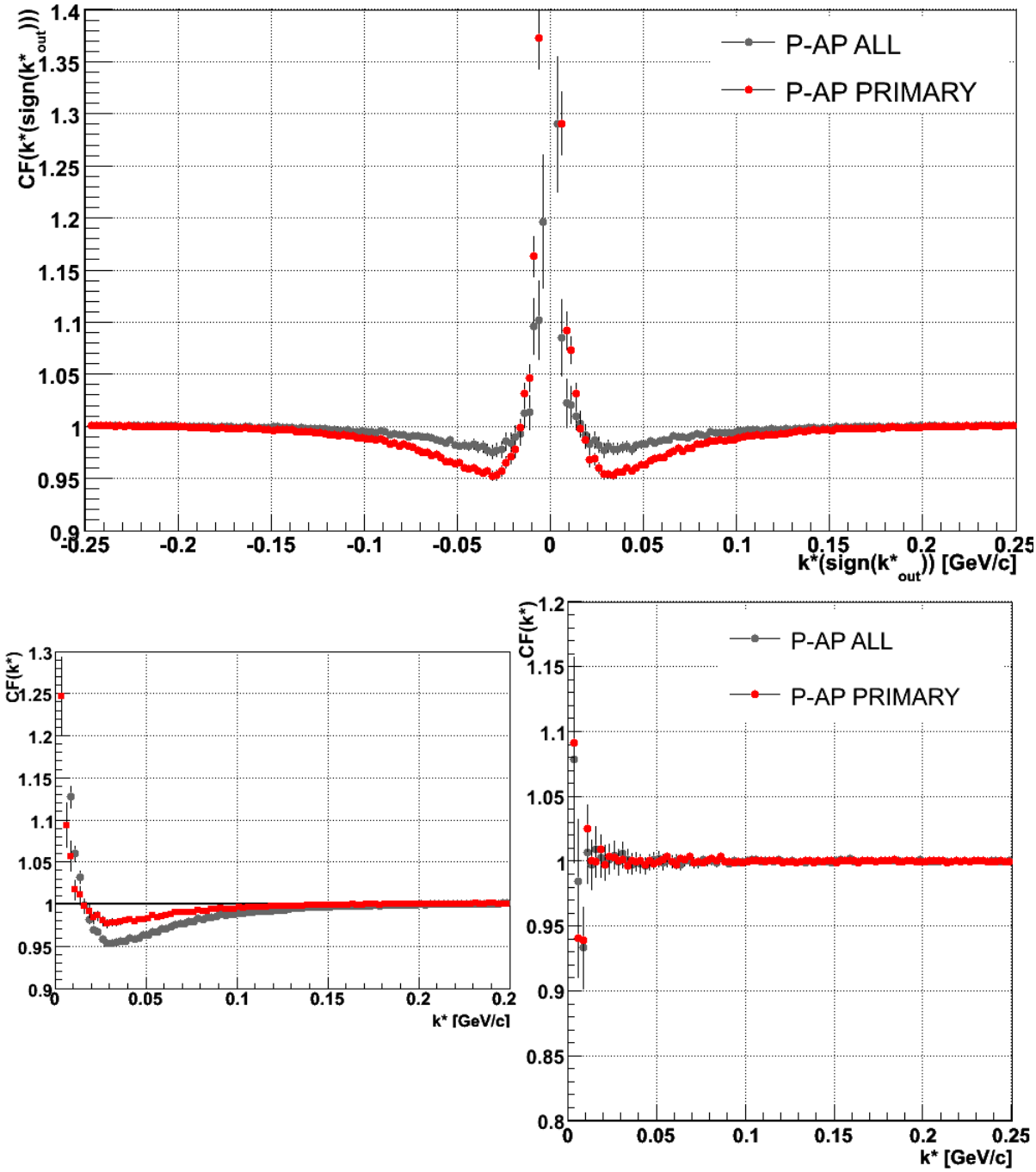

Figure 8.21: Proton - anti-proton correlation functions. Gray points show all particles, red squares only primordial ones. Top panel presents correlation function for positive and negative sign of $k*_{out}$, bottom-left panel shows their 'double ratio', right-bottom panel introduced one-dimensional correlation function.

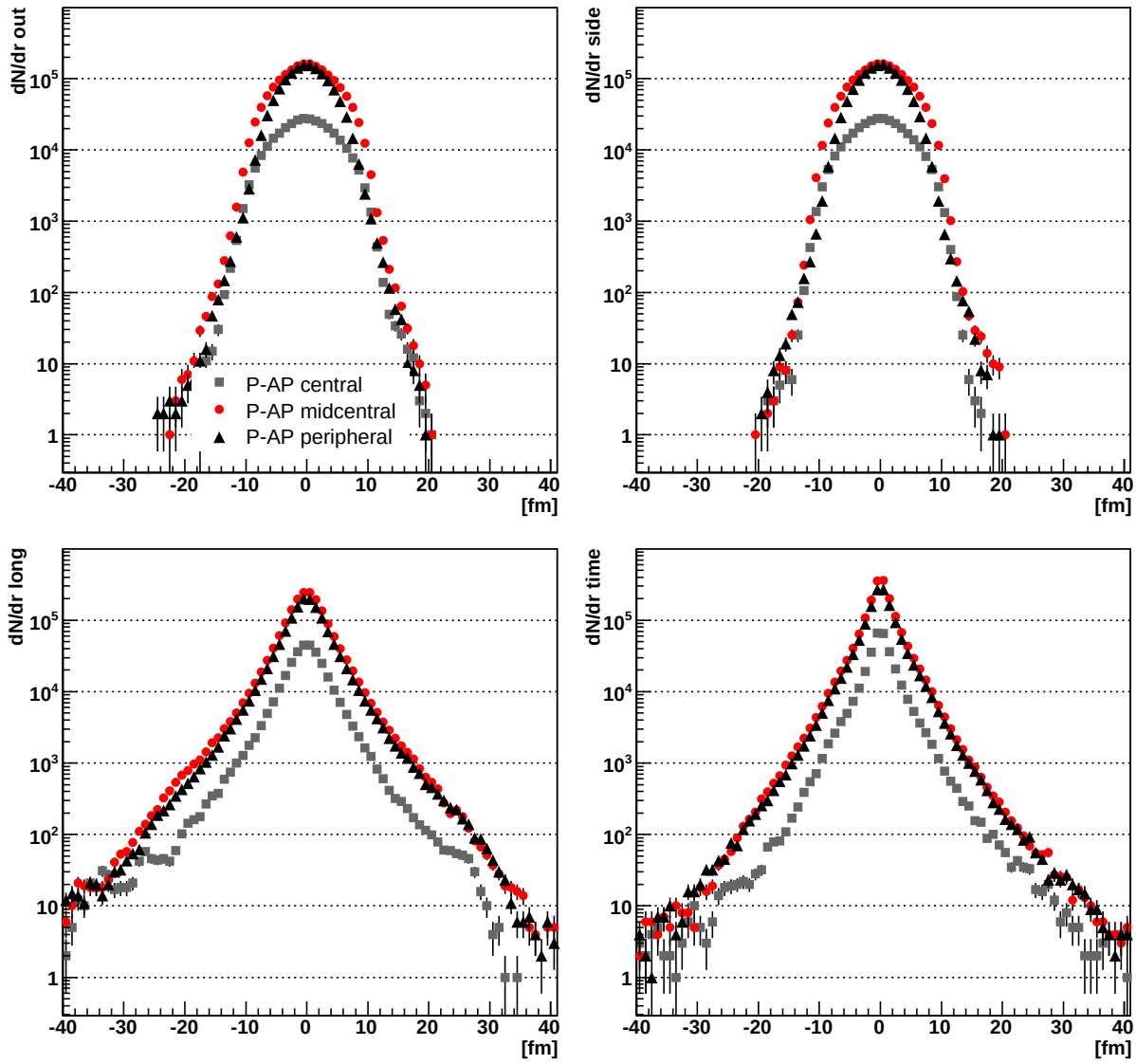

Figure 8.22: Proton -anti-proton (centrality dependencies) separation distributions. Gray points are for central collisions (0-10)% of the total hadron cross section of the collision, red points are for mid-central collisions (10-30)% and the black points are for peripheral data (30-80)%. The figure layout is the same as in 8.5.

Table 8.1: Proton - anti-proton separation distributions for CMS reference (centrality dependencies)

UrQMD	out	$side$	$long$	$time$
Central: mean value	-0.670	-0.003	0.003	1.224
Central: RMS value	9.979	10.293	12.786	16.776
Mid-central: mean value	-0.908	0.003	-0.003	1.884
Mid-central: RMS value	9.642	9.504	12.532	16.443
Peripheral: mean value	-1.204	0.002	0.001	2.183
Peripheral: RMS value	8.515	7.353	10.081	15.059
EPOS	out	$side$	$long$	$time$
Central: mean value	-0.022	-0.006	-0.003	0.052
Central: RMS value	4.421	4.388	4.213	3.401
Mid-central: mean value	-0.058	-0.004	-0.004	0.045
Mid-central: RMS value	4.191	4.138	4.197	3.351
Peripheral: mean value	-0.090	0.006	0.001	0.066
Peripheral: RMS value	3.486	3.413	4.179	3.421
Therminator	out	$side$	$long$	$time$
Central: mean value	0.002	-0.001	0.003	0.001
Central: RMS value	3.882	5.190	8.398	2.433
Mid-central: mean value	-0.002	-0.001	0.001	0.02
Mid-central: RMS value	3.041	4.041	6.994	1.914
Peripheral: mean value	-0.002	-0.003	0.001	0.002
Peripheral: RMS value	2.641	3.222	4.451	1.002

signs) and pion-kaon (un-like signs) respectively. Another three tables: 9.10, 9.11 and 9.12 contain results proton - proton, anti-proton - anti-proton and proton - anti-proton systems respectively. In all cases, RMS values are smaller for primordial particles only (smaller source size) within the same model, the tendency of a bigger source for higher particle mass is observed indicating that collective phenomena are applied in both models. EPOS reproduces stronger correlations (smaller RMS values). Concerning correlation functions, source sizes follow tendencies expressed in separation distributions. Both models can give reasonable correlation. Advanced correlation techniques (as the method for non-identical particles) deduce relative shifts in time and space between two particle's species. In the case of proton - anti-proton correlation functions, the correlation effect is stronger for UrQMD than for EPOS. Seen in data asymmetry in emission process between protons and anti-protons is observed in UrQMD model as well. Hydrodynamics does not reproduce any difference between protons and their anti-particles. Similar emission properties of such particles are assumed. The generator Therminator which includes resonances decays, but not rescattering processes, does not reflect such asymmetry as well (see Table 8.1). EPOS model does not include hadron rescattering (only parton scatterings), thus no asymmetry is seen. Finally UrQMD includes hadron rescatterings (here observed annihilation processes) and space-time differences between protons and anti-protons emission are reproduced. STAR data are not sensitive to the centrality dependence of space-time differences in emission process, however UrQMD shows such tendency.

Chapter 9

Conclusions

The results of this work complement information obtained earlier by the *HBT Physics Working group* of the STAR experiment at BNL. A detailed analysis performed already for identical mesons: pions and kaons and the pioneer work with the pion-kaon correlations have reveal a lot of unexpected effects commonly known as *RHIC HBT puzzle*. More information was clearly necessary. This work is a step forward to fill this gap.

Considerably larger mass of baryons with respect to the mass of pions and kaons points out to a new sort of information that can be obtained from the analysis of baryon correlations. Protons are not so copiously produced as pions and their mean number at midrapidity is still larger than that of antiprotons. The net-baryon free system has not been achieved yet at RHIC energies. The thermal motion in the state of equilibrium, results in smaller mean velocity of protons with respect to the velocity of lighter pions and kaons. On the other hand, the collective motion of particles superimposed on the thermal one, gives a specific pattern of particle velocity distributions. As a consequence, the final space time distribution of freeze-out points for different particle species reflect the relations between thermal and collective motion of hot and expanding system created in heavy ion collisions.

The length of homogeneity measured by femtoscopy methods includes the effects of space-momentum correlations. Together with the relations between thermal and collective motions, between chemical and thermal freeze-out, with the effects of resonance production and secondary rescattering the final image of space-time evolution of the system represents a very complex phenomena, difficult to quantitative description. A consistent description clearly needs the information coming both from the analysis of light (pions) and heavy (protons) systems.

The following classes of two-particle systems, incident energies and event centralities have been considered in the frame of this work:

- all combinations of two particle systems consisting of protons and antiprotons: ($p-p$), ($\overline{p}-\overline{p}$,$p-\overline{p}$),
- two energies of colliding gold nuclei: 200 GeV and 62 GeV per nucleon pair,
- three classes of event centralities, according to the percentage of the total hadronic cross-section: central (0-10)%, mid-central (10-30)%, peripheral (30-80)%.

The following experimental results have been obtained:

- For the first time the analysis of two antiproton correlations has been performed and the sizes of antiproton emission region in relativistic heavy ion collisions has been estimated.
- For the first time the analysis of two-particle correlations for all systems of protons and antiprotons, simultaneously and in the same experimental conditions, has been performed. The obtained quantitative results are consistent within the experimental uncertainties.
- For the first time the asymmetry between space-time parameters of proton and antiproton emission has been analyzed and quantitatively estimated. A small asymmetry has been found, showing that antiprotons are emitted earlier or more close to the edge of the emitting system.

The analysis for all three proton/antiproton systems have been performed in the same way in all energy/centrality classes; the same event selection criteria have been applied; the same corrections have been introduced and the same approach was used to estimate the influence of residual correlations. Thus the role of systematic errors was strongly reduced, what is important for the quantitative comparison and for common analysis of all the results obtained in this work.

The following physics conclusions can be drawn:

- The measured values of proton/antiproton emission regions sizes are systematically smaller then that of pions and kaons with similar transverse momenta. In frame of hydrodynamic approach and taking into account the larger mass of protons with respect to kaons and pions, one can understand it as an interplay of thermal and collective motion of hot and expanding system. Thus, pairs of lighter particles are on average emitted from the region of larger dispersion.

- The increase of measured sizes with the event centrality reflects the geometry of the colliding systems. This dependence is similar to that for pions and kaons.
- The values of emission sizes obtained for 200GeV are slightly larger than those for 62GeV. More statistics is necessary however to make quantitative conclusion.
- The obtained results are in qualitative agreement with the predictions of theoretical models: UrQMD and EPOS. It is not the case however for the asymmetry results of nonidentical particle correlations (see below).
- A small, but definitively nonzero, asymmetry shift have been found in the analysis of proton-antiproton correlations. One should mention here that a relatively large shift was experimentally found earlier for the pion-kaon system. This result is consistent with the hydrodynamic description, where the mass differences lead to the space-time asymmetries. Such effect cannot be attributed however to the particles with the same masses. The asymmetry shift is also absent in the results of simulations with the EPOS model but is seen in the results of UrQMD simulations. As the difference between EPOS and UrQMD, important for the final stage of the interaction dynamics, is the absence of rescattering processes in the EPOS model, one can conclude that the annihilation processes at the last stage of the collision can be responsible for the observed asymmetry. This conclusion is also consistent with the sign of asymmetry effect, showing that antiprotons are emitted earlier or more close to the edge of the emitting system than protons.

In order to obtain the physics results free of experimental distortions some specific kinds of methodical analysis have been performed.

- A set of cuts have been applied for the registered tracks to eliminate the merging effect which makes that instead of two separate tracks, only one is reconstructed.
- A dedicated analysis of the tracks located very close in the detector space have been performed in order to avoid the splitting effect which causes that instead of one single track, two track are found.
- The contamination of electron - positron pairs have been removed.
- The effect of finite detector resolution have been taken into account as well.

- A special attention have been put to the effect of residual correlations resulting mainly from the contamination of the proton/antiproton sample by the particles (also protons or antiprotons) coming from the week decays of hyperons. This effect is much more dangerous for protons than for pions. The kinematics of lambda-hyperon decay makes that proton practically follow the direction of lambda particle in the detector space and cannot be distinguished experimentally from that coming directly from the interaction point. A detailed procedure have been developed and the decays of lambda and sigma hyperons have been considered, including the decay kinematics. The reflection of FSI correlations in the proton/antiproton hyperon systems, in the studied proton-antiproton correlations have been taken into account. One should mention here that such analysis was made for the first time in the analysis of correlations for the baryonic systems. This can be important for the comparison of the results obtained here with the other results obtained elsewhere, where the residual correlations have not been taken into account properly.

The analysis performed here is a step forward in the direction of consistent description of the dynamics of heavy ion collisions, mainly in the part of so called soft processes.
The next steps can be the following:

- Complete the existing results for meson-meson and baryon-baryon systems by the analysis of meson-baryon correlations. It can serve as an important consistency test.
- Perform the analysis with larger statistics for more centrality bins.
- Continue the asymmetry analysis, also with larger statistics.
- Make the analysis and find the source sizes in three dimensions: out, $side$ and $long$. It will allow one to obtain information about the shape of the source.
- Perform common analysis of source sizes for different particle systems and for different transverse mass intervals. It will allow one to measure estimate the effects of collective motions with higher precision.
- Make the azimuthally-sensitive two-proton correlation studies. It will help to assess the source-size depending on reaction plane and to find the relations between the geometry and dynamic factors in heavy ion collisions

In order to perform the analysis proposed above it is necessary to have more statistics of experimental data. In a natural way it can be achieved in the next generation experiment ALICE being

prepared now at CERN. Much larger particle multiplicities and the better detection possibilities makes good perspectives for such measurements. However, at the LHC conditions it is not clear what one would expect. As nobody knows what system will be created (QGP or sQGP), it is not possible to predict what results concerning femtoscopy should be expected. On the other hand, it seems to be reasonable to check what RHIC II will bring as the accelerator and detector upgrades will allow to analyze data in the collision energy closer to the present RHIC observable. RHIC II plans to collect data with much higher luminosity that RHIC could do, so the following field of research are the main topic of interest:

- High P_T
- Heavy Flavor
- Equation of State
- Electromagnetic Probes
- Forward Physics
- Spin

The correlation analysis might be very interesting, however the program to study such measurements is not worked out.

Appendix 1- Elementary units, particles and their interactions

Elementary units

The basic units in physics are length, mass and time and the SI system expresses them in meters, kilograms and seconds. These units are not very appropriate in high energy physics, where typical lengths are 10^{-15}m and typical masses are 10^{-27}kg. The above table introduces basic units used in high energy physics. In calculations, the quantities of Planck constant and speed of light occur frequently, so their units are set to: $\hbar = \frac{h}{2\pi} = c = 1$. Basic units are listed below.

Quantity	High energy units	Value of SI units
length	1 fm	10^{-15}m
energy	1 GeV= 10^9 eV	1.602 $\times$ 10^{-10} J
mass	1 GeV/c^2	1.78 $\times$ 10^{-27} kg
$\hbar = h/(2\pi)$	6.588 $\times$ 10^{-25} GeV s	1.055 $\times$ 10^{-34} J s
c	2.998 $\times$ 10^{23} fm/s	2.998 $\times$ 10^{8} m/s
$\hbar c$	0.1975 GeV fm	3.162 $\times$ 10^{-26} J m

Particle classification

Fundamental particles [98] are of two types: particles with half-integer spin are called fermions because they obey Fermi-Dirac Statistic, while those with integer spin obey Bose-Einstein statistics and are called bosons. The statistics obeyed by a particles determine how the wave function Ψ describing an assemble of identical particles behaves under interchange of any pair of particles, say 1 and 2. The theory says that under exchange of identical bosons Ψ is symmetric and under exchange of identical fermions Ψ is anti-symmetric.

Fundamental fermions

The experimental data from high-energy experiments can be described by Standard Model [12, 13] of particles and their interactions, formulated in the second part of twentieth century. According to this model, all mater is built up from a small number of fundamental spin $1/2$ particles (fermions): 6 quarks and 6 leptons. For each constituent, its symbol and a ratio of of its electric charge Q to elementary charge e are given in the Table 9.1.

Table 9.1: A list of elementary fermions.

Particle	Flavor			Q/|e|
leptons	e	μ	τ	-1
	ν_e	ν_μ	ν_τ	0
quarks	u	c	t	+2/3
	d	s	b	-1/3

- Leptons

The leptons carry integer electric charge, the electron e is familiar to everybody and other leptons are muon μ and taon τ, heavier than electron. The neutral leptons are called "neutrinos" ν. A different flavor of neutrinos (e, μ, τ) is paired with each flavor of charged leptons. Neutrinos were postulated by Pauli in 1930 in order to explain energy and momentum missing in the process of nuclear β decay, where an electron is emitted together with its neutrino ν_e. The masses and mass limits are collected in Table 9.2.

Table 9.2: The masses of leptons taken from Particle Physics Booklet, edition 2004.

Flavor	Charge lepton mass	Neutron lepton mass
e	m_e=0.511 MeV	$m_{\nu_e} < 3$eV
μ	m_μ=105.658 MeV	$m_{\nu_\mu} < 0.19$ MeV
τ	m_τ=1776.990 MeV	$m_{\nu_\tau} < 18.2$ MeV

- Quarks

Quarks [99] (see Table 9.3) carry fractional charges of $+\frac{2}{3}|e|$ or $-\frac{1}{3}|e|$. Two quarks: b and t are called as 'beauty' or 'true' respectively as well. Leptons exist as free particles but quarks do

not. It is a peculiarity of the strong forces between quarks that they cannot be found existing separately. Protons and neutrons are composed of 3 quarks: $p = uud$, $n = udd$. The material of universe is composed of stable particles, i.e. electrons e and quarks u and d. The heavier quarks also combine to form particles, but much heavier and not stable, they decay rapidly and heavier leptons decay into electrons. Two types of quark combinations are established as existing in nature:

- 'baryon' = QQQ (three quark state) or 'anti-baryons'=$\overline{QQQ}$ (three anti-quark state)
- 'meson' = $Q\overline{Q}$ (quark - anti-quark pair).

These strongly interacting quark components are called to as 'hadrons'. Table 1.3 shows all quark flavors, where Q means the electrical charge, B is a baryon number, I_3 is the third component of spin, J^P means spin and parity. The last four columns reflect to quark flavors: S- Strangeness, B^b- Beauty, C- Charm, T-Top. Quark composition of few examples of mesons and baryons is

Table 9.3: Quarks and quark properties taken from Particle Physics Booklet, edition 2004.

Name	Symbol	Mass	Q	B	I_3	J^P	S	B^b	C	T
up	u	1.5- 4.0 MeV	+2/3	1/3	+1/2	$1/2^+$	0	0	0	0
down	d	4.0-8.0 MeV	-1/3	1/3	-1/2	$1/2^+$	0	0	0	0
strange	s	80.0-130.0 MeV	-1/3	1/3	0	$1/2^+$	-1	0	0	0
charm	c	1.15-1.35 GeV	+2/3	1/3	0	$1/2^+$	0	0	+1	0
bottom	b	4.1-4.9 GeV	-1/3	1/3	0	$1/2^+$	0	-1	0	0
top	t	174.3-178.1 GeV	+2/3	1/3	0	$1/2^+$	0	0	0	+1

presented in Table 9.4.

Table 9.4: Quarks compositions.

Meson	Composition	Baryon	Composition
π^+	$u\overline{d}$	p	uud
π^+	$\overline{u}d$	n	udd
π^0	$u\overline{u} + d\overline{d} + s\overline{s}$	Λ	uds
K^+	$u\overline{s}$	Ξ^0	uss
K^-	$s\overline{u}$	Ω^-	sss

Interactions

Standard Model does not describe all interactions of elementary particles. There are four funda-

Table 9.5: Fundamental interactions.

Interaction	Mediator	Spin/parity
Strong	gluon, G	1^-
Electromagnetic	photon, γ	1^-
Weak	$W^{\pm}, Z^0$	$1^-, 1^+$
Gravity	graviton, g	2^+

mental forces responsible for all interactions between any of objects, which are listed in Table 9.5 with their basic properties. Two of them (gravitational and electromagnetic) are commonly known and they share some common characteristics.

- 'Gravitational' interactions exist between any objects with non-zero mass. Such interactions are the weakest and their potential is determined by mass of interacting objects. They play a crucial role in astronomy and astrophysics. Supposedly that are mediated by 2 bosons called 'gravitons'. Experiments dedicated to explore such bosons (LIGO [100], VIRGO [101]) still perform their measurements.

- 'Electromagnetic' interactions are quite similar but the force acts upon electrical charge. There are two of types of electrical charge: "positive" and "negative". These interactions are responsible for many phenomena in nuclear physics, in particular for the bound states of electrons within nuclei, i.e. atoms and molecules and are carried by 'photon' exchange.

- 'Strong' interactions are responsible for confining quarks inside hadrons (in protons and neutrons), and the protons and neutrons within nuclei. The strength of these forces binds nucleons inside a nucleus exceeding a repulsion interactions between protons. The theory of strong interaction describes dependencies between quarks reviewed in the section 1.2. In addition to the other types of charges (mass, electric charge), quarks have a "color" (red, blue or green and three anti-colors: anti-red, anti-blue, anti-green), the charge of strong forces and they combine in two (quark-anti-quarks) or three quarks or anti-quarks to form a "white" meson or baryon. The energy in this field is increasing as the distance between quarks is growing! In the case of separating, the force of interaction is increasing to the point where a new pair quark-antiquark can be produced. The interactions between quarks are carried by 'gluons'.

- 'Weak' interactions are specified by the process of nuclear β-decay, involving the emission by a radioactive nucleus of an electron and neutrino. The carriers are $W^{\pm}, Z^0$ bosons with their masses of order 100 times of the proton mass.

To indicate the relative magnitudes of the four forces existing in present universe, the comparative strengths of the force between two protons are as presented in the Table 9.6.

Table 9.6: Strengths of forces.

strong	electromagnetic	weak	gravity
1	10^{-2}	10^{-7}	10^{-39}

Limitations of the Standard Model

Standard Model provides successful description of the properties of the fundamental constituents, as well as of the electromagnetic, strong and weak interactions between them. It describes perfectly many experimental data, however a model does have few limitations. Gravitational interactions are not included despite of many attempts to find a way to combine all interactions together. In the Standard Model neutrinos are considered as mass-less particles, when there is an evidence confirming non-zero mass of neutrinos. The Model contains many arbitrary parameters and the origin each of few of them is not clear. The phenomenon of dark matter still waits for an explanation and the problem of asymmetry between matter and anti-matter existing in present universe as well. However, the Standard Model forms an important part of a complete theory of elementary particles and their interactions.

Appendix 2- Symbols and conventions used

This part define the formulas which are used for two-particle separation distributions. In terms of two-particle correlations, distinguishable particles 1 and 2 are considered. Each particle is described by its coordinates of freeze-out: spatial x, y, z and time: t (four-vector $\mathbf{x} = \{t, \overrightarrow{x}\}$), and by its momentum coordinates: p_x, p_y, p_z (momentum) and E (energy) (four-momentum $\mathbf{p} = \{E, \overrightarrow{p}\}$) in the reference frame of the emitting source (CMS). When two particles are combined into a pair, a new reference frame can be introduced, a frame where the center-of-mass of the pair rests. This frame is called Pair Rest Frame (PRF). Values in PRF are marked with asterrisks *.
The total momentum of pair

$$\mathbf{P} = \mathbf{p}_1 + \mathbf{p}_2 = 2\mathbf{p} \tag{9.1}$$

and the relative momentum of pair

$$\mathbf{q} = \mathbf{p}_1 - \mathbf{p}_2 \tag{9.2}$$

are the most important quantities. For non-identical particles are generalized momentum difference is defined:

$$\tilde{q} = \mathbf{q} - \mathbf{P}(\mathbf{qP})/\mathbf{P}^2 \tag{9.3}$$

In PRF the one has

$$\tilde{q} = \{0, 2\overrightarrow{k^*}\} \tag{9.4}$$

where k^* is the momentum of first particle of pair in PRF. In CMS one also has the spatial coordinate

$$\mathbf{X} = [(\mathbf{P}_1\mathbf{P})\mathbf{x}_1 + (\mathbf{p}_2\mathbf{P})\mathbf{x}_2]/\mathbf{P}^2 \tag{9.5}$$

Also new directions can be defined, similar to the out, $side$ and $long$ decompositions of Bertsch and Pratt. The $long$ direction is the direction of beam axis, or z. In the transverse plane the out (or x) direction is the one of the momentum of the pair $\overrightarrow{P}$, and $side$ (or y) is perpendicular to out and $long$.

Pair separation can also be calculated:

$$\overrightarrow{r} = \overrightarrow{r_1} - \overrightarrow{r_2} \tag{9.6}$$

The $time$ difference:

$$\Delta t = t_1 - t_2 \tag{9.7}$$

Both of the variables can be calculated in the PRF and then they are denoted as $\overrightarrow{r^*}$ and t^*.
For non-identical particles it is significant which particle is first and which is second, as the signs of $\overrightarrow{r}$ and $\overrightarrow{q}$ depend on ordering. Therefore a convention is adopted that the first particle is always the one with lower mass, if both particles have the same masses, the one with larger value of charge is taken as first.
The procedure of decomposition of $\overrightarrow{r^*}$ and $\overrightarrow{k^*}$ into out, $side$ and $long$ is described below. First, the pair is boosted to the Longitudinally Co-Moving System (LCMS), that is the system where:

$$p_{1,z} = -p_{2,z} \tag{9.8}$$

along the z axis with velocity

$$\beta_z = |p_z|/E \tag{9.9}$$

Then

$$k^*_{long} = p^{LCMS}_{1,z} = -p^{LCMS}_{2,z} \tag{9.10}$$

$$r^*_{long} = r_{1,z} - r_{2,z} \tag{9.11}$$

Then a pair is rotated so that its x axis is along the pair transverse momentum. Then a pair is boosted to the PRF along x axis with

$$\beta_t = |p_t|/(E^2 - p_z^2) \tag{9.12}$$

Other components are given:

$$k^*_{out} = p^{PRF}_{1,x} = -p^{PRF}_{2,x} \tag{9.13}$$

and

$$k^*_{side} = p^{PRF}_{1,y} = -p^{PRF}_{2,y} \tag{9.14}$$

Similarly:

$$r^*_{out} = r^{PRF}_{1,x} - r^{PRF}_{2,x} \tag{9.15}$$

and

$$r^*_{side} = r^{PRF}_{1,y} - r^{PRF}_{2,y} \tag{9.16}$$

The initial separation in CMS $\overrightarrow{r}$ can also be decomposed into three components: r_{out}, r_{side}, r_{long}. Simple relations between the pair separation in two reference frames are given:

$$r^*_{side} = r_{side} \tag{9.17}$$

$$r^*_{long} = \gamma_z(r_{long} - \beta_z \Delta t) \tag{9.18}$$

$$\Delta t_{LCMS} = \gamma_z(\Delta t - \beta_z r_{long}) \tag{9.19}$$

$$r^*_{out} = \gamma_t(r_{out} - \beta_t \Delta t_{LCMS}) \tag{9.20}$$

$$t^* = \gamma_t(\Delta t_{LCMS} - \beta_t r_{out}) \tag{9.21}$$

where $\gamma_z = (1 - \beta_z^2)^{-1/2}$ and $\gamma_t = (1 - \beta_t^2)^{-1/2}$.

Appendix 3- Two-particle separation distributions - comparison of UrQMD and EPOS

This part contains the results of Mean and RMS values for two-particle separation distributions presented in Chapter 8. Here pairs of particles composed of pions and kaons are listed:

Table 9.7: Mean values and RMS for two-pion separation distributions for all pions and only primordial ones separately. The table contains numbers for out, $side$, $long$ and $time$ components. Precision of each number is of the order of ~ 1 %.

UrQMD	out	$side$	$long$	$time$
All: mean value	0.002	0.019	0.002	0.003
All: RMS value	11.632	11.163	16.464	17.660
Primary: mean value	-0.001	0.001	0.001	0.002
Primary: RMS value	7.845	7.735	2.564	14.324
EPOS	out	$side$	$long$	$time$
All: mean value	0.006	0.003	0.009	0.005
All: RMS value	5.828	5.693	7.817	9.782
Primary: mean value	-0.003	-0.002	0.002	-0.003
Primary: RMS value	4.125	3.732	6.129	5.031

Table 9.8: Mean values and RMS for pion-kaon (like signs) separation distributions for all particles and only primordial ones separately. The table contains numbers for out, $side$, $long$ and $time$ components. Precision of each number is of the order of ~ 1 %.

UrQMD	out	$side$	$long$	$time$
All: mean value	-2.102	0.002	0.003	0.910
All: RMS value	11.316	10.261	15.707	17.474
Primary: mean value	-2.343	0.001	0.001	1.786
Primary: RMS value	8.2090	7.601	12.643	14.82
EPOS	out	$side$	$long$	$time$
All: mean value	-0.623	0.000	0.012	0.523
All: RMS value	5.827	5.060	7.350	7.443
Primary: mean value	-0.121	0.002	0.012	0.624
Primary: RMS value	3.827	3.633	6.143	5.056

Table 9.9: Mean values and RMS for pion-kaon (un-like signs) separation distributions for all particles and only primordial ones separately. The table contains numbers for out, $side$, $long$ and $time$ components. Precision of each number is of the order of ~ 1 %.

UrQMD	out	$side$	$long$	$time$
All: mean value	-2.088	0.002	0.002	0.917
All: RMS value	11.333	10.274	15.719	17.484
Primary: mean value	-2.342	0.001	0.002	1.815
Primary: RMS value	8.218	7.602	12.629	14.826
EPOS	out	$side$	$long$	$time$
All: mean value	-0.626	0.000	0.005	0.277
All: RMS value	5.820	5.059	7.338	7.427
Primary: mean value	-0.120	0.001	0.004	0.613
Primary: RMS value	3.832	3.633	6.121	5.038

Table 9.10: Mean values and RMS for two-proton separation distributions for all particles and only primordial ones separately. The table contains numbers for out, $side$, $long$ and $time$ components. Precision of each number is of the order of ~ 1 %.

UrQMD	out	$side$	$long$	$time$
All: mean value	0.002	0.002	0.002	0.001
All: RMS value	16.784	14.307	17.728	20.542
Primary: mean value	0.001	0.002	0.001	0.001
Primary: RMS value	9.517	8.397	11.366	16.527
EPOS	out	$side$	$long$	$time$
All: mean value	-0.004	0.002	0.006	-0.004
All: RMS value	4.344	3.955	4.611	4.516
Primary: mean value	0.003	0.000	0.000	-0.003
Primary: RMS value	3.763	3.714	4.268	3.435

Table 9.11: Mean values and RMS for two - anti-proton separation distributions for all particles and only primordial ones separately. The table contains numbers for out, $side$, $long$ and $time$ components. Precision of each number is of the order of ~ 1 %.

UrQMD	out	$side$	$long$	$time$
All: mean value	0.000	0.002	0.004	0.004
All: RMS value	10.381	8.624	11.781	16.123
Primary: mean value	-0.001	0.002	0.002	0.003
Primary: RMS value	8.904	7.622	10.335	15.339
EPOS	out	$side$	$long$	$time$
All: mean value	-0.013	0.005	-0.009	-0.003
All: RMS value	4.372	3.966	4.541	4.507
Primary: mean value	-0.008	-0.002	-0.001	-0.001
Primary: RMS value	3.798	3.712	4.138	3.403

Table 9.12: Mean values and RMS for proton - anti-proton separation distributions for all particles and only primordial ones separately. The table contains numbers for out, $side$, $long$ and $time$ components. Precision of each number is of the order of ~ 1 %.

UrQMD	out	$side$	$long$	$time$
All: mean value	-6.481	0.004	0.004	6.770
All: RMS value	13.910	12.187	15.949	19.051
Primary: mean value	-0.818	0.003	0.002	1.591
Primary: RMS value	9.160	8.374	11.191	15.913
EPOS	out	$side$	$long$	$time$
All: mean value	-0.059	-0.005	0.013	0.048
All: RMS value	4.281	3.878	4.586	4.5087
Primary: mean value	-0.051	-0.003	-0.005	0.0323
Primary: RMS value	3.689	3.627	4.204	3.410

Glossary

Presented definitions refer to the subject of discussed here work. They may not contain full information about defined term.

Anti-particle - a particle associated with every particle, it is characterized by exactly the same mass and life-time, but opposite values of electric charge, magnetic moment, baryon number and flavor.

Baryon - the family of subatomic particles which are made of three quarks. The family includes the proton and neutron, which build up the atomic nucleus.

Big Bang - the cosmological model of the universe whose primary assertion is that the universe has expanded into its current state from a primordial condition of enormous density and temperature.

Boson - particles with an integer spin, they obey Bose-Einstein statistics, i.e. the wave-function describing two identical bosons is symmetric under particle exchange.

Bottom quark - quark which is also called 'beauty' quark, it has electric charge $-1/3|e|$, it was discovered in the form of upsilon meson ($b\bar{b}$).

Charm quark, charmonium - quark of electric charge $+2/3|e|$, it forms charmonium state $J/\Psi = c\bar{c}$

Chirality - Mathematically, it is the sign of the projection of the spin vector onto the momentum. Mass-less particles such as the photon or the gluon have absolute chirality: a mass-less particle appears to have spin in the same direction along its axis of motion regardless of point of view of the observer. A mass-less particle moves with the speed of light, so a real observer (who must always moves slower than the speed of light) cannot be in any reference frame where the particle appears to reverse its relative direction, meaning that

all real observers see the same chirality. Because of this, the direction of spin of mass-less particles is not affected by a Lorentz boost (change of viewpoint) in the direction of motion of the particle, and chirality is fixed for all reference frames, it is absolute. Particles which do have mass such as electrons or quarks have relative chirality, which depends on the observer's reference frame. In the case of these particles, it is possible for an observer to change to a reference frame that overtakes the spinning particle, in which case the particle will then appear to move backwards, and its apparent chirality will reverse.item [Color] - a fundamental property of quarks, was given to the strong charge of quarks, which interact with each other. As more than one fermion cannot exist in the same state with another fermion, color differs them.

Collider - a type of a particle accelerator involving two beams of particles approaching directly against each other. Particles collide moving in opposite directions.

Confinement - a property of strong color interaction between quarks, where quarks cannot exist in a single states, but they has to be bound inside hadrons.

Correlation function (of two particles with close velocities) - a function illustrating FSI and/or QS (depending on system) which allows one to deduce source size.

Cross section - the rate of particular reaction. This is an effective area subtended by the target particle to an incident beam. It is numerically equal to the reaction rate per target particle per unit incident flux.

Debye-screening - The effect known in electrostatics, in the case of few electric charges, the effective potential of interaction depends on e.g. Debye screening radius, which lead to that the electrical charge of some sources is screened by another ones. Then, it was proposed that similar screening can occur in QGP, and the interaction between quark 'c' and their anti-quark (J/Psi particle) becomes weaker with increasing their relative distance; thus production of J/Psi particle was proposed as one of signature of QCD.

Fermion - particles with a half-integer spin, such as protons and electrons. They obey Fermi-Dirac statistics, i.e. the wave-function describing two identical fermions is anti-symmetric under particle exchange.

Flavor - a generic name to describe different types of quarks (up, down, strange, charm, top, bottom).

FSI - Final State Interaction (Coulomb and Strong) present during final state of source evolution, in two-particle correlations FSI are reflected in the shape of correlation function

Flow - a collective motion of matter created in heavy-ion collisions.

Freeze-out - final part of hadronization, it can be thermal or chemical. After this part of source evolution- hadrons and other products move to detector and can be identified in the case, when do not decay before registration.

Gluon - elementary particle that cause quarks to interact, and is indirectly responsible for the binding of protons and neutrons together in atomic nuclei.

Hadron - strongly interacting composite subatomic particle. All hadrons are composed of quarks. Hadrons are divided into classes of mesons and baryons.

Hadronization - the process of the formation of hadrons out of quarks and gluons.

Hyperon - subatomic particle which is a baryon (and hence a hadron and a fermion) with non-zero strangeness, but with zero charm and zero bottomness.

Hydrodynamics - is a branch of theoretical fluid dynamics which deals with flow of an ideal fluid. An ideal fluid is both incompressible and inviscid.

Impact parameter b - parameter describing a collision centrality; it is the length of vector connecting centers of collided nuclei, while nuclei are collided. In the case of central collisions, parameter [b]=0, for non-central ones can achieve even two radii of nuclei; for ultra-peripheral collisions it exceeds [2R] (in symmetric collisions of two identical nuclei, where [R] is the radius of one nucleus).

Isospin - a quantum number related to the strong interaction and applies to the interactions of the neutron and proton, it differs proton and neutron.

Jet - a stream of particles produced in hard processes.

Meson - a strongly interacting boson, a hadron with integral spin, it is composed of combination of valence quark and anti-quark.

Mini-jet - is a pair of partons which go in opposite directions (like standard jet), but their transverse momentum can be considered as a lower limit of hard processes ($p_t \geq 2$ GeV).

Participant (of a collision) - part of collided nuclei which directly take part in the collision.

Resonance - unstable hadron due to strong interactions.

SH - Spherical Harmonics are angular portion of an orthogonal set of solutions to Laplace's equation represented in a system of spherical coordinates.

Spectator (of a collision) - nucleon from collided nuclei that does not take part during collision directly.

QED - Quantum electrodynamics (is a relativistic quantum field theory of electrodynamics. QED was developed by a number of physicists, beginning in the late 1920s, it mathematically describes all phenomena involving electrically charged particles interacting by means of exchange of photons.

QCD - Quantum chromodynamics is theory of the strong interaction (color force), a fundamental force describing the interactions of the quarks and gluons found in hadrons (such as the proton, neutron or pion). QCD is a quantum field theory of a special kind called a non-abelian gauge theory. It is an important part of the Standard Model of particle physics. A huge body of experimental evidence for QCD has been gathered over the years.

QGP - a quark-gluon plasma is a phase of quantum chromodynamics (QCD) which exists at extremely high temperature and/or density. This phase consists of (almost) free quarks and gluons which are the basic building blocks of matter.

QS - Quantum Statistics, a calculation of quantum mechanics for identical fermions or bosons.

Rapidity - a variable connects energy and longitudinal component of momentum: $y = \frac{1}{2} ln \left(\frac{E+p_z}{E-p_z} \right)$. Another relations are given: $dy = \frac{dp_Z}{E}$, cosy=$\frac{E}{m_T}$ and siny=$\frac{p_z}{m_T}$, where $m_T = \sqrt{m^2 + p_T^2}$ is a transverse mass and $E = \sqrt{p^2 + m^2}$.

Thermodynamics - a branch of physics that studies the effects of changes in temperature, pressure, and volume on physical systems at the macroscopic scale by analyzing the collective motion of their particles using statistics.

List of publications

1. Forward Lambda production and nuclear stopping power in d + Au collisions at $\sqrt{s_{NN}} = 200$ GeV; STAR Collaboration (B.I. Abelev, H.P. Gos et al.); Submitted to Phys.Rev.C; arXiv:0706.0472 [nucl-ex]

2. Measurement of transverse single-spin asymmetries for di-jet production in proton-proton collisions at $\sqrt{s_{NN}} = 200$GeV; STAR Collaboration (B.I. Abelev, H.P. Gos et al.); Phys.Rev.Lett.99:142003,2007; arXiv:0705.4629 [hep-ex]

3. Proton proton, anti-proton anti-proton, proton anti-proton correlations in Au + Au collisions measured by STAR at RHIC; H.P. Gos; Eur.Phys.J.C49:75-80,2007.

4. Enhanced strange baryon production in Au + Au collisions compared to p + p at $\sqrt{s_{NN}} = 200$GeV; STAR Collaboration (B.I. Abelev, H.P. Gos et al.); Submitted to Phys.Rev.Lett, arXiv:0705.2511 [nucl-ex]

5. Global polarization measurement in Au+Au collisions; STAR Collaboration (B.I. Abelev, H.P. Gos et al.); Phys.Rev.C76:024915,2007; arXiv:0705.1691 [nucl-ex]

6. Energy dependence of pi+-, p and anti-p transverse momentum spectra for Au+Au collisions at $\sqrt{s_{NN}} = 62$ and 200GeV; STAR Collaboration (B.I. Abelev, H.P. Gos et al.); Phys.Lett.B655:104-113,2007; nucl-ex/0703040

7. Partonic flow and phi-meson production in Au + Au collisions at $\sqrt{s_{NN}} = 200$GeV; STAR Collaboration (B.I. Abelev, H.P. Gos et al.); Phys.Rev.Lett.99:112301,2007; nucl-ex/0703033

8. Charged particle distributions and nuclear modification at high rapidities in d + Au collisions at $\sqrt{s_{NN}} = 200$GeV; STAR Collaboration (B.I. Abelev, H.P. Gos et al.); Submitted to Phys.Lett.B; nucl-ex/0703016

9. Mass, quark-number, and $\sqrt{s_{NN}}$ dependence of the second and fourth flow harmonics in ultra-relativistic nucleus-nucleus collisions; STAR Collaboration (B.I. Abelev, H.P. Gos et al.); Phys.Rev.C75:054906,2007; nucl-ex/0701010

10. Baryon - baryon correlations in Au+Au collisions at $\sqrt{s_{NN}} = 62$ and $\sqrt{s_{NN}} = 200$GeV, measured in the STAR experiment at RHIC; H.P. Gos; Nukleonika, Vol. 51, supplement 3, nucl-ex/0610030

11. Rapidity and species dependence of particle production at large transverse momentum for d+Au collisions at $\sqrt{s_{NN}} = 200$GeV; STAR Collaboration (B.I. Abelev, H.P. Gos et al.); Phys.Rev.C76:054903,2007; nucl-ex/0609021

12. Longitudinal double-spin asymmetry and cross section for inclusive jet production in polarized proton collisions at $\sqrt{s_{NN}} = 200$GeV; STAR Collaboration (B.I. Abelev, H.P. Gos et al.); Phys.Rev.Lett.97:252001,2006; hep-ex/0608030

13. Neutral kaon interferometry in Au+Au collisions at $\sqrt{s_{NN}} = 200$GeV; STAR Collaboration (B.I. Abelev, H.P.Gos et al.); Phys.Rev.C74:054902,2006; nucl-ex/0608012

14. Strange particle production in p+p collisions at $\sqrt{s_{NN}} = 200$GeV; STAR Collaboration (B.I. Abelev, H.P. Gos et al.); Phys.Rev.C75:064901,2007; nucl-ex/0607033

15. Transverse momentum and centrality dependence of high-p(T) non-photonic electron suppression in Au+Au collisions at $\sqrt{s_{NN}} = 200$GeV; STAR Collaboration (B.I. Abelev, H.P. Gos et al.); Phys.Rev.Lett.98:192301,2007; nucl-ex/0607012

16. Delta phi Delta eta Correlations in Central Au+Au Collisions at $\sqrt{s_{NN}} = 200$GeV; STAR Collaboration (J. Adams, H.P. Gos et al.); Phys.Rev.C75:034901,2007; nucl-ex/0607003

17. The particle interferometry method as a tool reflecting evolution of hadron source; H.P. Gos; AIP Conf.Proc.828:458-463,2006

18. The Multiplicity dependence of inclusive p(t) spectra from p-p collisions at $\sqrt{s_{NN}} = 200$GeV; STAR Collaboration (J. Adams, H.P. Gos et al.); Phys.Rev.D74:032006,2006; nucl-ex/0606028

19. Scaling Properties of Hyperon Production in Au+Au Collisions at $\sqrt{s_{NN}} = 200$GeV; STAR Collaboration (J. Adams, H.P. Gos et al.); Phys.Rev.Lett.98:062301,2007; nucl-ex/0606014

20. Identified baryon and meson distributions at large transverse momenta from Au+Au collisions at $\sqrt{s_{NN}} = 200$GeV; STAR Collaboration (B.I. Abelev, H.P. Gos et al.); Phys.Rev.Lett.97:152301,2006; nucl-ex/0606003

21. The Energy dependence of p(t) angular correlations inferred from mean-p(t) fluctuation scale dependence in heavy ion collisions at the SPS and RHIC; STAR Collaboration (J. Adams, H.P. Gos et al.); J.Phys.G33:451-466,2007; nucl-ex/0605021

22. Strange baryon resonance production in $\sqrt{s_{NN}} = 200$GeV p+p and Au+Au collisions; STAR Collaboration (J. Adams, H.P. Gos et al.); Phys.Rev.Lett.97:132301,2006; nucl-ex/0604019

23. Direct observation of di-jets in central Au+Au collisions at $\sqrt{s_{NN}} = 200$GeV;STAR Collaboration (J. Adams, H.P. Gos et al.); Phys.Rev.Lett.97:162301,2006; nucl-ex/0604018

24. Forward neutral pion production in p+p and d+Au collisions at $\sqrt{s_{NN}} = 200$GeV; STAR Collaboration (J. Adams, H.P. Gos et al.); Phys.Rev.Lett.97:152302,2006; nucl-ex/0602011

25. Measurements of identified particles at intermediate transverse momentum in the STAR experiment from Au + Au collisions at $\sqrt{s_{NN}} = 200$GeV; STAR Collaboration (J. Adams, H.P. Gos et al.); Submitted to Phys.Rev.C; nucl-ex/0601042

26. Identified hadron spectra at large transverse momentum in p+p and d+Au collisions at $\sqrt{s_{NN}} = 200$GeV; STAR Collaboration (J. Adams, H.P. Gos et al.); Phys.Lett.B637:161-169,2006; nucl-ex/0601033

27. Recent high-PT Results from STAR; STAR Collaboration (C.A. Gagliardi, H.P. Gos et al.); Eur.Phys.J.C43:263-270,2005

28. Charm Production in the STAR Experiment at RHIC, By STAR Collaboration (A.A.P. Suaide, H.P. Gos et al.). 2005, Eur.Phys.J.C43:193-200,2005

29. Open Charm Production from d+Au Collisions in STAR, STAR Collaboration (M. Calderon de la Barca Sanchez, H.P. Gos et al.); Eur.Phys.J.C43:187-192,2005

30. Strangelet Search at RHIC, STAR Collaboration (J. Adams, H.P. Gos et al.); Phys.Rev.C76: 011901,2007; nucl-ex/0511047

31. Multiplicity and Pseudorapidity Distributions of Charged Particles and Photons at Forward Pseudorapidity in Au+Au Collisions at $\sqrt{s_{NN}} = 62$GeV; STAR Collaboration (J. Adams, H.P. Gos et al.); Phys.Rev.C73:034906,2006; nucl-ex/0511026

32. Proton - lambda correlations in central Au+Au collisions at $\sqrt{s_{NN}} = 200$GeV; STAR Collaboration (J. Adams, H.P. Gos et al.); Phys.Rev.C74:064906,2006; nucl-ex/0511003

33. Directed Flow in Au+Au Collisions at $\sqrt{s_{NN}} = 62$GeV, STAR Collaboration (J. Adams, H.P. Gos et al.); Phys.Rev.C73:034903,2006; nucl-ex/0510053

34. Transverse Momentum p(T) Correlations on (Eta, Phi) from Mean p(T) Fluctuations in Au+Au Collisions at $\sqrt{s_{NN}} = 200$ GeV, STAR Collaboration (J. Adams, H.P. Gos et al.); J.Phys.G32:L37-L48,2006; nucl-ex/0509030

35. Incident Energy Dependence of p(T) Correlations at RHIC; STAR Collaboration (J. Adams, H.P. Gos et al.); Phys.Rev.C72:044902,2005; nucl-ex/0504031

36. Multi-strange Baryon Elliptic Flow in Au+Au Collisions at $\sqrt{s_{NN}} = 200$ GeV, STAR Collaboration (J. Adams, H.P. Gos et al.); Phys.Rev.Lett.95:122301,2005; nucl-ex/0504022

List of presentations

1. 04.02-10.02.2008; Quark Matter 2008; Jaipur, India; Poster: Baryon correlations in STAR
2. 01.08- 03.08.2007; Workshop on Particle Correlations and Femtoscopy; Santa Rosa; USA; Proton correlations in STAR.
3. 19.05- 26.05.2007; School on Collective Dynamics; Berkeley, San Francisco, USA; Proton-proton correlations in STAR
4. 19.02- 24.02.2007; Workshop of European Research Group on Ultra relativistic Heavy Ion Physics; Grybow, Poland; Proton femtoscopy in STAR
5. 19.02- 24.02.2007; Workshop of European Research Group on Ultra relativistic Heavy Ion Physics; Grybow, Poland; Hadron correlations in EPOS and UrQMD models
6. 09.02.2007; Given for: PLASMA group (SUBATECH) ; Nantes, France; Proton femtoscopy in STAR
7. 11.12- 13.12.2006; RHIC Winter School; Budapest, Hungary; Proton femtoscopy in STAR
8. 14.11- 20.11.2006; Quark Matter 2006; Shanghai, China; Poster: Proton femtoscopy in STAR
9. 25.09- 29.09.2006; SPHIC 2006; Catania, Italy; Proton femtoscopy in STAR
10. 10.07- 24.07.2006; Workshop: GDRE 2006; Nantes, France; Proton-proton correlations at STAR
11. 15.05- 20.05.2006; Hot Quarks 2006; Sardinia, Italy; Proton-proton correlations at STAR
12. 25.04.2006; Femtoscopy In Heavy Ion Collisions; Warsaw, Poland; HBT correlations at STAR

13. 09.03- 14.03.2006; Workshop of European Research Group on Ultrarelativistic Heavy Ion Physics; Dubna, Russia; Baryon-baryon correlations at STAR

14. 05.12- 07.12.2005; RHIC Winter School 05; Budapest, Hungary; Residual correlations in the STAR experiment

15. 31.08- 06.09.2005; Mazurian Lakes Conference on Physics; Piaski, Poland; Baryon- baryon correlations in the STAR experinent

16. 15.08- 17.08.2005; Workshop on Particle Correlations and Femtoscopy; Kromeriz, Czech Republic; Two- particle interferometry as method reflecting evolution of hadron source

17. 04-09.08.2005; Quark Matter Place: Budapest, Hungary; Poster: Baryon- baryon correlations in Au+Au collisions at sqrt(sNN)= 62GeV and sqrt(sNN)=200GeV measured in the STAR experiment at RHIC

18. 27.07- 02.08.2005; Star Collaboration Meeting- Pararell Session; Warsaw, Poland; Baryon-baryon correlations at STAR

19. 27.07- 02.08.2005; Star Collaboration Meeting- Juniors Session; Warsaw, Poland; Proton-proton correlations at STAR

20. 15.06- 15.07.2005; GDRE Meeting; Nantes, France; Particle correlations at STAR from the Other Side Of Mirror

21. 15.06- 15.07.2005; GDRE Meeting; Nantes, France; Analysis of particle correlations in the reactions: Au+Au, d+Au, p+p at RHIC

22. 05.06.2005; Given for: SUBATECH- Plasma Group; Nantes, France; Analysis of particle correlations in the reactions: Au+Au, d+Au, p+p at RHIC

23. 17.02.2005; Ohio State University; Columbus, USA; Non-identical particle correlations at the STAR experiment

24. 01.12- 03.12.2004; RHIC Winter School 04; Budapest, Hungary; Non-identical particle correlations at the STAR experiment

Bibliography

[1] U.W. Heinz; Concepts of heavy-ion physics; European School of High-Energy Physics (ESHEP 2002), Pylos, Greece, 25 Aug - 7 Sep 2002; Pylos 2002, High-energy physics; 127-178

[2] M. J. Tannenbaum; Heavy-ion Physics at RHIC; Proceedings of Symposium "50+ Years of High Energy Physics at UB", University at Buffalo, NY, October 20-21,2006

[3] M. Gasperini; Elementary introduction to pre-big bang cosmology and to the relic graviton background; Second SIGRAV School on “Gravitational Waves in Astrophysics, Comology and String Theory" (Villa Olmo, Como, 19-24 April 1999); arXiv:hep-th/9907067

[4] F. Karsch; Lattice QCD at high temperature and the QGP; AIP Conf.Proc.842:20-28,2006

[5] K. Redlich; Heavy ion collisions and lattice QCD at finite baryon density; 17th International Conference on Ultra Relativistic Nucleus-Nucleus Collisions (Quark Matter 2004), Oakland, California, 11-17 Jan 2004; J.Phys.G30:S1271-S1274,2004

[6] D. Kharzeev; QCD and heavy ions; Nucl.Phys.A699:95-102,2002

[7] E. V. Shuryak; Quark-Gluon Plasma and Hadronic Production of Leptons, Photons and Pions; Phys.Lett.B78:150,197

[8] J. Engels, O. Kaczmarek, F. Karsch, E. Laermann; The Quenched limit of lattice QCD at nonzero baryon number; Nucl.Phys.B558:307-326,1999

[9] E. V. Shuryak; The Role of Instantons in Quantum Chromodynamics. 3. Quark - Gluon Plasma; Nucl.Phys.B203:140,1982

[10] F. Karsch, 15th International Conference on Ultra-Relativistic Nucleus-Nucleus Collisions (QM 2001), Long Island, New York, January 15 - 20, 2001; Classical Chromo-Dynamics of Relativistic heavy-ion Collisions; Nucl.Phys. A698 (2002) 199-208

[11] M. Gyulassy, L. McLerran; New Forms of QCD Matter Discovered at RHIC; RBRC Scientific Artricles Vol.9, New Discoveries at RHIC: the current case for the strongly interactive QGP, BNL May 14,15 2004; Nucl.Phys. A750 (2005) 30-63

[12] M.J.Herrero; The Standard Model; Lectures presented at the NATO ASI 98 School, Techniques and Concepts of High Energy Physics; St. Croix, Virgin Islands, USA, June 18-29 1998; arXiv:hep-ph/9812242

[13] N. Cottingham, D.A. Greenwood, Derek A. Greenwood; An Introduction to the Standard Model of Particle Physics; Cambridge University Press, 1999

[14] W. Busza, A. S. Goldhaber; Nuclear Stopping Power; Phys.Lett.B139:235,1984

[15] J.D. Bjorken; QCD and the Space-Time Evolution of High-Energy e+ e-, p anti-p, and Heavy Ion Collisions; Stockholm Phys.in Coll.1982:0343

[16] J. Castillo, "Production de particules doublement etranges dans les collisions d'ions lourds ultra-relativistic a $\sqrt{s_{NN}}$=130 GeV"- Ph. D. thesis; Universite de Paris; 2002

[17] PHENIX Collaboration (S.S. Adler et al.); Identified charged particle spectra and yields in Au+Au collisions at $\sqrt{s_{NN}}$ = 200GeV; Phys.Rev.C69 (2004) 034909

[18] P. Braun-Munzinger, D. Magestro, K. Redlich, J. Stachel; Hadron production in Au-Au collisions at RHIC; Phys.Lett. B518 (2001) 41-46

[19] P. Braun-Munzinger, J. Stachel, C. Wetterich; Chemical freezeout and the QCD phase transition temperature; Phys.Lett.B596:61-69,2004

[20] BRAHMS Collaboration; Quark gluon plasma and color glass condensate at RHIC? The Perspective from the BRAHMS experiment; Nucl.Phys.A757:1-27,2005

[21] J. Rafelski, B. Muller; Strangeness Production in the Quark - Gluon Plasma; Phys.Rev.Lett.48:1066,1982, Erratum-ibid.56:2334,1986

[22] H. Caines, What's Interesting About Strangeness Production? - An Overview of Recent Results; J.Phys. G31 (2005) S101-S118

[23] http://wa97.web.cern.ch/WA97/

[24] STAR Collaboration, Enhanced strange baryon production in Au+Au collisions compared to p+p at $\sqrt{(}sNN) = 200$ GeV; arxiv: 0705.2511

[25] STAR Collaboration; Kaon Production and Kaon to Pion Ratio in Au + Au Collisions at $\sqrt{s_{NN}} = 130$ GeV; Phys. Lett. B 595 (2004) 143

[26] Pion and kaon production in central Pb+Pb collisions at 20A and 30A GeV: Evidence for the onset of deconfinement; NA49 Collaboration; arXiv:0710.0118

[27] http://na49info.web.cern.ch/na49info/

[28] J. Y. Ollitrault; Anisotropy as a signature of transverse collective flow; Phys.Rev.D46:229-245,1992

[29] STAR Collaboration; Identified Particle Elliptic Flow in Au+Au Collisions at $\sqrt{s_{NN}} = 130$ GeV; Phys.Rev.Lett. 87 (2001) 182301

[30] STAR Collaboration: J. Adams, et al; Experimental and Theoretical Challenges in the Search for the Quark Gluon Plasma: The STAR Collaboration's Critical Assessment of the Evidence from RHIC Collisions; Nucl.Phys. A757 (2005) 102-183

[31] B.B.Back et al (PHOBOS Collaboration); The PHOBOS Perspective on Discoveries at RHIC; Nucl.Phys. A757 (2005) 28-101

[32] T. Hallman; Quark Matter 2008 presentation.

[33] J. Adams, et al. (STAR Collaboration); Transverse momentum and collision energy dependence of high p_T hadron suppression in Au+Au collisions at ultrarelativistic energies; Phys.Rev.Lett. 91 (2003) 172302

[34] Physical Review Letters; Volume 91,Number 7 (2003) - cover

[35] STAR collaboration (M.J. Russcher for the collaboration); Direct photons in d+Au collisions at $\sqrt{s_{NN}} = 200$ GeV with STAR; Eur.Phys.J. C49 (2007) 231-234

[36] Phenix Collaboration; Centrality Dependence of Direct Photon Production in $\sqrt{s_{NN}} = 200$ GeV Au+Au Collisions; Phys.Rev.Lett. 94 (2005) 232301; arXiv:nucl-ex/0503003

[37] http://na50.web.cern.ch/NA50/

[38] P. Bordelo for the NA50 Collaboration; Recent Results on J/PSI from experiment; Nuclear Physics A698 (2002) 127c-134c

[39] STAR Collaboration; Transverse momentum and centrality dependence of high-p(T) non-photonic electron suppression in Au+Au collisions at $\sqrt{s_{NN}} = 200$ GeV; Phys. Rev. Lett.98 (2007) 192301; arXiv:nucl-ex/0607012

[40] PHENIX Collaboration; Energy Loss and Flow of Heavy Quarks in Au+Au Collisions at $\sqrt{s_{NN}} = 200$ GeV; Phys. Rev. Lett. 98 (2007), 172301; arXiv: nucl-ex/0611018

[41] E. Shuryak; The conical flow from quenched jets in sQGP; Nucl.Phys. A783 (2007) 31-38; nucl-th/0609013

[42] http://www-nsdth.lbl.gov/~xnwang/hijing/

[43] http://th.physik.uni-frankfurt.de/~urqmd/

[44] M. Bleicher, E. Zabrodin, C. Spieles, S.A. Bass, C. Ernst, S. Soff, L. Bravina, M. Belkacem, H. Weber, H. Stoker, W. Greiner; Relativistic Hadron-Hadron Collisions in the Ultra-Relativistic Quantum Molecular Dynamics Model (UrQMD); J.Phys. G25 (1999) 1859-1896

[45] S.A. Bass et al; Microscopic models for ultrarelativistic heavy ion collisions; Prog.Part.Nucl.Phys.41:255-369,1998, Prog.Part.Nucl.Phys.41:225-370,1998

[46] http://www-subatech.in2p3.fr/~theo/qmd/versions/qmdvers/node4.html

[47] http://tonic.physics.sunysb.edu/program/rqmd.html

[48] K. Werner, F. Ming Liu, T. Pierog; Parton ladder splitting and the rapidity dependence of transverse momentum spectra in deuteron-gold collisions at RHIC; Phys.Rev.C74:044902,2006

[49] D. H. Rischke, S.Bernard, J. A. Maruhn; Relativistic Hydrodynamics for Heavy–Ion Collisions – I. General Aspects and Expansion into Vacuum; Nucl.Phys. A595 (1995) 346-382

[50] D. H. Rischke, S.Bernard, J. A. Maruhn; Relativistic Hydrodynamics for Heavy–Ion Collisions – II. Compression of Nuclear Matter and the Phase Transition to the Quark–Gluon Plasma; Nucl.Phys. A595 (1995) 383-408; Erratum-ibid. A596 (1996) 717

[51] R. Lednicky; Correlation femtoscopy; Nucl.Phys. A774 (2006) 189-198

[52] R. Hanbury Brown, R.Q. Twiss; A Test of a new type of stellar interferometer on Sirius; Nature 178:1046-1048,1956

[53] R. Lednicky, V. Lyuboshitz; Spin correlations and consequences of quantum mechanical coherence; Phys.Lett.B508:146-154,2001; hep-ph/0102333

[54] G.I. Kopylov, M.I. Podgoretski; Correlations of identical particles emitted by highly excited nuclei; Sov.J.Nucl.Phys.15:219-223,1972, Yad.Fiz.15:392-399,1972

[55] R. Lednicky, V. Lyuboshitz; Effect of the relativistic spin rotation on two particle spin composition; Phys.Part.Nucl.35:S50-S53,2004; hep-ph/0302136

[56] B. Erazmus, R. Lednicky, V. Lyuboshitz; Multiboson effects in multiparticle production; Phys.Rev.C61:034901,2000; nucl-th/9911055

[57] M.I. Podgoretsky; On The Comparison Of Identical Pion Correlations In Different Reference Frames. (In Russian); Sov.J.Nucl.Phys.37:272,1983; Yad.Fiz.37:455-463,1983.

[58] G. Bertsch, M. Gong, M. Tohyama; Pion Interferometry in Ultrarelativistic Heavy Ion Collisions; Phys.Rev.C37:1896-1900,1988

[59] R. Lednicky, V.L. Lyuboshits; Final State Interaction Effect on Pairing Correlations Between Particles with Small Relative Momenta; Sov.J.Nucl.Phys.35:770,1982 and in Proceedings of the International Workshop on Particle Correlations and Interferometry in Nuclear Collisions (CORINNE 90), Nantes, 1990, Ed. by D. Ardouin (World Sci., Singapore, 1990), p. 42

[60] M. Gyulassy, S.K. Kauffmann, L.W. Wilson; Pion Interferometry of Nuclear Collisions. 1. Theory; Phys.Rev.C20:2267-2292,1979

[61] Alice Collaboration; ALICE: Physics Performance Report, J. Phys. G: Nucl. Part. Phys. 32 1295-2040; Section 6.3

[62] R. Lednicky, V.L. Lyuboshits, B. Erazmus, D. Nouais; How to measure which sort of particles was emitted earlier and which later; Phys.Lett.B373:30-34,1996

[63] A. Kisiel; private communication

[64] J. Adams, et al. (STAR collaboration); Pion-Kaon correlations in central Au+Au collisions at $\sqrt{s_{NN}} = 130$ GeV; Phys.Rev.Lett. 91 (2003) 262302

[65] STAR Collaboration (M. Lopez-Noriega for the collaboration); Pion interferometry in Au+Au collisions at $\sqrt{s_{NN}} = 200$ GeV; Phys.Rev. C71 (2005) 044906

[66] M. G. Bowler; Coulomb corrections to Bose-Einstein correlations have been greatly exaggerated; Phys.Lett.B270:69-74,1991

[67] Y. Sinyukov, B. Erazmus, J. Pluta, R. Lednicky; Coulomb corrections for interferometry analysis of expanding hadron systems; Phys.Lett.B432:248-257,1998

[68] Z. Chajecki; Identical particle correlations in STAR; 18th International Conference on Ultrarelativistic Nucleus-Nucleus Collisions: Quark Matter 2005 (QM 2005), Budapest, Hungary, 4-9 Aug 2005, Nucl.Phys.A774:599-602,2006

[69] M. Lisa, S. Pratt, R. Soltz, U. Wiedemann; Femtoscopy in Relativistic heavy-ion Collisions: Two Decades ofProgress; Ann.Rev.Nucl.Part.Sci. 55 (2005) 357-402

[70] S.E. Koonin; Proton Pictures of High-Energy Nuclear Collisions; Phys.Lett.B70:43-47,1977

[71] FOPI Collaboration; Two-proton small-angle correlations in central heavy-ion collisions: A Beam-energy and system-size dependent study; Eur.J.Phys.A23:271-278,2005

[72] By FOPI Collaboration; On the space-time difference of proton and composite particle emission in central heavy ion reactions at 400-A/MeV; Eur.Phys.J.A6:185-195,1999

[73] E814/E877 Collaboration; Two proton correlations from 14.6a-GeV / c Si +Pb and 11.5a-GeV / c Au + Au central collisions; Phys.Rev.C60:054905,1999

[74] E877 Collaboration; Proton and pion production relative to the reaction plane in Au + Au collisions at AGS energies; Phys.Rev.C56:3254-3264,1997

[75] NA44 Collaboration; Two proton correlations near mid-rapidity in p + Pb and S + Pb collisions at the CERN SPS; Phys.Lett.B458:181-189,1999

[76] NA49 Collaboration; Two proton correlations from 158-A-GeV Pb + Pb central collisions; Phys.Lett.B467:21-28,1999

[77] F. Retiere, M. Lisa; Observable implications of geometrical and dynamical aspects of freeze-out in heavy-ion collisions; Phys.Rev. C70 (2004) 044907

[78] R. Lednicky, V. Lyuboshitz, Yu. Sinyukov, B. Erazmus et al; Multiboson effects in multiparticle production; Phys.Rev.C61:034901,2000

[79] STAR Collaboration, J. Adams, et al; Proton-lambda correlations in central Au+Au collisions at $\sqrt{s_{NN}} = 200$ GeV; Phys.Rev. C74 (2006) 064906

[80] http://www.bnl.gov/rhic/

[81] http://www4.rcf.bnl.gov/brahms/WWW/

[82] http://www.phobos.bnl.gov/

[83] http://www.phenix.bnl.gov/

[84] http://www.star.bnl.gov/

[85] M. Anderson, J. Berkovitz, W. Betts et al; The STAR Time Projection Chamber: A Unique Tool for Studying High Multiplicity Events at RHIC; Nucl.Instrum.Meth. A499 (2003) 659-678; arXiv:nucl-ex/0301015

[86] R. J. Glauber; Asymptotic Theory Of Diffractive Scattering; Phys.Lett.B104:389,1981

[87] A. Kisiel, T. Taluc, W. Broniowski, W. Florkowski; THERMINATOR: THERMal heavy-IoN generATOR; Comput.Phys.Commun.174:669-687, 2006

[88] A. Kisiel, W. Broniowski, W. Florkowski; Femtoscopy in hydro-inspired models with resonances; Phys.Rev.C73:064902,2006

[89] W. Broniowski, W. Florkowski; Thermal model for RHIC. Part 1. Particle ratios and spectra; AIP Conf.Proc.660:177-184,2003; nucl-th/0212052

[90] W. Broniowski, W. Florkowski; A. Baran; Thermal model at RHIC. Part 2. Elliptic flow and HBT radii; AIP Conf.Proc.660:185-195,2003; nucl-th/0212053

[91] H.P. Gos for the STAR Collaboration; Baryon-baryon correlations in Au+Au collisions at $\sqrt{s_{NN}} = 62$ GeV and $\sqrt{s_{NN}} = 200$ GeV, measured in the STAR experiment at RHIC; Nukleonika 51(Supplement 3) (2006) 59-63

[92] http://aliceinfo.cern.ch/

[93] H.P. Gos for the STAR Collaboration; Proton proton, anti-proton anti-proton, proton anti-proton correlations in Au + Au collisions measured by STAR at RHIC; Eur.Phys.J.C49 (2007) 75-80

[94] BRAHMS Collaboration; Quark gluon plasma and color glass condensate at RHIC? The Perspective from the BRAHMS experiment; Nucl.Phys.A757:1-27,2005

[95] P. Danielewicz, S. Pratt; Analyzing correlation functions with tesseral and cartesian spherical harmonics; Phys.Rev.C75:034907,2007; nucl-th/0612076

[96] Z. Chajecki, M. A. Lisa; Global conservation laws and femtoscopy of small systems; Braz.J.Phys.37:1057-1064,2007; nucl-th/0612080

[97] Z. Chajecki; private communication

[98] D. Perkins; Introduction to High Energy Physics; Cambridge University Press, 4th Edition, 2000

[99] M. Gell-Mann; A Schematic Model of Baryons and Mesons; Phys.Lett.8:214-215,1964

[100] http://www.ligo.caltech.edu/

[101] http://www.virgo.infn.it/